

UNIVERSITÀ
DI PAVIA

SCUOLA DI ALTA FORMAZIONE DOTTORALE
MACRO-AREA SCIENZE E TECNOLOGIE

Dottorato di Ricerca in Scienze della Terra e dell'Ambiente

Niccolò Dematteis

Integrated ground-based remote sensing sensors for glaciological monitoring

Anno Accademico 2018-2019
Ciclo XXXII

Coordinatore
Prof. Roberto Sacchi

Tutor
Dott. Francesco Zucca

Co-tutors
Dott. Daniele Giordan
Dott Guido Luzi

INTEGRATED GROUND-BASED REMOTE SENSING SENSORS FOR GLACIOLOGICAL MONITORING

A thesis submitted to attain the degree of

PHILOSOPHIÆ DOCTOR IN EARTH SCIENCES

presented by

NICCOLÒ DEMATTEIS

Accepted on the recommendation of:

Dr Francesco Zucca, academic supervisor

Pavia University, Department of Earth and Environmental Sciences

Dr Daniele Giordan, co-tutor

Research Institute for Geo-Hydrological Protection

Dr Guido Luzi, co-tutor

Centre Tecnològic de Telecomunicacions de Catalunya

Prof. Àkos Török, examiner

Budapest University of Technology and Economics

Prof. Guglielmina Adele Diolaiuti, examiner

Milano University

Pavia 2020

RINGRAZIAMENTI

Questa tesi è il frutto del lavoro di quasi quattro anni svolto presso il Gruppo di Geomonitoraggio (GMG) dell'IRPI di Torino. Non mi sarebbe stato possibile raggiungere tale risultato senza il contributo dei miei tutor che mi hanno guidato lungo il percorso di dottorato elargendo preziosi consigli e critiche costruttive.

Innanzitutto sono grato al mio responsabile scientifico Daniele Giordan, che mi ha dato l'opportunità di lavorare nel GMG e che ha indirizzato la mia linea di ricerca in questi anni.

Desidero inoltre ringraziare il mio relatore Francesco Zucca e Guido Luzi, con i quali ho condiviso una comica disavventura durante una campagna di misura nelle remote Alpi Marittime.

A Francesco devo la possibilità di aver svolto il dottorato presso l'Università di Pavia, che rappresenterà una solida base per il prosieguo della mia carriera scientifica.

Ringrazio Guido per avermi ospitato presso il Centre Tecnològic de Telecomunicacions de Catalunya a Barcellona e per le chiacchierate di carattere scientifico e mondano intraprese in questi anni.

Porgo inoltre un ringraziamento speciale a tutti i miei colleghi, con i quali condivido le occupazioni quotidiane in un clima piacevole e spensierato che rendono leggero il lavoro al GMG.

Tutta la mia gratitudine è poi rivolta a mia moglie Rossella, che ha sempre supportato il mio lavoro di ricercatore anche nei momenti meno facili, e ai miei genitori, per tutto quello che hanno fatto per darmi la possibilità di giungere a praticare una professione che amo.

ACKNOWLEDGEMENTS

This thesis is the outcome of nearly four years-work carried out at the IRPI Geohazard Monitoring Group (GMG) in Torino. I would not be able to achieve such a result without the contribution of my tutors, who guided me during the doctoral program giving valuable advice and constructive critiques.

First of all, I am grateful to my scientific supervisor Daniele Giordan, who gave me the opportunity to work in the GMG and who directed my research line in these years.

I want to acknowledge my academic tutor Francesco Zucca and Guido Luzi, with whom I shared a comic misadventure during a survey campaign in the remote Maritime Alps.

I owe to Francesco the possibility to carry out the PhD at the Pavia University, which will be a solid base for my future scientific career.

I thank Guido for hosting me at the Centre Tecnològic de Telecomunicacions de Catalunya in his Barcellona and for the scientific and mundane talks in these years.

Furthermore, I give a special acknowledgement to my colleagues, with whom I share daily activities in a pleasing and cheerful atmosphere that makes light the work in the GMG.

Finally, all my gratitude is addressed to my wife Rossella, who always supported my researcher profession even in the hard times, and to my parents, for all they have done to give me the possibility to get to practise a job that I love.

TABLE OF CONTENTS

Introduction

Aim and Scope

DSLR camera

GB-SAR

Merging ICC & TRI

Case studies

Planpincieux glacier

Monte Perdido glacier

References

PhD publications

A low-cost optical remote sensing application for glacier deformation monitoring in an Alpine environment

Image Classification for Automated Image Cross-Correlation Applications in the Geosciences

Monitoring Alpine glacier surface deformations with GB-SAR

Terrestrial radar interferometry to monitor glaciers with complex atmospheric screen

Ku band terrestrial radar observations by means of circular polarized antennas.

4D surface kinematics monitoring through terrestrial radar interferometry and image cross-correlation coupling

Classification and kinematics of the Planpincieux Glacier break-offs using photographic time-lapse analysis

Ground-based remote-sensing techniques for diagnosis of the current state and recent evolution of the Monte Perdido Glacier, Spanish Pyrenees

Conclusions

INTRODUCTION

Glaciers represent the main source of freshwater for human activities of the surrounding regions (Barnett et al., 2005; Hock et al., 2005). Furthermore, glaciological processes (e.g., ice break-offs, glacier outbursts, snow/ice avalanches) can threaten the population, urban areas and infrastructures (Kääb et al., 2005). For their importance and potential hazard, it is necessary the study of their activity in order to understand their evolution and to develop strategies for preventive alert and mitigation actions.

The first step of the observation-alert-mitigation framework is the monitoring of such phenomena. One of the most relevant parameters to investigate is the surface deformation, as it provides a direct measurement of the process activity and it can give an insight into the response of glaciers to the global warming (Deline et al., 2012).

Glaciers are mostly located in the mountain environment and hence they are often placed in harsh and remote areas. A practical approach for their monitoring could be the adoption of remote-sensing apparatuses, which allow at not accessing into possible perilous investigated areas, with consequent reduction of human resources and risks.

The remote sensing systems can be classified into two main categories: i) systems installed on aerospace platforms and ii) ground-based sensors. To the first group belong satellites, aircraft and drones. The recent free availability of data acquired by satellite constellations such as Sentinel 1 and Sentinel 2 (<https://sentinel.esa.int/web/sentinel/missions>) is making their use widely adopted. However, such systems suffer limitation of low temporal resolution, with revisiting time of days or weeks, and the data availability of specific areas might not be guaranteed. Aircraft and helicopter platforms provide data of specific areas with high spatial resolution, but they require high financial costs. Moreover, complex geometries, typical of gravitational processes located in mountain areas, can affect the data acquisition from space and air.

Drones are becoming very popular in recent years (Giordan et al., 2018). In many applications, they can fill the gap between aerial- and ground-based sensors, as their cost is limited and they allow to acquire data with high spatial resolution. However, their revisiting time is constrained as they can not operate autonomously. Therefore, the use of drones in remote areas usually requires large human resources.

By contrast, ground-based apparatuses are able to acquire data in environments with complex geometry and they can often operate in continuous, providing data with high spatio-temporal resolution.

In general, a single monitoring system is able to measure specific parameters that can partially describe the state and the evolution of the investigated phenomenon. Therefore, a common approach consists in adopting different sensors and collecting separately their measurements to obtain a more comprehensive outline of the process. Often, the independent analysis of the data of each sensor might not be sufficient to exploit all the available information. For this reason, the merging different data in a coupled model can provide more informative results. Moreover, the data coupling allows at fully exploiting the qualities and potentialities of each sensor and to minimise their limits.

The realisation of an integrated system requires an accurate evaluation of the instrument capacities. The first step of such realisation involves the characterisation of the single monitoring devices. Moreover, the development of specific and innovative processing techniques might be necessary to optimise the coupling process.

Finally, the methodologies developed for processing data of single and coupled sensors can be applied to practical case studies, where the monitoring of glaciers can yield results about their current geophysical state, their dynamics and their possible evolution (Figure 1).

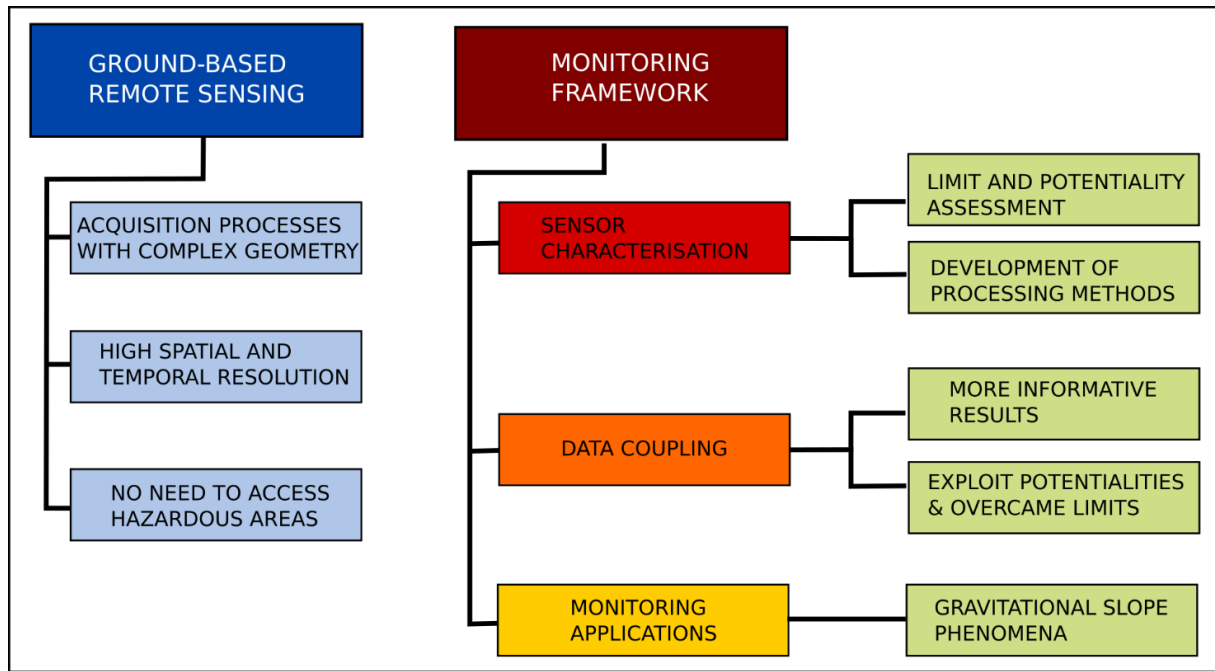


Figure 1. The integrated use of ground-based sensors allows monitoring gravitational slope phenomena with complex geometries at high spatio-temporal resolution. It requires the characterisation of the different sensors to evaluate their limits and potentialities. Then, their measurements can be coupled to obtain more informative data. Finally, the developed monitoring methodologies can be applied to observe natural phenomena.

AIM AND SCOPE

The objective of the thesis is the development of methodologies for coupling data collected by different ground-based remote sensing sensors in order to obtain 3D representations of the actual surface deformation vectors. The developed methodologies can be applied to study natural phenomena to define an interpretative model of the investigated processes. The monitoring techniques studied in the PhD have been adopted in two main case studies to detect the displacement of two mountain glaciers: the Planpincieux Glacier (Italian Alps), Monte Perdido Glacier (Spanish Pyrenees). However, such techniques might be used in general to monitor gravitational slope phenomena.

The sensors studied during the PhD are digital single-lens reflex (DSLR) camera and ground-based synthetic aperture radar (GB-SAR). The photographs acquired by the DSLR camera have been processed with image analysis techniques. In particular, the image cross-correlation (ICC) approach has been used to measure the surface deformations of Planpincieux Glacier. The ICC provides the two displacement components orthogonal to the line of sight (LOS). Furthermore, it has been developed an innovative technique to automatically apply ICC in monitoring surveys. The key of the method consists in the automatic selection of images acquired in conditions of diffuse illumination to minimise shadow-related errors.

The adoption of the terrestrial radar interferometry (TRI) to the GB-SAR data provides the surface displacement parallel to the LOS. Therefore, it is possible to detect the complementary component of the ICC measurements, hence obtaining the three displacement components by coupling the two instruments.

The techniques developed in the methodological part of the PhD study have been applied in operative case studies.

Different survey campaigns have been conducted to observe the Planpincieux Glacier. In particular, TRI has been applied using four different ground-based radar apparatuses. Moreover, a continuous monitoring activity with DSLR cameras is operative since 2013. In addition, in summer 2015, a survey campaign with a GB-SAR has been conducted to measure the displacement of the Monte Perdido Glacier (Figure 2).

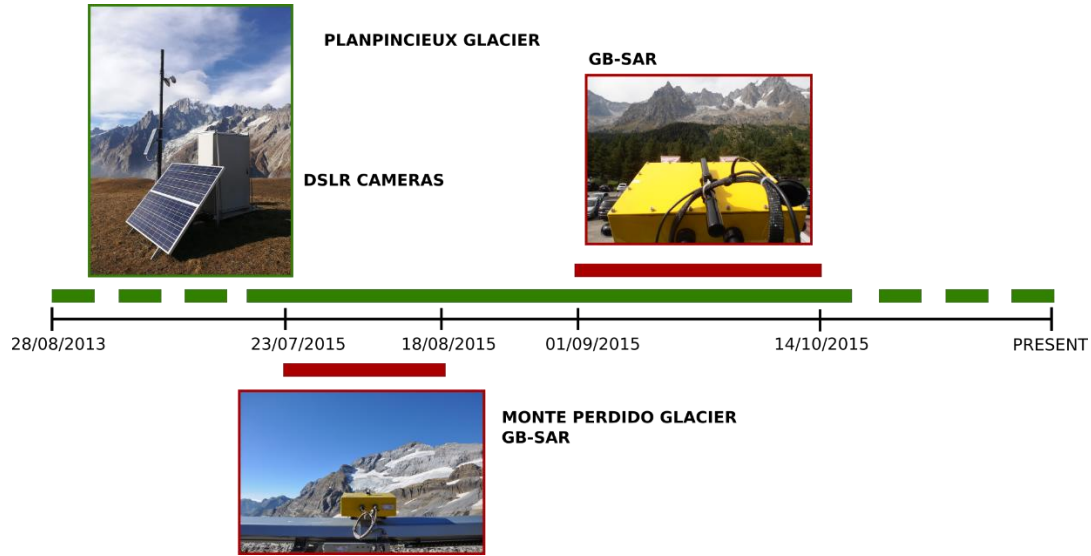


Figure 2. Survey campaigns conducted in Planpincieux Glacier (DSLIR camera and GB-SAR) and Monte Perdido Glacier (GB-SAR)

To achieve the aims of the PhD, the following studies have been conducted:

- > Development of image analysis techniques for DSLIR camera photographs.
- > Characterization of GB SAR application in mountain environment
- > Merging of ICC and TRI data for a 3D model generation
- > Application to Planpincieux and Monte Perdido Glaciers.

The obtained results are presented in a collection of published articles on international scientific journals, rationale of the PhD is presented in Figure 3.

The work is organised as follows: the two first articles deal with the characterisation of the DSLIR camera. The subsequent three papers focus on the GB-SAR analysis. The sixth article represents the core of the thesis, as it describes the coupling of the ICC and TRI techniques to obtain the 3D components of the surface deformation vectors of an Alpine glacier. The two last papers present the application of the developed methodologies to two case studies, the Planpincieux glacier and the Monte Perdido glacier.

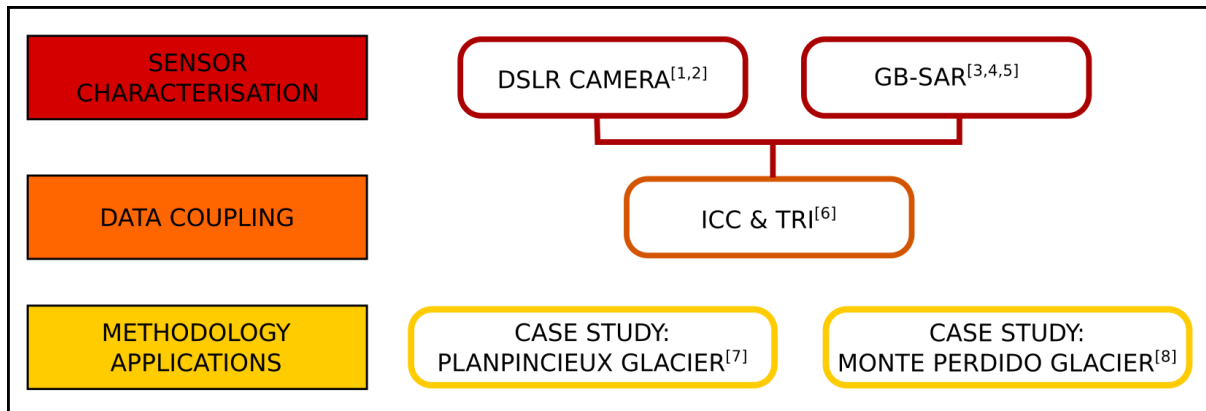


Figure 3. The rationale of the PhD thesis. The apexes refer to the PhD publications listed at the end of the introduction.

DSLIR CAMERA CHARACTERISATION AND IMAGE ANALYSIS

Time-lapse sequences acquired by DSLIR camera provide an immediate observation of the state and behaviour of the phenomenon. This is one of the major values of such an instrument as it allows a direct and easy interpretation of the data and of the studied process. Digital image correlation (DIC) (Schreier et al., 2009) is a technique of image analysis that can be applied to visual photographs collected by DSLIR cameras. DIC

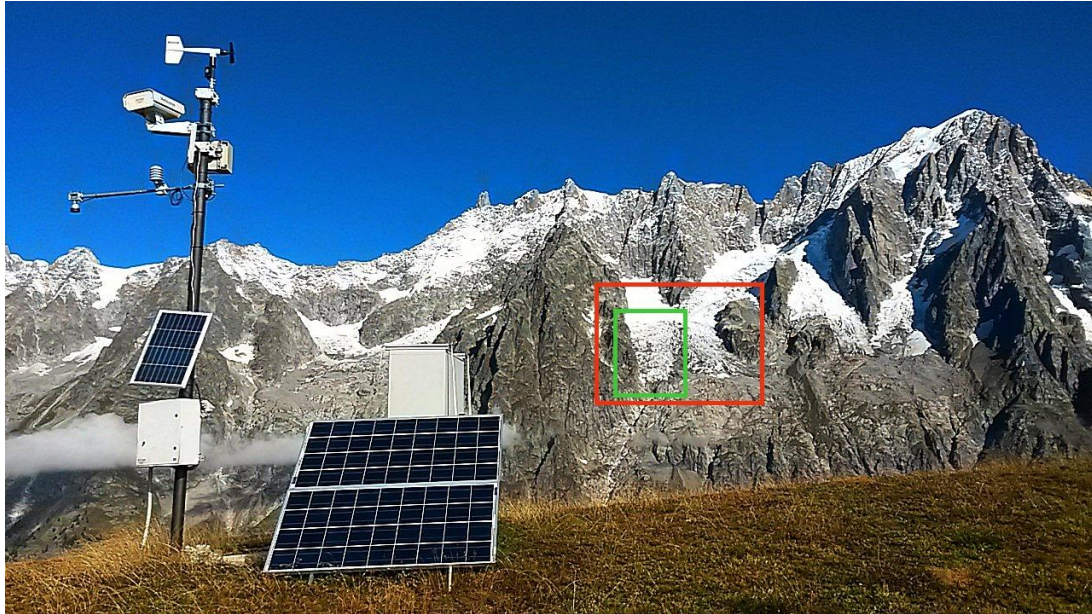


Figure 4. Monitoring station of the Planpincieux Glacier. The coloured boxes delimit the different portions of the glaciers observed by the DSLR cameras.

developed in the early 1970s (Anuta, 1970; Barnea & Silverman, 1972) due to the necessity of estimating the offsets between two images to the aim of registering them. The application of DIC to sub-portions of images yields the possibility to measure 2D surface deformations (Sutton et al., 1983) and flow patterns in PIV applications (Willert & Gharib, 1991). Among the possible methods to compute the offsets due to deformation and/or displacement, the most used is the calculation of the cross-correlation in the space or in the Fourier domains, whence the common reference to image cross-correlation (ICC) technique (Keane & Adrian, 1992; Pust, 2000).

Probably, the first digital ICC work to map the velocity field of moving ice was done by Scambos et al. (1992), who applied the ICC to satellite images of Antarctic glaciers. In the subsequent years, a number of studies used ICC with aerospace-borne images to measure the glacier flow (Berthier et al., 2005; Debella-Gilo & Kääb, 2011; Dehecq et al., 2015; Delacourt et al., 2004; Heid & Kääb, 2012; Kaab, 2002; Kääb, 2005; Leprince et al., 2007; Scherler et al., 2008). Moreover, the necessity of monitoring mountain glaciers with complex geometry yielded the development of ground-based time-lapse surveys (Ahn & Box, 2010; Benoit et al., 2015; Evans, 2000; Fallourd et al., 2011; Messerli & Grinsted, 2015; Schwalbe & Maas, 2017; Vernier et al., 2011).

The present thesis deals with the development of an ICC technique to measure the displacement of the Planpincieux Glacier (Italian Alps). This work is characterised by the application of image analysis technique to the photographs acquired by DSLR cameras installed on a low-cost and autonomous monitoring station located on the opposite side of the valley, several km far from the glacier (Figure 4). The used dataset consists of a series of images collected continuously since 2014 with an hourly frequency. Details of this study can be found in Giordan et al. (2016) “A low-cost optical remote sensing application for glacier deformation monitoring in an alpine environment”.

One of the most relevant limitations of the ICC technique is the need for manually selecting the images to be analysed. In fact, the presence of shadows created by the direct solar radiation might negatively affect the cross-correlation calculation. Therefore, human intervention is necessary to recognise the images most suitable for ICC processing. To solve the issue, it has been developed a method to automatically classify the images according to the visual and illumination conditions and to automatically apply the ICC processing to the suitable images. The method has been experimented during 2018 on the survey dataset of the Planpincieux glacier obtaining high performances and it is presently operative in such monitoring activity. This study is described in Dematteis et al. (2019) “Image Classification for Automated Image Cross-Correlation Applications in the Geosciences”.



Figure 5. GB-SAR installation in mountain environment.

GB-SAR CHARACTERISATION FOR TRI IN MOUNTAIN ENVIRONMENT

The GB-SAR is an instrument that emits and receives electromagnetic waves. The most common and commercial devices operate in the Ku band, that corresponds to a frequency of 12-18 GHz (wavelength of $\lambda = 1.5 - 2.5$ cm). The GB-SAR is equipped with one or two small antennas that slide on a rail. Thereby, a larger antenna is simulated to obtain finer spatial resolution.

GB-SAR is mostly used for interferometry, that is the calculation of the phase difference between two radar acquisitions. The phase difference is directly linked to the range variation between sensor and target, therefore it is used for surface deformation measurements. The first GB-SAR prototype was developed at the end of the 1990s, and the first acknowledged applications were conducted by Tarchi et al. (1999) and by Tarchi et al. (2003) to measure dam and landslide deformations respectively. In the subsequent years, GB-SAR demonstrated to be a valuable tool for earth surface deformation surveys (reviews can be founded in Monserrat et al., 2014 and Caduff et al., 2015). In particular, TRI was successfully applied to monitor glaciers (Allstadt et al., 2015; G. Luzi et al., 2007; Noferini et al., 2009; Riesen et al., 2011; Strozzi et al., 2012; Voytenko et al., 2012, 2015; Xie et al., 2016) and snow processes (Luzi et al., 2009; Martinez-Vazquez & Fortuny-Guasch, 2008).

Probably, the most relevant quality that yielded popularity to the GB-SAR is the high sensitivity of the instrument, which can reach sub-millimetre precision in optimal conditions. On the other hand, the interferometry processing might reveal quite tricky in two aspects: i) phase wrapping and ii) atmospheric phase screen (APS).

In fact, the results of the phase difference are limited in the range $\pm\pi$, which corresponds to a displacement of $\pm\frac{\lambda}{2}$. Therefore, the measurements are affected by ambiguity due to the phase periodicity that allows measuring displacements lower than $\frac{\lambda}{4}$ in absolute value (a factor $\frac{1}{2}$ is comprised to account for the two-way path). To resolve the ambiguity, unwrapping algorithms have been developed in the last decades (Goldstein et al., 1988; Costantini, 1998).

The second issue is related to the variation of the atmospheric variables between two acquisitions that causes the change of the dielectric properties of the medium and introduces a phase delay. Therefore, the APS must be filtered out from the interferometry calculation to obtain reliable results. The first study of the

atmospheric effects on TRI was conducted by Luzi et al. (2004) and in recent years the topic is becoming more popular, in particular for surveys conducted in mountain environments (Baffelli et al., 2018; Barucci et al., 2010; Butt et al., 2017; Caduff et al., 2014; Hu et al., 2019; Iannini & Monti Guarnieri, 2011; Iglesias et al., 2014; Noferini et al., 2005; Pipia et al., 2008). Nevertheless, the complexity of applying TRI in mountain and/or glacier surveys makes important the research in this field.

A methodological analysis of TRI to observe mountain glacier was conducted during the PhD (Figure 5). In particular, two datasets have been analysed, acquired in Monte Perdido glacier (summer 2015) and in Planpincieux glacier (autumn 2015). A simple model to compensate for APS has been developed and successfully applied. The results of these works are described in Dematteis et al. (2017) “Monitoring Alpine glacier surface deformations with GB-SAR” and in Luzi et al. (2018) “Terrestrial radar interferometry to monitor glaciers with complex atmospheric screen”.

In addition, it was conducted an experimental analysis on the adoption of circular polarimetric antennas to GB-SAR measurements, to the aim of evaluating the potentiality of such a technology for interferometry applications. In fact, circular polarisation should provide better performances in terms of phase stability (Izumi et al., 2017). Moreover, using different polarimetric configurations might help in filtering the APS (Iglesias et al., 2015).

The work on the circular polarimetry is reported in Luzi & Dematteis (2019) “Ku band terrestrial radar observations by means of circular polarized antennas”.

GENERATION OF 3D DISPLACEMENT BY MERGING ICC & TRI

Gravitational slope phenomena are often characterised by complex dynamics, depending on the velocity of the process, the dimensions and the geophysical features. Glaciers are relatively fast processes, especially in mountain environment where they lie on steep terrains. Their long-term motion behaves like a fluid and hence they are quite conditioned by rigid constraints and their morphology can vary. Moreover, they are sensitive to the temperature, which can modify their physical properties. Their behaviour can change rapidly during the course of the year (Allstadt et al., 2015) and even during a single day (Liu et al., 2019). Such kinematics evolution makes difficult to define uniquely their state, especially when the geometry changes as well, for example when collapses occur.

The possible variation in dimensions and shape of the kinematic domains and the possible loss of sensors installed within the active process, make inappropriate the adoption of in-situ sensors and/or sensors that provide punctual measurements such as GNSS (Lenzano et al., 2013; Zech et al., 2016) or total station (TS) (Faillietaz et al., 2016). Therefore, spatially-distributed data with high spatio-temporal resolution are essential to monitor the glacier evolution.

ICC and TRI provide spatially-distributed displacement maps, but they can observe only partial components of the actual motion. In fact, the TRI is able to measure the displacement component parallel to the line of sight (LOS), while the ICC can detect the two components perpendicular to the LOS. Terrestrial laser scanners (TLS) (Godone & Godone, 2012; Petlicki, 2018) provide 3D digital terrain models (DTM) that can be used to calculate a difference of DTMs acquired in different times. However, as the DTMs are defined on the 2D surface $f(x, y) = z$, their difference provides 1D deformations along the vertical axis (Monserrat & Crosetto, 2008).

Several studies have been published to propose methods for estimating the 3D displacement components of gravitational slope phenomena. Manconi et al. (2013) proposed to spatially interpolate punctual TS data over a DTM. Other works projected single components along the expected maximum gradient direction (Gabrieli et al., 2016; Luzi et al., 2007; Schwalbe & Maas, 2017), while Ahn & Box (2010), Messerli & Grinsted (2015) and Travelletti et al. (2012) adjusted ICC results in accordance with the pixel footprint calculated through image orthorectification. But these approaches made the strong assumption of temporal morphology invariance.

During the PhD, an innovative methodology to couple the results of TRI and ICC was developed. The methods can be applied also for sensors installed in different locations. Thereby, flexibility is high. The hardest

issue to be solved was data georeferencing. The photographs have been orthorectified with common photogrammetric technique (Messerli & Grinsted, 2015), while for the radar images it was developed a new method that guarantees finer precision with respect to usual approaches.

The paper Dematteis et al. (2018) “4D surface kinematics monitoring through terrestrial radar interferometry and image cross-correlation coupling” contains the details of the work conducted on the Planpincieux glacier case study.

APPLICATIONS OF DEVELOPED TECHNIQUES TO MONITOR PLANPINCIEUX AND MONTE PERDIDO GLACIERS

The use of two different test sites has been an important add value during the PhD because of the possibility of developing and testing the different methodologies on real case studies. The applications of such methodologies to monitor glacier yielded the determination of interpretative models of their dynamics, recent evolution and current state.

PLANPINCIEUX GLACIER

The Planpincieux glacier is located in the Italian side of the mount Grandes Jorasses (part of the Mont Blanc massif). It lies at an elevation that ranges between 2500-3500 m asl (Figure 6). Its morphology is composed of three main portions, an accumulation area formed of two cold-based cirques that merge in a wide plateau at 2900-3000 m asl. The lower portion is in temperate regime and it is composed of two lobes divided by a central moraine. The right lobe is steep ($\approx 30\text{-}35^\circ$) and crevassed. Due to its steepness, this part is quite active and the surface velocity is high. The terminus is located in correspondence of a sub-vertical bedrock cliff. Such a morphology causes an intense ice calving from the snout and in the past several large collapses occurred (Figure 7).

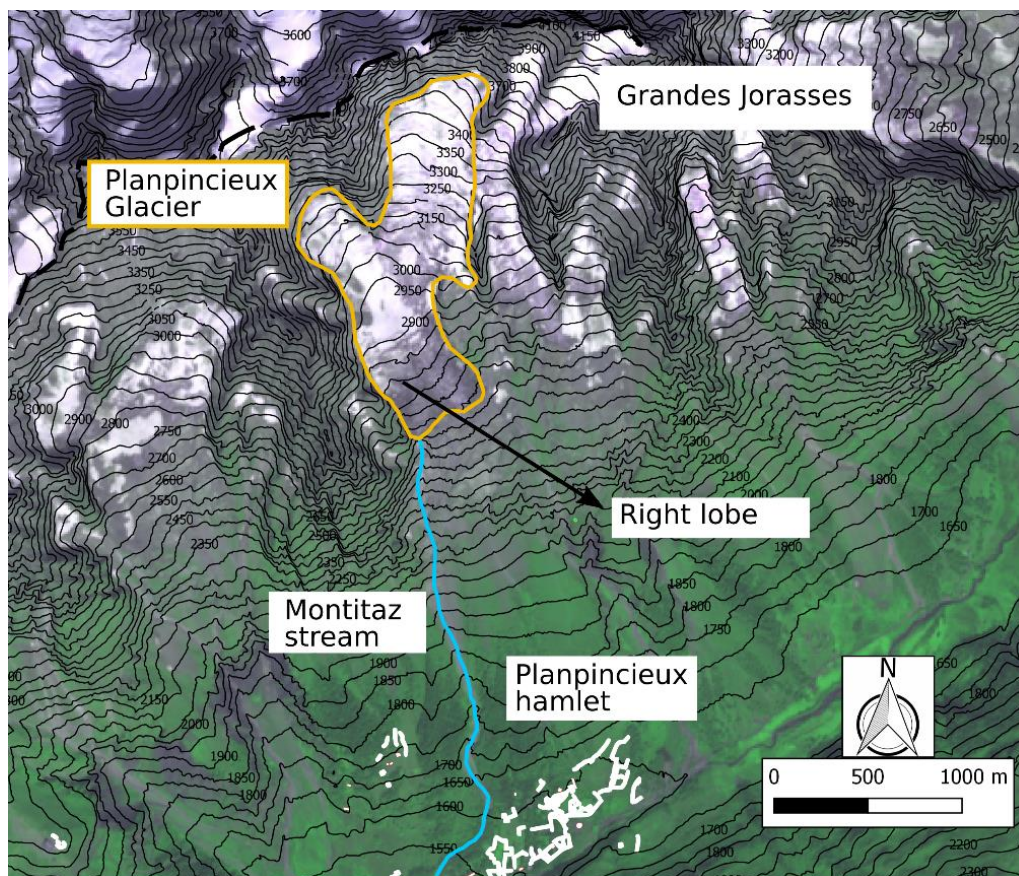


Figure 6. Overview of the Planpincieux Glacier area. One can note the two upper cirques that merge in the central plateau. The lower part is divided in two lobes. The right and most active lobe is indicated by a black arrow.



Figure 7. Aerial views of the Planpincieux Glacier. On the left, the entire glacier is visible. it is possible to recognise the two upper cirques, the central plateau and the lower temperate portion. On the right, particular of the right crevassed lower tongue. It is possible to note the large crevasse halfway of the glacier body.

Since 2013, the glacier has been monitored for civil security, because a wide crevasse opened and destabilised a volume of 250000 m³. The Geohazard Monitoring Group of the Research Institute for the Hydrogeological Protection (IRPI) installed an experimental station equipped with two DSLR cameras that measure the surface velocity using ICC. The monitoring station is presently active and it has collected more than 30000 images. Thanks to this framework, it was possible to daily monitor the evolution of the glacier behaviour during the emergency of September 2019, when the entire lower portion of the right lobe, with an estimated volume of 250000 m³, became to accelerate and threatened the valley road (<https://www.nytimes.com/2019/09/25/world/europe/glacier-italy-climate-change.html>).

In the time span 2015-2018, the glacier kinematics was characterised by a series of speedup periods that culminated with large break-offs. It was found a monotonic relationship that linked the larger collapses to the highest velocities. Moreover, acceleration and velocity thresholds were observed in all the active phases. This study is presented in Giordan et al. (2019) “Classification and kinematics of the Planpincieux Glacier break-offs using photographic time-lapse analysis”.

MONTE PERDIDO GLACIER

The Monte Perdido Glacier is located in Central Spanish Pyrenees beneath the Monte Perdido peak. It is composed of two unconnected bodies that lie respectively at 2900 and 3100 m asl on average. The two masses are north facing and lie on steep slopes ($\approx 40^\circ$). Despite the high elevation, the snow accumulation of the upper body is minimal due to its steepness, while the 0°C isotherm in the last years was located at approximately 2950 m asl (Figure 8).

Between 2011 and 2017, a series of survey campaigns have been conducted using different sensors, to the aim of determining the current state and recent evolution of the two glaciers. In particular, in summer 2017, a 30 days-long GB-SAR campaign was carried out to measure the surface velocity with TRI. Other sensors used in the glacier monitoring include a TLS to estimate the elevation change and snow accumulation, a series of seven ablation stakes installed in the lower glacier to measure the annual movement and two ground-penetrating radar (GPR) surveys that detected the ice thickness in 2016.

The combined use of different sensors allowed at determining the advanced stage of degradation of the Monte Perdido Glacier whose extinction is foreseen within the next three to five decades.

The contribute of the PhD candidate to the work López-Moreno et al. (2018) “Ground-based remote-sensing techniques for diagnosis of the current state and recent evolution of the Monte Perdido Glacier”, appertains to the interferometric processing of the GB-SAR data.

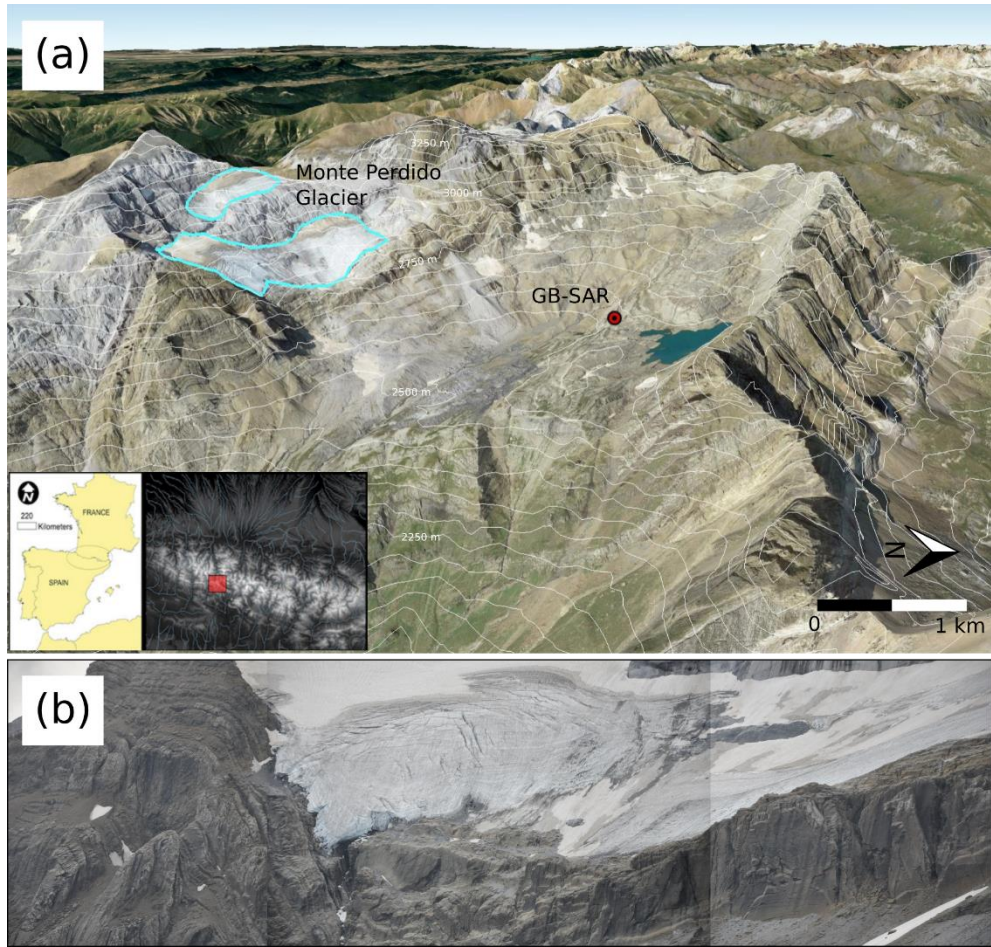


Figure 8. (a) Overview of the Monte Perdido area. The upper and lower parts of the glacier are delimited in sky blue. The position of the GB-SAR during the survey is indicated with a red circle. (b) Lower body of the Monte Perdido Glacier.

REFERENCES

- Ahn, Y., & Box, J. E. (2010). Instruments and Methods Glacier velocities from time-lapse photos: Technique development and first results from the Extreme Ice Survey (EIS) in Greenland. *Journal of Glaciology*, 56(198), 723–734. <https://doi.org/10.3189/002214310793146313>
- Allstadt, K. E., Shean, D. E., Campbell, A., Fahnestock, M., & Malone, S. D. (2015). Observations of seasonal and diurnal glacier velocities at Mount Rainier, Washington, using terrestrial radar interferometry. *Cryosphere*, 9(6), 2219–2235. <https://doi.org/10.5194/tc-9-2219-2015>
- Anuta, P. E. (1970). Spatial Registration of Multispectral and Multitemporal Digital Imagery Using Fast Fourier Transform Techniques. *IEEE Transactions on Geoscience Electronics*, 8(4), 353–368. <https://doi.org/10.1109/TGE.1970.271435>
- Baffelli, S., Frey, O., & Hajnsek, I. (2018). Geostatistical analysis and mitigation of atmospheric phase screens in Ku-band terrestrial radar interferometry. In *International Geoscience and Remote Sensing Symposium (IGARSS)* (Vol. 2018-July, pp. 6504–6507). <https://doi.org/10.1109/IGARSS.2018.8517479>
- Barnea, D. I., & Silverman, H. F. (1972). A Class of Algorithms for Fast Digital Image Registration. *IEEE Transactions on Computers*, C-21(2), 179–186. <https://doi.org/10.1109/TC.1972.5008923>
- Barnett, T. P., Adam, J. C., & Lettenmaier, D. P. (2005). Potential impacts of a warming climate on water availability in snow-dominated regions. *Nature*. <https://doi.org/10.1038/nature04141>
- Barucci, A., MacAluso, G., Mecatti, D., Noferini, L., Fanelli, D., Facchini, A., et al. (2010). Universal fluctuations in tropospheric radar measurements. *Epl*, 89(2), 20006. <https://doi.org/10.1209/0295-5075/89/20006>
- Benoit, L., Dehecq, A., Pham, H. T., Vernier, F., Trouvé, E., Moreau, L., et al. (2015). Multi-method monitoring of Glacier d’Argentière dynamics. *Annals of Glaciology*, 56(70), 118–128. <https://doi.org/10.3189/2015AoG70A985>
- Berthier, E., Vadon, H., Baratoux, D., Arnaud, Y., Vincent, C., Feigl, K. L., et al. (2005). Surface motion of mountain glaciers derived from satellite optical imagery. *Remote Sensing of Environment*, 95(1), 14–28. <https://doi.org/10.1016/j.rse.2004.11.005>
- Butt, J., Wieser, A., & Conzett, S. (2017). Intrinsic random functions for mitigation of atmospheric effects in terrestrial radar interferometry. *Journal of Applied Geodesy*, 11(2), 89–98. <https://doi.org/10.1515/jag-2016-0042>
- Caduff, R., Kos, A., Schlunegger, F., McArde, B. W., & Wiesmann, A. (2014). Terrestrial radar interferometric measurement of hillslope deformation and atmospheric disturbances in the Illgraben debris-flow catchment, Switzerland. *IEEE Geoscience and Remote Sensing Letters*, 11(2), 434–438. <https://doi.org/10.1109/LGRS.2013.2264564>
- Caduff, R., Schlunegger, F., Kos, A., & Wiesmann, A. (2015). A review of terrestrial radar interferometry for measuring surface change in the geosciences. *Earth Surface Processes and Landforms*, 40(2), 208–228. <https://doi.org/10.1002/esp.3656>
- Debella-Gilo, M., & Kääb, A. (2011). Sub-pixel precision image matching for measuring surface displacements on mass movements using normalized cross-correlation. *Remote Sensing of Environment*, 115(1), 130–142. <https://doi.org/10.1016/j.rse.2010.08.012>
- Dehecq, A., Gourmelen, N., & Trouve, E. (2015). Deriving large-scale glacier velocities from a complete satellite archive: Application to the Pamir-Karakoram-Himalaya. *Remote Sensing of Environment*, 162, 55–66. <https://doi.org/10.1016/j.rse.2015.01.031>
- Delacourt, C., Allemand, P., Casson, B., & Vadon, H. (2004). Velocity field of the “La Clapière” landslide measured by the correlation of aerial and QuickBird satellite images. *Geophysical Research Letters*, 31(15). <https://doi.org/10.1029/2004GL020193>
- Deline, P., Gardent, M., Magnin, F., & Ravanel, L. (2012). The morphodynamics of the mont blanc massif in a changing cryosphere: A comprehensive review. *Geografiska Annaler, Series A: Physical Geography*, 94(2), 265–283. <https://doi.org/10.1111/j.1468-0459.2012.00467.x>
- Evans, A. N. (2000). Glacier surface motion computation from digital image sequences. *IEEE Transactions on Geoscience and Remote Sensing*, 38(2 II), 1064–1072. <https://doi.org/10.1109/36.841985>
- Faillietaz, J., Funk, M., & Vagliasindi, M. (2016). Time forecast of a break-off event from a hanging glacier. *Cryosphere*, 10(3), 1191–1200. <https://doi.org/10.5194/tc-10-1191-2016>
- Fallourd, R., Trouvé, E., Roşu, D., Vernier, F., Bolon, P., Harant, O., et al. (2011). Monitoring Temperate Glacier Displacement by Multi-Temporal TerraSAR-X Images and Continuous GPS Measurements. *IEEE Journal of Selected Topics in Applied Earth Observations and Remote Sensing*, 4(2), 372–386.

<https://doi.org/10.1109/JSTARS.2010.2096200>

- Gabrieli, F., Corain, L., & Vettore, L. (2016). A low-cost landslide displacement activity assessment from time-lapse photogrammetry and rainfall data: Application to the Tessina landslide site. *Geomorphology*, 269, 56–74. <https://doi.org/10.1016/j.geomorph.2016.06.030>
- Giordan, D., Hayakawa, Y. S., Nex, F., & Tarolli, P. (2018). Preface: The use of remotely piloted aircraft systems (RPAS) in monitoring applications and management of natural hazards. *Natural Hazards and Earth System Sciences*, 18(11), 3085–3087. <https://doi.org/10.5194/nhess-18-3085-2018>
- Godone, D., & Godone, F. (2012). *The Support of Geomatics in Glacier Monitoring: The Contribution of Terrestrial Laser Scanner. Laser Scanner Technology*. INTECH Open Access Publisher. <https://doi.org/10.5772/33463>
- Goldstein, R. M., Zebker, H. A., & Werner, C. L. (1988). Satellite radar interferometry: Two-dimensional phase unwrapping. *Radio Science*, 23(4), 713–720. <https://doi.org/10.1029/RS023i004p00713>
- Heid, T., & Kääb, A. (2012). Evaluation of existing image matching methods for deriving glacier surface displacements globally from optical satellite imagery. *Remote Sensing of Environment*, 118, 339–355. <https://doi.org/10.1016/j.rse.2011.11.024>
- Hock, R., Jansson, P., & Braun, L. N. (2005). Modelling the Response of Mountain Glacier Discharge to Climate Warming. In *Global change and mountain regions (A state of knowledge overview)* (pp. 243–252). Springer. https://doi.org/10.1007/1-4020-3508-x_25
- Hu, C., Deng, Y., Tian, W., Sensing, Z. Z.-R., & 2019, U. (2019). A Compensation Method for a Time–Space Variant Atmospheric Phase Applied to Time-Series GB-SAR Images. *Remote Sensing*, 11(20), 2350. Retrieved from <https://www.mdpi.com/2072-4292/11/20/2350>
- Iannini, L., & Monti Guarnieri, A. (2011). Atmospheric phase screen in ground-based radar: Statistics and compensation. *IEEE Geoscience and Remote Sensing Letters*, 8(3), 537–541. <https://doi.org/10.1109/LGRS.2010.2090647>
- Iglesias, R., Fabregas, X., Aguasca, A., Mallorqui, J. J., Lopez-Martinez, C., Gili, J. A., & Corominas, J. (2014). Atmospheric phase screen compensation in ground-based sar with a multiple-regression model over mountainous regions. *IEEE Transactions on Geoscience and Remote Sensing*, 52(5), 2436–2449. <https://doi.org/10.1109/TGRS.2013.2261077>
- Iglesias, R., Aguasca, A., Fabregas, X., Mallorqui, J. J., Monells, D., Lopez-Martinez, C., & Pipia, L. (2015). Ground-Based Polarimetric SAR Interferometry for the Monitoring of Terrain Displacement Phenomena-Part II: Applications. *IEEE Journal of Selected Topics in Applied Earth Observations and Remote Sensing*, 8(3), 994–1007. <https://doi.org/10.1109/JSTARS.2014.2366711>
- Izumi, Y., Demirci, S., Baharuddin, M. Z., Sumantyo, J. T. S., & Yang, H. (2017). Analysis of circular polarization backscattering and target decomposition using gb-sar. *Progress In Electromagnetics Research B*, 73(1), 17–29. <https://doi.org/10.2528/PIERB16081701>
- Kaab, a. (2002). Monitoring high-mountain terrain deformation from repeated air- and spaceborne optical data: examples using digital aerial imagery and ASTER data. *ISPRS Journal of Photogrammetry and Remote Sensing*, 57(1–2), 39–52. Retrieved from <http://linkinghub.elsevier.com/retrieve/pii/S0924271602001144>
- Kääb, A. (2005). Combination of SRTM3 and repeat ASTER data for deriving alpine glacier flow velocities in the Bhutan Himalaya. *Remote Sensing of Environment*, 94(4), 463–474. <https://doi.org/10.1016/j.rse.2004.11.003>
- Kääb, A., Huggel, C., Fischer, L., Guex, S., Paul, F., Roer, I., et al. (2005). Remote sensing of glacier- and permafrost-related hazards in high mountains: an overview. *Natural Hazards and Earth System Science*, 5(4), 527–554. <https://doi.org/10.5194/nhess-5-527-2005>
- Keane, R. D., & Adrian, R. J. (1992). Theory of cross-correlation analysis of PIV images. *Applied Scientific Research*, 49(3), 191–215. <https://doi.org/10.1007/BF00384623>
- Lenzano, M. G., Lenzano, L., Liaudat, D. T., Barón, J., & Lannutti, E. (2013). Applying GNSS and DTM Technologies to Monitor the Ice Balance of the Horcones Inferior Glacier, Aconcagua Region, Argentina. *Journal of the Indian Society of Remote Sensing*, 41(4), 969–980. <https://doi.org/10.1007/s12524-013-0294-z>
- Leprince, S., Barbot, S., Ayoub, F., & Avouac, J. P. (2007). Automatic and precise orthorectification, coregistration, and subpixel correlation of satellite images, application to ground deformation measurements. *IEEE Transactions on Geoscience and Remote Sensing*, 45(6), 1529–1558. <https://doi.org/10.1109/TGRS.2006.888937>
- Liu, L. I. N., Jiang, L., Sun, Y., Wang, H., Sun, Y., & Xu, H. (2019). Diurnal fluctuations of glacier surface

- velocity observed with terrestrial radar interferometry at Laohugou No. 12 Glacier, western Qilian mountains, China. *Journal of Glaciology*, 65(250), 239–248. <https://doi.org/10.1017/jog.2019.1>
- Luzi, G., Pieraccini, M., Mecatti, D., Noferini, L., Guidi, G., Moia, F., & Atzeni, C. (2004). Ground-based radar interferometry for landslides monitoring: Atmospheric and instrumental decorrelation sources on experimental data. *IEEE Transactions on Geoscience and Remote Sensing*, 42(11), 2454–2466. <https://doi.org/10.1109/TGRS.2004.836792>
- Luzi, G., Pieraccini, M., Mecatti, D., Noferini, L., Macaluso, G., Tamburini, A., & Atzeni, C. (2007). Monitoring of an alpine glacier by means of ground-based SAR interferometry. *IEEE Geoscience and Remote Sensing Letters*, 4(3), 495–499. <https://doi.org/10.1109/LGRS.2007.898282>
- Luzi, Guido, Noferini, L., Mecatti, D., Macaluso, G., Pieraccini, M., Atzeni, C., et al. (2009). Using a ground-based SAR interferometer and a terrestrial laser scanner to monitor a snow-covered slope: Results from an experimental data collection in Tyrol (Austria). In *IEEE Transactions on Geoscience and Remote Sensing* (Vol. 47, pp. 382–393). <https://doi.org/10.1109/TGRS.2008.2009994>
- Manconi, A., Allasia, P., Giordan, D., Baldo, M., Lollino, G., Corazza, A., & Albanese, V. (2013). Landslide 3D Surface Deformation Model Obtained Via RTS Measurements. In *Landslide Science and Practice* (pp. 431–436). Berlin, Heidelberg: Springer Berlin Heidelberg. https://doi.org/10.1007/978-3-642-31445-2_56
- Mario Costantini, T. (1998). A novel phase unwrapping method based on network programming. *IEEE Transactions on Geoscience and Remote Sensing*, 36(3), 813–821. <https://doi.org/10.1109/36.673674>
- Martinez-Vazquez, A., & Fortuny-Guasch, J. (2008). A GB-SAR processor for snow avalanche identification. *IEEE Transactions on Geoscience and Remote Sensing*, 46(11), 3948–3956. <https://doi.org/10.1109/TGRS.2008.2001387>
- Messerli, A., & Grinsted, A. (2015). Image georectification and feature tracking toolbox: ImGRAFT. *Geoscientific Instrumentation, Methods and Data Systems*, 4(1), 23–34. <https://doi.org/10.5194/gi-4-23-2015>
- Monserat, O., & Crosetto, M. (2008). Deformation measurement using terrestrial laser scanning data and least squares 3D surface matching. *ISPRS Journal of Photogrammetry and Remote Sensing*, 63(1), 142–154. <https://doi.org/10.1016/j.isprsjprs.2007.07.008>
- Monserat, O., Crosetto, M., & Luzi, G. (2014). A review of ground-based SAR interferometry for deformation measurement. *ISPRS Journal of Photogrammetry and Remote Sensing*, 93, 40–48. <https://doi.org/10.1016/j.isprsjprs.2014.04.001>
- Noferini, L., Pieraccini, M., Mecatti, D., Luzi, G., Atzeni, C., Tamburini, A., & Broccolato, M. (2005). Permanent scatterers analysis for atmospheric correction in ground-based SAR interferometry. *IEEE Transactions on Geoscience and Remote Sensing*, 43(7), 1459–1470. <https://doi.org/10.1109/TGRS.2005.848707>
- Noferini, L., Mecatti, D., Macaluso, G., Pieraccini, M., & Atzeni, C. (2009). Monitoring of Belvedere Glacier using a wide angle GB-SAR interferometer. *Journal of Applied Geophysics*, 68(2), 289–293. <https://doi.org/10.1016/j.jappgeo.2009.02.004>
- Petlicki, M. (2018). Subglacial topography of an icefall inferred from repeated terrestrial laser scanning. *IEEE Geoscience and Remote Sensing Letters*, 15(9), 1461–1465. <https://doi.org/10.1109/LGRS.2018.2845342>
- Pipia, L., Fàbregas, X., Aguasca, A., & López-Martínez, C. (2008). Atmospheric artifact compensation in ground-based DInSAR applications. *IEEE Geoscience and Remote Sensing Letters*, 5(1), 88–92. <https://doi.org/10.1109/LGRS.2007.908364>
- Pust, O. (2000). PIV: Direct cross-correlation compared with FFT-based cross-correlation. In *10th International Symposium on Applications of Laser Techniques to Fluid Mechanics* (Vol. 27, pp. 1–12).
- Riesen, P., Strozzi, T., Bauder, A., Wiesmann, A., & Funk, M. (2011). Short-term surface ice motion variations measured with a ground-based portable real aperture radar Interferometer. *Journal of Glaciology*, 57(201), 53–60. <https://doi.org/10.3189/002214311795306718>
- Scambos, T. A., Dutkiewicz, M. J., Wilson, J. C., & Bindaschadler, R. A. (1992). Application of image cross-correlation to the measurement of glacier velocity using satellite image data. *Remote Sensing of Environment*, 42(3), 177–186. [https://doi.org/10.1016/0034-4257\(92\)90101-O](https://doi.org/10.1016/0034-4257(92)90101-O)
- Scherler, D., Leprince, S., & Strecker, M. R. (2008). Glacier-surface velocities in alpine terrain from optical satellite imagery-Accuracy improvement and quality assessment. *Remote Sensing of Environment*, 112(10), 3806–3819. <https://doi.org/10.1016/j.rse.2008.05.018>
- Schreier, H., Orteu, J. J., & Sutton, M. A. (2009). *Image correlation for shape, motion and deformation*

-
- measurements: Basic concepts, theory and applications*. Boston, MA: Springer US. <https://doi.org/10.1007/978-0-387-78747-3>
- Schwalbe, E., & Maas, H. G. (2017). The determination of high-resolution spatio-temporal glacier motion fields from time-lapse sequences. *Earth Surface Dynamics*, 5(4), 861–879. <https://doi.org/10.5194/esurf-5-861-2017>
- Strozzi, T., Werner, C., Wiesmann, A., & Wegmuller, U. (2012). Topography mapping with a portable real-aperture radar interferometer. *IEEE Geoscience and Remote Sensing Letters*, 9(2), 277–281. <https://doi.org/10.1109/LGRS.2011.2166751>
- Sutton, M., Wolters, W., Peters, W., Ranson, W., & McNeill, S. (1983). Determination of displacements using an improved digital correlation method. *Image and Vision Computing*, 1(3), 133–139. [https://doi.org/10.1016/0262-8856\(83\)90064-1](https://doi.org/10.1016/0262-8856(83)90064-1)
- Tarchi, D., Rudolf, H., Luzi, G., Chiarantini, L., Coppo, P., & Sieber, A. J. (1999). SAR interferometry for structural changes detection: a demonstration test on a dam. In *International Geoscience and Remote Sensing Symposium (IGARSS)* (Vol. 3, pp. 1522–1524). Retrieved from <https://ieeexplore.ieee.org/abstract/document/772006/>
- Tarchi, D., Casagli, N., Fanti, R., Leva, D. D., Luzi, G., Pasuto, A., et al. (2003). Landslide monitoring by using ground-based SAR interferometry: An example of application to the Tessina landslide in Italy. *Engineering Geology*, 68(1–2), 15–30. [https://doi.org/10.1016/S0013-7952\(02\)00196-5](https://doi.org/10.1016/S0013-7952(02)00196-5)
- Travelletti, J., Delacourt, C., Allemand, P., Malet, J. P., Schmittbuhl, J., Toussaint, R., & Bastard, M. (2012). Correlation of multi-temporal ground-based optical images for landslide monitoring: Application, potential and limitations. *ISPRS Journal of Photogrammetry and Remote Sensing*, 70, 39–55. <https://doi.org/10.1016/j.isprsjprs.2012.03.007>
- Vernier, F., Fallourd, R., Friedt, J. M., Yan, Y., Trouvé, E., Nicolas, J.-M., & Moreau, L. (2011). Fast correlation technique for glacier flow monitoring by digital camera and space-borne SAR images. *EURASIP Journal on Image and Video Processing*, 2011(1), 11. <https://doi.org/10.1186/1687-5281-2011-11>
- Voytenko, D., Dixon, T. H., Werner, C., Gourmelen, N., Howat, I. M., Tinder, P. C., & Hooper, A. (2012). Monitoring a glacier in southeastern Iceland with the portable Terrestrial Radar Interferometer. In *International Geoscience and Remote Sensing Symposium (IGARSS)* (pp. 3230–3232). <https://doi.org/10.1109/IGARSS.2012.6350736>
- Voytenko, D., Dixon, T. H., Howat, I. M., Gourmelen, N., Lembke, C., Werner, C. L., et al. (2015). Multi-year observations of Breioamerkurjökull, a marine-terminating glacier in southeastern Iceland, using terrestrial radar interferometry. *Journal of Glaciology*, 61(225), 42–54. <https://doi.org/10.3189/2015JoG14J099>
- Willert, C. E., & Gharib, M. (1991). Digital particle image velocimetry. *Experiments in Fluids*, 10(4), 181–193. <https://doi.org/10.1007/BF00190388>
- Xie, S., Dixon, T. H., Voytenko, D., Holland, D. M., Holland, D., & Zheng, T. (2016). Precursor motion to iceberg calving at Jakobshavn Isbræ, Greenland, observed with terrestrial radar interferometry. *Journal of Glaciology*, 62(236), 1134–1142. <https://doi.org/10.1017/jog.2016.104>
- Zech, C., Schöne, T., Neelmeijer, J., Zubovich, A., & Galas, R. (2016). Geodetic monitoring networks: GNSS-derived glacier surface velocities at the global change observatory inylchek (kyrgyzstan). In *International Association of Geodesy Symposia* (pp. 557–563). https://doi.org/10.1007/1345_2015_38

PHD PUBLICATIONS

1. Giordan, D.; Allasia, P.; **Dematteis, N.**; Dell’Anese, F.; Vagliasindi, M.; Motta, E. (2016). A low-cost optical remote sensing application for glacier deformation monitoring in an alpine environment. *Sensors*, 16. doi:10.3390/s16101750
2. **Dematteis, N.**; Giordan, D.; Allasia, P. (2019). Image Classification for Automated Image Cross-Correlation Applications in the Geosciences. *Applied Sciences*, 9, 2357. doi:10.3390/app9112357
3. **Dematteis, N.**; Luzi, G.; Giordan, D.; Zucca, F.; Allasia, P. (2017). Monitoring Alpine glacier surface deformations with GB-SAR. *Remote Sensing Letters*, 8, 947–956. doi:10.1080/2150704X.2017.1335905
4. Luzi, G.; **Dematteis, N.**; Zucca, F.; Monserrat, O.; Giordan, D.; López-Moreno, J.I. (2018). Terrestrial radar interferometry to monitor glaciers with complex atmospheric screen. In *Proceedings of the International Geoscience and Remote Sensing Symposium (IGARSS)*; Vol. 2018-July, pp. 6243–6246. doi:10.1109/IGARSS.2018.8519008
5. Luzi, G. & **Dematteis, N.** (2019). Ku band terrestrial radar observations by means of circular polarized antennas. *Remote Sensing*, 11. doi:10.3390/rs11030270
6. **Dematteis, N.**; Giordan, D.; Zucca, F.; Luzi, G.; Allasia, P. (2018). 4D surface kinematics monitoring through terrestrial radar interferometry and image cross-correlation coupling. *ISPRS Journal of Photogrammetry and Remote Sensing*, 142, 38–50. doi:10.1016/j.isprsjprs.2018.05.017
7. Giordan, D.; **Dematteis, N.**; Allasia, P.; Motta, E. (2019). Classification and kinematics of the Planpincieux Glacier break-offs using photographic time-lapse analysis, *Journal of Glaciology*. In press. doi:10.1017/jog.2019.99
8. López-Moreno, J.I.; Alonso-González, E.; Monserrat, O.; Del Río, L.M.; Otero, J.; Lapazaran, J.; Luzi, G.; **Dematteis, N.**; Serreta, A.; Rico, I.; Serrano-Canadas, E.; Bartolomé, M.; Moreno, A.; Buisan, S.; Revuelto, J. (2018). Ground-based remote-sensing techniques for diagnosis of the current state and recent evolution of the Monte Perdido Glacier, Spanish Pyrenees. *Journal of Glaciology*, 65, 85–100. doi:10.1017/jog.2018.96

Note

The reproduction of the articles in this document is made under the Editors permission, in accordance with the rights of free dissemination for thesis dissertation.

<https://www.mdpi.com/authors/rights>

<https://authorservices.taylorandfrancis.com/publishing-open-access/oa-options-finder/>

<https://journals.ieeeauthorcenter.ieee.org/choose-a-publishing-agreement/avoid-infringement-upon-ieee-copyright/#reuse-thesis>

<https://www.elsevier.com/about/open-science/open-access/journal-embargo-finder/journal-embargo-finder>

<https://www.cambridge.org/core/journals/journal-of-glaciology/information/open-access-information-for-journal-of-glaciology-and-annals-of-glaciology>

The paper "Terrestrial radar interferometry to monitor glaciers with complex atmospheric screen" is ©2018 IEEE. Reprinted with permission, from Luzi, et al. (2018). Terrestrial radar interferometry to monitor glaciers with complex atmospheric screen. In *Proceedings of the International Geoscience and Remote Sensing Symposium (IGARSS)*; Vol. 2018-July, pp. 6243–6246. It is reported the full text article in the preprint version.

The public dissemination of the paper "4D surface kinematics monitoring through terrestrial radar interferometry and image cross-correlation coupling" is under embargo up to June 2020.

The manuscript "Classification and kinematics of the Planpincieux Glacier break-offs using photographic time-lapse analysis" has been accepted for publication in 03/12/2019. The manuscript is presented in preprint version.

The remaining papers are reported in their final published version.

Article

A Low-Cost Optical Remote Sensing Application for Glacier Deformation Monitoring in an Alpine Environment

Daniele Giordan ¹, Paolo Allasia ¹, Niccolò Dematteis ^{1,*}, Federico Dell’Anese ¹, Marco Vagliasindi ² and Elena Motta ²

¹ GeoHazard Monitoring Group—Institute of Research for the Geo-Hydrological Protection—National Council of Research of Italy, 10135 Turin, Italy; daniele.giordan@irpi.cnr.it (D.G.); paolo.allasia@irpi.cnr.it (P.A.); federico.dellanese@irpi.cnr.it (F.D.A.)

² Fondazione Montagna Sicura, 11013 Courmayeur, Italy; mvagliasindi@fondms.org (M.V.); emotta@fondms.org (E.M.)

* Correspondence: niccolo.dematteis@irpi.cnr.it; Tel.: +39-011-397-7832

Academic Editor: Assefa M. Melesse

Received: 19 July 2016; Accepted: 17 October 2016; Published: 21 October 2016

Abstract: In this work, we present the results of a low-cost optical monitoring station designed for monitoring the kinematics of glaciers in an Alpine environment. We developed a complete hardware/software data acquisition and processing chain that automatically acquires, stores and co-registers images. The system was installed in September 2013 to monitor the evolution of the Planpincieux glacier, within the open-air laboratory of the Grandes Jorasses, Mont Blanc massif (NW Italy), and collected data with an hourly frequency. The acquisition equipment consists of a high-resolution DSLR camera operating in the visible band. The data are processed with a Pixel Offset algorithm based on normalized cross-correlation, to estimate the deformation of the observed glacier. We propose a method for the pixel-to-metric conversion and present the results of the projection on the mean slope of the glacier. The method performances are compared with measurements obtained by GB-SAR, and exhibit good agreement. The system provides good support for the analysis of the glacier evolution and allows the creation of daily displacement maps.

Keywords: image matching; glacier kinematics; low-cost equipment; monitoring; remote sensing

1. Introduction

During the last century, global warming has caused a great retreat of glaciers, especially in the Northern Hemisphere [1]. Glaciers have an important impact on population because they store fresh water, thereby affecting agriculture, water management and hydroelectric power plants [2]. This trend has increased the frequency of glacier-related instabilities, which constitute a major concern in mountain areas, in particular in the Alps, where they can interact with densely populated areas [3–5]. An important example of these processes is the break-off of temperate or polythermal glaciers, resulting from a combination of geometric, thermal and water flow conditions. Unfortunately, these conditions are still poorly understood, making prediction of break-off events difficult. This is partially due to the lack of systematic long-term observations of temperate glaciers and to the difficulty of monitoring this particular geomorphological process.

The use of monitoring system for the study of glaciers is often focused on the definition of long-term evolution through periodic acquisitions of remotely sensed data [6–8]. These applications, usually combined with the use of in situ devices, have been adopted to periodically acquire the geometry of the ice mass and to evaluate its changes [9].

Approaches for the remote sensing monitoring of glaciers include: (i) SAR interferometry [10,11]; (ii) amplitude tracking [12,13]; (iii) LiDAR surveys [14–16]; (iv) multispectral image analysis [17]; (v) photogrammetry [18,19]. The major constraints of these methods are the long revisit times of the airborne and satellite applications and the high cost in terms of economic and logistical resources related to long-lasting surveys involving devices such as ground-based synthetic aperture radar (GB-SAR). From this perspective, the application of monitoring systems must be able to offer a high acquisition rate with an approach very similar to the one used in landslide monitoring [20–23].

Due to recent hardware and software improvements in the field of photogrammetry, the use of computer vision applications can be now considered a new effective approach for the monitoring of the evolution of gravitational processes using low-cost equipment [24]. The use of photogrammetric systems was initially tested with satellite images for landslide monitoring [25] and in other contexts, such as glaciers [18,19] or river reaches [26,27].

Jiang et al. [28] developed one of the first ground-based applications of close-range photogrammetry, which ensures a much finer resolution than other approaches. To the authors' knowledge a few studies have been published using this approach for monitoring glaciers [29–31].

Ground-based optical systems are often composed of one or more stations acquiring a sequence of high-resolution photos of the studied area, and these photos are then processed using different approaches. One possible method is stereoscopy, which is usually based on the creation of a 3D model based on the simultaneous acquisition of two images of the same target from two acquisition points [30,32]. Other possibilities include the use of a single camera for a multi-temporal analysis based on image matching [29,33], change detection [34], pixel tracking [31,35], and, in recent years, UAV-borne photogrammetry for operative purposes [36,37].

One of the added values of these techniques is the possibility of obtaining a dataset of optical images that can be used not only for numerical analysis but also for morphological analysis of the studied phenomenon [38,39]. A photo sequence of the evolution of a geomorphological process can often be very useful for understanding the dynamics that control and characterize its evolution.

The aim of the present work is twofold: firstly, the technological development of an operational, low-cost, optically-based monitoring system that is robust enough to resist the extreme weather of the Alpine winter at high altitude; and secondly, the development of software for processing the acquired data to estimate the glacier surface deformation.

In this paper, we present the design of an experimental application of an optical system based on image cross-correlation [34,40,41], hereafter called the Pixel Offset (PO) method, developed for monitoring the evolution of the Planpincieux glacier, on the Italian side of Mont Blanc (Aosta Valley Region, NW Italy). The research project started in September 2013 and remains active, continuously acquiring photographs. The principal steps presented here are as follows: (i) the development of a methodology for the acquisition and selection of images; (ii) the identification of a methodology for morphological analysis; (iii) the application of the PO method.

The paper is organized as follows: in Section 2, the study area is presented. In Section 3, the installed ground-based equipment and the features of the consumer-grade camera are described in detail, with some discussion of the ancillary radar surveys. In Section 4, we present the operative methodology of the long-term monitoring programme, from the acquisition to the data processing. In Sections 5 and 6, the results and discussion are presented. Our conclusions follow.

2. Study Area

The Aosta Valley Region is located in north-western Italy and is characterized by the presence of the highest mountain in the Alps. The Planpincieux glacier (located at approximately 45.85° N 6.97° E) is in the Ferret Valley (Aosta Valley) on the south side of the Mont-Blanc Massif in the Italian Alps. This glacier is within the open-air laboratory of the Grandes Jorasses and is part of the Grandes Jorasses—Planpincieux glacier composite, lying at elevations between 3700 and 2530 m asl and covering approximately 1 km².

The glacier is composed of two different ice streams, starting at 3700 and 3300 m asl, and merging into a wide plateau (15° slope) between 2950 and 2900 m asl. Below this altitude, the steep tongue of the glacier starts (32° slope), and reaches an elevation of 2530 m asl.

The glacier tongue is intensely crevassed. Based on the crevasse pattern, the glacier tongue appears to be separated into two different ice flows by a central ridge in the bedrock. The eastern side of the glacier margin lies on an open slope (Figure 1), while the westernmost side (in yellow in Figure 2) is confined by a steep rock wall and lies just above a significant increase in the bedrock slope. This part of the glacier fits the definition of a “*terrace avalanching glacier*” [42]. This part of the glacier is the most active, and the paper focuses on the study of the western tongue. The entire glacier can be classified as a “*temperate steep glacier*” [43].

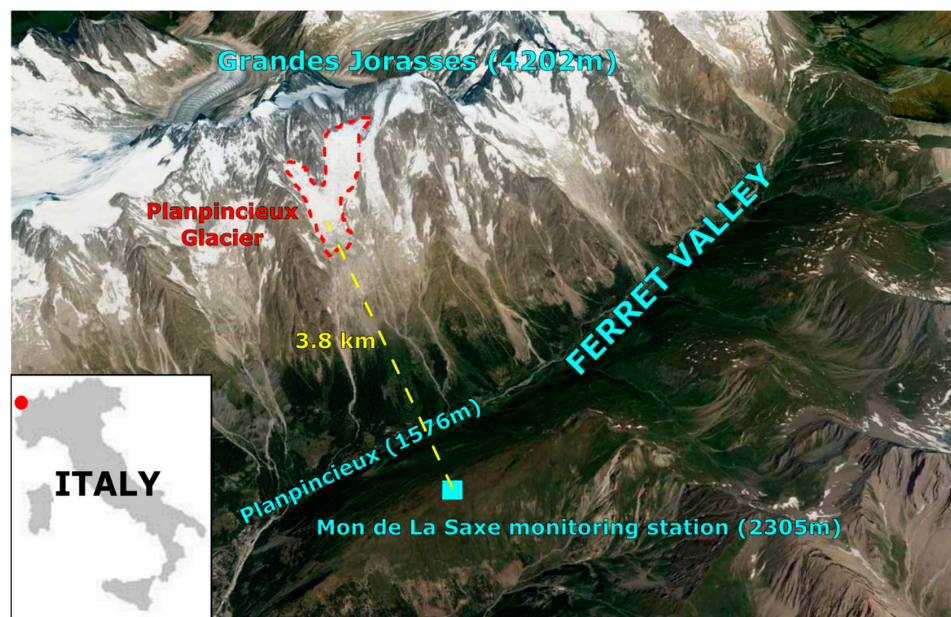


Figure 1. Aerial view of the Ferret Valley. The Planpincieux glacier is located in the upper part of the image. In the bottom part of the Ferret Valley, the Planpincieux hamlet represents the main element at risk of possible ice avalanche activation. On the opposite side of the valley, at a distance of 3.8 km, the monitoring station is located on the top of Mon de La Saxe.

Historical photos show that this rock-step has always interrupted the glacier flow, even when the terminus of the glacier was hundreds of metres down-valley. Therefore, the westernmost side of the glacier margin can be considered a single unit with its own dynamics. The temporal analysis presented in this paper focuses on this single unit.

A long series of historical instabilities affecting the glacier is recorded. The recurrent processes consist of floods or hyper-concentrated flows triggered by outbursts of glacial water pockets. Such events were recorded in 1929, 1984, 1985, 1986, 1987, 1996, 1998 and 2008. Floods or flows usually cause damage to the road at the bottom of the valley and to the bridge on the Montitaz stream. In some cases, the flood waves propagated over 10 km downstream.

In October 2011, a large crevasse opening was observed in the westernmost part of the glacier margin. This crevasse, which was considered anomalous, sealed later in the next month and then appeared again for a few months in September 2012. Nevertheless, because the glacier has been categorized as potentially dangerous in the frame of a monitoring plan for glacier-related hazards (set up by the regional authorities and managed by Fondazione Montagna Sicura, FMS), this event raised some concern. Historical data describe some mixed ice-snow avalanches that were triggered by the glacier and reached the valley bottom. The most important of these events occurred in December 1952.



Figure 2. Overview of the Grandes Jorasses massif (northern sector of the Mount Blanc massif) with the Grandes Jorasses Glacier (on the right side of the image) and the Planpincieux Glacier (highlighted in dashed red line). The image was acquired by the webcam of the monitoring station. The yellow box indicates the part acquired by the ZOOM camera, which is the most active region of the Planpincieux glacier.

Therefore, we decided that the Planpincieux glacier could represent an interesting case study in order to better understand temperate glacier dynamics and detect possible instability indicators.

3. Dataset and Equipment

In the following sections, we illustrate the optical monitoring system developed for the evaluation of the glacier deformation using PO analysis. Moreover, we present the radar surveys performed for comparison with the PO results and a LiDAR campaign.

3.1. Monitoring Station

The aim of the project was to produce a monitoring system able to capture the evolution of the glacier over time, but the choice of the type of the monitoring system has been conditioned by some critical issues: (i) the steepness of the glacier and surrounding rock walls and the highly crevassed area make difficult to install in situ monitoring systems; (ii) the high evolution rate of the glacier and the frequent icefalls hinder the installation of in situ measurement targets (e.g., topographic benchmarks or GPS); and (iii) the only possible sites for the instrumentation are the valley floor and the opposite side of the valley. Hence, remotely sensed systems have been judged to be the only possible solution for quantitative measurements.

LiDAR and GB-SAR have been considered too expensive for long-term installations and consequently were only used for short campaigns to support the study. After considering numerous remote sensing systems, we decided to construct a low-cost monitoring station based on the acquisition of optical images. The stereoscopic photogrammetric approach, which requires the installation of at least two different acquiring cameras in different locations, was excluded for logistic and financial reasons. A single-camera system that can be used for the detection of movement orthogonal to the line of sight was considered the most suitable solution.

For the identification of the location of the monitoring station, the main movement direction of the glacier was first estimated in order to acquire the largest motion component as possible. Two possibilities were considered: near Planpincieux village at the bottom of the valley and on

top of Mon de La Saxe. The monitoring station was installed at the end of August 2013 on the opposite side of the valley, on top of Mon de La Saxe because this positioning ensures good visibility of the entire glacier (Figure 1). The mean distance between the monitoring station and the glacier is 3.8 km, which is longer than the distances typically associated with other similar ground-based applications [29,30,44]. The choice of Mt. de La Saxe produces several accessibility problems, especially during the winter season when the trail is at risk of snow avalanches. This problem of accessibility has necessitated the use of a remote controlled system to reduce the need for direct access to the station.

We developed a monitoring station composed by different modules (Table 1, Figure 3). The first module is hosted by a plastic box and contains a EOS 600D DSLR camera (Canon, Tokyo, Japan; http://www.canon.it/for_home/product_finder/cameras/digital_slr/eos_600d/) (hereafter called ZOOM) with a DG-OS HSM lens (Sigma, Ronkonkoma, NY, USA) and all the relevant hardware. Additionally, a similar camera (WIDE) with a small focal lens (capturing a larger field of view) is also installed in the shelter box. The optical zooms are manually set and mechanically locked. The ZOOM observes the most active part of the glacier, while the WIDE camera acquires images of the entire glacier. The focus is set at infinite, with a hyperfocal distance of approximately 500 m. This set-up ensures the observed part of the glacier is always in focus.

Table 1. Main characteristics of the cameras mounted in the monitoring station.

Monitoring Module	Camera	Sensor/Resolution	Aperture Lens	Camera Lens	Focus	ISO
ZOOM	Canon EOS 600D	CMOS APS-C/ 5184 × 3456 px	f/8	(120–400 mm) Settled at 297 mm	Manual ∞	200
WIDE	Canon EOS 100D	CMOS APS-C/ 3456 × 5184 px	f/8	(100–300 mm) Settled at 120 mm	Manual ∞	200
Webcam	Canon Powershot	CMOS 8 Mpx	Auto f/2.6–5.5	(28–110 mm)	Auto 9 points	100

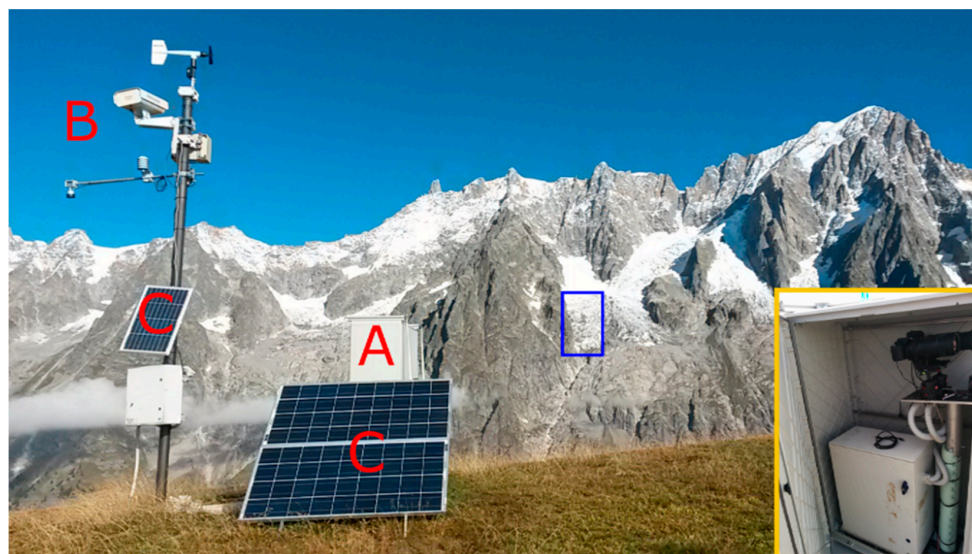


Figure 3. Monitoring station: (A) Box containing the two cameras. (B) Webcam and weather station. (C) Solar panels. The area acquired is highlighted in blue. In the yellow box: detail of the acquisition system within the shelter box.

Another module is mounted on top of a 3-m-high pole, which hosts a webcam that acquires medium-quality images of the glacier throughout the year. The use of the pole ensures the possibility of acquiring images during the winter season, when the box can be covered by snow. Figure 2 shows an example of a picture taken by the webcam, and the yellow box indicates the area acquired by ZOOM, which corresponds to the most active part of the Planpincieux glacier.

We compared the results of the installed cameras with calibrated cameras under laboratory conditions to evaluate the performances of the image correlations. The errors were some orders of magnitude lower than the measured data. Thus, we decided to not calibrate the cameras, as the committed error is much lower than the system precision.

The monitoring station also includes (i) a low-power PC; (ii) a UMTS modem; (iii) a battery pack and (iv) a solar power supply. All these components are stored inside a plastic box mounted to four supports cemented into the ground. To minimize the effect of the vibration caused by the wind (which can be very strong especially during the winter season), the two cameras are mounted to a pole cemented into the ground and separated from the external box.

The ZOOM and WIDE systems are able to acquire a picture every 2–3 min and to transfer the images to the server of the National Council of Research (CNR) in Torino, where they are stored and analysed. The frequency of the acquisition can be remotely controlled and depends on the glacier activity. During the summer, when the movements and number of icefalls are high, the acquisition frequency is set to 30 min. During the other seasons, when the activity of the glacier progressively decreases, the frequency is set to one hour. Since the system acquires RGB images, the acquisition is limited to the diurnal part of the day.

3.2. LiDAR and GB-SAR

As mentioned before, the use of LiDAR and radar has been evaluated but considered not suited for long-term acquisitions. To support the optical system with a high-resolution digital terrain model (DTM) and to have data collected via different technological methods that are able to measure the glacier movements, LiDAR and radar surveys have been performed.

The airborne LiDAR survey was performed on 9 June 2014, and a high-resolution DTM has been produced. In 2015, during the period between 2 September and 15 October, a radar campaign with an Ibis-S ground-based synthetic aperture radar (GB-SAR) was performed from the Planpincieux hamlet.

The data have been processed by the author using an interferometric approach [10,11,45]. The time separation between consecutive acquisitions is 16 min. Pixels with a Mean Coherence (MC) lower than a given threshold ($MC < 0.6$) were excluded from the processing. The atmospheric noise (Atmospheric Phase Screen, APS) was computed using fixed pixels, identified by Amplitude Dispersion, $DA < 0.35$. APS was estimated by fitting a 2D linear model [46] and was then subtracted from the interferometric phase. The unwrapping algorithm [47] was applied before and after the APS filtering in order to correct possible errors introduced during the APS subtraction. Finally, the results were georeferenced, and the actual metric displacement was estimated by projecting the measured deformation along the steepest gradient direction [11].

The results of the radar survey in 2015 will be described in detail in a future paper. However, some results are included in this study and compared with the results of the PO analysis.

4. Methodology

This chapter focuses on the monitoring chain, from the data acquisition to the processing and PO application. The workflow identifies four main steps: (i) data acquisition and transfer; (ii) co-registration; (iii) visual analysis and image selection and (iv) Pixel Offset analysis. The scheme of the method is illustrated in Figure 4. This procedure has been developed and tested on the area monitored by the ZOOM camera, which is the most active part of the glacier. Future applications will be extended to the dataset collected by the WIDE camera, which monitors the entire lower part of the glacier.

In the following, we present the different steps of the methodology and the results obtained based on the analysis of the available dataset. Hereafter, all the data are from the ZOOM system.

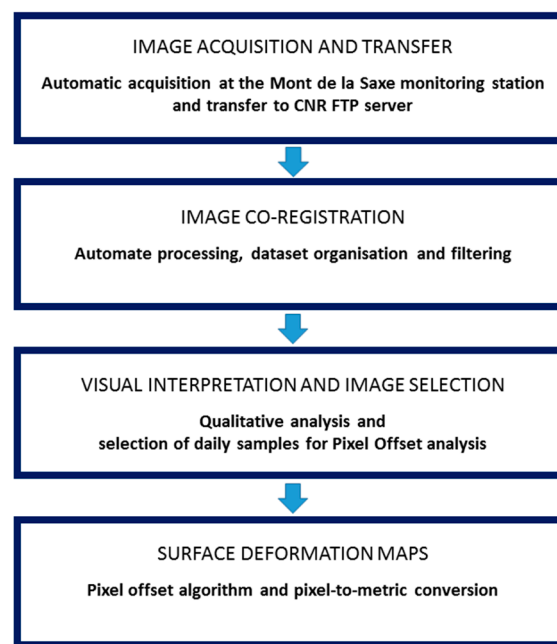


Figure 4. Work flow of the image processing.

4.1. Image Acquisition and Transfer

The monitoring station has been designed to acquire and transfer the images to CNR servers. The system can be remotely controlled to define the target area and the frequency of acquisition of images to ensure an accurate description of the glacier evolution.

The images have been continuously captured since August 2013. The acquisition system has been demonstrated to be rugged enough to withstand poor weather conditions and has produced a dataset containing sufficient images for the application of the method, ensuring a nearly continuous monitoring of the glacier movement.

The monitoring system has acquired and transferred more than 15,000 images from September 2013 to June 2016. The number of days in which the ZOOM system acquired images corresponds to approximately 63% (Table 2) of the considered period.

Table 2. Summary of the acquisitions during different visibility conditions. During winter, the system is frequently subjected to power failures and/or extreme weather conditions, during which data acquisition is impossible. In summer, the system runs almost continuously.

	Conditions	Number of Days	Fraction
Acquired images	Good visibility	414	40%
	Poor visibility	235	23%
Images not acquired	Technical problems	69	7%
	Power failure due to snow coverage	305	30%

The remaining 37% represents cases in which there were exceptional weather events (e.g., very strong wind or abundant snowfall) or problems with the power supply due to the insufficient production of power by the solar panels due to snow cover. Technical problems were related to improvements and maintenance of the system, which caused a system stop. If we consider the entire dataset, 40% of the images were acquired in ideal conditions (absence of clouds in the field of view during daytime). 23% of the images were captured correctly but with poor visibility (issues related to cloud cover, shadows, snow cover, and atmospheric dust).

4.2. Co-Registration

The system has been configured to minimize the movement of the camera and to always acquire the same area. However, several factors, such as fluctuations in temperature and humidity and the effect of air refraction, can create some shifts between pictures. The first step for the application of the pixel offset algorithm is image co-registration to obtain perfectly superimposed images. The co-registration algorithm achieves image registration by normalized spatial cross-correlation with sub-pixel precision [40,48].

The cross-correlation of each pair of images is computed in a reference tile, which is assumed to be time-invariant (i.e., it does not change over time due to movement and/or deformation). In this study, the reference tile uses a portion of the bedrock outcrop characterized by a steep slope in order to limit the incidence of snow cover and shadows and to minimize optical distortions due to the photographing of sloping surfaces (Figure 5a). Cross-correlation is computed to define the 2-dimensional shifts necessary to exactly superimpose the first picture (Master) on the second picture (Slave). The Slave image is then shifted to achieve superimposition.

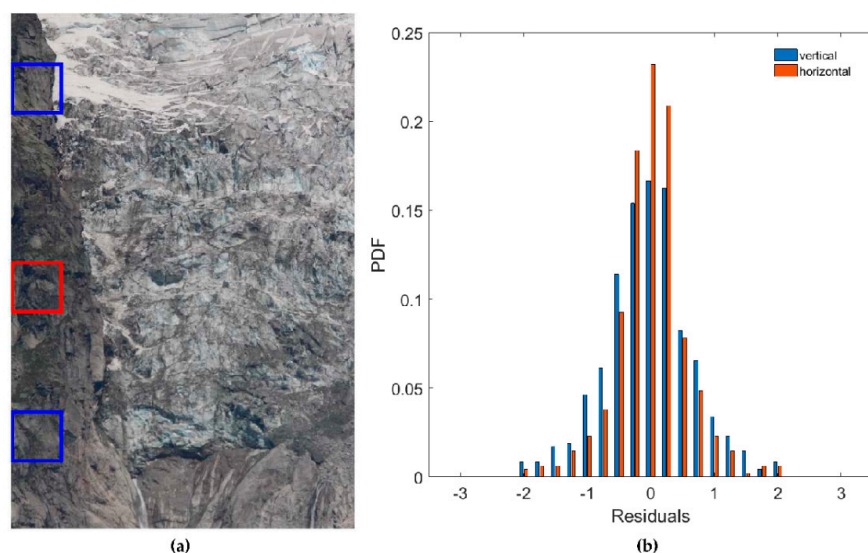


Figure 5. (a) In red the reference window used for the co-registration process, lying on the rock outcrop. In blue the two windows used for error estimation; (b) Frequency distributions of Mean Absolute Error computed separately for the vertical (blue) and horizontal (orange) dimensions.

The co-registration is performed automatically by a software package that verifies the coherence (see Section 4.4.1) between images. Moreover, a counting of the RGB colours is performed as a further control on image quality. The system discards images that do not satisfy the given conditions.

Environmental conditions, such as particles, air refraction and light conditions, can affect result precision, causing a loss of image sharpness and scaling phenomena. For these reasons, an error evaluation is recommended.

In this study, the residual errors after co-registration have been estimated as follows: two different windows of similar size are defined on the top and at the bottom of the outcrop (Figure 5a). After the first co-registration step, cross-correlation is computed again between the respective windows of the co-registered images. The frequency distributions of the resultant 2-dimensional shifts obtained by the analysis of more than 300 images (i.e., one image per day) are shown in Figure 5b with respect to both the horizontal and vertical dimensions. The Mean Absolute Error (MAE) is computed and is assumed to be the residual error of the co-registration application. The obtained MAE along the horizontal dimension is 0.92 pixels (px), and the MAE along the vertical dimension is 0.76 px. The different amounts of the MAE along the two directions can be due to different pixel metric

dimension (i.e., the Ground Sampling Distance, GSD). In fact, the reference tile features a very steep but not vertical rock wall, hence, the vertical GSD is larger than the horizontal (as explained in Section 4.4.2).

Based on the error distributions, in the current work a value of ± 1 px has been considered to be the system precision in both dimensions. Therefore, in this study the resulting shifts are rounded at the nearest integer. This choice is supported by two factors: (i) the value of the MAE, that is on the order of 1 px and (ii) based on a posteriori observations, the measured glacier deformations are quite large (on the order of a few pixels/day) and a sub-pixel offset estimate is not necessary.

This process has also demonstrated the non-occurrence of rotational effects due to camera vibrations for the frequency distributions of residuals are approximately symmetric (Figure 5b). Other more complex optical aberrations could be present, but working only in differential mode (i.e., comparing images taken by the same camera), these geometric distortions do not affect the results of the pixel offset algorithm.

4.3. Visual Analysis and Image Selection

Image analysis techniques can provide an objective, automatic and quantitative description of changes in selected scenes, thus avoiding uncertainties and inaccuracies due to the sensitivity of the operator, as well as considerable time-consuming work [34]. Nevertheless, a thorough analysis with the human eye still remains essential to the interpretation of changes in glacial dynamics (i.e., major icefalls and all the morphological changes), even with a qualitative approach [38,39].

The visual interpretation procedure has been carried out on the co-registered images for the entire dataset. This analysis involves the following steps:

- Manual selection of one image per day, ideally taken at the same hour (approximately midday) in order to have the same light conditions. When weather conditions make this impossible, the closest available image is chosen.
- Superposition of a reference grid on each image in order to detect, localize and describe the analysed processes.
- Visual comparison between images (one-to-one, each day with the previous) in order to detect sudden changes such as icefalls, sudden changes in water discharge, etc.
- Editing of a sequence of images covering the entire dataset period; this allows to detect long-term and slow processes, such as continuous displacement or crevasses widening.

Basically, this qualitative analysis focuses on four type of processes: (i) glacier flow; (ii) icefalls; (iii) crevasse opening and widening; and (iv) water discharge.

4.3.1. Glacier Flow

The analysis of the glacier flow has been conducted by focusing on recognizable features of the glacier surface, such as crevasses with a well-defined shape, fine debris spots, or ice surfaces bounded by two crevasses. The superimposition of a regular grid on the images allows the comparison of the flow features between different areas. In Figure 6 the images of 2 August 2015 and 8 October 2015 are shown, and it is evident that considerable displacement occurred in the right part.

4.3.2. Icefalls

Although the glacier flows downstream with discrete velocity, the front remains almost at the same position throughout the year, just above an area with a steeper slope. When the glacier oversteps the slope break, the flow is balanced by an increase in the frequency of small icefalls from the glacier margin.

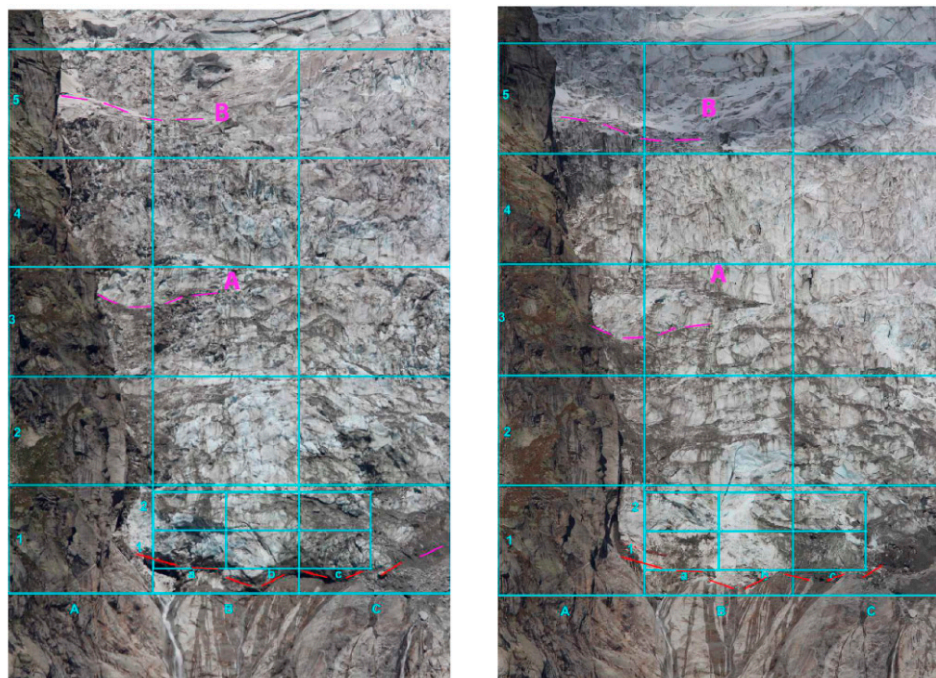


Figure 6. Visual analysis of the glacier flow on 2 August 2015 (**left**) and 8 October 2015 (**right**). The superimposed grid simplifies the comparison between different areas. In particular the movement of the pattern highlighted by the letter A appears evident. The B pattern appears less changed.

4.3.3. Crevasses Opening and Widening

Qualitatively, the flow movement seems to be balanced both by new fracturing or widening of existing crevasses and by ice deformation. However, the first process is likely the most relevant. The lower part of the glacier has a stair-shaped morphology, i.e., steep ice walls are separated by major fractures, probably following the bedrock shape. The opening and widening of crevasses causes the ice walls to slide down, allowing them to maintain their shape for a long period. In some cases, the glacier has experienced sudden widening of crevasses, causing the lower block to move down quickly, or even to collapse.

4.3.4. Water Discharge

Water circulation and pressure at the glacier/bedrock interface can significantly affect glacier stability. Therefore, changes in water discharge from the glacier have been observed, as they may indicate changes in the subglacial or englacial flow. In the studied images, only great changes in flow rate can be observed, as well as shifts in the stream position. Of course, seasonal variation in flow rate is normal and must be taken into account.

Although water traces are detected below the glacier front, the stream coming from the right part of the glacier mainly remains at the extreme right side, and it flows into a channel in the rock wall below the glacier itself. In just few cases, water discharge has spread along the entire front, e.g., in spring and early summer 2014. No anomalous changes in flow rate were detected during the observed period (i.e., sudden decreases or increase in the flow or sudden changes in the position of water flow).

4.3.5. Glacier Sectors

From the visual analysis, different sectors of the glacier have been broadly identified, based on particular flow, collapse and crevasse behaviours. From the bottom to the top of the image: (i) the *front sector* features an ice wall lying on a very steep bedrock formation partially covered by the vertical

front of the glacier and is subjected to frequent ice-falls; (ii) the *crevasse sector* is characterized by the highest velocity and by the formation of crevasses which causes entire ice walls to slide down; (iii) the *middle sector* also exhibits high velocity but the flow is more homogeneous; and (iv) the *plateau sector* is located in the uppermost part and is plateau-shaped.

4.4. Surface Deformations Estimation

The Pixel Offset method aims to determine information on shifts in position orthogonal to the line of sight (LOS) by comparing two co-registered images captured at different times [29,35]. The PO method is commonly used in remote sensing to determine superficial displacements on images acquired at different times [41]. In this study, the use of this application for the measurement of the glacier surface movements is possible due to the availability of a dataset composed of high-resolution images. The PO method is applied to pairs of co-registered images called Master and Slave. A two-dimensional displacement map is the result of the cross-correlation process between each Master/Slave sample. To produce useful information for interpretation, the discrete results are visualized as LOS-orthogonal displacement maps overlaid to the Master image, with the convention that the y-axis is positive downward and the x-axis is positive towards the right side of the image.

The algorithm consists of the iteration of the cross-correlation process between different images on pairs of tiles identified by a sliding window (Figure 7a) and it produces displacement maps expressed in px (Figure 7b). Sliding step dimension must be smaller than the tile, for the maximum detectable shift is half the size of the sliding window per the Nyquist criterion. The size of the sliding window is a compromise between the measurement accuracy, for which a small window is preferable, and the measurement precision (i.e., the signal-to-noise ratio). In this case, a large window ensures a better performance [44]. Moreover, the size of the sliding window can significantly affect the measurement [49].

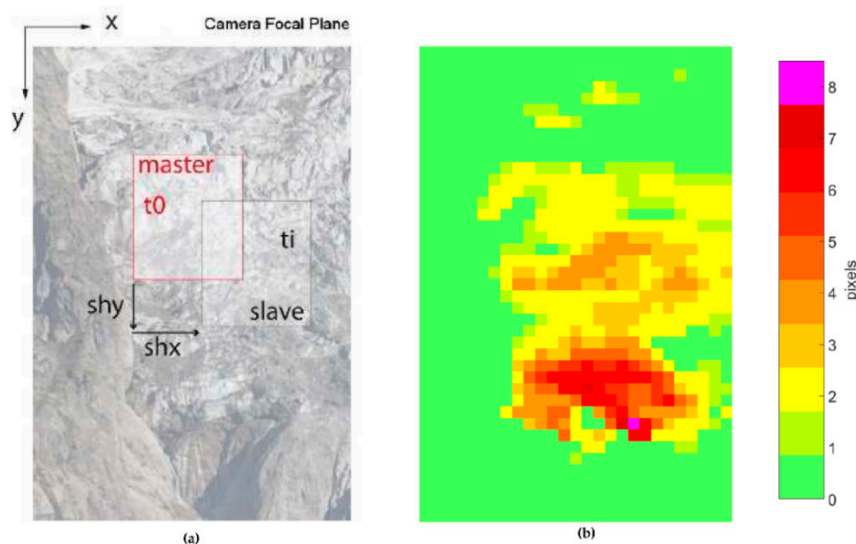


Figure 7. (a) Representation of the Pixel Offset iterative algorithm: the tile of the Master image is compared with the same tile of the Slave image. The procedure is applied to all the tiles. (b) Example of a result of the Pixel Offset algorithm with the vertical displacement between images computed in pixels.

In the current work, the sliding window is a square of 256 px per side, and the moving step is 128 px along both the vertical and horizontal axes. No oversampling factor is adopted because the requested accuracy and the mean error during co-registration are higher than unity and because Casu et al. [49] have proven that this parameter does not affect the results.

4.4.1. Coherence Estimation

Due to many factors (e.g., meteorological events and surface changes), the cross-correlation between images may worsen with time. Therefore, a variable describing the minimum level of correlation necessary to consider tiles comparable is needed. For each pair of tiles, the complex correlation is computed as follows:

$$\gamma = \frac{\langle I_1 I_2^* \rangle}{\sqrt{\langle |I_1|^2 \rangle \langle |I_2|^2 \rangle}} \quad (1)$$

where $I_{1,2}$ are the Fourier transforms of the Master and Slave images, respectively; * is the complex conjugate operator, and the angular brackets represent the spatial mean extended over the whole tile. The magnitude of this variable, $|\gamma|$, is called *coherence*, as it is related to the signal-to-noise ratio [50] and thus to the quality and reliability of the PO analysis.

In this study, a threshold of $|\gamma| \geq 0.75$ has been set, not including in the analysis of those pixels with a lower coherence. A further quality check has been adopted, based on a heuristic rule from data observations and physical considerations: tiles showing a negative displacement along the y-axis greater than the system precision (i.e., ± 1 px) are rejected because upward movement of the glacier flow is very unlikely.

According to our experience, to achieve a satisfying result, it is important to compare images taken under similar weather conditions and at similar times, i.e., approximately at midday to limit shadow effects.

4.4.2. Displacement Maps

The raw results of the PO application are displacement maps expressed in pixels (Figure 7b). In this section the procedure for the estimation of the metric displacement, i.e., the real displacement amount projected along the surface of deformation, is described. To accomplish this, it is necessary to know the direction of the displacement vectors point-by-point. Thus, it is possible to adopt the DTM surface, and assume that the movement is along the steepest gradient direction. However, in our study, the images are not orthorectified. Thus, in order to explain the method of the metric estimation, we suppose that the glacier movement is parallel to the mean slope of the glacier surface, as observed from the DTM produced by the LiDAR survey in June 2014 (Figure 8). The proposed method is easy to extend to general surfaces.

To estimate the metric displacement, it is necessary to evaluate the Ground Sample Distance (GSD, i.e., the spatial dimension of the pixels projected on ground). This can be achieved using the principles of the optics theory.

Let us consider a surface at a distance D . It is possible to compute the GSD ($\text{cm} \cdot \text{px}^{-1}$) as follows [51]:

$$\alpha = \frac{\text{atan}\left(\frac{S}{2f}\right)}{R} \quad (2)$$

$$\text{GSD}_p = 2 \cdot D \cdot \tan(\alpha) \quad (3)$$

$$\text{GSD} = \frac{\text{GSD}_p}{\cos(\sigma)} \quad (4)$$

where α is the angle of view of one pixel (i.e., the solid angle illuminated by one pixel), S is the sensor size (mm), f is the focal length (mm), R is the camera resolution (px), σ is the angle of incidence on the considered pixel and p stands for perpendicular to the LOS.

In this case study, D and σ are unknown, as the images are not georeferenced. Thus, the method is applied approximating the movement direction to a flat plane, and D and σ are estimated with simple geometric calculus. The portion of glacier illuminated by the camera lies on a plane with the horizontal axis orthogonal to the LOS and a slanted vertical axis. A section profile derived by an aerial

laser-scanner acquisition yielded a mean glacier slope of 32° (with respect to the horizontal), and the camera elevation angle is approximately 6° .

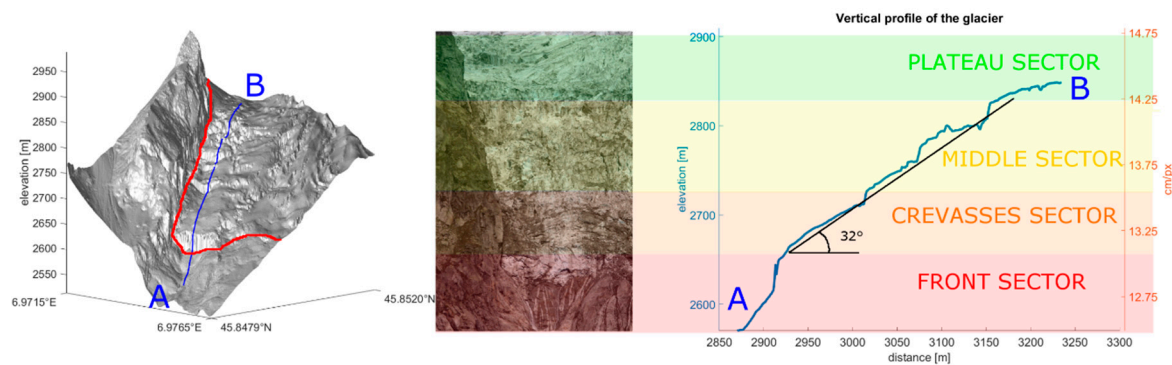


Figure 8. On the left, the DTM produced by the LiDAR survey in June 2014. Blue line identifies the location of the selected vertical profile. The red line highlights the glacier margins. On the right, representation of the vertical profile of the glacier. On average, the glacier lies on a flat plane with a mean slope of 32° . Different colours highlight the sectors of the glacier characterized by different physical features. The right vertical axis reports the pixel dimension increasing upward within the image.

The horizontal GSD varies with the distance, in accordance with Equation (3). However, because the LOS is not orthogonal to the glacier, the vertical GSD is corrected with Equation (4). This system scheme involves a GSD that linearly increases upward in both the vertical and horizontal dimensions.

In Table 3, we report the geometrical and optical variables of the system.

Table 3. Environmental and optical parameters of the system.

Mean distance (m)	3800	LOS angle of incidence	64°
Horizontal AOV	2.87°	Vertical AOV	4.3°
Vertical GSD at the bottom (cm)	12.49	Vertical GSD at the top (cm)	14.79
Horizontal GSD at the bottom (cm)	5.35	Horizontal GSD at the top (cm)	5.68

The obtained pixel size is the actual GSD of the image projected along the surface of the glacier. The main error during the procedure is the approximation of the deformation surface parallel to the mean slope of the glacier. This can cause an overestimation of the actual GSD in steep areas (e.g., ice walls) and underestimation in gently sloping areas (e.g., plateau). It was not possible to estimate the actual pixel-by-pixel GSD [31,44] because it would require an ultra-high-resolution DTM (comparable to the GSD) up-to-date at the acquisition time of each image (necessitating at least one DTM per season) as the glacier evolution causes great surface changes within short periods of time. Moreover, the deformation surface could not coincide with the glacier surface, as usually the glaciers are affected by the creeping process, which involves a movement direction steeper than the glacier surface [52–54]. By way of example, if the glacier movement direction is 90° , the GSD is approximately 5 cm; if the movement direction is half of the mean slope, the GSD is approximately 35 cm.

4.4.3. EAPOE

To support the management of a large dataset for the post-processing analysis, a graphical user interface tool for Matlab, called Effective Analysis for Pixel Offset Evaluation (EAPOE), has been developed. EAPOE creates a graphical representation of the maps of cumulative vertical displacement, mean vertical velocity and the fraction of data with acceptable coherence for the chosen period. In addition, the user can select a tile of the map to show the time series of cumulative vertical displacement and daily vertical velocity.

Moreover, by selecting one point of the temporal line, EAPOE displays the photographs of the current, the previous and the next day zoomed in on the neighbourhood of the selected tile.

This tool allows for fast and effective post-processing analysis, combining numerical and visual information. The graphical interface is designed to be user-friendly, which makes it possible to introduce EAPOE on open platforms, such as web sites.

In Figure 9, example of the output of EAPOE is reported. In the time series, the data under the coherence threshold (or outside the acceptable movement interval) are shown in yellow. As an example, a tile belonging to the middle sector is chosen (highlighted in blue in the maps on the left side). The selected tile shows a loss of coherence between the 9 and 10 of July 2015 due to an icefall, which can be observed in the photographs at the bottom.

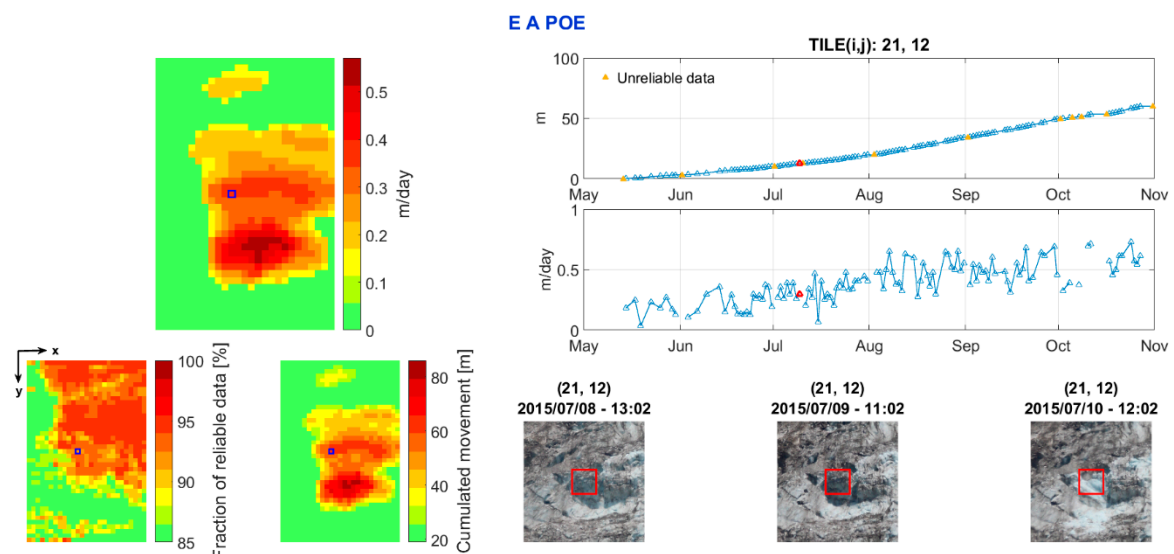


Figure 9. EAPOE output. On the left, there is a mean vertical velocity map (**top**), a fraction of days with acceptable coherence map (**bottom left**) and a cumulative vertical displacement map (**bottom right**). The time series of cumulative displacement and daily velocities of the selected tile are plotted on the right. At the bottom, the images show the glacier evolution.

5. Results

In the following, only the vertical displacement results are presented, as the horizontal deformations are negligible in the considered portion of glacier. As previously mentioned, the analysis is made using one image per day from approximately midday to limit the effects of shadow.

5.1. Displacement Time Series and Maps

The cumulative deformation maps are compared between the years 2014 and 2015, within the period 13 May to 31 October. Pixels representative of the different sectors are selected to display the time series of displacement, shown in Figure 10. As a result, it is possible to observe a great difference between the years in terms of total displacement. In contrast, the patterns of deformation appear quite similar. The pixel time series present different behaviour between years and between sectors.

This comparison shows the capabilities of the PO method in terms of the analysis of the glacier kinematics. The results document possible inter-annual changes and the yearly glacier behaviours of different regions, thereby potentially leading to the identification of break-off precursors or anomalies.

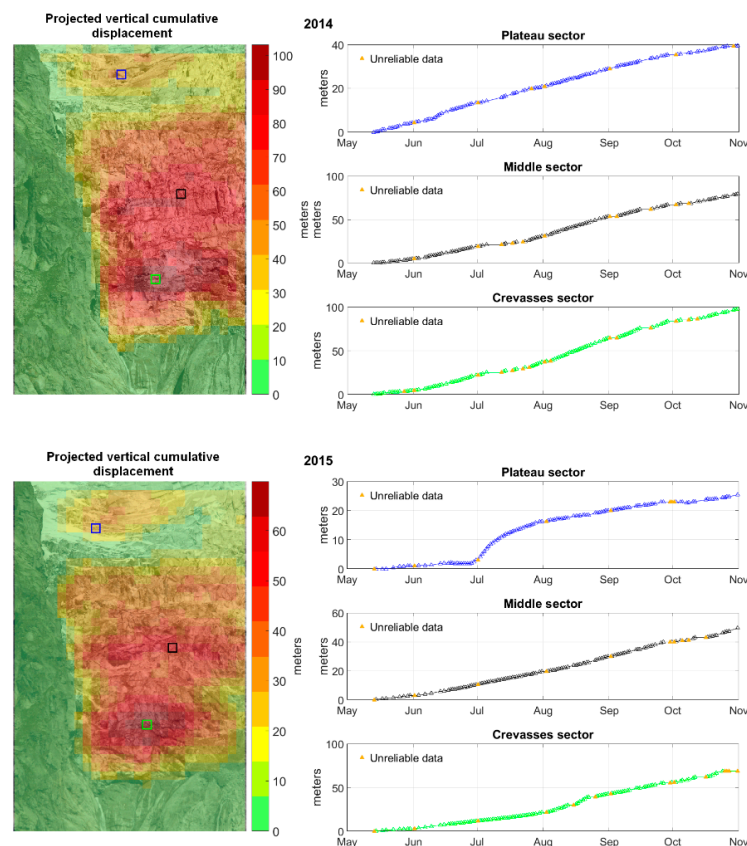


Figure 10. Projected vertical cumulative displacement maps for 2014 and 2015 and time series of displacement of different sectors. From the comparison one can note the behaviour changes and anomalies during time and space and identifies critical data.

5.2. Sectors

The post-processing analysis with EAPOE confirms the visual definition of the four different sectors of the glacier based on their different behaviours. Figure 8 shows a representation of the study area and a representation of the vertical section with an estimate of the resolution in $\text{cm} \cdot \text{px}^{-1}$ of different sectors. The relatively slow velocity recorded in the *plateau sector* is partially due to the gentle slope, which induces an underestimation of the ground resolution (due to the optical incidence). Therefore, the PO analysis computes only small displacements. The *front sector*, characterized by recurring icefalls, is the most difficult to analyse with the PO analysis due to the loss of coherence related to the collapses.

5.3. Comparison between PO and GB-SAR Measurements

In this section, we present a comparison of the glacier deformations estimated with the PO method and with GB-SAR. The dimensions of the pixels captured by the two devices are quite different. With the PO method, the dimensions of a single tile of the deformation maps are approximately $14 \times 5.7 \text{ m}^2$ (vertical and horizontal, respectively), whereas the pixel dimensions of the GB-SAR are approximately $0.5 \times 10 \text{ m}^2$. Moreover, because the results are not geo-referenced in a common reference system, the comparison is rather qualitative. Nevertheless, the movement pattern is similar for both techniques and, considering the great difference in resolution, it is possible to compare the mean displacement of entire sectors, which are recognizable within the deformation maps of both devices.

We note that the GB-SAR analysis is preliminary and that the GB-SAR acquires better data in very steep areas, where the angle of the movement direction is probably greater than the mean slope.

For these reasons, the GSD is estimated for an angle of 40° , which is the mean slope in the vicinity of the ice walls.

The comparison between the PO results and GB-SAR measurements during the period from 4 September 2015 and 27 September 2015 is performed and shown in Table 4. For this comparison, the mean daily velocities and the standard deviations computed for each sector are reported for both methods, except for the plateau sector, which was not viewed by the GB-SAR.

The agreement is good, i.e., within the error bars, although the values of the PO are slightly larger. This is likely due to an underestimation of the slope of the deformation surface. Future work will focus on the coupling of the data from both devices.

Table 4. Comparison of mean daily velocities between the Pixel Offset method and GB-SAR. The acquisition time refers to the period from 4 September 2015 to 27 September 2015. The error is given as the standard deviation.

Sectors	GB-SAR (cm/day)	Pixel Offset (cm/day)
<i>Front sector</i>	29.2 ± 3.8	31.4 ± 10.3
<i>Crevasses sector</i>	23.0 ± 2.6	29.9 ± 4.5
<i>Middle sector</i>	20.8 ± 3.9	26.0 ± 7.2

6. Discussion

In this paper, we have presented a low-cost monitoring and processing chain with an optical system for the evaluation of glacier deformations. The described procedure includes all the steps necessary to achieve this aim, including the installation of the monitoring station, the data acquisition, and the visual and computer analysis with the Pixel Offset technique. This work aims to assess the performances of the PO analysis and to define a processing chain for the collection and analysis of photographic data.

The combination of remote sensing and image processing approaches based on low-cost equipment allows us to study dangerous areas where in situ instrumentations cannot be installed. Furthermore, optical data permits a visual approach for the interpretation and control of the results. Our experience shows that the visual analysis allows the study of the flow of the glacier both in term of displacement and dynamics (e.g., water discharge, crevasse opening and closing, and collapses). Some of these phenomena are interesting but difficult to describe quantitatively. Therefore, a visual analysis of the images can provide information that is not detectable with the PO technique. In contrast, the PO method produces quantitative results, which are necessary for a deep understanding of the glacier behaviour. Moreover, PO results show good agreement with data recorded by a GB-SAR system.

Applying the PO algorithm, some sources of uncertainty can affect the measurements. Among these, the most important are as follows. (i) Camera vibrations and thermal effects during the co-registration phase (these errors have been statistically analysed and quantified); (ii) shadow effects and extreme light conditions and (iii) icefalls and the presence/absence of snow (these uncertainties are addressed in the coherence evaluation, although a heuristic empirical threshold may be required to exclude the data that satisfy the coherence threshold but are still subject to great errors); (iv) changes in the slope, which affect the pixel-to-metric conversion. In the current work, the deformation surface is approximated to be parallel to the mean glacier slope, but for the comparison with GB-SAR data, a local slope is used for the GSD estimation.

The current work focuses on a limited portion of the glacier because it aims to define a procedure for the PO analysis rather than to study the glacier kinematics. Many factors were involved in the choice of the studied area, such as the possibility of placing the monitoring station in front of it. Moreover, the LOS is perpendicular to the maximum gradient direction; thus, the movement of the glacier in the images is maximized in the vertical dimension and negligible in the horizontal dimension. The dimension of the area has been set to maximise the pixel resolution.

In this paper, we have proposed a method for the metric conversion of the observed pixel displacement. The main issue is the knowledge of the actual direction of the deformation vectors, which do not coincide with the mean slope because of local changes in the gradient and perhaps not even with the glacier surface because of creeping processes [52–54]. The proposed method can be easily applied to orthorectified images in general.

Future work will focus on two main lines of inquiry. The first will focus on processing improvements, including process automation, e.g., the identification of icefalls. This could lead to the realization of a completely automatic remote sensing system, able to relatively inexpensively monitor glacier deformation even in dangerous and difficult-to-reach areas. The second research line will focus on a practical application of the current PO system to the entire glacier (of which there are already three years of data) as a means to analyse the geophysics of the glacier. The use of this systems might be useful for improving the understanding of glacier kinematics and for the evaluation of numerical models. According to the state-of-the-art knowledge [3,55], there is no way to predict break-off events with significant forewarning by means of measurable parameters. Nevertheless, according to modelling applied to the analysis of historical cases, some morphological evidence can be considered predictive of potential instabilities, such as (i) a sudden increase or decrease in water runoff, (ii) rapid advance of the glacier tongue, or (iii) increase fracturing of the glacier tongue [43]. According to our experience, these elements might be detected using the presented system, which is a monitoring system that is able to analyse daily evolution but currently cannot be considered ready for civil protection purposes and/or early warning applications.

7. Conclusions

In the last decade, advances in hardware and software have led to the design of optical and visual technologies for the quantitative monitoring of gravitational processes [24]. Different approaches have been proposed, most commonly involving satellite [18,19,25] and airborne images [14,15]. More recently, ground-based photogrammetry began to be applied for Earth science purposes [29,44]. This approach has two main advantages: (i) low-cost equipment and (ii) the possibility of implementing continuous and long-lasting survey campaigns.

In this paper, we have presented a low-cost monitoring and processing chain based on an optical system for the evaluation of glacier deformation. Data have been acquired with an hourly frequency since September 2013 by the monitoring station, which has proven to be rugged enough to withstand the mountain weather. Such a large amount of data allows for a visual morphological analysis of the glacier. This analysis is able to recognize the most important features that characterized the observed phenomena. For the evaluation of the glacier displacement, a Pixel Offset algorithm has been developed to process one image per day. For an easier and faster post-analysis, a Matlab GUI has been developed to produce a user-friendly application with which non-expert end-users can process entire datasets.

We proposed a method for the pixel-to-metric conversion, and the observed pixel shifts between different images have been projected along the maximum gradient direction of the mean slope of the glacier surface. The acquired dataset allows for the first time the possibility of measuring the glacier evolution, in particular during the warm season, when the displacement rate is higher.

The results have been compared with GB-SAR surveys, adopting local mean slope for the metric conversion. The results of the comparison are in agreement, considering the errors of the PO algorithm. This demonstrates the reliability of the developed method in terms of measuring glacier deformations.

Future improvements might consist of image georeferencing, a better description of the glacier surface for 3D projection, and the automatic detection of areas subject to collapses.

Author Contributions: D.G. and P.A. conceived the research project and managed the monitoring system; N.D. and F.D.A. performed the data processing; M.V. and E.M. produced the visual analysis; D.G. and N.D. wrote the paper.

Conflicts of Interest: The authors declare no conflict of interest.

References

1. Nigrelli, G.; Lucchesi, S.; Bertotto, S.; Fioraso, G.; Chiarle, M. Climate variability and Alpine glaciers evolution in Northwestern Italy from the Little Ice Age to the 2010s. *Theor. Appl. Climatol.* **2015**, *122*, 595–608. [\[CrossRef\]](#)
2. Intergovernmental Panel on Climate Change (IPCC). *Climate Change 2014—Impacts, Adaptation and Vulnerability: Regional Aspects*; Cambridge University Press: Cambridge, UK, 2014.
3. Faillettaz, J.; Funk, M.; Sornette, D. Instabilities on Alpine temperate glaciers: New insights arising from the numerical modelling of Allalingsletscher (Valais, Switzerland). *Nat. Hazards Earth Syst. Sci.* **2012**, *12*, 2977–2991. [\[CrossRef\]](#)
4. Huggel, C.; Allen, S.; Deline, P.; Fischer, L.; Noetzli, J.; Ravanel, L. Ice thawing, mountains falling—Are alpine rock slope failures increasing? *Geol. Today* **2012**, *28*, 98–104. [\[CrossRef\]](#)
5. Clague, J.J.; Huggel, C.; Korup, O.; McGuire, B. Climate change and hazardous processes in high mountains Cambio climático y peligros naturales en altas montañas. *Rev. Asoc. Geol. Argent.* **2012**, *69*, 328–338.
6. Luckman, A.; Quincey, D.; Bevan, S. The potential of satellite radar interferometry and feature tracking for monitoring flow rates of Himalayan glaciers. *Remote Sens. Environ.* **2007**, *111*, 172–181. [\[CrossRef\]](#)
7. Kääb, A. Combination of SRTM3 and repeat ASTER data for deriving alpine glacier flow velocities in the Bhutan Himalaya. *Remote Sens. Environ.* **2005**, *94*, 463–474. [\[CrossRef\]](#)
8. Kääb, A.; Huggel, C.; Fischer, L.; Guex, S.; Paul, F.; Roer, I.; Salzmann, N.; Schlaefli, S.; Schmutz, K.; Schneider, D.; et al. Remote sensing of glacier-and permafrost-related hazards in high mountains: An overview. *Nat. Hazards Earth Syst. Sci.* **2005**, *5*, 527–554. [\[CrossRef\]](#)
9. Fallourd, R.; Harant, O.; Trouvé, E.; Nicolas, J.-M.; Gay, M.; Walpersdorf, A.; Mugnier, J.-L.; Serafini, J.; Rosu, D.; Bombrun, L.; et al. Monitoring temperate glacier displacement by multi-temporal TerraSAR-X images and continuous GPS measurements. *IEEE J. Sel. Top. Appl. Earth Obs. Remote Sens.* **2011**, *4*, 372–386. [\[CrossRef\]](#)
10. Luzi, G.; Pieraccini, M.; Mecatti, D.; Noferini, L.; Macaluso, G.; Tamburini, A.; Atzeni, C. Monitoring of an alpine glacier by means of ground-based SAR interferometry. *IEEE Geosci. Remote Sens. Lett.* **2007**, *4*, 495–499. [\[CrossRef\]](#)
11. Noferini, L.; Mecatti, D.; Macaluso, G.; Pieraccini, M.; Atzeni, C. Monitoring of Belvedere Glacier using a wide angle GB-SAR interferometer. *J. Appl. Geophys.* **2009**, *68*, 289–293. [\[CrossRef\]](#)
12. Strozzi, T.; Luckman, A.; Murray, T.; Wegmuller, U.; Werner, C.L. Glacier motion estimation using SAR offset-tracking procedures. *IEEE Trans. Geosci. Remote Sens.* **2002**, *40*, 2384–2391. [\[CrossRef\]](#)
13. Yan, S.; Liu, G.; Wang, Y.; Ruan, Z. Accurate determination of glacier surface velocity fields with a DEM-assisted pixel-tracking technique from SAR imagery. *Remote Sens.* **2015**, *7*, 10898–10916. [\[CrossRef\]](#)
14. Avian, M.; Kellerer-Pirklbauer, A.; Bauer, A. LiDAR for monitoring mass movements in permafrost environments at the cirque Hinteres Langtal, Austria, between 2000 and 2008. *Nat. Hazards Earth Syst. Sci.* **2009**, *9*, 1087–1094. [\[CrossRef\]](#)
15. Arnold, N.S.; Rees, W.G.; Devereux, B.J.; Amable, G.S. Evaluating the potential of high-resolution airborne LiDAR data in glaciology. *Int. J. Remote Sens.* **2006**, *27*, 1233–1251. [\[CrossRef\]](#)
16. Godone, D.; Godone, F. *The Support of Geomatics in Glacier Monitoring: The Contribution of Terrestrial Laser Scanner*; INTECH Open Access Publisher: Rijeca, Croatia, 2012.
17. Racoviteanu, A.E.; Williams, M.W.; Barry, R.G. Optical remote sensing of glacier characteristics: A review with focus on the Himalaya. *Sensors* **2008**, *8*, 3355–3383. [\[CrossRef\]](#)
18. Berthier, E.; Vadon, H.; Baratoux, D.; Arnaud, Y.; Vincent, C.; Feigl, K.L.; Remy, F.; Legresy, B. Surface motion of mountain glaciers derived from satellite optical imagery. *Remote Sens. Environ.* **2005**, *95*, 14–28. [\[CrossRef\]](#)
19. Scherler, D.; Leprince, S.; Strecker, M.R. Glacier-surface velocities in alpine terrain from optical satellite imagery—Accuracy improvement and quality assessment. *Remote Sens. Environ.* **2008**, *112*, 3806–3819. [\[CrossRef\]](#)
20. Manconi, A.; Allasia, P.; Giordan, D.; Baldo, M.; Lollino, G.; Corazza, A.; Albanese, V. Landslide 3D surface deformation model obtained via RTS measurements. In *Landslide Science and Practice*; Springer: Berlin, Germany, 2013; pp. 431–436.

21. Delacourt, C.; Allemand, P.; Berthier, E.; Raucoules, D.; Casson, B.; Grandjean, P.; Pambrun, C.; Varel, E. Remote-sensing techniques for analysing landslide kinematics: A review. *Bulletin de la Société Géologique de France* **2007**, *178*, 89–100. [[CrossRef](#)]
22. Giordan, D.; Dell'Anese, F.; Manconi, A.; Allasia, P. Managing landslide monitoring networks with near real time Geo-browsers. In Proceedings of the EGU General Assembly 2015, Vienna, Austria, 12–17 April 2015; Volume 17, p. 12193.
23. Lollino, G.; Manconi, A.; Giordan, D.; Allasia, P.; Baldo, M. Infrastructure in geohazard contexts: The importance of automatic and near-real-time monitoring. In *Environmental Security of the European Cross-Border Energy Supply Infrastructure*; Springer: Berlin, Germany, 2015; pp. 73–89.
24. Leprince, S.; Berthier, E.; Ayoub, F.; Delacourt, C.; Avouac, J.-P. Monitoring earth surface dynamics with optical imagery. *Eos Trans. Am. Geophys. Union* **2008**, *89*, 1–2. [[CrossRef](#)]
25. Malet, J.-P.; Auzet, A.-V.; Maquaire, O.; Ambroise, B.; Descroix, L.; Esteves, M.; Vandervaere, J.-P.; Truchet, E. Soil surface characteristics influence on infiltration in black marls: Application to the Super-Sauze earthflow (southern Alps, France). *Earth Surf. Process. Landf.* **2003**, *28*, 547–564. [[CrossRef](#)]
26. Javernick, L.; Brasington, J.; Caruso, B. Modeling the topography of shallow braided rivers using Structure-from-Motion photogrammetry. *Geomorphology* **2014**, *213*, 166–182. [[CrossRef](#)]
27. Carbonneau, P.E.; Lane, S.N.; Bergeron, N.E. Cost-effective non-metric close-range digital photogrammetry and its application to a study of coarse gravel river beds. *Int. J. Remote Sens.* **2003**, *24*, 2837–2854. [[CrossRef](#)]
28. Jiang, R.; Jáuregui, D.V.; White, K.R. Close-range photogrammetry applications in bridge measurement: Literature review. *Measurement* **2008**, *41*, 823–834. [[CrossRef](#)]
29. Fallourd, R.; Vernier, F.; Friedt, J.-M.; Martin, G.; Trouvé, E.; Moreau, L.; Nicolas, J.-M. Monitoring temperate glacier with high resolution automated digital cameras—Application to the Argentière Glacier. In Proceedings of the ISPRS Technical Commission III Symposium on Photogrammetry Computer Vision and Image Analysis (PCV 2010), Paris, France, 1–3 September 2010.
30. Benoit, L.; Dehecq, A.; Pham, H.-T.; Vernier, F.; Trouvé, E.; Moreau, L.; Martin, O.; Thom, C.; Pierrot-Deseilligny, M.; Briole, P. Multi-method monitoring of Glacier d'Argentière dynamics. *Ann. Glaciol.* **2015**, *56*, 118–128. [[CrossRef](#)]
31. Messerli, A.; Grinsted, A. Image georectification and feature tracking toolbox: ImGRAFT. *Geosci. Instrum. Methods Data Syst. Discuss.* **2015**, *4*, 491–513. [[CrossRef](#)]
32. Pham, H.-T.; He, H.; Vernier, F.; Trouvé, E.; Benoit, L.; Moreau, L.; Girard, B. Analyse de “Time-Lapse” stéréo pour la mesure de déformation 3D, application au suivi du glacier d'Argentière. In Proceedings of the 2014 Reconnaissance de Formes et Intelligence Artificielle (RFIA), Rouen, France, 30 June–4 July 2014.
33. Ahn, Y.; Box, J.E. Glacier velocities from time-lapse photos: Technique development and first results from the Extreme Ice Survey (EIS) in Greenland. *J. Glaciol.* **2010**, *56*, 723–734. [[CrossRef](#)]
34. Radke, R.J.; Andra, S.; Al-Kofahi, O.; Roysam, B. Image change detection algorithms: A systematic survey. *IEEE Trans. Image Process.* **2005**, *14*, 294–307. [[CrossRef](#)] [[PubMed](#)]
35. Debella-Gilo, M.; Kääb, A. Sub-pixel precision image matching for measuring surface displacements on mass movements using normalized cross-correlation. *Remote Sens. Environ.* **2011**, *115*, 130–142. [[CrossRef](#)]
36. Giordan, D.; Manconi, A.; Facello, A.; Baldo, M.; Dell'Anese, F.; Allasia, P.; Dutto, F. Brief Communication: The use of an unmanned aerial vehicle in a rockfall emergency scenario. *Nat. Hazards Earth Syst. Sci.* **2015**, *15*, 163–169. [[CrossRef](#)]
37. Giordan, D.; Manconi, A.; Tannant, D.D.; Allasia, P. UAV: Low-cost remote sensing for high-resolution investigation of landslides. In Proceedings of the 2015 IEEE International Geoscience and Remote Sensing Symposium (IGARSS), Milan, Italy, 26–31 July 2015; pp. 5344–5347.
38. Lim, M.; Petley, D.N.; Rosser, N.J.; Allison, R.J.; Long, A.J.; Pybus, D. Combined digital photogrammetry and time-of-flight laser scanning for monitoring cliff evolution. *Photogramm. Rec.* **2005**, *20*, 109–129. [[CrossRef](#)]
39. Sturzenegger, M.; Stead, D. Close-range terrestrial digital photogrammetry and terrestrial laser scanning for discontinuity characterization on rock cuts. *Eng. Geol.* **2009**, *106*, 163–182. [[CrossRef](#)]
40. Guizar-Sicairos, M.; Thurman, S.T.; Fienup, J.R. Efficient subpixel image registration algorithms. *Opt. Lett.* **2008**, *33*, 156–158. [[CrossRef](#)] [[PubMed](#)]
41. Scambos, T.A.; Dutkiewicz, M.J.; Wilson, J.C.; Bindshadler, R.A. Application of image cross-correlation to the measurement of glacier velocity using satellite image data. *Remote Sens. Environ.* **1992**, *42*, 177–186. [[CrossRef](#)]

42. Pralong, A.J.W. On the Instability of Hanging Glaciers: Study on the Fracture Processes and the Predictability of Failures. Ph.D. Thesis, Swiss Federal Institute of Technology in Zürich, Zürich, Switzerland, 2005.
43. Faillietaz, J.; Funk, M.; Vincent, C. Avalanching glacier instabilities: Review on processes and early warning perspectives. *Rev. Geophys.* **2015**, *53*, 203–224. [[CrossRef](#)]
44. Travelletti, J.; Delacourt, C.; Allemand, P.; Malet, J.-P.; Schmittbuhl, J.; Toussaint, R.; Bastard, M. Correlation of multi-temporal ground-based optical images for landslide monitoring: Application, potential and limitations. *ISPRS J. Photogramm. Remote Sens.* **2012**, *70*, 39–55. [[CrossRef](#)]
45. Allstadt, K.E.; Shean, D.E.; Campbell, A.; Fahnestock, M.; Malone, S.D. Observations of seasonal and diurnal glacier velocities at Mount Rainier, Washington, using terrestrial radar interferometry. *Cryosphere* **2015**, *9*, 2219–2235. [[CrossRef](#)]
46. Luzi, G.; Monserrat, O.; Crosetto, M.; Copons, R.; Altimir, J. Ground-Based SAR interferometry applied to landslide monitoring in mountainous areas. In Proceedings of the International Conference “Mountain Risks”, Florence, Italy, 24–26 November 2010.
47. Costantini, M. A novel phase unwrapping method based on network programming. *IEEE Trans. Geosci. Remote Sens.* **1998**, *36*, 813–821. [[CrossRef](#)]
48. Fienup, J.R.; Kowalczyk, A.M. Phase retrieval for a complex-valued object by using a low-resolution image. *J. Opt. Soc. Am. A* **1990**, *7*, 450–458. [[CrossRef](#)]
49. Casu, F.; Manconi, A.; Pepe, A.; Lanari, R. Deformation time-series generation in areas characterized by large displacement dynamics: The SAR amplitude pixel-offset SBAS technique. *IEEE Trans. Geosci. Remote Sens.* **2011**, *49*, 2752–2763. [[CrossRef](#)]
50. Bamler, R.; Just, D. Phase Statistics and Decorrelation in SAR Interferograms. In *International Geoscience and Remote Sensing Symposium*; Institute of Electrical & Electronics Engineers, Inc. (IEEE): Tokyo, Japan, 1993; Volume 3, pp. 980–980.
51. Northey, N.W. The angle of view of your lens. In *The Camera*; Columbia Photographic Society: Philadelphia, PA, USA, 1916.
52. Gudmundson, G.H. Glacier sliding over sinusoidal bed and the characteristics of creeping flow over bedrock undulations. *Int. J. Rock Mech. Min. Sci. Geomech. Abstr.* **1995**, *4*, 195A.
53. Kääb, A.; Gudmundsson, G.H.; Hoelzle, M. Surface deformation of creeping mountain permafrost. Photogrammetric investigations on rock glacier Murtèl, Swiss Alps. In Proceedings of the 7th International Conference on Permafrost, Yellowknife, NT, Canada, 23–27 June 1998; Volume 57, pp. 531–537.
54. Paterson, W.S.B. *The Physics of Glaciers*; Butterworth-Heinemann: Oxford, UK, 1994.
55. Faillietaz, J.; Sornette, D.; Funk, M. Numerical modeling of a gravity-driven instability of a cold hanging glacier: Reanalysis of the 1895 break-off of Altelsgletscher, Switzerland. *J. Glaciol.* **2011**, *57*, 817–831. [[CrossRef](#)]



Article

Image Classification for Automated Image Cross-Correlation Applications in the Geosciences

Niccolò Dematteis , Daniele Giordan *  and Paolo Allasia

Research Institute for Hydrogeological Protection, National Council of Research of Italy, 10135 Turin, Italy; niccolo.dematteis@irpi.cnr.it (N.D.); paolo.allasia@irpi.cnr.it (P.A.)

* Correspondence: danielle.giordan@irpi.cnr.it

Received: 1 April 2019; Accepted: 4 June 2019; Published: 8 June 2019



Featured Application: This study proposes a method that enables the automatic application of image cross-correlation when monitoring any displacements in the geosciences. As such, it solves one of the main current image processing issues: The requirement of manual image selection. The method reduces the need for extensive financial and human resources when conducting surveys, and it can be applied in a preventive warning context.

Abstract: In Earth Science, image cross-correlation (ICC) can be used to identify the evolution of active processes. However, this technology can be ineffective, because it is sometimes difficult to visualize certain phenomena, and surface roughness can cause shadows. In such instances, manual image selection is required to select images that are suitably illuminated, and in which visibility is adequate. This impedes the development of an autonomous system applied to ICC in monitoring applications. In this paper, the uncertainty introduced by the presence of shadows is quantitatively analysed, and a method suitable for ICC applications is proposed: The method automatically selects images, and is based on a supervised classification of images using the support vector machine. According to visual and illumination conditions, the images are divided into three classes: (i) No visibility, (ii) direct illumination and (iii) diffuse illumination. Images belonging to the diffuse illumination class are used in cross-correlation processing. Finally, an operative procedure is presented for applying the automated ICC processing chain in geoscience monitoring applications.

Keywords: image cross-correlation; monitoring; geosciences; automated systems; machine learning; image classification; image shadowing

1. Introduction

Image cross-correlation (ICC) is a well-known methodology used in the geoscience field to measure earth surface dynamics and deformation phenomena [1–4]. Ground-based ICC applications enable observations of relatively fast natural processes at a medium range and at a high spatiotemporal resolution. In addition, the low costs, minimal equipment required to conduct photographic surveys and the certain degree of automation used in data processing, make ground-based ICC applications valuable tools for use in monitoring phenomena, even in harsh environments [3]. The adoption of an automated procedure for processing monitoring data allows high-frequency-updated results to be obtained without the need for continuous human supervision, and can be applied in early warning system applications, thereby reducing human and economic costs [5]. Different automatic approaches used to collect and process monitoring data have been reported in literature, such as those for the inclinometer [6], total station [7,8], ground-based SAR [9] and integrated systems [10].

However, the major limitation of the technology used in the ICC approach for natural phenomena monitoring, is its dependence on visual conditions, since adequate illumination (i.e., sunlight) and

a complete view of the scene (i.e., clear sky) are required. This prevents an automated ICC procedure being applied in near-real-time that could be used for warning purposes, as a human intervention to selecting suitable images is required. In addition, the presence of shadows formed by the interaction between direct illumination and surface roughness can cause errors in the cross-correlation (CC) process, and this problem has often been considered in literature [1,11–16]. The most popular solution used to avoid such effects is to consider pictures that have a similar visual appearance, and have been acquired in a similar light (usually in the middle of the day [12,17,18] when the length of shadows is reduced, due to the higher sun elevation angle). However, Ahn and Box [12], and Giordan et al. [15] proposed the use of images acquired in conditions of diffuse illumination (such as the evening hours) when any shadows are minimal or absent. Both of these approaches involve the manual selection of images, and images with a partial or absent view (caused by fog or the presence of obstacles), and with non-homogeneous illumination, are thus discarded. In this respect, Gabrieli et al. [14] developed a method for automatically discarding images taken during adverse meteorological conditions; this involved analysing the mean and standard deviation of colour values along predefined lines in the image. Hadhri et al. [19] also automatically identified images containing artefacts, or where vision was obscured, using a posteriori statistical analysis based on image entropy. Furthermore, Schwalbe and Maas [16] developed a method for automatically detecting shadowed areas, and then removing them from the CC computation.

In our work, we describe a method of classifying images according to visible and illumination conditions that enables the selection of images with diffuse illumination. To correctly classify the images, we adopted a support vector machine (SVM) approach. This supervised machine learning method was originally developed by Boser et al. [20] and Cortes and Vapnik [21]; it is a well-known methodology used in remote sensing and geoscience, and it has been adopted in a wide range of fields and applications (please, see reviews in [22–25]). In addition, we present the use of completely automated processing in monitoring active gravitational processes through ICC. The principal innovation relies on applying autonomous image selection to ICC according to the a posteriori probability that an image belongs to a certain class of illumination.

2. Methods

The objective of this study was to develop a procedure that conducts image cross-correlation (ICC) autonomously, and which can be implemented for monitoring geophysical processes. The ICC method is briefly described in Section 2.1. As already mentioned, one of the main sources of uncertainty in ICC results relates to the presence of the shadows; therefore, the impact of shadows on the ICC is analysed here to demonstrate how they negatively affect any results (Section 2.2). With respect to this inherent problem, a method that autonomously selects images acquired with diffuse illumination is developed, and to achieve this, a support vector machine (SVM) is trained to distinguish between three classes of images in accordance with the presenting illumination (Section 2.3). Finally, an operative and autonomous procedure is designed to conduct ICC, with the aim of being used in geoscience monitoring applications (Section 2.4).

2.1. Image Cross-Correlation Processing

Digital image correlation (DIC) developed following the advent of performant computer machines and digital photography in the early 1990s, and has been applied predominantly in fluid dynamics [26,27] and satellite imagery [1]. The rationale behind DIC is to determine the field of motion using spatial cross-correlation between corresponding subsets of two images (image cross-correlation, ICC), where ICC analyses the texture of an image rather than specific recognisable elements (as in feature tracking methods [28,29]).

ICC can be computed in the spatial domain (direct cross-correlation, DCC) [1,3,26] or in the frequency domain (phase cross-correlation, PCC) using the discrete Fourier transform (DFT). In the former case, a subset of the original (master) image slides into a larger interrogation area of the slave

image. In this respect, a two-dimensional (2D) correlation coefficient is computed for each possible position, and a map of correlation values is obtained. The coordinates of the element with the maximum correlation coefficient correspond to the displacement of the slave image in relation to the master. Although DCC requires high computational costs, it suffers less from decorrelation associated with motion, because it computes correlations between the same tiles in different positions (the Lagrangian approach). Conversely, the PCC computes the correlation between master and slave tiles (that are in the same position) into the image (the Eulerian approach). Therefore, part of the original texture is removed with respect to motion from the interrogation area, and this causes possible decorrelation. The PCC is computed through a complex product involving the Fourier transforms of the master and slave images, and this is equivalent to conducting a spatial cross-correlation in accordance to the convolution theorem.

In our work, the ICC is operated in the phase domain, as it provides a faster computation [30,31] process than DCC, but a similar performance [32]. Specifically, we use the two-step computation method proposed by Guizar-Sicairos et al. [33]. In the first run, the CC is computed with integer precision, thereby avoiding the zero-padding operation, and the centre of the slave matrix is then translated according to the shifts obtained. In the second run, the DFT is applied only to a small subset of the data to obtain subpixel accuracy. This method has the advantage of strongly limiting the zero-padding operation, thereby reducing the computational costs, and limiting the loss of information intrinsic in the PCC due to the Eulerian approach used in measurements [16,31].

The processing chain adopted in this study is based upon the approach presented in Dematteis et al. [34], and can be divided into four steps. First, certain image enhancement operations are conducted [12–14]. The scene illuminant is computed using principal components analysis (PCA) [35] and then subtracted from the trichromatic (RGB) image. The removal of the illuminant allows the reduction of possible low-frequency signals caused by illumination changes that can affect the computation of the DFT [36]. Subsequently, the image is converted to greyscale, and a sharpen mask is applied to enhance the details in the image texture. Such an operation aims to reduce any possible defocusing or blurring effects that are frequent in images acquired with limited illumination; in this respect, Ahn and Box [12] stated that the application of a sharpen mask can improve the ICC results in hazy situations. Second, the images are coregistered with respect to a common image to correct possible misalignments. The CC is computed on an area that is assumed to be stable, and the images are planarly translated according to the shifts obtained. Third, a sliding window identifies corresponding tiles on both the master and the slave images; the CC is then computed on the tile couples. Adjacent windows are overlapped by 50% to improve the robustness of the results. Fourth, outlier removal is conducted. The usual approaches employed to correct possible outliers rely on heuristic and manual analysis [15,17], but Ahn and Box [12] identified outliers using cluster analysis during the CC procedure, and then applied a combined statistic-heuristic method in the post-interrogation phase. In this study, outlier correction is conducted using the universal outlier detection (UOD) approach [37] as this has the advantages of being automated, unsupervised, and non-subjective, which are fundamental requisites for automatic processing.

2.2. Analysis of Shadow Impact in ICC

Shadow lengths that change in relation to the sun's position during the course of the day can affect the CC results by producing apparent motion. However, their influence has been rarely quantified [13,16]. For example, Travelletti et al. [13] observed that changes in illumination can lead to an average CC offset $\mu > 1\text{px}$ for images acquired over a time lag of 1–3 h, and also noticed that the correlation coefficient diminishes at a low sun elevation angle.

In this study, the effects of shadows on the results of the CC are investigated by considering four groups of images that have different illumination conditions: (i) Diffuse illumination; (ii) direct illumination in images acquired at the same hour in the day (12:00), when the sun azimuth and elevation were almost the same; (iii) direct illumination in images taken at different times during the

day (i.e., when the sun was in different positions); and (iv) synthetic images produced from an existing digital surface model using a set of shaded reliefs. In the latter, the position of the lighting point was changed, thereby simulating the motion of the sun during the course of a day.

For each dataset, ICC was conducted for each possible pair of images and 45 CC maps were produced. The mean and standard deviation of the shifts for each map were then analysed, as these are associated with measurement accuracy and precision, respectively.

The possibility that a shadow's presence could have differing effects on the CC results performed in phase or space domains was investigated, and the same analysis described above was conducted using both DCC and PCC. Results showed no relevant differences between the two techniques.

2.3. Image Classification

As previously mentioned, using images acquired in conditions that are diffusely illuminated enables a reduction in the apparent motion caused by changes in shadow shapes in relation to surface roughness. To this aim, it is fundamental that images are categorized in accordance with their visual appearance. In this study, three classes of visual and illumination states are considered: (i) Direct illumination (SunLight), (ii) diffuse illumination (DiffLight), and (iii) blocked or limited view (NoVis).

To identify the class of the images, SVMs are trained based on defining optimal decision hyper-planes that separate objects belonging to different classes [38]. In addition, the SVM assigns an a posteriori probability that each image belongs to a particular class. The objects are represented as vectors in an n -dimensional space, where the axes correspond to specific features that describe the objects. The elements of vectors represent feature values of each object that will be classified (for a didactic description of the SVM methods, please see Haykin [39]).

To describe the images, seven different features are identified as follows: (i) The number of RGB triplets (i.e., the values for R, G, and B bands) (*colorNum*), where the number of triplets is divided by the number of pixels in the image. The division is conducted to make the datum comparable for different image resolutions; (ii–iii) the number of pixels in the range 0–63 (*blackNum*) and 64–127 (*greyNum*) of the intensity histogram, which are determined using an 8-bit colour chart; (iv–v) the mean value of the hue (*hueMean*) and saturation (*satMean*) channels in the HSV colour space; (vi) the value of the maximum peak in the image intensity histogram (*maxPeak*), and (vii) the corresponding bin position (*posPeak*) (Figure 1). The image intensity (or greyscale) is defined as the mean value of the RGB channels.

We choose features that could be informative about the image appearance, and that were not correlated among them. Specifically, *colorNum* should be directly associated with the amount of light in the image, which enhances the colour contrast, while *blackNum* and *greyNum* indicate different levels of image darkness. *hueMean* is the average colour shade, and can be related to ambient skylight (i.e., diffuse illumination) [40], while *satMean* is high when the colours are vivid, and low when they tend toward grey. *posPeak* represents the dominant colour, while *maxPeak* is the magnitude of the dominant colour. Figure 1a shows an 8-bit (256 colour bins per RGB channel) NoVis class image. Only 0.5% of the possible RGB triplets are present, which is evident from the narrow spatial distribution of the RGB values shown in Figure 1d. The upper portion of the picture has an almost uniform and grey colour that implies low *satMean* (Figure 1b); this produces a prominent dark peak (high *maxPeak*, low *posPeak*) (Figure 1e).

To reduce the dimensionality of the decision plane (i.e., to reduce the number of features used to train the SVM), a Monte Carlo cross-validation is conducted [41,42], with the aim of selecting a group of features (i.e., the estimator) that minimize misclassification errors. The fundamental of that approach is to randomly divide the available known data into two groups, one to train the SVM (training set) and one to evaluate the misclassification error (test set), and the feature selection procedure is repeated many times. Features are sequentially added to the candidate estimator by selecting the feature or group of features that minimize the misclassification error (averaged on the multiple iterates). This procedure guarantees a higher generality of the SVM and enables overfitting to be avoided.

To maintain generality no a priori information on the probability of class occurrence is introduced during the tuning of the SVM.

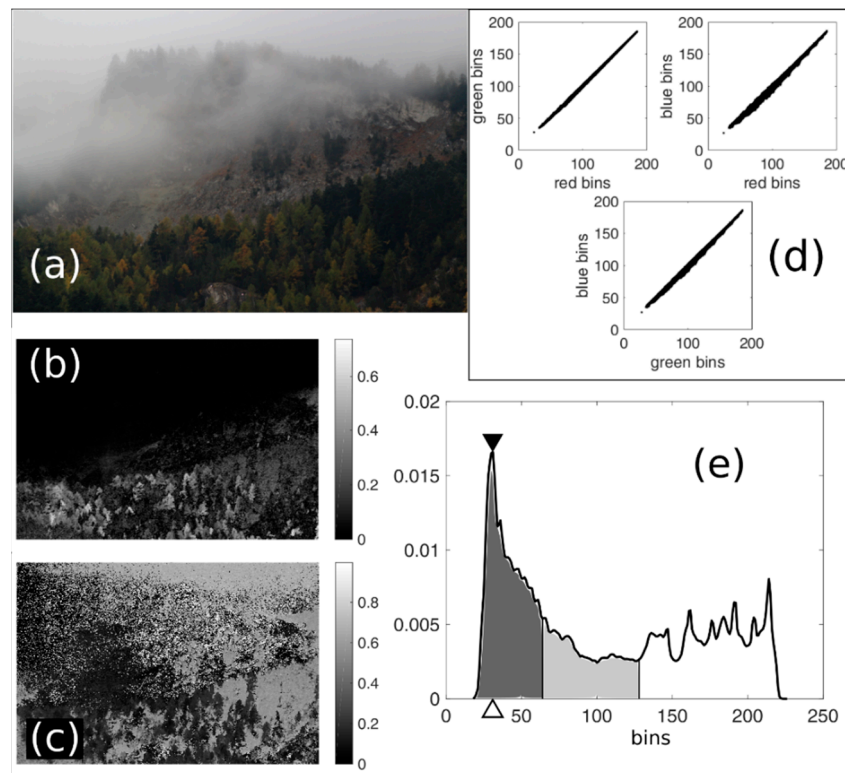


Figure 1. (a) Original 8-bit trichromatic (RGB) image of NoVis class; (b) saturation map; (c) hue map; (d) 8-bit RGB values, and (e) intensity histogram in which the ordinate value of the black triangle indicates the *maxPeaks* and the abscissa value of the white triangle represents *posPeaks* features. The dark and light grey areas are *blackNum* and *greyNum* features, respectively.

2.4. Automated ICC Procedure

The procedure presented here automatically selects images on which to perform ICC and obtains displacement maps of geophysical phenomena. This procedure was developed in 2018 and its effectiveness was tested in the monitoring of the Planpincieux glacier on the Italian side of the Mont Blanc massif. The processing chain is designed for automatic, continuous, and autonomous monitoring via ICC in the typical situation of daily acquisitions. The procedure is best suited for surveying natural phenomena at velocities greater than the common ICC uncertainty, i.e., $\sim 10^{-1}$ px [12,13]. It can thus be applied to observe relatively fast natural processes such as glacier flows and slope instabilities that are quite active. Depending on the phenomenon monitored, it is possible to vary the scheduled image acquisition and processing frequencies.

The procedure is conducted on a daily frequency and it is divided into four independent subroutines (Figure 2).

- (i) Image acquisition. First, the images are acquired at an hourly frequency by the monitoring system and are then transferred in real time to the data collection section of the operative server.
- (ii) Image classification and selection. The images acquired in the current day are classified through SVM according to the visual and illumination conditions. It is attributed a posteriori probability to belong to the classes. The results are saved in a list of classified images, and this list is subsequently browsed to search for the image with the highest probability score to belong to the DiffLight class. Such an image is labelled as suitable for ICC. If there are no new images, a warning is released and the process skips to the next subroutine.

- (iii) Image coregistration. This subroutine coregisters the new images acquired. A common reference image is used to coregister all the images and the coregistered images are saved. Such images are used for ICC and for possible manual vision inspection.
- (iv) Image cross-correlation. The list of images suitable for ICC is browsed to check for possible new image couples. If identified, the new images are cross-correlated and displacement maps are computed.

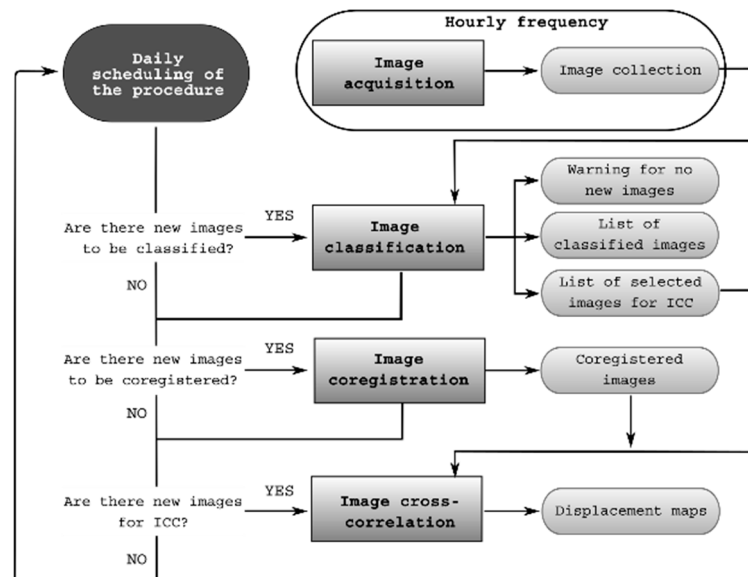


Figure 2. Workflow of an automated procedure used in image cross-correlation (ICC) applications.

To evaluate the performance of the automated image selection, we manually classified the images and selected the images suitable for ICC. On several occasions (i.e., approximately 10% of cases), manual classification of images was difficult, and there was a certain ambiguity between the classes. Therefore, three new bivalent classes were introduced relating to images that could be arbitrarily classified as either SunLight or DiffLight, SunLight or NoVis, and DiffLight or NoVis (respectively SD, SN, DN).

Moreover, the performances of automated selection through SVM were then compared with other possible simpler alternatives of automatic criteria. We analysed the cases of selecting images at a fixed hour of the day: At 12:00 (the SunLight class) and at 18:00 (the DiffLight class). To simulate such automated selection methods, photos were picked without applying quality control to verify whether the scene was adequately visible.

3. Dataset

To develop and test the analysis described in Section 2, various dedicated datasets were employed (Table 1). These comprise images of natural environment sites with heterogeneous geo-hydrological phenomena in north-western (NW) Italy (Figure 3). The generality of the method was thus strengthened by using a wide range of images.

Two different datasets comprise images from Monesi village (Liguria region, NW Italy), which is an Alpine village partially affected by a rotational slide activated during a flood in October 2016. MNS1 is the shaded relief extracted from a digital surface model (DSM) acquired using a drone and MNS2 is an RGB dataset acquired using a fixed camera installed on the opposite side of the valley.

The ACC dataset (Piemonte region, NW Italy) comprises a sequence of images acquired by a fixed camera installed to monitor the evolution of a large bedrock outcrop that has historically been affected by rock falls. During the monitoring period, there was no evidence of any slope instability activation in the area studied.

Table 1. Datasets adopted in the current study. The first column lists the type of analysis employed using the various datasets. Also presented is the site where images were acquired for each dataset, the type of environment and image, the number of elements, the image resolution and the symbol attributed to the dataset.

Analysis	Site	Environment	Image Type	# Images	Resolution [px]	Dataset Symbol
Shadow effect	Monesi	Alpine village	Shaded relief	10	656 × 875	MNS1
		Rotational landslide	RGB	30	3456 × 5184	MNS2_a
Image classification	Acceglio	Bedrock outcrop	RGB	278	3456 × 5184	ACC
	La Saxe	Rockslide	RGB	159	3240 × 4320	SAXE1
	La Saxe	Rockslide	RGB	163	1536 × 2048	SAXE2
	La Saxe	Rockslide	RGB	268	3312 × 4416	SAXE3_a
	Monesi	Rotational landslide	RGB	117	3456 × 5184	MNS2_b
	Planpincieux	Glacier	RGB	225	3456 × 5184	PPCX1
	Planpincieux	Glacier	RGB	195	3456 × 5184	PPCX2_a
Automated ICC procedure	La Saxe	Rockslide	RGB	139	3312 × 4416	SAXE3_b
	Planpincieux	Glacier	RGB	1549	3456 × 5184	PPCX2_b

Three different datasets comprise images of the Mont de la Saxe rockslide (Valle d'Aosta region, NW of Italy); this is an active landslide with an estimated volume of 10^7 m³ that endangers the underlying village and road, which road provides access to the Mont Blanc tunnel, an important communication route between Italy and France [5,43–45]. The three different datasets that were acquired from three different view perspectives for this rockslide are SAXE2 and SAXE3, which were acquired by cameras positioned outside the area of gravitational instability, and SAXE1, the camera for which was installed on the rockslide and controlled one of the most active sectors.

SAXE3 is divided into two subsamples: SAXE3_a, which includes pseudo-random images taken in 2014 and 2015, and SAXE3_b, which is a time-lapse relating to the period 15–30 April 2014, when activity was pronounced, and a large failure occurred. There are no images included in either SAXE3_a or SAXE3_b.

The last dataset consists of images of the Planpincieux glacier on the Italian side of the Mont Blanc massif. The glacier is characterised by relevant kinematics and dynamics; numerous detachments from the snout have endangered the underlying hamlet of Planpincieux. This glacier has therefore been the subject of various remote sensing surveys in the recent past [15,34,46]. Two different cameras monitor the evolution of the glacier: PPCX1 acquires images of the lower part of the glacier while PPCX2 acquires images of the right lower tongue, the most active part of the glacier. The PPCX2 dataset, like the SAXE3 dataset, is divided into two distinct subsamples: PPCX2_a, which comprises images acquired during the years 2014–2017; and PPCX2_b, which includes the complete dataset acquired between 18 May and 3 October 2018. During this period, the automated ICC procedure described in Section 2.4 was applied in real time and more than 1500 images were collected.

The following text describes and discusses the use of every dataset in the procedures described in Sections 2.2–2.4.

To evaluate the effect of shadows we conducted two different analyses: (1) A synthetic set of ten shaded reliefs of a DSM was produced by changing the lighting source position to simulate the sun's motion during the day. Shadows cast by obstacles were projected by computing the viewshed from the light source. Three of the ten shaded reliefs produced are shown in Figure 4a.1–a.3. (2) Ground-based RGB pictures of the same area acquired in different illumination conditions were considered. Three groups of ten images were selected that were acquired in (i) diffuse illumination (Figure 4(b.1)), (ii) direct illumination (Figure 4(b.2)), and (iii) direct illumination at the same hour (at 12:00) (Figure 4(b.3)), so that similar direct illumination was maintained in the photos.

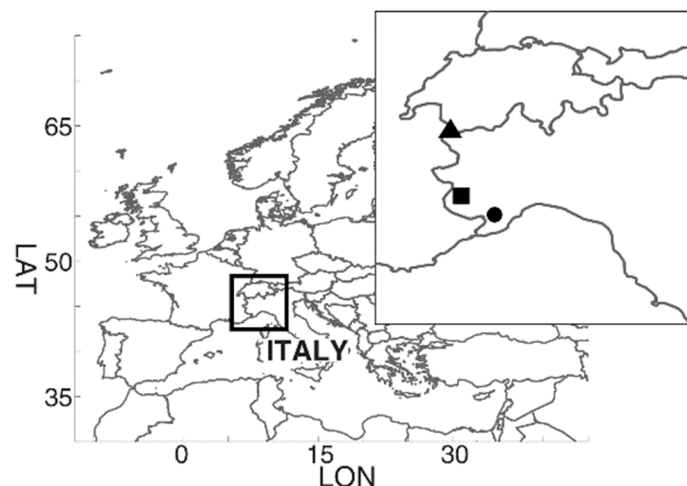


Figure 3. Locations of sites corresponding to the various datasets adopted. The black circle, square, and triangle correspond to Monesi di Mendatica, the Acceglio rock face, and the Mont de La Saxe landslide and Planpincieux glacier, respectively. This image was produced using the Matlab package borders [47].

An ensemble of seven datasets representing scenes from various natural environments was used to study the image classification methodology and to ensure that the method could be generalised. Specifically, datasets ACC, SAXE1, SAXE2, SAXE3_a, MNS2_b, PPCX1 and PPCX2_a were employed, and samples of images from these datasets acquired in different visual conditions are shown in

Figure 4c1–i3. Each dataset comprises photos belonging to different classes (i.e., acquired in different illumination and visual conditions), as catalogued during the process described in Section 2.3. The numbers of images in each class employed from the different datasets are presented in Table 2.

The images included in all the datasets were acquired during different years and seasons. The results showed that the SVMs classified the images accurately, even when dissimilar environmental conditions and morphological changes were presented. However, although it is considered that SVM training by adopting photos taken during specific seasons could improve its performance, this could result in a loss of generality.

Table 2. Numbers of images belonging to different classes used in each dataset.

Dataset	SunLight	DiffLight	NoVis
A	94	97	87
B	77	45	37
C	53	60	50
D	95	96	77
E	59	31	27
F	75	75	75
G	65	65	65

The last application is automated ICC processing, and this was conducted using two-hourly time-lapses. The first dataset (PPCX2_b) comprised more than 1500 images, and it was collected to monitor the activity of the Planpincieux glacier from 18 May to 3 October. During this period, the automated ICC procedure described in Section 2.4 was applied in real time to monitor the glacier's evolution. The second dataset used was SAXE3_b, where 139 images of the Mont de La Saxe landslides were selected. Table 3 shows the number of images employed from PCCX2_b and SAXE3_b datasets and their distribution among the different classes (considering also the bivalent classes described in Section 2.4).

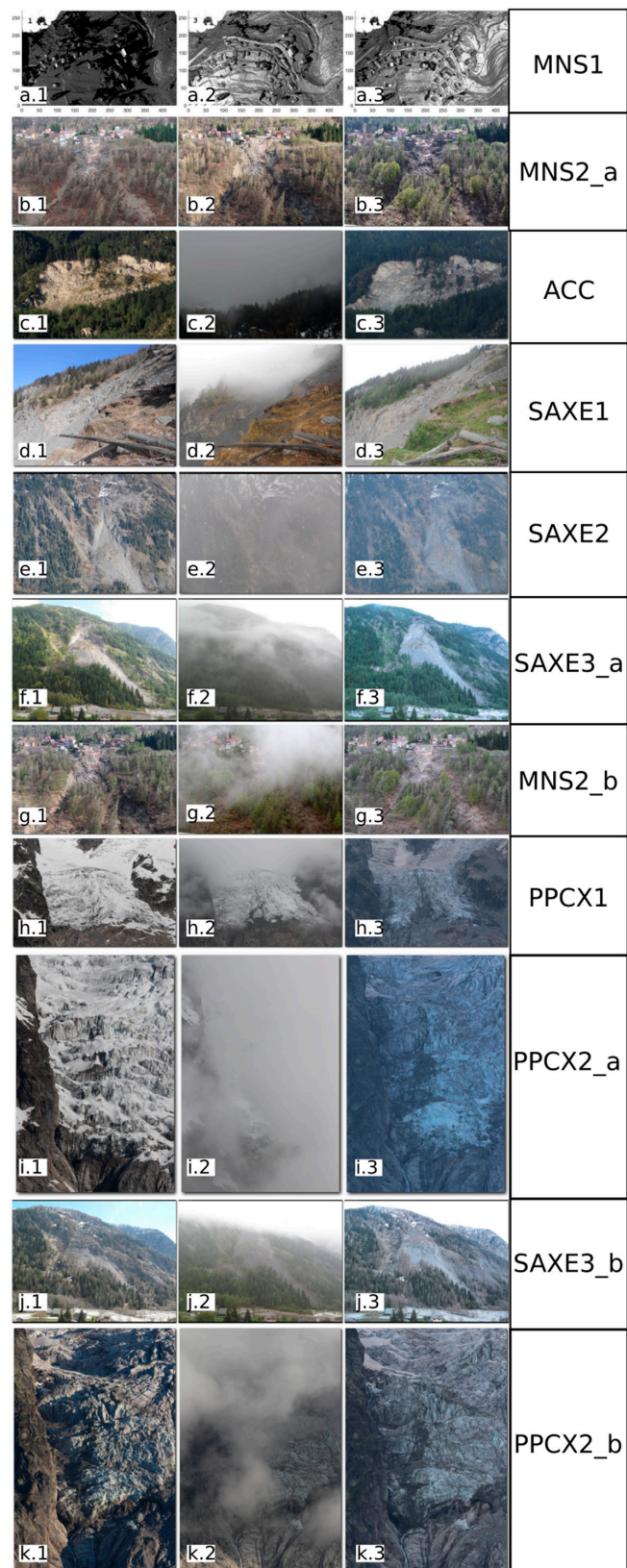


Figure 4. Examples of images taken from different datasets. Row (a) shows the 1st, 3rd and 7th shading reliefs with changes in the light source position; (b.2,b.3) were acquired in direct illumination at different hours of the day; and rows (c–i) show examples of each class from the datasets used in image classification analysis. The photographs in rows (j,k) were used to develop the automatic procedure.

Table 3. Number of images manually classified for datasets D1 and G1.

Dataset	SunLight	DiffLight	NoVis	SD	SN	DN
D1	24	78	11	16	0	10
G1	838	386	171	105	15	34

4. Results

A quantitative analysis of how the shadow effects affect the ICC performance is presented in Section 4.1, and this demonstrates the negative impact of that phenomenon. In Section 4.2, the results of the Monte Carlo cross-validation are presented, with the aim of determining the best features that can be used to train the SVMs. Finally, Section 4.3 presents the results of the automatic ICC processing chain with respect to two operative case studies.

4.1. Shadow Impacts of ICC

The MNS2_a dataset comprises three groups of ten images with different illumination states. As the acquired scene is fixed, it is valid to assume that any possible change in the results relates principally to the shadow effect. Figure 5 shows a boxplot of the mean (μ) and standard deviation (σ) of the single CC maps of each group; these were computed for all possible image couples, and differentiated for the vertical (y) and horizontal (x) directions. It is evident that the dispersion of the two variables is at a minimum for the images acquired with diffuse illumination. Moreover, the σ obtained with images acquired at the same hour and in direct illumination are approximately two and three times greater, on average, than that obtained for images acquired in diffuse illumination. It is also evident that the μ of the horizontal component has slightly greater variability, while there are no significant differences between the two components for the σ .

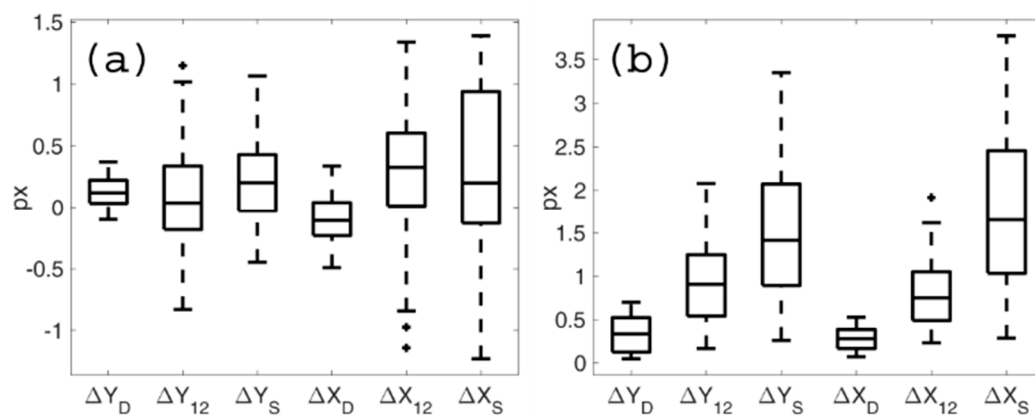


Figure 5. Boxplots of (a) mean and (b) standard deviation of CC. Subscripts D, 12 and S are as follows: D represents images acquired respectively with diffuse illumination, 12 denotes images with direct illumination taken at a fixed hour of the day (i.e., 12:00), and S concerns images taken in direct illumination with different sun azimuths and elevation angles.

Figure 6 presents the μ and σ of the ICC maps produced using all of the couples of the available images from the dataset MNS1, where the results are ordered according to the simulated position of the sun during the day. The results obtained with synthetic shaded relief show that both μ and σ increase with an increase in the difference between the azimuth and elevation of the sun's position. In addition, both values are higher for the horizontal direction, which indicates that the change in the sun's azimuth has a greater effect on CC results than the change in elevation.

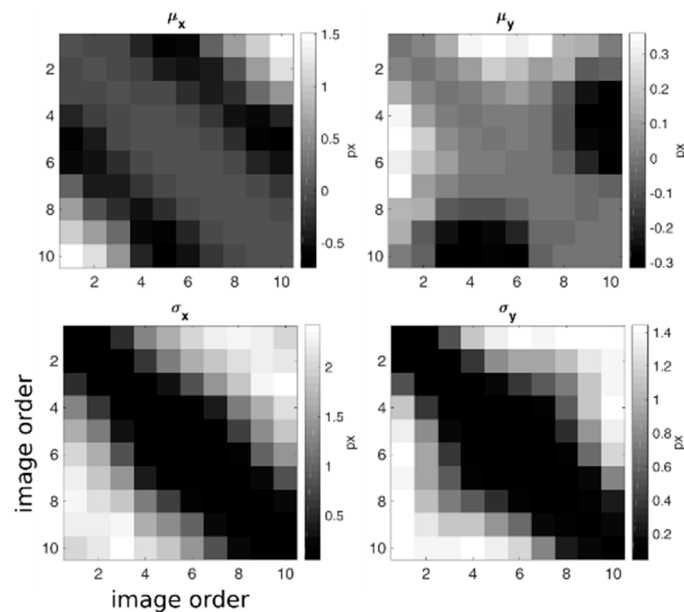


Figure 6. Mean and standard deviation of cross-correlation maps for all possible couples of shaded relief images. The two matrices on the left refer to the horizontal direction and those on the right refer to the vertical. The elements of the matrices correspond to the couples formed from the i th and j th images of a sequence of ten images that were ordered to simulate the motion of the sun during the day.

4.2. Cross-Validation and Image Classification

The results of the cross-validation (Table 4) show that the minimum classification curve is achieved by using three or four features to train the SVMs (Figure 7), where the minimum error obtained ranges between 0.03% and 7.9% (with a weighted mean of 5.2%). In contrast, greater errors are obtained when more than four features are employed; this can probably be ascribed to overfitting in the training phase, as the number of training elements is limited.

Table 4. Order of features identified during cross-validation analysis for each dataset; features in black are those selected for classification.

Dataset	I	II	III	IV	V	VI	VII
ACC	<i>colorNum</i>	<i>hueMean</i>	<i>maxPeak</i>	<i>posPeak</i>	<i>satMean</i>	<i>greyNum</i>	<i>blackNum</i>
SAXE1	<i>colorNum</i>	<i>posPeak</i>	<i>hueMean</i>	<i>blackNum</i>	<i>maxPeak</i>	<i>greyNum</i>	<i>satMean</i>
SAXE2	<i>colorNum</i>	<i>maxPeak</i>	<i>posPeak</i>	<i>hueMean</i>	<i>greyNum</i>	<i>satMean</i>	<i>blackNum</i>
SAXE3_a	<i>colorNum</i>	<i>hueMean</i>	<i>greyNum</i>	<i>maxPeak</i>	<i>satMean</i>	<i>posPeak</i>	<i>blackNum</i>
MNS2_b	<i>colorNum</i>	<i>blackNum</i>	<i>maxPeak</i>	<i>greyNum</i>	<i>hueMean</i>	<i>satMean</i>	<i>posPeak</i>
PPCX1	<i>colorNum</i>	<i>hueMean</i>	<i>blackNum</i>	<i>posPeak</i>	<i>satMean</i>	<i>greyNum</i>	<i>maxPeak</i>
PPCX2_a	<i>colorNum</i>	<i>posPeak</i>	<i>hueMean</i>	<i>blackNum</i>	<i>maxPeak</i>	<i>greyNum</i>	<i>satMean</i>

The *colorNum* is evidently the predominant and most relevant feature in the classification. For each dataset, it is found to be the most important feature; it alone provides a misclassification error in the range of 6% to 18%. *hueMean* is included in the group of relevant features in five of the datasets, whereas *greyNum* and *satMean* are never selected as relevant features. However, the features required for a proper training of the SVM differ between the datasets, and it is thus necessary to train a dedicated SVM for each specific scene.

For the MNS2_b dataset, a local minimum is achieved with only two features, while the absolute maximum is obtained with four features. Considering that this dataset comprises a limited number of images, training the SVM with two features is probably the best solution to avoid overfitting.

It is also worth noting that to select the minimum number of features, it may be a good criterion to use the features up to where the error curve decreases by less than 0.5% when one more feature is added. Using this approach, two or three features would be sufficient, depending on the dataset.

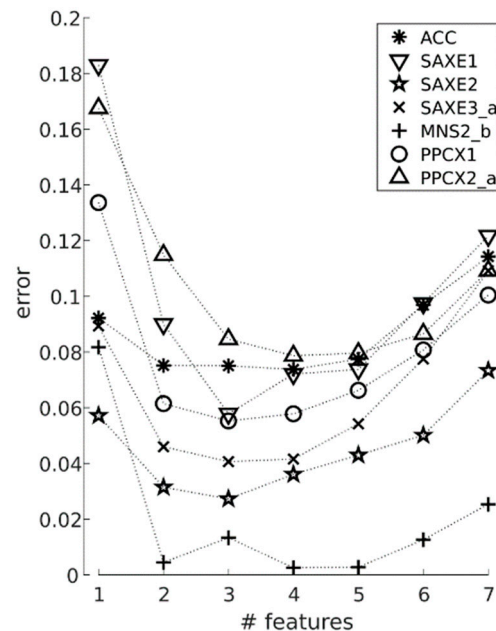


Figure 7. Error curves (expressed as fraction of misclassification) obtained from cross-validation of the support vector machine (SVM) training. The minimum was always reached by employing three or four features.

Figure 8 shows an example of image classification using the two of the most relevant features obtained from the cross-validation (Table 4), to illustrate the migration of feature values among the different visual conditions. From the graph, it can be seen how *colorNum* increases from the NoVis, DiffLight and SunLight classes (which is expected) while *hueMean* of the SunLight class is lower.

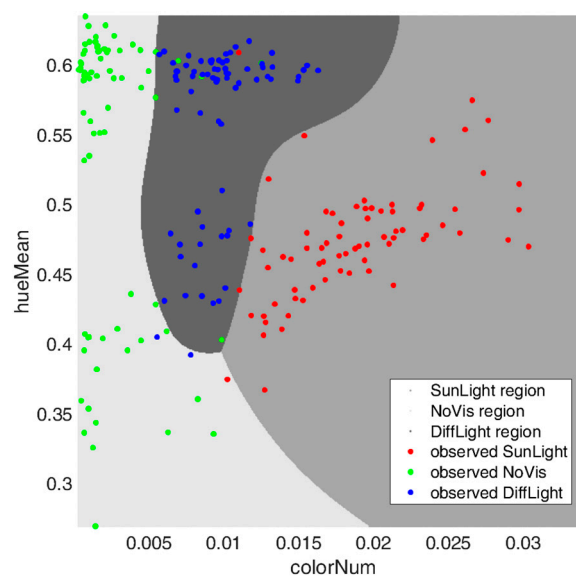


Figure 8. Image classification of PPCX_1 images using the two principal features *hueMean* and *colorNum*. The regions delimit the areas where new elements within are classified as belonging to the corresponding class.

4.3. Automated ICC Procedure

To evaluate the results of the automated ICC procedure, image classification and selection performances were analysed. Table 5 shows the results of automatic classification. In the case of images belonging to the bivalent class, an image was considered to be correctly classified if it was classified into one of the two classes that had been identified manually. Results therefore show that the classification error for dataset SAXE3_b is 4.3%, while the selection error is 0%. For dataset PPCX2_b, the misclassification is 7.7%, while the error in determining whether the correct image should be included in the ICC processing is 13%. For both datasets, the classification error is comparable with the value obtained during the cross-validation analysis. However, the selection error is related more to the occurrence of DiffLight false positives, which are higher in dataset PPCX2_b but considerably lower in SAXE3_b.

Table 5. Results of automatic classification and selection for datasets SAXE3_b and PPCX2_b. The number of images for each class are reported and correspond to exact, bivalent and erroneous classification. The percentage of correctly classified images is shown in the row below (in relation to the sum of exact and bivalent classifications). The two columns on the right show the percentage overall classification error and selection error, respectively.

Dataset	SunLight			NoVis			DiffLight			Classification Error	Selection Error
SAXE3_b	22	2	4	11	2	0	74	22	2	4.3%	0%
	86%			100%			98%				
PPCX2_b	781	45	52	166	23	26	335	79	42	7.7%	13%
	94%			88%			91%				

We also compared the ICC results obtained with automatic images selection through SVM, and the results of the automatic image selection using images selected at fixed hours, in conditions of direct and diffuse illumination. The correlation and mean absolute error (MAE) were computed with respect to results obtained using the manual selection of images (Table 6). The comparison was conducted pixel-by-pixel; therefore, more than $2 \cdot 10^5$ and $5 \cdot 10^5$ elements were considered for datasets SAXE3_b and PPCX2_b, respectively.

Table 6. Correlation ρ and MAE of two dimensions for dataset D1.

Dataset	Method	ρ_x	MAE _x [px]	ρ_y	MAE _y [px]
SAXE3_b	SVM	0.69	0.18	0.84	0.24
	SunLight	0.12	1.30	0.19	1.44
	DiffLight	0.38	0.44	0.69	0.57
PPCX2_b	SVM	0.31	0.34	0.71	0.51
	SunLight	0.02	1.78	0.14	2.21
	DiffLight	0.08	1.71	0.22	1.97

The results obtained with SVM selection show much higher correspondence with ICC results than the other two methods. Two principal factors provided lower performances in the other two selection methods: (1) As the state of view of the images was not controlled, it was possible to include images with obscured or partial views in the number of images that were processed; (2) the images with direct illumination suffered from the negative effects of shadows; therefore, any results for images with direct illumination are of a lower quality.

Furthermore, the correlation along the vertical direction was higher than that along the horizontal direction. As previously observed in the synthetic image analysis, the incidence of the sun's azimuth angle is greater because its value varies more than the sun's elevation, which influences the vertical direction. The MAEs of the vertical direction were thus greater because the values of displacement of these dimensions were greater.

Furthermore, a rather low correlation was noted between the horizontal direction of the images selected through SVM and those selected manually for the PPCX2_b dataset. An analysis of the absolute mean horizontal displacement value (Table 7) showed that this quantity was lower than the uncertainty. Therefore, the low correlation coefficient was likely due to the low signal-to-noise ratio.

Table 7. Mean absolute velocity and uncertainty δ of the two motion directions for two considered datasets; data are expressed in pixels.

Dataset	$ \overline{V_x} $	$ \overline{V_y} $	δ_x	δ_y
SAXE3_b	0.39	0.83	0.10	0.09
PPCX2_b	0.26	1.79	0.33	0.44

5. Conclusions

This study quantitatively analyses the disturbing effect caused by the shape and length of shadows on the results of image cross-correlation (ICC). First, the impact of shadows on the development of an automatized procedure for the selection of images was determined, and it was demonstrated that adopting images acquired in conditions of diffuse illumination enables the shadow-related uncertainty to be minimized. Therefore, a possible solution was developed to ensure that the images selected were taken in diffuse illumination.

A method for automatically classifying the images according to the illumination appearance was then proposed. Considering photos taken of various natural environments (e.g., landslides, glaciers, rock faces), SVMs were trained using different features that were representative of the photo's appearance. Of these, the number of RGB triplets was found to be the most significant feature used to discriminate between the classes. Training the SVMs with two or three features was sufficient for achieving an average misclassification error of 5.5%.

The processing chain used to automatically select images suitable for ICC application, which includes the abovementioned classification method, is also described herein. The application of the method was applied during a survey campaign in 2018 to monitor the activity of the Planpincieux glacier for civil protection purposes, and the results showed that a high correspondence was obtained with results obtained using images selected manually. The same experiment was then conducted using time-lapse photos acquired for the Mont de La Saxe landslide.

These results show the possibility of developing a monitoring system based on ICC that automatically selects and processes the pictures acquired. The use of image sequence analysis enables financial and human resources to be reduced in monitoring active geo-hydrological instabilities. The development of an automatic solution is a valuable tool for use in developing an autonomous monitoring system that supplies daily updates.

Author Contributions: Conceptualization, N.D. and D.G.; methodology and analysis, N.D.; data curation, P.A.; writing—original draft preparation, N.D.; writing—review and editing, D.G.

Funding: This research received no external funding.

Conflicts of Interest: The authors declare no conflict of interest.

References

- Scambos, T.A.; Dutkiewicz, M.J.; Wilson, J.C.; Bindshadler, R.A. Application of image cross-correlation to the measurement of glacier velocity using satellite image data. *Remote Sens. Environ.* **1992**, *42*, 177–186. [[CrossRef](#)]
- Duffy, G.P.; Hughes-Clarke, J.E. Application of spatial cross correlation to detection of migration of submarine sand dunes. *J. Geophys. Res. Earth Surf.* **2005**, *110*, F04S12. [[CrossRef](#)]
- Delacourt, C.; Allemand, P.; Berthier, E.; Raucoules, D.; Casson, B.; Grandjean, P.; Pambrun, C.; Varel, E. Remote-sensing techniques for analysing landslide kinematics: A review. *Bull. Société Géologique Fr.* **2007**, *178*, 89–100. [[CrossRef](#)]

4. Leprince, S.; Berthier, E.; Ayoub, F.; Delacourt, C.; Avouac, J.-P. Monitoring earth surface dynamics with optical imagery. *EOS Trans. AGU* **2008**, *89*, 1–2. [[CrossRef](#)]
5. Wrzesniak, A.; Giordan, D. Development of an algorithm for automatic elaboration, representation and dissemination of landslide monitoring data. *Geomat. Nat. Hazards Risk* **2017**, *8*, 1898–1913. [[CrossRef](#)]
6. Allasia, P.; Lollino, G.; Godone, D.; Giordan, D. Deep displacements measured with a robotized inclinometer system. In Proceedings of the 10th International Symposium on Field Measurements in Geomechanics—FMGM2018, Rio de Janeiro, Brazil, 16–20 July 2018.
7. Manconi, A.; Giordan, D. Landslide early warning based on failure forecast models: The example of the Mt. de La Saxe rockslide, northern Italy. *Nat. Hazards Earth Syst. Sci.* **2015**, *15*, 1639–1644. [[CrossRef](#)]
8. Allasia, P.; Baldo, M.; Giordan, D.; Godone, D.; Wrzesniak, A.; Lollino, G. Near real time monitoring systems and periodic surveys using a multi sensors UAV: The case of Ponzano landslide. In Proceedings of the IAEG/AEG Annual Meeting Proceedings, San Francisco, CA, USA, 17–21 September 2018; Springer: New York, NY, USA, 2019; Volume 1, pp. 303–310.
9. Roedelsperger, S.; Becker, M.; Gerstenecker, C.; Laeuffer, G. Near real-time monitoring of displacements with the ground based SAR IBIS-L. In Proceedings of the ESA Fringe Workshop, Frascati, Italy, 30 November–4 December 2009.
10. Giordan, D.; Wrzesniak, A.; Allasia, P. The importance of a dedicated monitoring solution and communication strategy for an effective management of complex active landslides in urbanized areas. *Sustainability* **2019**, *11*, 946. [[CrossRef](#)]
11. Berthier, E.; Vadon, H.; Baratoux, D.; Arnaud, Y.; Vincent, C.; Feigl, K.L.; Remy, F.; Legresy, B. Surface motion of mountain glaciers derived from satellite optical imagery. *Remote Sens. Environ.* **2005**, *95*, 14–28. [[CrossRef](#)]
12. Ahn, Y.; Box, J.E. Glacier velocities from time-lapse photos: Technique development and first results from the Extreme Ice Survey (EIS) in Greenland. *J. Glaciol.* **2010**, *56*, 723–734. [[CrossRef](#)]
13. Travelletti, J.; Delacourt, C.; Allemand, P.; Malet, J.-P.; Schmittbuhl, J.; Toussaint, R.; Bastard, M. Correlation of multi-temporal ground-based optical images for landslide monitoring: Application, potential and limitations. *ISPRS J. Photogramm. Remote Sens.* **2012**, *70*, 39–55. [[CrossRef](#)]
14. Gabrieli, F.; Corain, L.; Vettore, L. A low-cost landslide displacement activity assessment from time-lapse photogrammetry and rainfall data: Application to the Tessina landslide site. *Geomorphology* **2016**, *269*, 56–74. [[CrossRef](#)]
15. Giordan, D.; Allasia, P.; Dematteis, N.; Dell’Anese, F.; Vagliasindi, M.; Motta, E. A low-cost optical remote sensing application for glacier deformation monitoring in an alpine environment. *Sensors* **2016**, *16*, 1750. [[CrossRef](#)] [[PubMed](#)]
16. Schwalbe, E.; Maas, H.-G. The determination of high-resolution spatio-temporal glacier motion fields from time-lapse sequences. *Earth Surf. Dyn.* **2017**, *5*, 861–879. [[CrossRef](#)]
17. Debelli-Gilo, M.; Kääb, A. Sub-pixel precision image matching for measuring surface displacements on mass movements using normalized cross-correlation. *Remote Sens. Environ.* **2011**, *115*, 130–142. [[CrossRef](#)]
18. Messerli, A.; Grinsted, A. Image georectification and feature tracking toolbox: ImGRAFT. *Geosci. Instrum. Methods Data Syst.* **2015**, *4*, 23–34. [[CrossRef](#)]
19. Hadhri, H.; Vernier, F.; Atto, A.M.; Trouvé, E. Time-lapse optical flow regularization for geophysical complex phenomena monitoring. *ISPRS J. Photogramm. Remote Sens.* **2019**, *150*, 135–156. [[CrossRef](#)]
20. Boser, B.E.; Guyon, I.M.; Vapnik, V.N. A training algorithm for optimal margin classifiers. In Proceedings of the Fifth Annual Workshop on Computational Learning Theory, Pittsburgh, PA, USA, 27–29 July 1992; ACM: New York, NY, USA, 1992; pp. 144–152.
21. Cortes, C.; Vapnik, V. Support-vector networks. *Mach. Learn.* **1995**, *20*, 273–297. [[CrossRef](#)]
22. Pal, M.; Mather, P.M. Support vector machines for classification in remote sensing. *Int. J. Remote Sens.* **2005**, *26*, 1007–1011. [[CrossRef](#)]
23. Mountrakis, G.; Im, J.; Ogole, C. Support vector machines in remote sensing: A review. *ISPRS J. Photogramm. Remote Sens.* **2011**, *66*, 247–259. [[CrossRef](#)]
24. Lary, D.J.; Alavi, A.H.; Gandomi, A.H.; Walker, A.L. Machine learning in geosciences and remote sensing. *Geosci. Front.* **2016**, *7*, 3–10. [[CrossRef](#)]
25. Maxwell, A.E.; Warner, T.A.; Fang, F. Implementation of machine-learning classification in remote sensing: An applied review. *Int. J. Remote Sens.* **2018**, *39*, 2784–2817. [[CrossRef](#)]
26. Willert, C.E.; Gharib, M. Digital particle image velocimetry. *Exp. Fluids* **1991**, *10*, 181–193. [[CrossRef](#)]

27. Westerweel, J. Fundamentals of digital particle image velocimetry. *Meas. Sci. Technol.* **1997**, *8*, 1379. [[CrossRef](#)]
28. Lowe, D.G. Object recognition from local scale-invariant features. In Proceedings of the Seventh IEEE International Conference on Computer Vision, Kerkyra, Greece, 20–27 September 1999; Volume 2, pp. 1150–1157.
29. Bay, H.; Ess, A.; Tuytelaars, T.; Van Gool, L. Speeded-up robust features (SURF). *Comput. Vis. Image Underst.* **2008**, *110*, 346–359. [[CrossRef](#)]
30. Pust, O. Piv: Direct cross-correlation compared with fft-based cross-correlation. In Proceedings of the 10th International Symposium on Applications of Laser Techniques to Fluid Mechanics, Lisbon, Portugal, 10–13 July 2000; Volume 27, p. 114.
31. Thielicke, W.; Stamhuis, E. PIVlab—Towards user-friendly, affordable and accurate digital particle image velocimetry in MATLAB. *J. Open Res. Softw.* **2014**, *2*, e30. [[CrossRef](#)]
32. Bickel, V.; Manconi, A.; Amann, F. Quantitative assessment of digital image correlation methods to detect and monitor surface displacements of large slope instabilities. *Remote Sens.* **2018**, *10*, 865. [[CrossRef](#)]
33. Guizar-Sicairos, M.; Thurman, S.T.; Fienup, J.R. Efficient subpixel image registration algorithms. *Opt. Lett.* **2008**, *33*, 156–158. [[CrossRef](#)] [[PubMed](#)]
34. Dematteis, N.; Giordan, D.; Zucca, F.; Luzi, G.; Allasia, P. 4D surface kinematics monitoring through terrestrial radar interferometry and image cross-correlation coupling. *ISPRS J. Photogramm. Remote Sens.* **2018**, *142*, 38–50. [[CrossRef](#)]
35. Cheng, D.; Prasad, D.K.; Brown, M.S. Illuminant estimation for color constancy: Why spatial-domain methods work and the role of the color distribution. *JOSA A* **2014**, *31*, 1049–1058. [[CrossRef](#)]
36. Manduchi, R.; Mian, G.A. Accuracy analysis for correlation-based image registration algorithms. In Proceedings of the 1993 IEEE International Symposium on Circuits and Systems, Chicago, IL, USA, 3–6 May 1993; pp. 834–837.
37. Westerweel, J.; Scarano, F. Universal outlier detection for PIV data. *Exp. Fluids* **2005**, *39*, 1096–1100. [[CrossRef](#)]
38. Lary, D.J. Artificial intelligence in geoscience and remote sensing. In *Geoscience and Remote Sensing New Achievements*; Imperatore, P., Riccio, D., Eds.; InTech: Vienna, Austria, 2010; ISBN 978-953-7619-97-8.
39. Haykin, S. *Neural Network. A Comprehensive Foundation*, 2nd ed.; Prentice Hall: Upper Saddle River, NJ, USA, 1999; ISBN 0-13-273350-1.
40. Sunkavalli, K.; Romeiro, F.; Matusik, W.; Zickler, T.; Pfister, H. What do color changes reveal about an outdoor scene? In Proceedings of the 2008 IEEE Conference on Computer Vision and Pattern Recognition, Anchorage, AK, USA, 23–28 June 2008; pp. 1–8.
41. Picard, R.R.; Cook, R.D. Cross-validation of regression models. *J. Am. Stat. Assoc.* **1984**, *79*, 575–583. [[CrossRef](#)]
42. Xu, Q.-S.; Liang, Y.-Z. Monte Carlo cross validation. *Chemom. Intell. Lab. Syst.* **2001**, *56*, 1–11. [[CrossRef](#)]
43. Crosta, G.B.; Di Prisco, C.; Frattini, P.; Frigerio, G.; Castellanza, R.; Agliardi, F. Chasing a complete understanding of the triggering mechanisms of a large rapidly evolving rockslide. *Landslides* **2014**, *11*, 747–764. [[CrossRef](#)]
44. Crosta, G.B.; Lollino, G.; Paolo, F.; Giordan, D.; Andrea, T.; Carlo, R.; Davide, B. Rockslide monitoring through multi-temporal LiDAR DEM and TLS data analysis. In *Engineering Geology for Society and Territory-Volume 2*; Springer: New York, NY, USA, 2015; pp. 613–617.
45. Manconi, A.; Giordan, D. Landslide failure forecast in near-real-time. *Geomat. Nat. Hazards Risk* **2016**, *7*, 639–648. [[CrossRef](#)]
46. Dematteis, N.; Luzi, G.; Giordan, D.; Zucca, F.; Allasia, P. Monitoring Alpine glacier surface deformations with GB-SAR. *Remote Sens. Lett.* **2017**, *8*, 947–956. [[CrossRef](#)]
47. Greene, C. Borders. In *MATLAB Central File Exchange*; MATLAB: Natick, MA, USA, 2019.





Monitoring Alpine glacier surface deformations with GB-SAR

Niccolò Dematteis ^{a,c}, Guido Luzi ^b, Daniele Giordan ^a, Francesco Zucca ^c
and Paolo Allasia^a

^aGeohazard Monitoring Group, Research Institute for Hydro-Geological Protection, National Council of Research of Italy, Turin, Italy; ^bGeomatics Division, Centre Tecnològic de Telecomunicacions de Catalunya (CTTC/CERCA), Castelldefels, Spain; ^cDepartment of Earth Science and Environment, University of Pavia, Pavia, Italy

ABSTRACT

We present methods and results from interferometric data processing of a long-lasting survey campaign monitoring the Planpincieux glacier, located on the Italian side of the Mont Blanc, using a ground-based synthetic aperture radar (GB-SAR). Monitoring a European Alpine glacier during the winter, when the meteorological conditions are highly variable, presents some difficulties in radar data interpretation. The main issues to tackle in interferometric processing are unwrapping errors and high amplitude dispersion (DA), mainly due to the high velocity and dielectric heterogeneity of the backscattering surface. To improve the reliability of the results, a coherence-driven pixel-selection criterion for identifying the glacier area and a simple approach to reduce possible unwrapping errors in interferograms with low coherence are here proposed. The development of a new 2D polynomial regression model, as a function of elevation, for atmospheric phase screen (APS) estimation is also discussed. A comparison with the results obtained with a vision-based approach gave showed good agreement.

ARTICLE HISTORY

Received 25 January 2017
Accepted 21 May 2017

1. Introduction

In the past two decades, space-based synthetic aperture radar (SAR) systems have become valuable tools for monitoring glaciers when the satellite revisiting time, at best on the order of a few days, is adequate for the required temporal sampling (constrained by the process and contexts under investigation). Usually, when the survey needs shorter observation durations, as in case of short-live phenomena with significant variations on time scales as small as an hour, or in the presence of unfavourable geometries (e.g., steep or north-facing slopes), the installation of ground-based survey networks appears to unavoidable. The costs and difficulties related to the setup of on-site sensors suggest the use of terrestrial radar. The first applications on snow-covered and glacial surfaces (Luzi et al. 2007; Noferini et al. 2009; Martinez-Vazquez and Fortuny-Guasch. 2008) demonstrated the capabilities of terrestrial radar to monitor glacier and snow evolution. More recently, in Strozzi et al. (2012) and Riesen et al. (2011), the

authors focused on monitoring a short-term surface ice motion linked to the fast drainage of an adjacent lake. In Allstadt et al. (2015) the results of a radar survey were used as validation of a glacier deformation model.

Although this novel technique is able to provide only a partial estimate of the actual ice flow, displacement maps of glaciers of some square kilometres in size, from 3–4 km distances and entirely remotely sensed, can be obtained. Exhaustive reviews of this state of the art technique, the different instrumentation available, and the performances thereof, are available in Caduff et al. (2015) and Monserrat, Crosetto, and Luzi (2014). Especially in the case of alpine glaciers, which are particularly affected by cryosphere changes due to global warming (Deline et al. 2012), research and monitoring can largely benefit from the spatial and temporal sampling provided by terrestrial radar surveys.

In this paper, we discuss the results of a 40-day experimental campaign carried out with a commercial Ku-band terrestrial radar based on interferometric processing. During this campaign, we monitored the surface deformations of the Planpincieux glacier, which is found on the Italian side of the Mont Blanc massif.

2. Methods

The interferometric procedure used in this work to estimate the glacier surface deformation is based on the analysis of the differential phase between two consecutive ground-based SAR (GB-SAR) images. In the following, we briefly explain the main steps performed during data processing and present a novel approach to estimating the atmospheric phase screen (APS).

The ground-based interferometric procedure addresses some issues to obtain the differential phase due to the target displacement, φ_{displ} . In particular, thermal and scattering noise, φ_{noise} , phase wrapping, 2π multiple, and the phase change due to atmospheric effects, φ_{atm} , must be removed from the observed interferometric phase, Φ_{int} (Monserrat, Crosetto, and Luzi 2014).

To estimate the contribution of these terms, some procedures are applied directly to the radar image. The first step of the processing chain consists of applying a 2D unwrapping algorithm (Costantini 1998) to all the images. The unwrapping is performed on pixels selected with a coherence-driven criterion (Berardino et al. 2002), with the condition $\bar{\gamma} > 0.55$, where $\bar{\gamma}$ is the temporal mean coherence. The high value of the coherence assures the statistical significance of the measured phase.

Second, the interferograms with high noise and significant unwrapping errors are excluded from the stack of the interferograms (Allstadt et al. 2015). In the case at hand, the huge number of radar images necessitates the definition of a criterion for identifying the interferograms to be rejected. The interferograms with mean spatial coherence, $\langle \gamma \rangle < 0.65$ are excluded from the stack, and the related displacement is estimated with linear interpolation.

Third, the disturbance of the atmosphere caused by meteorological variables (i.e., humidity, temperature, and pressure, in order of relevance [Zebker, Rosen, and Hensley 1997]) is filtered from the interferometric data. The first study of the APS in GB-SAR applications (Luzi et al. 2004) found an empirical linear relationship between φ_{atm} and range. Some studies applied polynomial (Noferini et al. 2005) or multilinear regressions

(Iglesias et al. 2014; Caduff et al. 2014) to the phase observed in areas assumed to be stable, where $\Phi_{\text{int}} \simeq \varphi_{\text{atm}}$, to estimate spatial maps of the APS.

Linear regression assumes homogeneous atmosphere conditions, but in our circumstance the line of sight (LOS) crosses areas with great elevation change and the assumption of a homogeneous atmosphere is no longer satisfied.

In the case at hand, the horizontal variability of the meteorological fields is considered homogeneous over distances of a few kilometres; hence, in the horizontal direction, the APS varies linearly with the range. In the vertical direction, the temperature lapse rate is linear, while humidity and pressure decrease exponentially with the height; nevertheless, it is possible to approximate with linear behaviour for limited differences in elevation (Iglesias et al. 2014). Therefore, it is necessary to introduce a term to describe the vertical atmospheric change.

According to what was just discussed, let us consider the general relationship between φ_{atm} and range, r :

$$\varphi_{\text{atm}} = \int \mathfrak{N}(r) dr = \int \langle \mathfrak{N} \rangle + \frac{d\mathfrak{N}}{dr} dr \quad (1)$$

Here, we described the term $\mathfrak{N}(r)$, which represents the atmospheric disturbance as divided in a horizontally homogeneous term, $\langle \mathfrak{N} \rangle = \text{const}$, and a term varying with the range, $d\mathfrak{N}/dr$. Considering that the atmospheric conditions are constant in the horizontal direction and vary linearly with elevation and writing $dr = dx + dy + dz$, we obtain:

$$\begin{cases} d\mathfrak{N}/dx = 0 \\ d\mathfrak{N}/dy = 0 \\ d\mathfrak{N}/dz = c_1 + c_2 z \end{cases} \quad (2)$$

Therefore, substituting Equation (2) in Equation (1) we have:

$$\varphi_{\text{atm}} = \langle \mathfrak{N} \rangle r + \int (c_1 + c_2 z)(dx + dy + dz) = \langle \mathfrak{N} \rangle r + c_1 r + c_2 z^2 + c_0 \quad (3)$$

Where the scalar products $z \cdot dx$ and $z \cdot dy$ are null. Therefore, writing $\langle \mathfrak{N} \rangle r = c'_1 r$, the φ_{atm} can be estimated with the following regression of the interferometric phase over static areas (e.g., bedrock):

$$\varphi_{\text{atm}} = a_0 + a_1 r + a_2 z^2 \quad (4)$$

Where $a_0 = c_0$ is the residual offset of the integral and corresponds to the phase observed at the reference point, $a_1 = c_1 + c'_1$ and $a_2 = c_2$.

Equation (4) is similar to the APS models proposed by Noferini et al. (2005) and Iglesias et al. (2014), but here the quadratic term is a function of the elevation because horizontal and vertical atmospheric behaviours are treated independently.

3. Site study and dataset

The Planpincieux glacier is located at approximately 45.85°N 6.97°E in the Aosta Valley Region (North-Western Italy). The glacier lies on the southern side of the Mont Blanc massif towards the Ferret Valley, and it is part of the composite Grandes Jorasses-Planpincieux

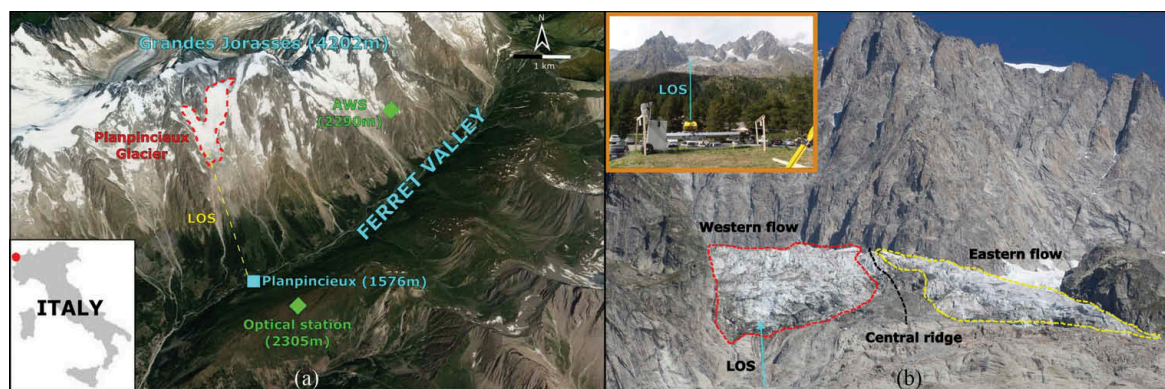


Figure 1. (a) Overview of the study site. The Planpincieux glacier is highlighted in dashed red and it is located on the southern side of the Grandes Jorasses, part of the Mount Blanc massif. The location of the GB-SAR is indicated by the sky-blue square in the Planpincieux hamlet at the bottom of the Ferret valley. Green diamonds indicate the Ferrachet automatic weather station (AWS) and to the optical monitoring station on the top of Mon de La Saxe. (b) Perspective of the glacier from the GB-SAR location. The two main flows are highlighted in red (the western) and yellow (the eastern); the central bedrock ridge is in black. In the orange box, the GB-SAR installation is displayed. The LOS is in light blue.

glacier at an elevation between 2530–3700 m asl, covering approximately 1 km² (Figure 1(a)).

As described by (Giordan et al. 2016), the lower part of the Planpincieux glacier is intensely crevassed. The morphological analysis indicates that this part is separated into two different ice flows by a central ridge of bedrock (Figure 1(b)).

The Research Institute for Hydro-geological Protection of the National Council of Research of Italy (CNR IRPI) considers the Grandes Jorasses massif an open-air laboratory for the development of monitoring systems and techniques. Since 2013, CNR IRPI is monitoring the glacier with low-cost vision-based equipment, installed in the opposite side of the valley (for further details, see Giordan et al. 2016).

Within a common research activity, CNR IRPI, the University of Pavia and the Technological Centre of Telecommunications of Catalonia (CTTC), installed a GB-SAR in the Planpincieux hamlet in August 2015 (Figure 1(a)). The positioning of the apparatus aims at maximizing the parallel condition of the LOS to the estimated direction of the western flow. This choice affected the measurement of the eastern tongue that flows diagonally w.r.t. the LOS. The mean distance to the glacier is approximately 2700 m with differences in elevation of 1200–1400 m (Figure 2). Radar images are georeferenced on a 1 m-resolution digital surface model (DSM).

During this study, an Ibis-L IDSTM instrument is used with a revisiting time of 16 minutes; the total number of processed images is 3567. The survey lasted 40 days, from 4th September to 14th October 2015. Figure 3(a,b) represent the mean amplitude (MA) and the DA maps, respectively. The APS estimate is applied in the area within the frames.

3.1. Meteorological data

To discover the role of the APS, we analysed the meteorological dataset from the Ferrachet automatic weather station (AWS), which was provided by the Centro

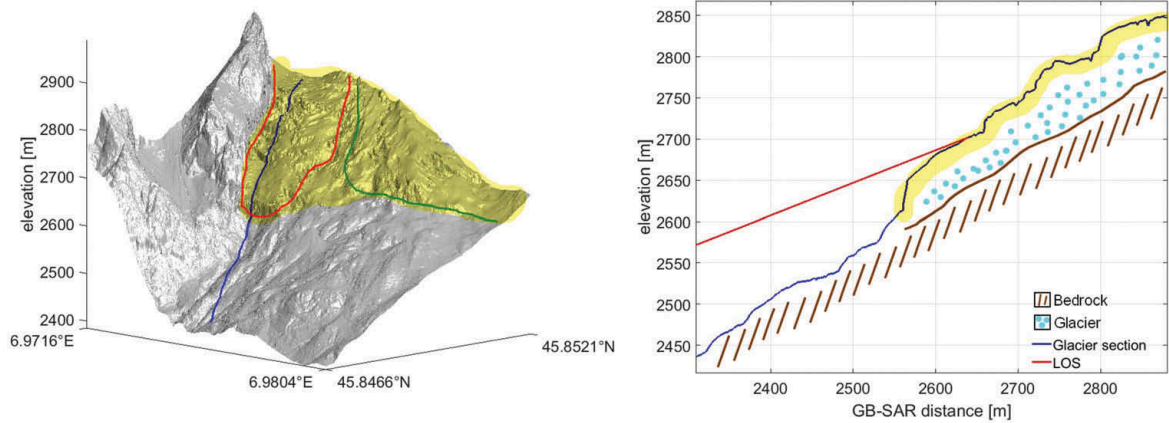


Figure 2. Left: DSM of the study area. The glacier is highlighted in yellow and the line section parallel to the LOS is in blue. The western flow is surrounded in red and the eastern flow in green. Right: section profile of the DSM. The glacier is in yellow (the glacier thickness is only figurative). The LOS is drawn in red.

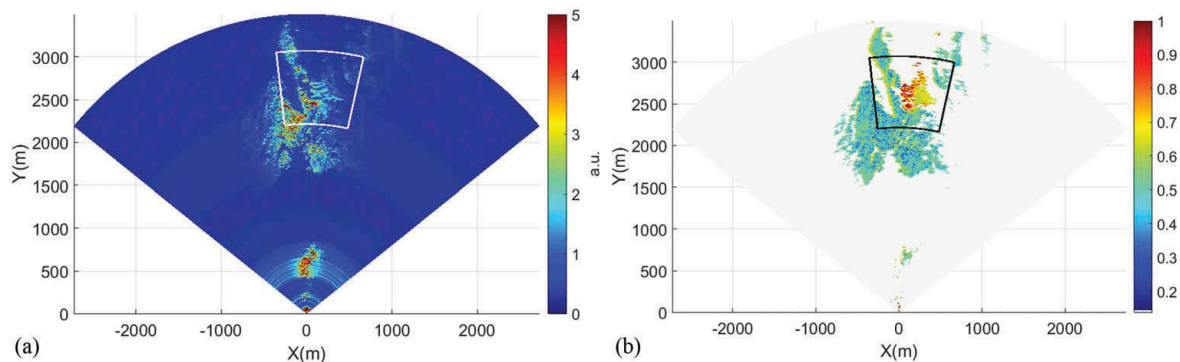


Figure 3. (a) Mean amplitude (MA) map in arbitrary units. Glacier and rocks features high amplitude. Minimum MA values indicate shadow areas. (b) Amplitude dispersion (DA) map. A coherence-based mask is applied to the pixels. The glacier features high DA, while the rocks display lower values. Atmospheric effects are evaluated within the frames.

Funzionale della Valle d'Aosta. The AWS was placed at 2290 m asl on the same side of the valley as the Planpincieux glacier (Figure 1(a)). The following variables were collected: air temperature, air relative humidity (RH), cumulative rainfall in 30 minutes, and snow deposited on the ground. Figure 4 reports the acquired weather data.

The period of the survey coincided with the beginning of the Alpine cold season. The temperature was close to 0°C, and some snowfall events occurred. Cold temperatures and a high RH affected the radar signal with an increased APS. To take into account the effects of the altitude difference between the AWS location and the glacier, the air temperature of the glacier should be corrected according to the Standard Atmosphere lapse rate of $-0.007^{\circ}\text{C}/\text{m}$; therefore, the air temperature of the glacier was approximately 3°C lower, and RH and precipitation varied accordingly.

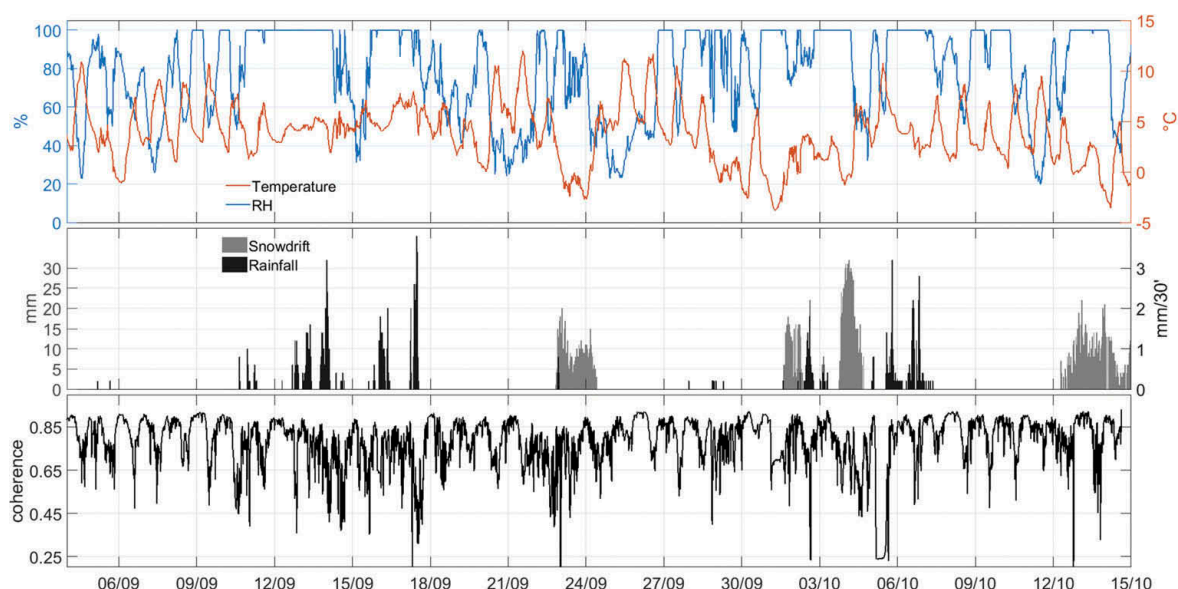


Figure 4. Meteorological data collected by the Ferrachet AWS. In the upper box, RH (in blue) and temperature (in red) are displayed. In the middle box, the snow deposit at ground level is drawn in grey (mm), the rainfall over 30 minutes is drawn in black (mm/30'). In the lower box, the time series of the mean spatial coherence is shown.

4. Results and discussion

As previously mentioned, the first step of the processing consisted of applying a 2D unwrapping algorithm (Costantini 1998).

In the next step, the interferograms with $\langle \gamma \rangle < 0.65$ were excluded from the stack and the displacement occurred during the rejected data was estimated with linear interpolation of the contiguous interferograms. The temporal distribution of the rejected data (i.e., $\langle \gamma \rangle < 0.65$) is well correlated with adverse meteorological conditions (Figure 4) that can provoke the change of the dielectric properties due to snowdrift, snow melting and metamorphism (Luzi et al. 2009). The discarded interferograms account for approximately 16% of the total. The comparison between the 'cleaned' and 'raw' results exhibited a difference of 2–5%; therefore, probable unwrapping errors due to noise effects are strongly reduced.

The APS is evaluated in the stable areas in the surroundings of the glacier. We considered static points those pixels with $DA < 0.35$. Figure 5(a) represents the cumulative APS in radians in the considered area, computed with Equation (4). Figure 5(b) shows the cumulative surface deformation map of the glacier. Negative data indicate points approaching the radar along the LOS, while positive data are moving away.

The deformation results in Figure 5(b) agree with the morphological observation of the glacier, highlighting two main streams with different kinematics (Giordan et al. 2016). In fact, the western flow moves downstream almost parallel to the LOS, while the eastern part flows with a remarkable horizontal component towards east. Therefore, the LOS-aligned motion component of this region is moving away.

The eastern flow presents a very low amplitude. Moreover, the radar signal passes through an atmospheric layer with strong turbulence and heat fluxes that affect the

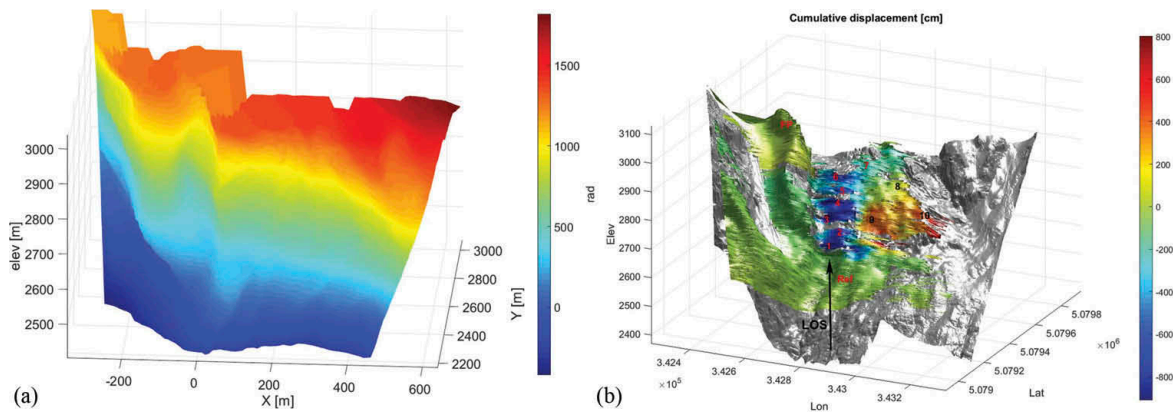


Figure 5. (a) Calculated cumulative APS in radians as a function of the radar coordinates (range and elevation), obtained according to Equation (4) and projected on the DSM. (b) Cumulative deformation map projected on the DSM of the monitored area. Negative and positive values correspond to motion towards and away from the radar, respectively. Numbers indicate the location of the considered pixels for the evaluation of the time series; numbers in red are located in the western flow, black number are in the eastern flow. 'Ref' and 'FP' are fixed points on the bedrock used for control. 'Ref' is the reference point used during the unwrapping procedure.

wave phase (Iannini and Monti Guarnieri 2011; Barucci et al. 2010). For these reasons, the reliability of the results of this area is low.

Bedrock areas display almost no movement, as expected, but in the bedrock ridge on the right side (downstream) of the glacier, a sharp difference is present between the upper and the lower part. This result is probably due to unwrapping errors between non-continuous areas.

In Figure 6, time series of cumulative displacement of a set of selected points are displayed. The point locations are shown in Figure 5(b). The picture shows the stability of the two fixed points (black and grey lines) as expected, apart from a low drift that had occurred since the end of September. Points belonging to the same glacier sectors have similar behaviours. Points 1 and 2 display probable errors in the final part of the period due to their location in the front sector of the glacier, which was particularly affected by ice collapses and loss of coherence. We note a slowing down of the deformation ratio of the points in the western flow some days after the two coldest periods on 23rd September and 29th September. The delay is probably due to the thermal inertia of the ice.

Finally, the accuracy of the results was estimated by analysing the distribution of the interferometric phase in stable areas (Tarchi et al. 2003; Luzi et al. 2006). The mean value of the distribution is 1°, which is very close to the theoretical value of 0°, and the standard deviation converted to metric displacement is approximately 0.75 mm.

4.1. Comparison with photographic data

In the following, we compare the main radar data outcomes with some results of a contemporary monitoring campaign based on a completely independent methodology, performed by vision-based sensors (Giordan et al. 2016) during the period from 4–27 September 2015. Optical photographs estimate the surface deformation through normalized cross-correlation of consecutive co-registered images.

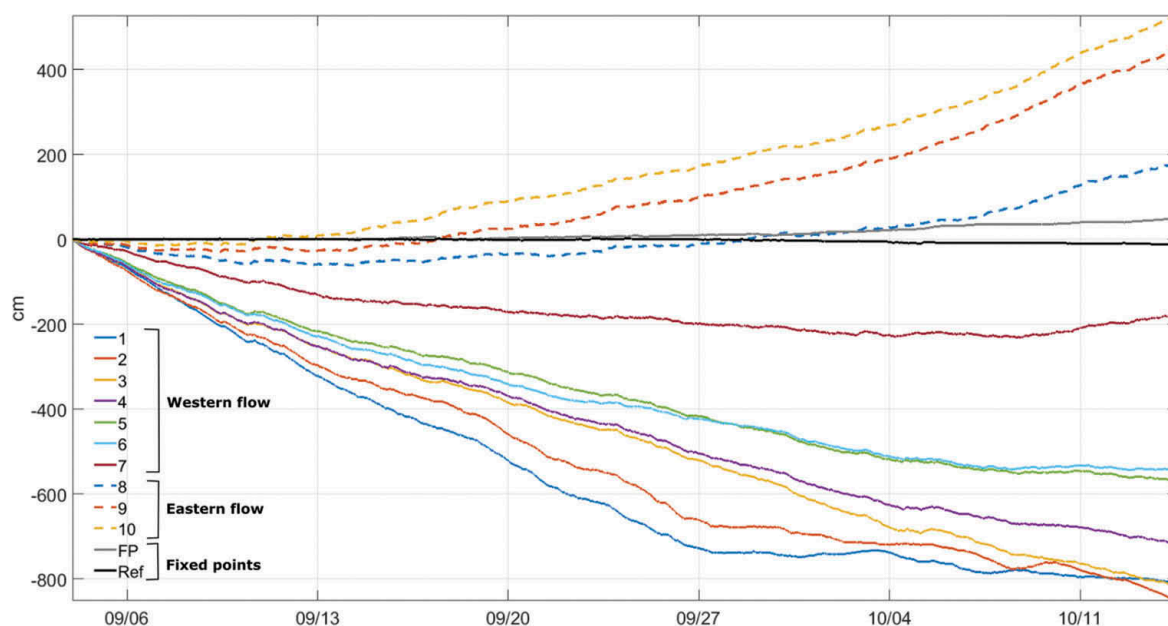


Figure 6. Displacement time series of a set of selected points. Solid coloured lines represent the points of the western flow, dashed coloured lines for points of the eastern flow. The reference point is in black and the second fixed point positioned on the bedrock wall for control is in grey; this line shows a low drift due to possible unwrapping errors.

Table 1. Comparison between two different systems for evaluating the glacier surface deformation (from Giordan et al. 2016).

Sectors	GB-SAR (cm/day)	Optical system (cm/day)
Front sector	29.2 ± 3.8	31.4 ± 10.3
Crevasses sector	23.0 ± 2.6	29.9 ± 4.5
Middle sector	20.8 ± 3.9	26.0 ± 7.2

The two systems measure different components of movement: the GB-SAR detects the component parallel to the LOS, while the vision-based system detects the component orthogonal to the LOS. The actual displacement is estimated by correcting the measured deformations with the known slope angle (Caduff et al. 2014).

In Table 1, we report the results of the comparison between the two methods, considering the mean value of the pixels within three glacier sectors of the western flow and the related standard deviation as reported in Giordan et al. (2016). The data are adjusted with a local mean slope of 45° . The results are compatible within the error interval, showing a good reliability of the GB-SAR processed data.

5. Conclusions

We presented the results of a survey campaign aimed at estimating the surface deformation of an Alpine glacier using a GB-SAR. A new method capable of correcting atmospheric artefacts in this specific case has been described and applied to the acquired data. The measurement campaign, which lasted forty days, was carried out within a project monitoring the lower part of the Planpincieux glacier. Critical issues in

the data processing were identified owing to the large distance of the observed target and to the difference in elevation, especially for the resulting atmosphere influence, which were typical of the Alpine climate, including some snowfalls.

In the presented method, we reduced possible unwrapping errors by discarding interferograms with low coherence, and the displacement of the rejected interferograms is estimated with linear interpolation. Moreover, we developed a new APS-filtering model based on a 2D polynomial regression explicitly taking elevation into account.

The results of the data processing were compared with the results of a recent study based on the cross-correlation of optical images (Giordan et al. 2016), obtaining good agreement.

We believe that our study might be useful for developing a better methodology for GB-SAR data processing for use in monitoring the fast surface deformation processes of glaciers.

Acknowledgments

The authors are grateful to the staff of Fondazione Montagna Sicura, in particular Jean Pierre Fasson, Marco Vagliasindi and Elena Motta, for their logistic support and field assistance. Many thanks also to Centro Funzionale della Valle d'Aosta for having provided the meteorological data from the Ferrachet weather station. An acknowledgement is addressed to OBH Italia SpA, which provided the IBIS-L GB-SAR equipment.

ORCID

Niccolò Dematteis  <http://orcid.org/0000-0002-9232-7531>
 Guido Luzi  <http://orcid.org/0000-0001-8924-9029>
 Daniele Giordan  <http://orcid.org/0000-0003-0136-2436>
 Francesco Zucca  <http://orcid.org/0000-0003-4119-5484>

References

- Allstadt, K. E., D. E. Shean, A. Campbell, M. Fahnestock, and S. D. Malone. 2015. "Observations of Seasonal and Diurnal Glacier Velocities at Mount Rainier, Washington, Using Terrestrial Radar Interferometry." *The Cryosphere* 9 (6): 2219–2235. doi:10.5194/tc-9-2219-2015.
- Barucci, A., G. Macaluso, D. Mecatti, L. Noferini, D. Fanelli, A. Facchini, M. Materassi, M. Pieraccini, and C. Atzeni. 2010. "Universal Fluctuations in Tropospheric Radar Measurements." *EPL (Europhysics Letters)* 89 (2): 20006. doi:10.1209/0295-5075/89/20006.
- Berardino, P., G. Fornaro, R. Lanari, and E. Sansosti. 2002. "A New Algorithm for Surface Deformation Monitoring Based on Small Baseline Differential SAR Interferograms." *IEEE Transactions on Geoscience and Remote Sensing* 40 (11): 2375–2383. doi:10.1109/TGRS.2002.803792.
- Caduff, R., A. Kos, F. Schlunegger, B. W. McArde, and A. Wiesmann. 2014. "Terrestrial Radar Interferometric Measurement of Hillslope Deformation and Atmospheric Disturbances in the Illgraben Debris-Flow Catchment, Switzerland." *IEEE Geoscience and Remote Sensing Letters* 11 (2): 434–438. doi:10.1109/LGRS.2013.2264564.
- Caduff, R., F. Schlunegger, A. Kos, and A. Wiesmann. 2015. "A Review of Terrestrial Radar Interferometry for Measuring Surface Change in the Geosciences." *Earth Surface Processes and Landforms* 40 (2): 208–228. doi:10.1002/esp.3656.
- Costantini, M. 1998. "A Novel Phase Unwrapping Method Based on Network Programming." *IEEE Transactions on Geoscience and Remote Sensing* 36 (3): 813–821. doi:10.1109/36.673674.

- Deline, P., M. Gardent, F. Magnin, and L. Ravel. 2012. "The Morphodynamics of the Mont Blanc Massif in A Changing Cryosphere: A Comprehensive Review." *Geografiska Annaler: Series A, Physical Geography* 94 (2): 265–283. doi:10.1111/geoa.2012.94.issue-2.
- Giordan, D., P. Allasia, N. Dematteis, F. Dell'Anese, M. Vagliasindi, and E. Motta. 2016. "A Low-Cost Optical Remote Sensing Application for Glacier Deformation Monitoring in an Alpine Environment." *Sensors* 16 (10): 1750. doi:10.3390/s16101750.
- Iannini, L., and A. Monti Guarnieri. 2011. "Atmospheric Phase Screen in Ground-Based Radar: Statistics and Compensation." *IEEE Geoscience and Remote Sensing Letters* 8 (3): 537–541. doi:10.1109/LGRS.2010.2090647.
- Iglesias, R., X. Fabregas, A. Aguasca, J. J. Mallorqui, C. López-Martínez, J. A. Gili, and J. Corominas. 2014. "Atmospheric Phase Screen Compensation in Ground-Based SAR with a Multiple-Regression Model over Mountainous Regions." *IEEE Transactions on Geoscience and Remote Sensing* 52 (5): 2436–2449. doi:10.1109/TGRS.2013.2261077.
- Luzi, G., M. Pieraccini, D. Mecatti, L. Noferini, G. Macaluso, A. Galgaro, and C. Atzeni. 2006. "Advances in Ground-Based Microwave Interferometry for Landslide Survey: A Case Study." *International Journal of Remote Sensing* 27 (12): 2331–2350. doi:10.1080/01431160600554975.
- Luzi, G., M. Pieraccini, D. Mecatti, L. Noferini, G. Macaluso, A. Tamburini, and C. Atzeni. 2007. "Monitoring of an Alpine Glacier by Means of Ground-Based SAR Interferometry." *IEEE Geoscience and Remote Sensing Letters* 4 (3): 495–499. doi:10.1109/LGRS.2007.898282.
- Luzi, G., L. Noferini, D. Mecatti, G. Macaluso, M. Pieraccini, C. Atzeni, A. Schaffhauser, R. Fromm, and T. Nagler. 2009. "Using a Ground-Based SAR Interferometer and a Terrestrial Laser Scanner to Monitor a Snow-Covered Slope: Results from an Experimental Data Collection in Tyrol (Austria)." *IEEE Transactions on Geoscience and Remote Sensing* 47 (2): 382–393. doi:10.1109/TGRS.2008.2009994.
- Luzi, G., M. Pieraccini, D. Mecatti, L. Noferini, G. Guidi, F. Moia, and C. Atzeni. 2004. "Ground-Based Radar Interferometry for Landslides Monitoring: Atmospheric and Instrumental Decorrelation Sources on Experimental Data." *IEEE Transactions on Geoscience and Remote Sensing* 42 (11): 2454–2466. doi:10.1109/TGRS.2004.836792.
- Martinez-Vazquez, A., and J. Fortuny-Guasch. 2008. "A GB-SAR Processor for Snow Avalanche Identification." *IEEE Transactions on Geoscience and Remote Sensing* 46 (11): 3948–3956. doi:10.1109/TGRS.2008.2001387.
- Monserat, O., M. Crosetto, and G. Luzi. 2014. "A Review of Ground-Based SAR Interferometry for Deformation Measurement." *ISPRS Journal of Photogrammetry and Remote Sensing* 93: 40–48. doi:10.1016/j.isprsjprs.2014.04.001.
- Noferini, L., D. Mecatti, G. Macaluso, M. Pieraccini, and C. Atzeni. 2009. "Monitoring of Belvedere Glacier Using a Wide Angle GB-SAR Interferometer." *Journal of Applied Geophysics* 68 (2): 289–293. doi:10.1016/j.jappgeo.2009.02.004.
- Noferini, L., M. Pieraccini, D. Mecatti, G. Luzi, C. Atzeni, A. Tamburini, and M. Broccolato. 2005. "Permanent Scatterers Analysis for Atmospheric Correction in Ground-Based SAR Interferometry." *IEEE Transactions on Geoscience and Remote Sensing* 43 (7): 1459–1471. doi:10.1109/TGRS.2005.848707.
- Riesen, P., T. Strozzi, A. Bauder, A. Wiesmann, and M. Funk. 2011. "Short-Term Surface Ice Motion Variations Measured with a Ground-Based Portable Real Aperture Radar Interferometer." *Journal of Glaciology* 57 (201): 53–60. doi:10.3189/002214311795306718.
- Strozzi, T., C. Werner, A. Wiesmann, and U. Wegmüller. 2012. "Topography Mapping with a Portable Real-Aperture Radar Interferometer." *IEEE Geoscience and Remote Sensing Letters* 9 (2): 277–281. doi:10.1109/LGRS.2011.2166751.
- Tarchi, D., N. Casagli, S. Moretti, D. Leva, and A. J. Sieber. 2003. "Monitoring Landslide Displacements by Using Ground-Based Synthetic Aperture Radar Interferometry: Application to the Ruinon Landslide in the Italian Alps." *Journal of Geophysical Research: Solid Earth* 108 (B8). doi:10.1029/2002JB002204/full.
- Zebker, H. A., P. A. Rosen, and S. Hensley. 1997. "Atmospheric Effects in Interferometric Synthetic Aperture Radar Surface Deformation and Topographic Maps." *Journal of Geophysical Research: Solid Earth* 102 (B4): 7547–7563. doi:10.1029/96JB03804.

TERRESTRIAL RADAR INTERFEROMETRY TO MONITOR GLACIERS WITH COMPLEX ATMOSPHERIC SCREEN

G. Luzi¹, N. Dematteis², F. Zucca³, O. Monserrat¹, D. Giordan², J.I. López-Moreno⁴

1 Centre Tecnològic de Telecomunicacions de Catalunya (CTTC/CERCA) Av. C.F. Gauss, 7, E-08860
Castelldefels (Barcelona), Spain

2 Geohazard Monitoring Group, Research Institute for Hydro-Geological Protection, National Council
of Research of Italy, Torino, Italy.

3 Department of Earth Science and Environment, University of Pavia, Pavia, Italy

4 Instituto Pirenaico de Ecología, Consejo Superior de Investigaciones Científicas (IPE-CSIC)
Zaragoza, Spain

ABSTRACT

This paper reports the results of two terrestrial surveys aimed at monitoring two Alpine glaciers located in Italy and Spain respectively, and carried out using a Ground Based SAR interferometer. Although the monitoring of glaciers based on this technique does not represent a novelty, these two case studies are peculiar, due to the characteristics of the Alpine glaciers among which the dominant role of the atmospheric phase screen (APS) on the radar signal propagation. These kind of glaciers, with their climate and geographical features, often demand a detailed analysis of the acquired data, at small temporal (less than an hour), and spatial (a few square meters) scale. The meteorological conditions, which affect the dynamics of the glaciers, deeply influenced the backscattering behavior, demanding a careful analysis of the amplitude of the radar signal, to characterize the surface, and of the interferometric phase, to evaluate the role of the APS. Only after the correction of the APS, a final accuracy of a few millimeters/day was attained in the daily velocity of the glacier in both cases.

Index Terms— GB SAR Interferometry, Glaciers, Atmosphere, Deformation.

1. INTRODUCTION

Terrestrial Radar interferometry mainly consolidated in the last decades for the monitoring of landslides, to estimate the deformation behavior of instable slopes, dams and mines [1]. One of the applications where the technique appeared a valuable tool is also the monitoring of glaciers: see for example [2], [3] [4] [5] [6]. One of the main reasons is that the alpine glaciers are often located on steep flanks, steep slopes and narrow valleys, often making spaceborne data not usable. In addition, the repetition times of satellite

observations provide a too coarse temporal sampling for studying alpine glacier during the period of their maximum activity, when the air temperature daily fluctuates across zero Celsius degree, and instable cloud coverage makes also the sun radiation highly variable. In this paper we confirm that the Alpine glaciers, with surface areas of the order of a few square kilometers, despite the critical role of the Atmospheric Phase Screen (APS) can benefit from this technique (i.e., radar interferometry) in deformation retrieval. The results of two experimental campaigns carried out in Italy and Spain, monitoring the Planpincieux (Monte Bianco-Alps) and Monte Perdido (Pyrenees), are here investigated. In particular, amplitude and phase of the received radar signal have been both analyzed to separate glacier surfaces from stable rocks, whose radar backscattering can be similar, and to perform interferometric processing. The dispersion of amplitude and the coherence of a set of images acquired during some days are analyzed to finally reconstruct the glacier movement. These two parameters were also used to refine APS calculation, identifying stable points, and to finally provide estimates of the glacier deformation with an accuracy of a few centimeters.

2. THE MEASURING SYSTEM

The system used to acquire radar images is a commercial radar system the IBIS-L [6] based on a coherent continuous wave step frequency transceiver able to provide SAR images of a few square kilometers slopes moving along a two meters long rail. Its main parameters are listed in Table 1. SAR images were acquired in an almost continuous mode, with a time interval between image acquisitions of about 5 minutes, with the exception of some breaks caused by power supply interruptions. Raw data are focused in radar coordinates and

then projected on the digital surface model DSM of the monitored area.

Table 1

Central frequency/wavelength	17.1 GHz/1.75 cm
Polarization	VV
Range resolution	0.43 m
Azimuth resolution (angular)	4.4 mrad
Azimuth resolution (linear)	10 m @ 2000m



Fig.1: View of the Planpincieux glacier with indicated: the glacier's area (red dashed line), the positions of the radar (sky square), a weather station and an optical monitoring system.



Fig.2: View of the Monte Perdido glacier.

2. MEASUREMENT CAMPAIGN

2.1. Planpincieux test site

The Planpincieux glacier is located approximately at 45.85°N 6.97°E, in the Aosta Valley Region (North-Western Italy). The glacier lies on the southern side of the Mont Blanc massif, towards the Ferret Valley, and it is part of the composite Grandes Jorasses-Planpincieux glacier, at an elevation between 2530-3700 m asl, covering approximately 1 km²: in fig. 1 a view of the area with indicated the main locations is shown. The lower part of the Planpincieux glacier is intensely crevassed. The morphological analysis evidences that this part is separated in two different ice flows by a central ridge of bedrock. The radar system was positioned to optimize the parallel condition of the LOS to the estimated direction of the western flow, while the measurement of the eastern tongue

that flows diagonally w.r.t. the LOS is handicapped. The mean distance of the glacier is about 2700 m with differences in elevation of 1200-1400 m. The radar images are georeferenced on a 1 m-resolution DSM: Terrestrial Laser Scanning (TLS) acquisitions have been carried out in late April or early May 2015s balance of the glacier. GB SAR data were collected between September 4 and October 14 2015

2.2 Monte Perdido test site

The glaciers in the Pyrenees are nowadays in a critical situation with clear evidence of very advanced stage of degradation; due to their small size, they are highly sensitive geo-indicators of the most recent climatic variations. The Monte Perdido Glacier is the third largest glacier in the Pyrenees and recent strong losses in glacier surface area have been reported; it is located in the Central Spanish Pyrenees (42°40'50"N 0°02'15"E) (see Fig. 2). The ice masses are north-facing, lie on structural flats beneath the main summit of the Monte Perdido Peak (3355 m) in the Ordesa and Monte Perdido National Park (OMPNP). The ice body is divided in three stepped ice masses connected by serac falls by the mid-20th century; the lower ice body disappeared during the 1970s. The upper and lower ice bodies have mean elevations of 3110 m and 2885 m. Despite the high elevation of the upper glacier, snow accumulation is limited due to the minimal avalanche activity above the glacier and its marked steepness ($\approx 40^\circ$). According to recent measurements of air temperature (July 2014 to October 2017) at the foot of the glacier (2700 m a.s.l.) and slightly below the summit of the Monte Perdido peak (at 3295 m a.s.l.), the 0°C is found to lie at 2945 m a.s.l., and the average summer (JJAS) temperature at the foot of the glacier is 7.3°C. The mean distance of the glacier from the radar is about 1800 m with differences in elevation of 400-600 m. Radar images, acquired between July 15 2015 and 30 July 2015, are georeferenced on a 1 m-resolution digital surface model (DSM) derived from a terrestrial Laser Scanner campaign (September 2016). The monitoring here reported covers a seven days lapse, from 21h35m06s 2015.07.22 to 18h52m04s 2015.07.30, with an almost hourly repetition time, corresponding to 160 acquired images for seven days.

3. EXPERIMENTAL RESULTS

The same processing chain was used for the data sets acquired in the two experimental campaigns. The amplitude images are analyzed to distinguish the different areas of the glacier, and identify stable points to later carry out the APS calculation [6]. The critical parameters analyzed are the Mean amplitude, the amplitude dispersion (DA), defined as $DA = \sigma_A / A$ where σ_A and A are respectively the standard deviation and the mean value of the measured amplitudes,

and coherence. The processing includes first the application of a 2D unwrapping algorithm: unwrapping errors are mainly due to the high velocity and dielectric heterogeneity of the backscattering surface. To reduce possible errors, in this phase, interferograms with low coherence, which usually correspond to particular meteorological conditions (e.g. snow falls, zero air temperature crossing) are discarded and the displacement of the rejected interferograms is estimated with a linear interpolation between the previous and the subsequent interferogram. To correct atmospheric effects, a new APS-filtering model based on a 2D polynomial regression which takes into account the elevation was applied, for details see [6].

3.1. Planpincieux

The monitoring lasted more than one month: 3500 GB-SAR images were collected between September 4 and October 14 2015. In fig.3 the amplitude image, obtained with a coherent mean of the set of all the images, is shown. In general the signal, due to a low signal to noise ratio, does not allow at a first glance a clear distinguishing between the rocks, glaciers and shadowed area. On the other hand, coherence, shown in fig. 4, appears to be a fine mean to separate the different surfaces. A statistical analysis of the DA behavior, shown in fig. 5, supported a better understanding and a classification of the different surfaces, i.e. glacier, rock and shadow areas (noise). Rocks' DA decreases towards zero, maintaining greater than zero. The DA of the glacier is lower than noise only for a few hours. When the DA is computed for a longer period (>5 -10 days) the DA of the glacier is higher than noise. At the end of this analysis, glacier points were selected with a Mean Amplitude threshold which appeared to be more reliable: a $MA > 1.5$ is considered for the glacier area. As far as the APS is concerned, on the bases of the meteorological observations (air temperature and humidity), an empirical formula is applied, where a quadratic term is added, function of the elevation [6]. The final product of this procedure is a deformation map projected on the DSM of the imaged area which is shown in fig.6. Considering as error of the radar retrieval the standard deviation of the cumulative motion on the bedrock i.e. a stable area, we obtain for example, for the front sector a 29.2 ± 0.2 cm/day velocity, a relative error close to 1%.

3.2. Monte Perdido

In the Monte Perdido campaign the logistic was more complicated with respect to the Italian site. The powering was based on the use of solar panels, and this makes the image acquisition often discontinuous. Harsh weather conditions also affected the regular use of system. The processing procedure was the same. For the APS correction the same approach was used. In fig. 7 a mean amplitude map of the monitored area is shown. To distinguish the different

areas, the same rationale used for the previous test site was applied. Fig. 8 shows the final product consisting in a deformation map, cm/day unit. A detailed analysis of single points temporal behavior is shown in fig. 9. As for the Planpincieux site, from these data we evaluated the accuracy of the achieved map, estimated through the residual cumulative displacement obtained in the fixed points (rocks) less than ± 3 mm/day. Considering a typical value of the velocity for the glacier points around 2/3 cm/day, this accuracy can be considered satisfactory although worse than the previous case.

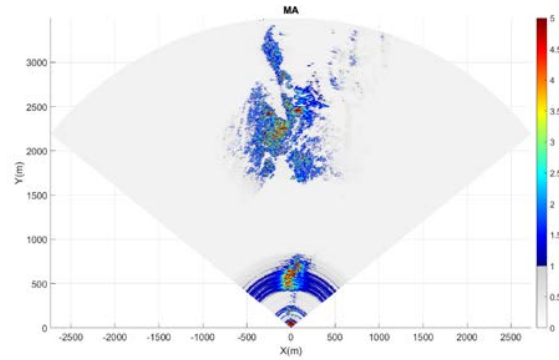


Fig.3: Mean amplitude in radar coordinates of the entire acquired area of the Planpincieux glacier; values in amplitude normalized to the clutter.

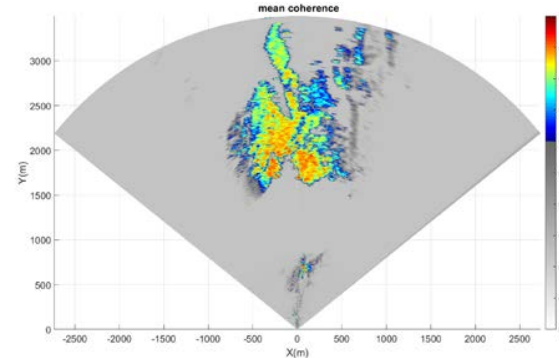


Fig.4: Coherence calculated for the Planpincieux area.

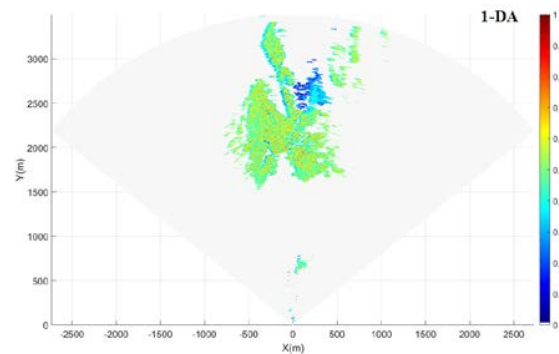


Fig.5: One's complement of amplitude dispersion $DA = 1 - \sigma_A / A$, calculated for the monitored area of the Planpincieux glacier.

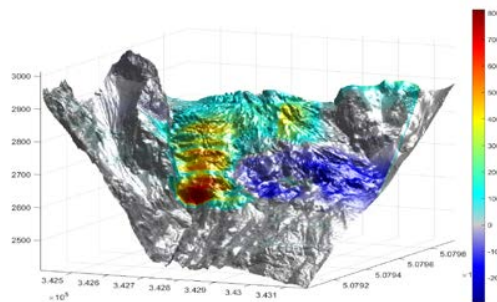


Fig.6: Cumulative deformation map of the Planpincieux glacier projected on the DSM. Displacements are in cm.

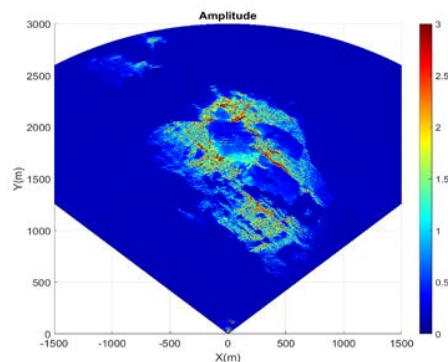


Fig.7: SAR Mean amplitude image of the Monte Perdido glacier. Values in amplitude normalized to the clutter.

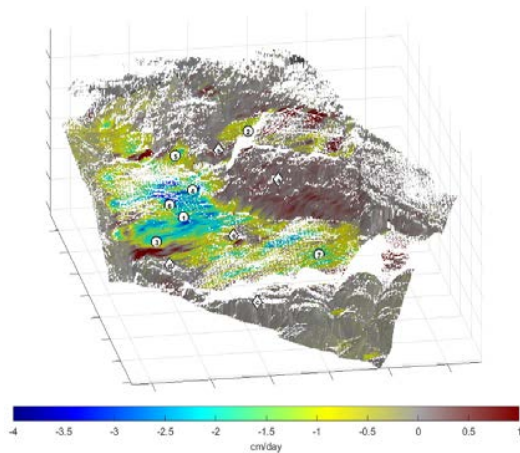


Fig.8: Deformation map of Monte Perdido with selected points; diamonds: stable pixels (letters); circles: glacier pixels (numbers).

4. CONCLUSIONS

Two survey campaigns aimed at estimating the surface deformation of two Alpine glaciers using a GB-SAR have been discussed. After the analysis of wrapping occurrence, and the role and the effects of the APS, deformation maps of the monitored area and glacier velocity of different sectors

of the glaciers were estimated. The study confirmed that the GB-SAR technique can be successfully applied to the monitoring of Alpine glaciers, providing displacement map with adequate accuracy provided that atmospheric effect are carefully considered.

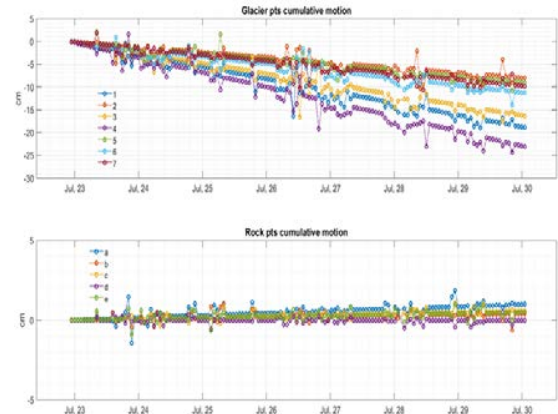


Fig.9: Cumulative motion for some points of Monte Perdido glacier; (see fig.8). Top: glacier points; bottom: stable rocks.

5. REFERENCES

- [1] Caduff, R., Schlunegger, F., Kos, A., Wiesmann, A., 2015. A review of terrestrial radar interferometry for measuring surface change in the geosciences. *Earth Surf. Process. Land.* 40, 208–228. DOI: 10.1002/esp.3656
- [2] Luzi G, Pieraccini M, Mecatti D, Noferini L, Macaluso G, Tamburini A, Atzeni C. 2007. Monitoring of an alpine glacier by means of groundbased SAR interferometry. *GRSL* 4: 495–499. DOI: 10.1109/LGRS.2007.
- [3] Riesen P., T. Strozzi, A. Bauder, A. Wiesmann, and M. Funk, 2011. Short-Term Surface Ice Motion Variations Measured with a Ground-Based Portable Real Aperture Radar Interferometer.” *Journal of Glaciology* 57 (201): 53–60.
- [4] Noferini L., Mecatti D., G. Macaluso, M. Pieraccini, Atzeni C., Monitoring of Belvedere Glacier using a wide angle GB-SAR interferometer, *Journal of Applied Geophysics*. 68, 2, June 2009, pp 289-293.
- [5] Allstadt K. E., D. E. Shean, A. Campbell, M. Fahnestock and S. D. Malone, 2015. Observations of seasonal and diurnal glacier velocities at Mount Rainier, Washington, using terrestrial radar interferometry. *The Cryosphere*, 9, doi:10.5194/tc-9-2219-2015.
- [6] Dematteis, N., Luzi, G., Giordan, D., Zucca, F., Allasia, P., 2017. Monitoring Alpine glacier surface deformations with GB-SAR. *Rem. Sens. Lett.* 8, 947–956.

ACKNOWLEDGEMENTS

The activities focused on the Monte Perdido, have been partially funded by the CRIORDESA project (844/2013) by the Spanish “Ministerio de Agricultura, Alimentación y Medioambiente”. An acknowledgment is also addressed to OBH Italia SpA which provides the IBIS-L equipment for the Planpincieux site, and to Fondazione Montagna Sicura, and to Centro Funzionale della Valle d’Aosta for providing meteorological data.

Article

Ku Band Terrestrial Radar Observations by Means of Circular Polarized Antennas

Guido Luzi ^{1,*}  and Niccolò Dematteis ^{2,3} ¹ Geomatics Division, Centre Tecnològic de Telecomunicacions de Catalunya, 08860 Castelldefels, Spain² Geohazard Monitoring Group, Institute of Research for Hydro-Geological Protection, National Council of Research, 10133 Torino, Italy; niccolo.dematteis@irpi.cnr.it³ Department of Earth Science and Environment, University of Pavia, 27100 Pavia, Italy

* Correspondence: gluzi@cttc.es

Received: 22 January 2019; Accepted: 24 January 2019; Published: 30 January 2019



Abstract: This paper reports some experimental results obtained by means of a commercial apparatus used by many researchers and users, where a pair of novel and specifically developed circular polarized antennas, designed to operate with Ku band-terrestrial radar interferometers, are used alternatively to the most conventional linear vertical polarized horns provided by the manufacturer of the apparatus. These radar acquisitions have been carried out to investigate for the first time the potential of circular polarization (CP) configurations for terrestrial radar interferometers (TRI) applications, aiming at improving monitoring of landslides, mines, and semi-urban areas. The study tries to evaluate whether the circular polarization response of natural and man-made targets can improve the interpretation of the radar images, with respect to the standard approach used in terrestrial radar interferometry, usually carried out in co-polar vertical polarization. The goal is to investigate how different polarization combinations, in terrestrial radar interferometry, affect the coherence and amplitude dispersion of natural media, potentially improving the identification of stable scatter.

Keywords: GB-SAR; interferometry; circular polarization; microstrip antennas

1. Introduction

The monitoring of natural media and man-made structures at small scale, through ground based SAR (GB-SAR) interferometers, or more generally terrestrial radar interferometers (TRI), as it is referred to when not exploiting SAR techniques, has rapidly grown in the last decades. The most consolidated applications of this technique are the monitoring of open mines, natural processes (i.e., landslides, glaciers), and artificial facilities: For the reader's convenience, an overview of this technique and its main applications is available in [1,2]. These applications are based on interferometric techniques, where the main goal is to provide deformation maps, estimating the evolution of the surface kinematics under observation. Usually, in these measurements, the understanding of the scattering behaviour is mainly related to the amplitude information, which is analyzed for image interpretation purposes, and to select good points from the interferometric point of view, estimating the behaviour of some parameters as coherence (COH) and dispersion of amplitude (DA) [3]. Almost the totality of terrestrial radar measurements discussed in the literature are acquired using linearly polarized (LP) sensors, and mainly using a single linear co-polar configuration, usually co-polar vertical (VV). It is well known that polarimetry can provide highly profitable information in different applications of radar imaging of natural media, such as rough, bare, and vegetated soil, snow, and glaciers: The availability of polarimetric data provided by recent SAR satellite missions has strongly pushed studies based on spaceborn, large scale, data [4]. On the other hand, so far in GB-SAR imaging, this approach has been

rarely used, and only a few case studies have been discussed in the literature [5–8]. The main reason of this lack of research is probably due to the fact that commercial terrestrial radars do not provide multi-polarization capability, and they usually operate in single co-polar configuration (mostly vertical). In addition, the main use of these terrestrial apparatus is focused on interferometric processing for deformation measurements, where polarization features are of minor concern, and have not been deeply investigated so far.

The few studies where multi-polarization terrestrial radar data are analyzed are generally based on data acquisitions performed through laboratory prototypes and wide band sensors, not necessarily working at the Ku band, the spectrum allocation reserved to terrestrial interferometric systems [9]. In [10], for example, the authors showed some results of polarimetric acquisitions obtained through a terrestrial radar prototype, VNA based (details about this technical issue in [11]), and operating at the C band to investigate the characteristics of terrain targets, using as a classification tool the H/A/Alpha polarimetric decomposition [12], with encouraging results for improving the classifications of natural targets, thus providing a better understanding of their scattering mechanism. In a further paper [13], an improved version of the same apparatus used in [10] was calibrated through reference artificial targets, and 3D polarization-sensitive images acquired in different seasons were reconstructed from the acquired data, observing differences among the polarization signatures. In [14], the authors investigated the polarimetric response at the X and C-band using a ground-based synthetic aperture radar, aiming at providing two and three-dimensional images of indoor and outdoor wheat canopy samples, respectively, to understand the scattering processes and the role of soil under the vegetation on the cross- and co-polarimetric response. In [15,16], multi-temporal analysis of the polarimetric features of an urban environment using a ground-based dataset in the X-band was carried out. The temporal behaviour of the entropy, H , was estimated to provide a description of the polarimetric stability of the urban scenario. More recently, the upgrade of a commercial apparatus with polarimetric capabilities, the Gamma Remote Sensing's GPRI-II, namely KAPRI, was tested [17]. Other papers have been published where polarimetry is used for the specific goals of characterizing advanced reflectors for calibration [18]. Circular polarization (CP) backscattering using a GB-SAR has been investigated in [19,20], and calibration of the used apparatus was carried out with a rigorous approach in a controlled environment, and with reference targets. In particular, in [19], the authors provide for the first time the results of a set of SAR laboratory experiments, where circular polarization acquisitions are discussed.

Anyway, circular polarization has been analyzed in a very few cases, and the interest to investigate the CP response of natural media, the topic of this paper, comes from the general features of this polarization, among which its ability to be less affected by the multipath effect is outstanding. It is well known that when the transmitted circular polarized wave is reflected from a surface, along a direction whose incidence angle is higher than the Brewster angle [21], it turns the handedness of the rotating electromagnetic field. In Figure 1, we resume the features that characterize the propagation of CP in the presence of symbolic targets.

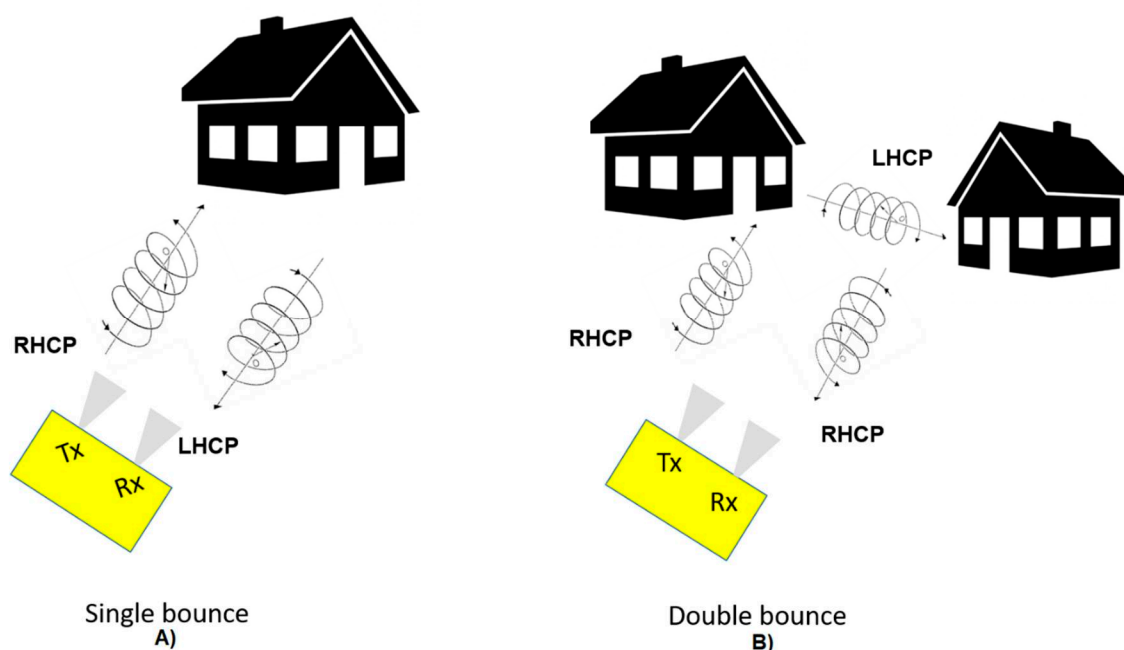


Figure 1. Single (A) and double (B) bounce effect on circularly polarized signal. RHCP: right-handed circular polarization, LHCP: left-handed circular polarization.

After a bounce, the backscattered field propagates in the opposite direction with respect to the transmitted signal. The same rotation direction that would be described as “right-handed” circular polarization, RHCP, for the incident beam is “left-handed” circular polarization, LHCP, for propagation in the receiver direction, and vice versa. For this reason, in the case of a single bounce, a radar provided with the transmitting and receiving antennas with the opposite direction of rotation receives a strong signal. On the contrary, if the two antennas are co-pol, i.e., with the same direction of rotation, the detected signal is very low. When two bounces occur before reaching the receiving antenna, the situation is the opposite. In general, for an odd or even number of bounces, the situation is analogous; although due to the rapid decrease of the signal strength occurring after multiple bounces, the phenomenon is of minor concern. Therefore, by combining co-pol (RHCP and RHCP or LHCP and LHCP) and cross-pol (RHCP and LHCP or LHCP and RHCP) pairs of transmitting and receiving antennas, the contribution from even or odd bounds can be enhanced or minimized. Furthermore, using linear polarized antennas, the reflecting surface does not reflect the signal precisely in the same plane, therefore, the signal strength is weakened. Since circular polarized antennas send and receive in all planes, the signal strength suffers a minor decrease. In circularly-polarized systems, the reflected signal is returned in the opposite orientation, largely avoiding conflict with the propagating signal; the result is that circularly-polarized signals can better penetrate and bend around obstructions. Multi-path is caused when the primary signal and the reflected signal reach a receiver at nearly the same time; linear polarized antennas are more susceptible to multi-path due to the increased possibility of reflection.

Infrastructures and natural media often exhibit non-regular surfaces, and targets’ distribution, and multiple reflections frequently occur: CP measurements are theoretically expected to provide better performances in terms of phase stability and targets’ identification, due to the reduced multipath interferences which characterize this polarization configuration. Furthermore, in literature examples, the potential of CP measurements to detect targets with a specific shape can also be found, especially in studies based on planetary missions based on radar imaging sensors [22,23]. On the other hand, the main drawbacks of the CP system are: (i) A lower efficiency in antenna gain, (ii) a complex design especially when CP is requested in a large bandwidth, and, finally, (iii) a lower diffusion and availability.

This paper reports some experimental results obtained acquiring data through a terrestrial radar, using different combinations of linear and circular polarized antennas. The polarization diversity is evaluated with an empirical approach comparing and analyzing the different responses, looking for the main differences between circular and linear combinations. The study introduces the topic, showing some tests carried out with simple targets using a pair of patch antenna arrays designed to operate at the Ku band frequencies reserved for TRI/GB-SAR use. The two circular polarized patch arrays specifically designed and developed for this study [24] were mounted as transmitting and receiving antennas in a largely diffused GB-SAR commercial system, the Ibis-L manufactured by Ids. The antennas can be used, in principle, with any similar apparatus working in the same band, provided that the used radar sensor is capable to interface through standard connectors or waveguide flanges. The study tries to evaluate, on the basis of some experimental data, if the circular polarization response of natural media and artificial targets can improve the interpretation of the radar images, with respect to the standard co-polar VV configuration, commonly used in TRI. The goal is to investigate how different polarization combinations in terrestrial radar interferometry affect the coherence and amplitude dispersion of natural media, and in particular whether the circular polarization can improve the identification of stable scatters.

The paper is organized in five sections. After this general introduction, the instrumentation characteristics and the methods used to acquire the radar response with different polarizations are described. The following section describes the results of some experimental tests designed to estimate the polarimetric features of single targets and a heterogeneous scenario, including an urban area surrounded by vegetation. First, simple tests using the radar sensor in a real aperture radar (RAR) mode are carried out to assess the capability of the system to provide a sufficient polarization purity. Then, the results of a two-days experimental campaign, carried out in an area including a small village affected by a large landslide, and monitored using the radar in the GB SAR mode, are presented and commented on. Different combinations of receiving and transmitting antennas are used to evaluate the behaviour of some parameters of main concern to individuate coherent areas in radar interferometry. A discussion section is then dedicated to the main outcomes of the study. A conclusions section is dedicated to a summary of the paper content, and suggestions for planning further experiments.

2. Materials and Methods

In this section, the measuring system and the novel antennas used to carry out the experimental campaigns are introduced, with a more detailed description dedicated to the antennas, which represent the novel aspect of the proposed approach. The basic rationale of this study consists in first evaluating the polarimetric performances of the new acquisition system, using circular polarized antennas in a real aperture radar (RAR) configuration to measure the response of simple basic targets. Furthermore, the same radar transceiver is used to acquire, by means of a standard linear GB synthetic aperture configuration, images of a natural scenario, with different polarization combinations.

2.1. The Radar Setup

This study is based on the use of an apparatus, the Ibis-S [25], which in the commercial version, is not provided by multipolarization equipment, acquiring only the co-polar vertical polarization. The design of the radar with polarimetric capabilities, performing simultaneous acquisitions of the different polarization signals, demands an increased complexity of the system: At least two different receiving sections, with different antennas guaranteeing an adequate purity in their polarization response, are necessary. In addition, this approach requires complex calibration procedures, which jointly involves the transceiver and the antennas: See, for example, [17]. When the simultaneity of the acquisitions is not necessary, because the polarization properties of the observed media are supposed to be stable or slow and varying with time, a single transceiver section can be adequate. In this case, acquisitions with different polarizations can be obtained by simply substituting the antennas in subsequent acquisitions, and only the mutual antenna performances determine the

polarization purity of the measurement. On this basis, for this study, two original antennas operating as CP were developed for remote sensing (RS) applications based on ground-based microwave interferometers, in both RAR [26] or SAR configurations [1,2], as an alternative to the standard linear polarized antenna.

The radar transceiver is a commercial apparatus, a Ku band step frequency continuous wave, widely used by researchers and users, which can be used in two different modes: As an RAR, and as GB-SAR. The main parameters are shown in Table 1 [25].

Table 1. Main parameters of the radar transceiver used to acquire RAR and GB-SAR data, respectively.

Radar Parameters		
Mode	RAR	SAR
Central frequency/wavelength	17.1 GHz/0.0175 m	17.1 GHz/0.0175 m
Range resolution	0.5 m	0.5 m
Azimuth resolution	NA	4.4 mrad (<2 m @ 500 m)
Maximum Range	400 m	4 km
Sampling frequency	200 Hz	6 min
Output Data format	1D Range profile	2D Images

2.2. The Circular Polarization Antennas

In this study, two type of antennas are used. The acquisition of linear polarized (LP) data is carried out using two pyramidal horn antennas provided by the producer of the apparatus, both with an approximated value of 20 dBi gain. This type of antenna is usually used for its regular phase response, high isolation between orthogonal fields (V/H linear), and high gain. Despite these qualities, with respect to a patch array, plane, and light, this aperture antenna is bulky and heavy. To arrange a multipolarization system able to acquire cross-and co-CP responses, two patch antennas were implemented, respectively, for LHCP and RHCP. As printed antennas, they offer the possibility of low cost, low weight, and scalability to a high gain version compared to conventional horn antennas; this latter condition results in the selection of microstrip technology. The requirements of this antenna array to be used in a terrestrial radar are: (i) An operating band of 17.05 ± 0.15 GHz [27], (ii) sufficient polarization purity in this band, and, finally, (iii) the capability to be mounted into the available radar apparatus. The design of the array is based on the combination of four linear polarization elements to be produced, with an appropriate sequential rotation of the elements and the feeding network, RHCP and LHCP [24]. The parameter which allows the evaluation of the degree of circularity of a polarized antenna, which is important to assure in this study as a reliable comparison between the different responses of a target when observed through LP or CP observations, is the axial ratio, AR, [28]. AR is 0dB when the antenna provides a perfect circular polarization; in fact, it varies with the frequency and the direction of the antenna pattern [28]. In the operating band of the Ibis-S transceiver used in this study, from 16.9 GHz to 17.2 GHz, the AR was calculated during the design of the array, carried out using HFSS software [29], and it was also measured in an anechoic chamber. Results of the antenna tests are reported in Figure 2, which shows the comparison between simulated and measured AR as a function of the frequency, and Figure 3, showing the simulated AR as a function the viewing angle theta with respect to the antenna axis for three frequency values spanning the entire operating bandwidth. Observing these results, and considering that 3 dB is usually considered a satisfactory value, the results of the measurements and of the simulation assess a sufficient degree of circular polarization for the implemented patch arrays.

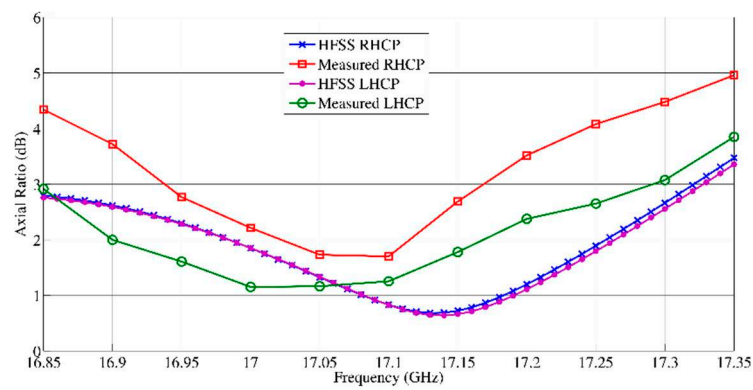


Figure 2. Simulated and measured axial ratio of the two implemented patch arrays vs frequency.

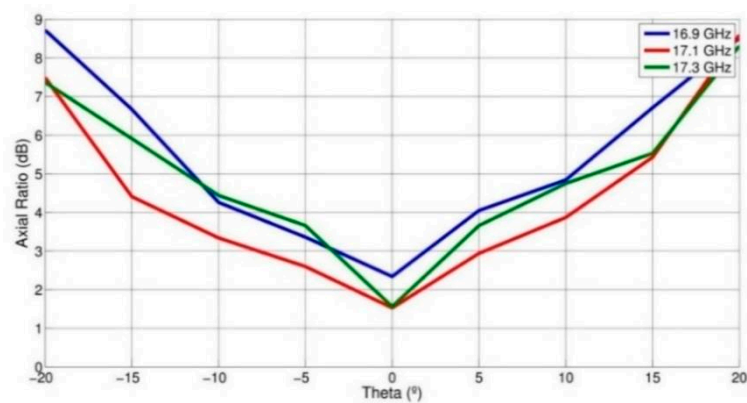


Figure 3. Simulated axial ratio of the implemented patch array (LHCP) vs the angle of the direction, for three frequencies covering the operating band.

To characterize the two patch array antenna, the radiation pattern, for the horizontal and vertical plane were first simulated, and then measured in an anechoic chamber: Figure 4 shows the results.

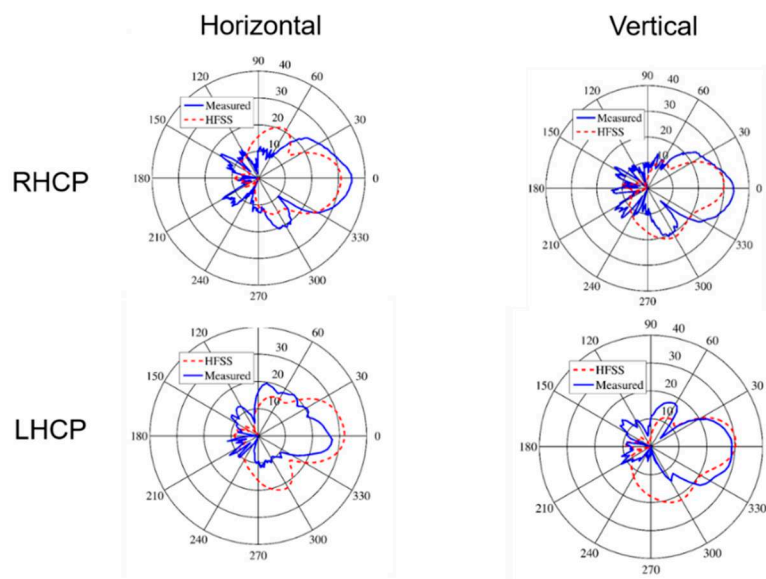


Figure 4. Antenna pattern, simulated through HFSS software [29] (dashed lines) and measured (solid line) for the vertical and horizontal plane.

The two antenna array prototypes were designed, produced, and tested at CTTC. In Figure 5, a photo of the two prototypes mounted on the Ibis transceiver is shown; it is of note that the two patch arrays are connected through a waveguide-SMA connector adapter, which can worsen the matching between antennas and the transceiver, but which is necessary to interface the antennas to the Ibis transceiver. The microstrip circuits used to obtain the RHCP and LHCP patch are specular with respect to the feed line direction (see Figure 5).

When comparing the data acquired with the two different configurations, it must be considered that, with respect to the LP horn antennas, the patch antennas developed for LHCP and RHCP are worse performing in terms of gain directivity, antenna efficiency, and isolation between the receiving and transmitting elements, all factors which affect the amplitude response. This inconvenience is partially due to the design choice, i.e., a limited size of the patch, and to the higher mismatch expected for fitting the patch antenna and the waveguide connection of the sensor (see Figure 5).

As measurements of the patch antenna gain in an anechoic chamber were not available, we decided to estimate the CP antenna gain in a free space environment, using a less rigorous approach, described in the next Section 2.3. Although these estimates can be affected by errors due to multipath, we used these results in our analysis on the basis of the following rationales: (i) The measurements were carried out with the targets in a largely fulfilled far field condition, where the free space condition is similar to an anechoic chamber response; (ii) our main goal was not to evaluate the absolute gain of the CP arrays, but their relative values with respect to those of the standard horn provided by the transceiver manufacturer: A high accuracy is not mandatory. The objective was to compare the performances of the different transceiver-antenna setup; (iii) all the data used to compare the gain from the two different polarization configurations were obtained in the same environment, where multipath is negligible. In addition, radiation measurements were operated in a far field condition. For this reason, as far as the different radar acquisitions are concerned, to compare the acquired data, we first provided an estimate of the new antennas' gain when mounted on the transceiver.



Figure 5. Photo of the two circular polarized antenna arrays mounted on the Ibis-S sensor. To the left is the LHCP and to the right is the RHCP array.

2.3. Circularly Polarized Antennas' Gain Estimate

To compare the amplitude responses from measurements carried out with different antennas' combinations, we needed to estimate the gain of the two CP antennas when mounted on the transceiver.

The apparatus is placed in a fixed position in front of a reference target: An aluminum square plate, size of 30 cm, located at 9 m from the antennas, a distance complying with the antennas' far field condition, with an estimated radar cross-section (RCS) at a perpendicular incidence of 25.3 dBsm;

in this first test, in the RAR configuration, targets are ranged with a 0.5 m resolution. Using the gain comparison technique [28], considering the LP horn (20 dBi) as a reference, assuming that at first approximation the two CP patch arrays get the same value, we can execute a simple procedure based on two measurements. In Figure 6, a scheme of the setup and a picture is shown. In the first acquisition, the transmitting and receiving antennas are a VV horn and CP patch array, respectively; in the second acquisition, two patch arrays in a cross-polar configuration are used: RHCP and LHCP. In Table 2, the values of the received power, estimated through the peaks identified in correspondence to the target location, with respect to the thermal noise of the receiver [25], are reported. To calculate the gain of the patch, after applying a simplified form of the radar equation [30], the following expressions for the received power, P_{rec} , were obtained:

$$P_{rec1} = P_0 + G_{horn} + G_{patch} + RCS_{plate} - 3dB + L_{path} = 60dB \quad (1)$$

$$P_{rec2} = P_0 + G_{patch} + G_{patch} + RCS_{plate} + L_{path} = 50dB \quad (2)$$

where:

P_{reci} : Received power at measurement $i = 1, 2$.

P_0 : Transmitted power (at the port of the transmitting antenna).

G_{horn} : Gain of the linear polarized horn.

G_{patch} : Gain of the circularly polarized patch array.

RCS_{plate} : radar cross section of the target.

L_{path} : propagation and loss factor.

Combining Equations (1) and (2):

$$P_{rec1} - P_{rec2} = 10dB = -G_{patch} + G_{horn} - 3dB \quad (3)$$

$$G_{patch} = G_{horn} - 13dB = 7dB \quad (4)$$

The 3 dB term in Equation (1) is added to compensate the comparison of the gain between a linear polarized and a circular polarized antenna [28]. The value of 7 dBi, which includes possible loss mismatching, is in agreement with the value expected from the simulation.

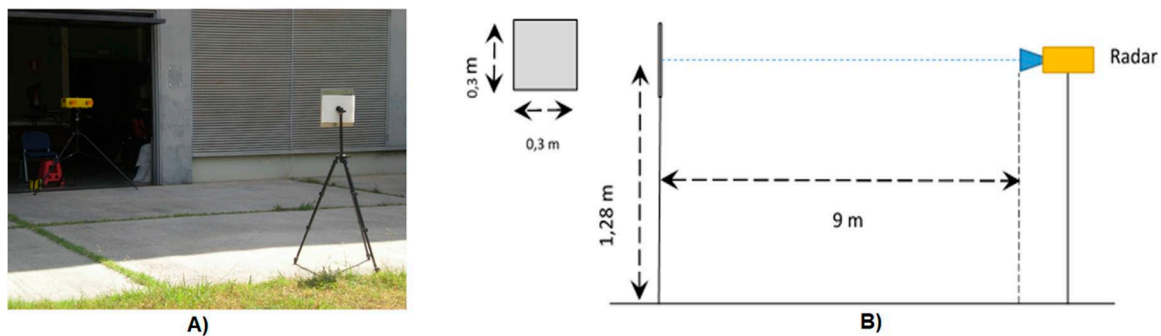
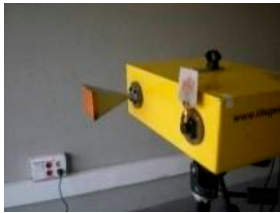
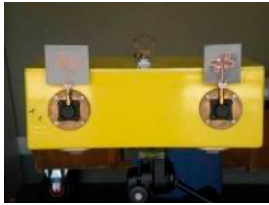


Figure 6. (A) Picture of the experiment setup. (B) Scheme of the measurements carried out to estimate the gain of the system when measuring through CP patch arrays a single target (i.e., a metal square 30 cm × 30 cm).

Table 2. Results of the measurements carried out to estimate the gain of the system when measuring through CP patch arrays a single target (i.e., a metal square 30 cm × 30 cm).

	Measurement 1	Measurement 2
		
Transmitting antenna	Horn 20 dB Pol: V	Patch LHCP/RHCP
Receiving antenna	Patch RHCP	Patch RHCP/LHCP
Max received power (db)	60 dB	50 db ± 1 dB

Using this value, we can compare the backscattering response of different polarization configurations for any targets, and hence better understand their polarimetric features.

3. Experimental Results

This study is based on the acquisition of experimental data, collected to evaluate whether coherence and amplitude dispersion of backscattering responses from natural media have different behaviours when observed through circular polarization antennas, potentially improving the identification of stable scatters. To this aim, two experimental campaigns were carried out: The first dedicated to measure the co-polar and cross-polar response of elementary targets, namely a concrete wall and a light pole, in the RAR mode. Then, images of a small urban area acquired in the SAR mode, and using different combinations of polarization, and during two different temporal time intervals, were analyzed.

3.1. RAR Acquisitions: The Response of a Wall

To evaluate the actual capability of the system to separate the two polarization configurations, a radar acquisition was carried out in front of a wall. Figure 7 shows a picture of the set up. In Table 3, the values of the received power for three different combinations are shown: Co-polar VV LP linear, Cross-polar CP Circular, and co-polar CP. We did not acquire this combination focusing on the cross pol and co-pol difference. Considering the geometric and dielectric characteristics of the target, we did not expect significant differences to change the polarization rotation verse. In Figure 8, the corresponding range profiles are plotted, where the wall surface is identified in bin 17–18. This slight difference between the LP and the CP measurements can be due to the delay introduced by the patch array match. As expected, the highest amplitude of the reflected signal is for the VV configuration, while the weakest response is the circular co-polar CP.

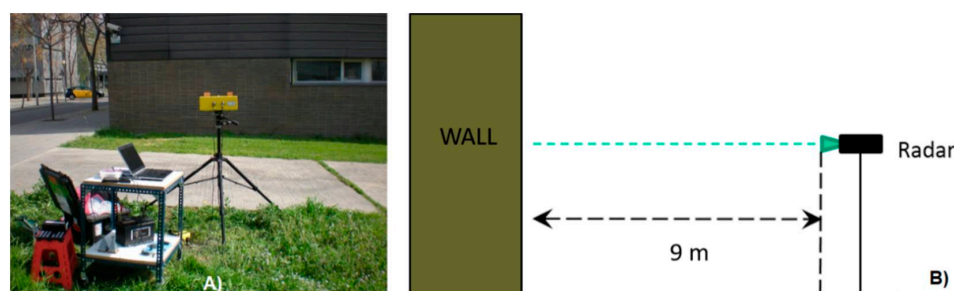





Figure 7. (A) Picture of the experiment setup. (B) Scheme of the measurements carried out to evaluate the response of the system with different polarization configurations in front of a perpendicular dielectric surface: A concrete wall.

Considering that the target is a dielectric surface, perpendicular to the radar line of sight (LOS), and which completely fills the antenna's field of view (FOV), the measurements can be used to estimate the difference between the cross and co-polar CP response. In this case, where a single bounce is expected, the estimated value is 23 dB. It is of note that the difference between VV and cross-polar CP, measurement 1 and 2, is attributable to the difference of gain.

Table 3. Results of the measurements carried out to estimate the difference among VV, cross-polar, and co-polar CP wall response.

	Measurement 1	Measurement 2	Measurement 1
			
Transmitting antenna	Horn 20 dB. Pol: V	Patch LHCP	Patch RHCP
Receiving antenna	Horn 20 dB. Pol: V	Patch RHCP	Patch RHCP
Max received power (db)	77 dB	60 db	37 dB

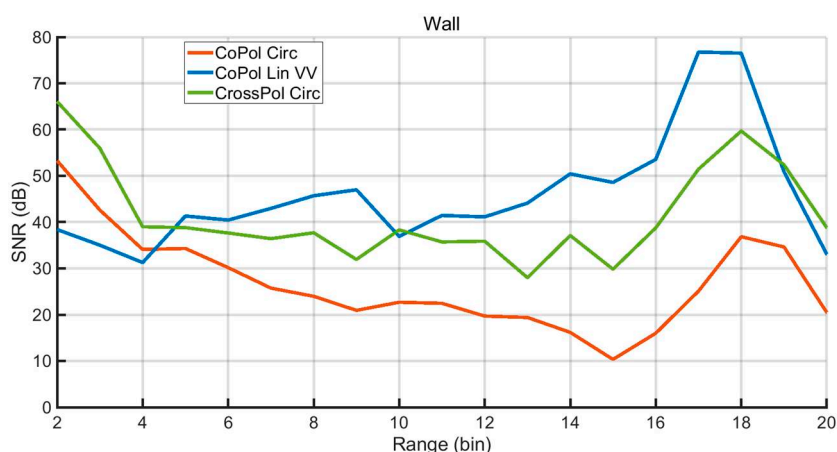


Figure 8. Range profile (1 bin = 0.5 m), obtained in front of a wall with three different polarization configurations: VV (green line), cross-pol circular (red line), co-pol circular (blue line).

3.2. RAR Acquisitions: The Response of a Lightpole

A further test to analyze the different responses between LP and CP antennas was carried out, acquiring data in front of a lightpole. In Figure 9, the geometry of the acquisition and a picture of the setup are shown. Observing the signal-to-noise ratio (SNR) profile in Figure 10A, VV obtains, as expected, the highest intensity, while RR is the lowest.

In Figure 10B, the relative values of measured intensity, normalized to the maximum, are also shown to check the influence of the different gain of the antennas on data interpretation. The presence of a single bounce and the vertical structure, like a cylinder, gives a strong reflection of VV polarization. In the SNR profile, we observe that the cross-polar CP signal is much higher (>20 dB), than the co-polar CP. Observing the scheme of Figure 10B, some reflections (minor peaks) are present previous to the light pole, which are associable to the discontinuities in the asphalt. The data analyzed confirm that the measuring apparatus has a sufficient polarimetric capability that is able to enhance the features of the two CP configurations.

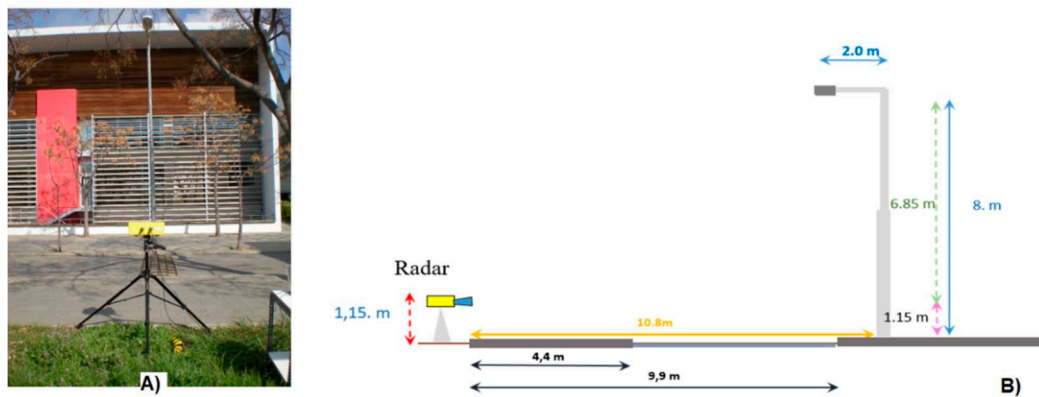


Figure 9. (A) Picture of the measurement setup. (B) Scheme of measurement geometry used to evaluate the response of a light pole with different polarization configurations.

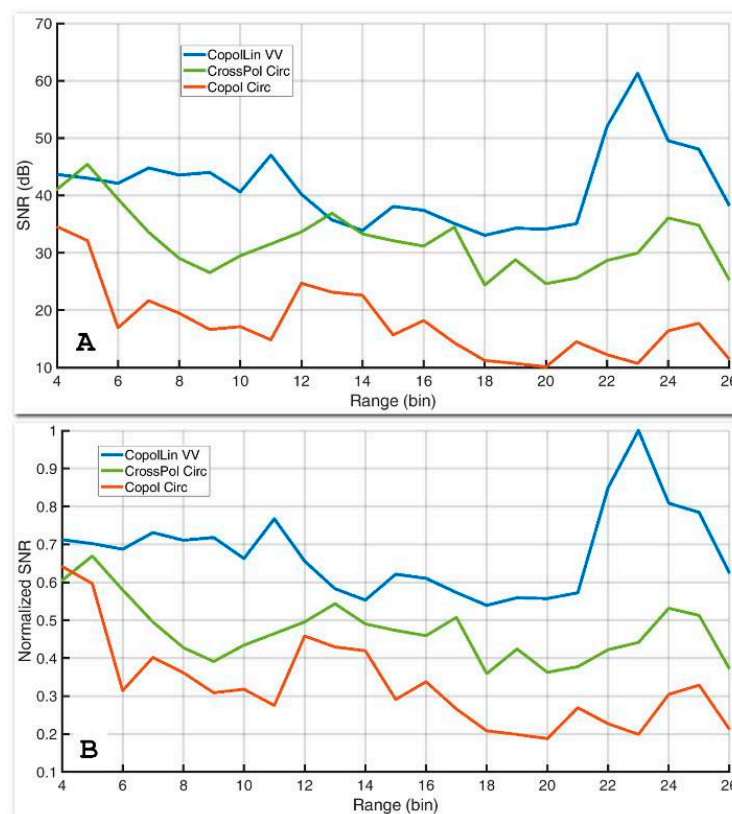


Figure 10. Range profiles (1 bin = 0.5 m), obtained in front of a light pole with three different polarization configurations: VV (blue line), cross-polar circular (green line), co-polar circular (brown line). (A) SNR. (B) Data normalized to the maximum.

3.3. GBSAR Acquisitions of a Landslide Area

In this section, the data used to analyze the response of different polarization combinations were obtained during a two day long GB SAR image acquisition. The scenario is heterogeneous, consisting of a small urban area, including buildings, and debris due to a landslide; all is surrounded by a vegetated area. Figure 11 shows the orthophoto of the area monitored through the GBSAR. In the centre of the picture the collapsed area is clearly distinguishable, composed of very heterogeneous material: E.g., bricks, rocks, roof pieces, undulated metal plates, soil. The radar data used in this study were acquired during a monitoring campaign organized within a H2020 project (HEIMDALL Project Number 740689 [31]). The site is a small village located in Northern Italy, at 1300 m asl, namely Monesi

di Mendatica, where a large landslide occurred in November 2016, destroying a main road and several buildings, and causing the evacuation of all the inhabitants. The GB-SAR was installed in 2017, in a site in front of the area affected by the landslide, placed at approximately 300 m from the scene, and at the same altitude; therefore, the elevation angle of the radar antennas is zero.

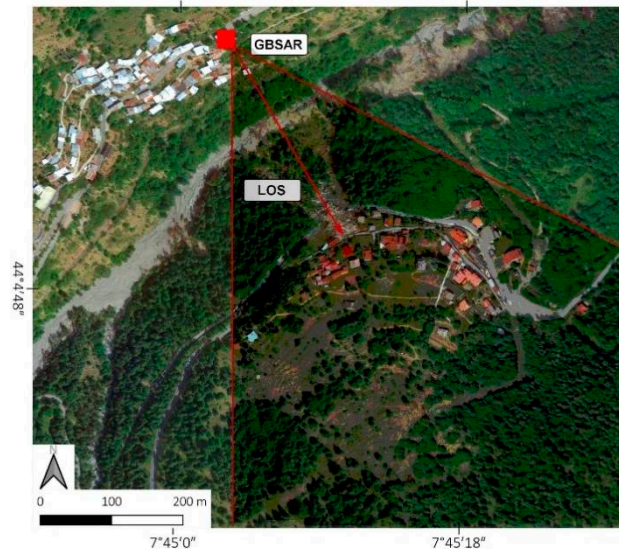


Figure 11. Aerial view of the area of the Monesi di Mendatica landslide with the radar location, LOS direction, and rough extension of the radar FOV indicated.

Figure 12A,B show an amplitude image (VV pol) in radar coordinates, and a photo of the main area of the landslide, respectively.

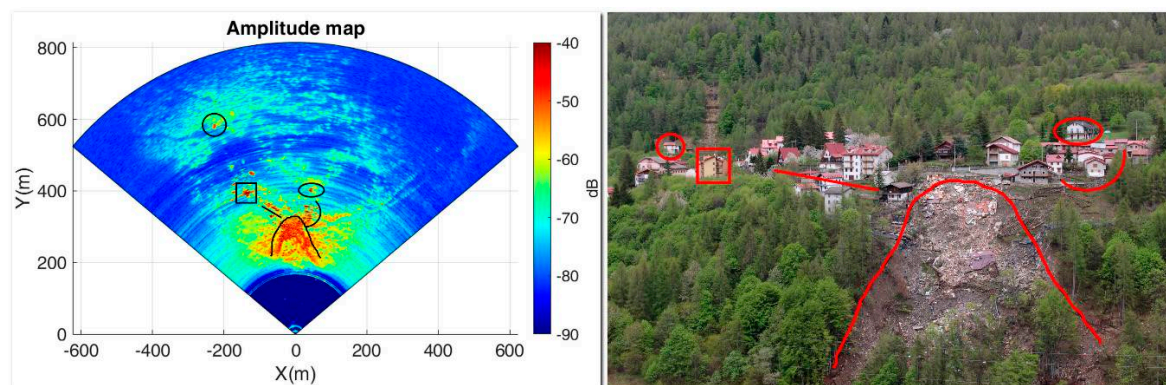


Figure 12. (A) Amplitude image (VV) of a radar acquisition in radar coordinates with some outstanding targets indicated. (B) Picture of the main area with indicated the areas marked in Figure 12A.

Some targets are marked to make it easier to recognize the correspondence between the radar map and the real scene. Figure 13 shows the same radar data of Figure 12A projected on the digital surface model (DSM) to support the data interpretation.

The data were analyzed by comparing the polarization differences considering two temporal scales: A short one, where several combinations were observed, and a long one, focused on the linear vertical co-polar and the circular crosspolar cases. The first case corresponds to a temporal interval of approximately 3 h (i.e., 20 images), while the second one covers a 24 h lapse (i.e., 200 images).

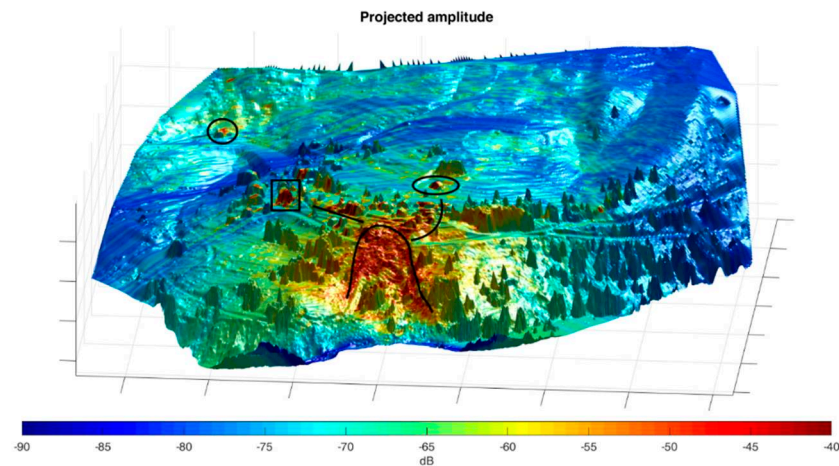


Figure 13. Amplitude (VV) of the radar images projected on the DSM of the monitored area.

In the following section, we focus on the radar response considering two parameters: The temporal dispersion of amplitude (DA) and the coherence (COH), which are the main parameters related to the statistical reliability of interferometric processing. High values of coherence and/or low values of DA are quality indexes related to the accuracy of the retrieved interferometric parameters. DA is defined by Equation (5):

$$D_A = \frac{\sigma_A}{m_A} \quad (5)$$

where m_A , σ_A are the temporal mean and standard deviation of the amplitude of the analyzed pixel, respectively.

3.3.1. The Short Time Series

The set of images below were acquired during two hours (20 images) for each configuration. Figure 14 shows the DA and the COH of the five cases shown in Table 4. From these plots, we observe the following main remarks. VV shows the lowest DA on buildings, as expected, but also vegetation is low, due to the short temporal lapse analyzed: Indeed, coherence also maintains very high values. In this specific case, it is difficult to identify the differences among different targets, due to the short time lapse. The cross-polar HV shows high coherence values on buildings, but very low values on vegetation.

Table 4. Configurations of the short time measurements.

Symbol	Pol Transmitting Antenna	Pol Receiving Antenna	# Images
VV	Linear vertical	Linear vertical	20
RL	Circular right-hand	Circular left-hand	20
RR	Circular right-hand	Circular right-hand	16
HV	Linear horizontal	Linear vertical	14
VR	Linear vertical	Circular right-hand	20

The very high and noisy DA reduces its utility when interferometric techniques are applied. RL shows a low DA and high coherence on buildings. As for VV, considering that the coherence on the vegetation is low, RL can be used both for selecting interferometric scatters and for classification purposes. The RR configuration shows good coherence on buildings, and some specific targets where even bounces are present, but vegetation backscattering is very low, comparable with the noise of the areas where no radar targets are present. Furthermore, RR presents a high amplitude variability.

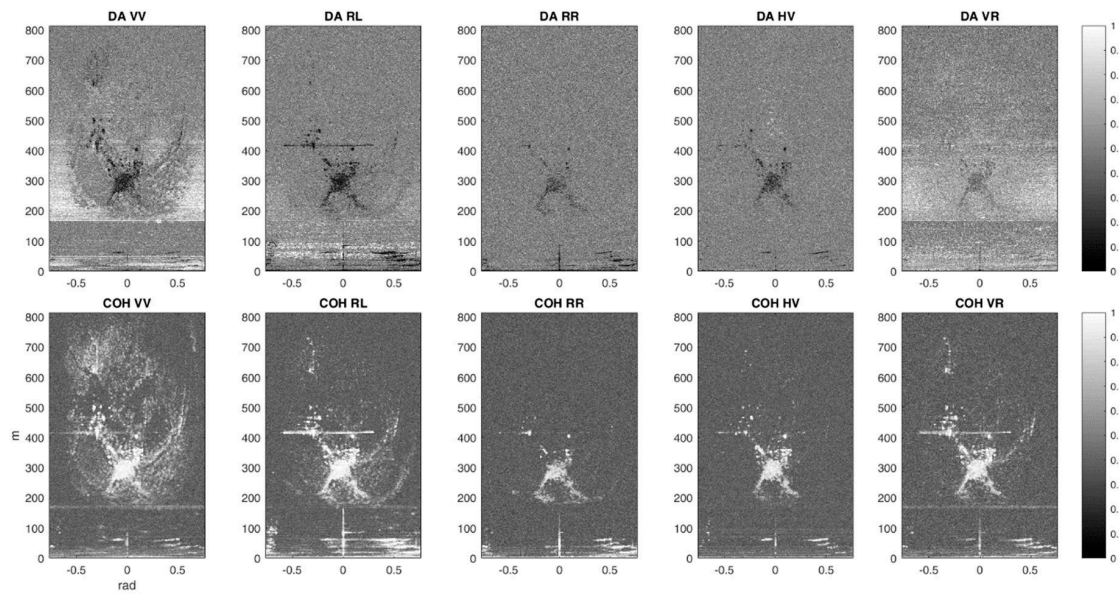


Figure 14. DA and COH for the different combinations analyzed in the short interval images series.

Finally, for the “hybrid configuration”, VR, i.e., transmitting in linear vertical configuration and receiving in RHCP, one can observe a coherence similar to that of RL, but it has the highest DA. This result is not peculiar considering that this combination can be considered at the same time as being partially co-polar (VV) and cross-polar (VH). Observing these results, the two configurations which show a good range in DA and COH are VV and RL; for this reason, we dedicated the second part of the data acquisitions, lasting a longer temporal interval, only to these two combinations (see Section 3.3.2).

An attempt to benefit from these comments is to try a simple classification among elementary classes, such as buildings, vegetation, and incoherent material in the middle of the landslide area. To this aim, we composed images in false colours combining in a RGB image, the DA and COH of three different polarization configurations. Therefore, we associated to the channels red, green, and blue the polarizations of RR, RL, and VV, respectively. From the false color-DA map (Figure 15), no clear indications arise, while the false color-COH, plotted in Figure 16A, deserves some comments. Cyan colour reveals that RL and VV have almost the same behaviour. Vegetation is represented by dark blue due to relatively low COH. The map demonstrates from a qualitative point of view a certain capability to separate building from vegetation areas using this combination of the three polarizations.

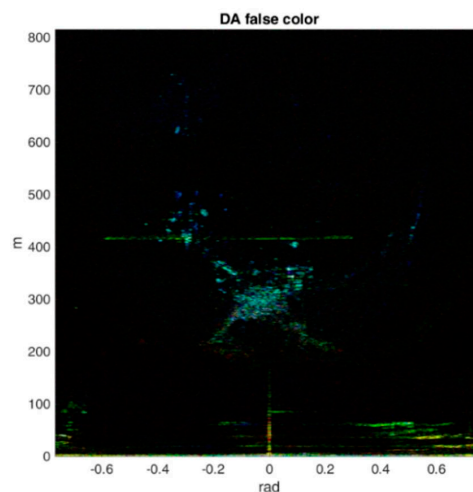


Figure 15. DA false colour map code: Red = RR, Green = RL, blue = VV.

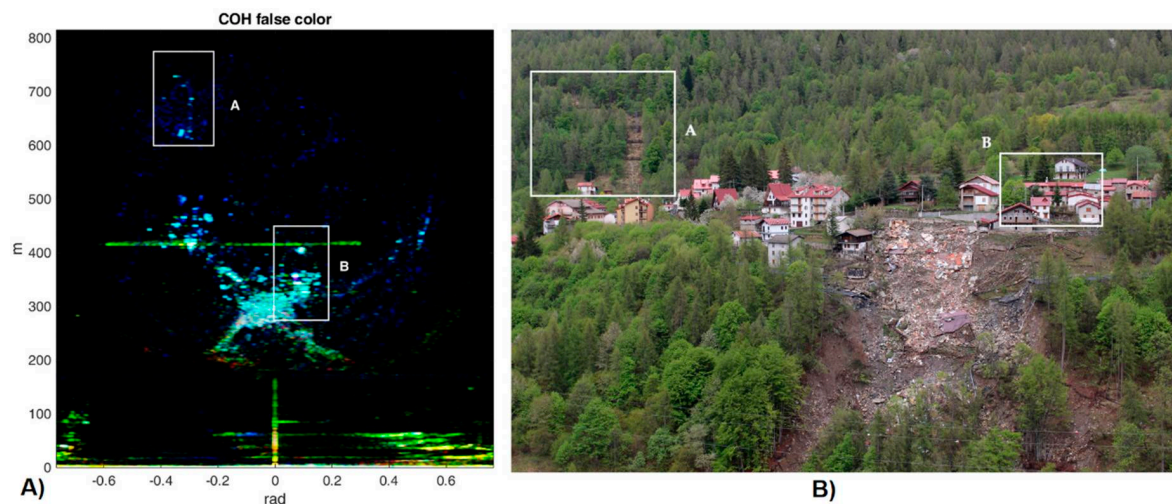


Figure 16. (A) Coherence false colour map with two specific indicated areas, A and B. (B) Picture of the monitored areas with the corresponding A and B sectors indicated.

A more detailed analysis on the coherence behaviour was carried out for two specific areas, which are marked in Figure 16A, and detailed in the pictures of Figures 17B and 18B. The two areas correspond to some fences and vegetated areas (A) and a group of buildings (B), respectively.

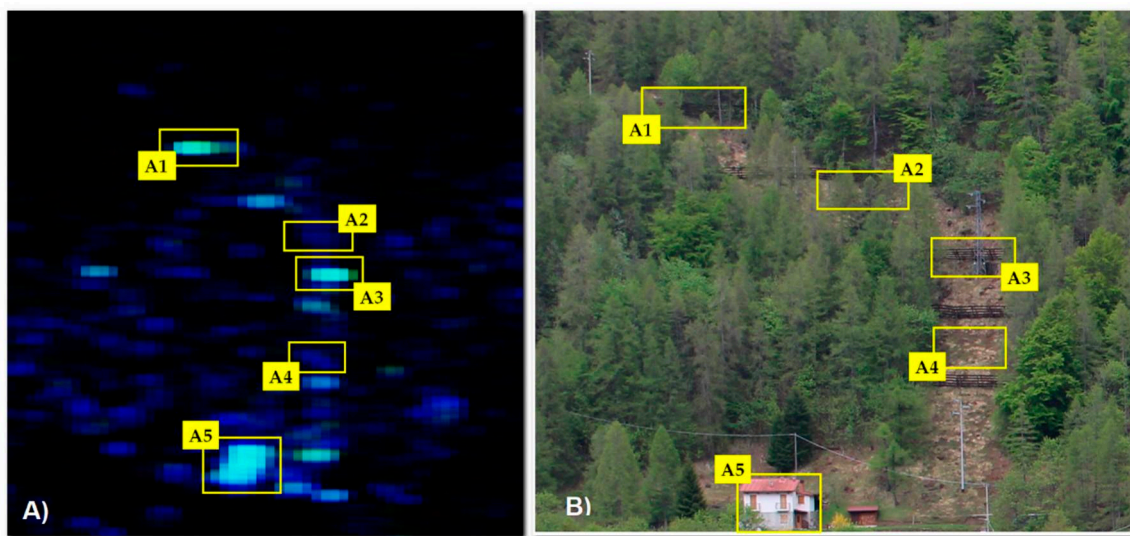


Figure 17. (A) Zoomed area of fences areas with yellow rectangles indicating the location of these targets. (B) Corresponding picture of the zoomed area.

The VV and RL coherence values are almost equivalent on fences and buildings, but VV is much higher than RL and RR on vegetation. RR is generally low everywhere due to the prevalence of a single bounce response. In the area B, the response is different. Observing Figure 18A, where the targets are more visible, we note that for B1, B2, and B4, the backscattering amplitude is high for all the polarizations due to multiple bounces. For target B3, probably due to even bounces, the circular cross-polarization is low. A low value is obtained for the circular co-polarization due to a single bounce in B5.

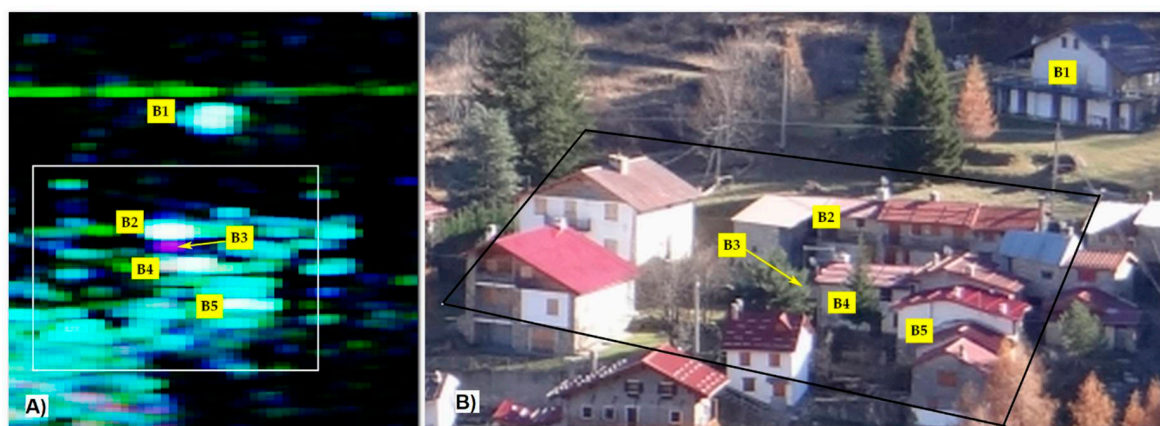


Figure 18. (A) Zoomed area of the map of Figure 16a: Houses are labeled to identify them in the corresponding picture. (B) The white and black rectangles indicate the area analysed in greater detail in Figure 19.

In Table 5, the single channel values are reported. Figure 19 shows the buildings from an aerial view and projected on the DSM. This picture allows for better interpretation of the response. For B2 and B4, the received signal comes from a multiple bounce, as confirmed by the high value for all the polarization. Target B3 differentiates from the others with a high RR, probably due to a wall-floor double bounce. In Figure 19C, a simplified scheme of the two scattering modes occurring in the small area is shown.



Figure 19. (A) False colour map projected on the DSM; (B) picture of two to four houses with a number label and LOS direction. (C) Scheme of the two scattering modes. The apparent longer range depends on the additional path covered by the radar signal after the first bounce.

Table 5. List of the targets identified in Figure 19. Different grey intensities in the table rows enhance the different behaviour as commented in the text.

Target	Red VV	Green RL	Blue RR
B1	222	250	250
B2	250	255	250
1-4 B3	173	23	240
1-4 B4	245	255	250
1-4 B5	1	245	250

The relative phase between RR and RL was also calculated and analyzed. Nevertheless, we could not find any relevant behaviour, probably because the site is strongly affected by atmospheric effects that disturb the signal and that cause phase wrapping. Finally, in Figure 20, we show the RR/RL amplitude ratio. As expected, the amplitude of the void areas is almost equal, while the amplitude of vegetation is slightly higher for RL. More interesting is the analysis of this variable on the buildings, as shown in Figure 20B. In this case, the RL amplitude is much higher than RR, as already discussed in

the previous sections, and it allows identification of the artificial targets, where the RL amplitude is stronger. Nevertheless, the ratio is not homogeneous on all the structures; its analysis reveals where the even/odd bounce modes prevail. In particular, Figure 20B shows that the targets, B4 and B5, reflect mostly in the single bounce mode, while in B1 and B2, the double bounce has a relevant component. On the contrary, B3 reveals that the RR amplitude is stronger than RL because a double bounce process occurs. Observing Figure 19A,B, one can note that the position of B3 corresponds to a flat area just a few meters behind a vertical concrete wall that forms a 90° dihedral where the double bounce occurs. The apparent farther position of the target can be ascribed to the path covered between the two bounces that is summed to the range between the radar and the concrete wall (i.e., the position of the first bounce).

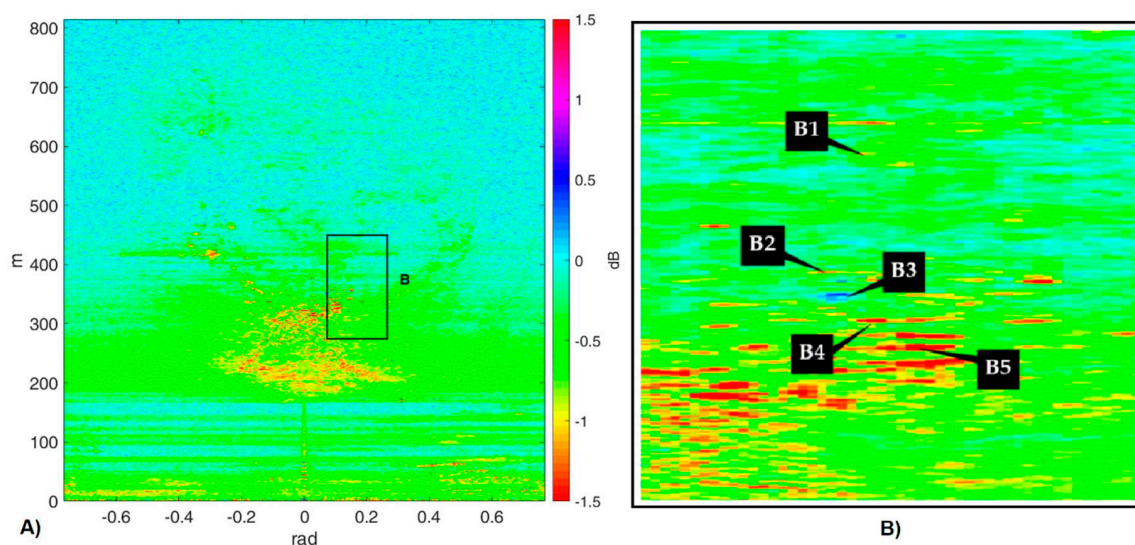


Figure 20. (A) Ratio of the RR/RL amplitude. (B) Zoomed area of the B area (included in the black rectangle in Figure 20A). The positions of the scatters are labelled in black.

3.3.2. The Long Time Series

In this section, the results of two configurations, namely VV and RL, for a day-long temporal interval, are discussed, as shown in Table 6. In Figure 21, DA and COH are shown.

Table 6. Configurations of the long time measurements.

Symbol	Pol Transmitting Antenna	Pol Receiving Antenna	# Images
VV	Linear vertical	Linear vertical	200
RL	Circular right-hand	Circular left-hand	185

In general, DA VV is very high in the first 300 m, but this can be ascribed to the absence of targets and hence only represents the noise of the system. On the other hand, on the targets, it maintains a lower DA. DA of RL is quite uniform and assumes values similar to the areas subjected by relevant decorrelation in void areas, such as wood or grass. COH RL is high on trees despite the large temporal interval for the long series, and improves with respect to short measurements.

In this case, three areas were defined to further detail the analysis, as shown in Figure 22, where the DA is depicted on the DSM, with different colours for stable scatters (buildings), changeable scatters (mostly trees), and no signal (void).

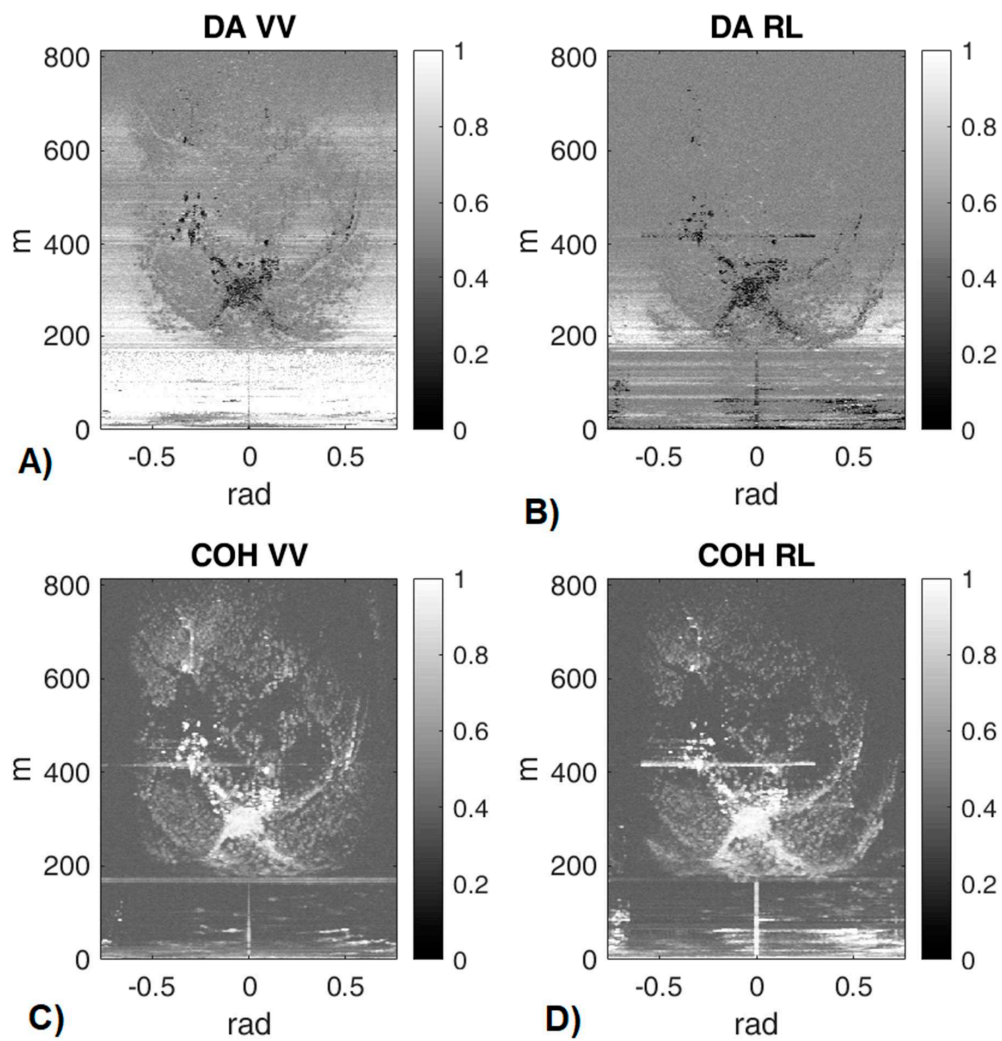


Figure 21. DA and COH maps calculated for the VV and RL configuration, for the long temporal interval. (A) DA VV; (B) DA RL; (C) COH VV; (D) COH RL.

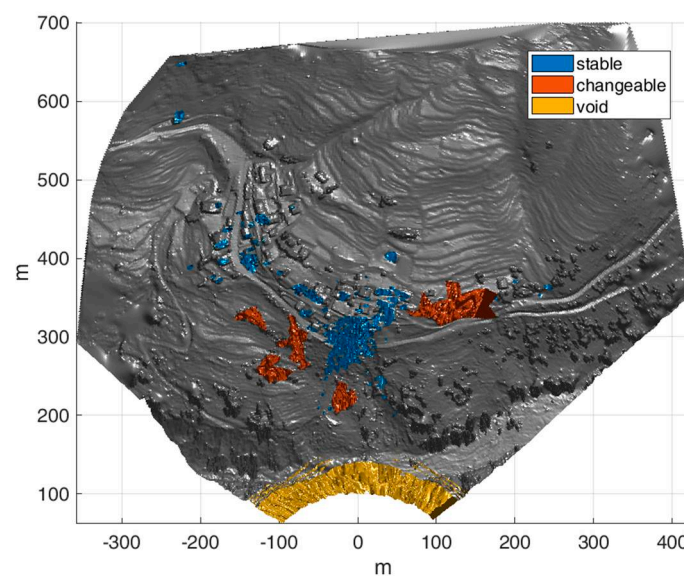


Figure 22. DA map divided in three classes and projected on the DSM.

Calculating the probability density function (PDF) of the three ensembles, shown in Figure 23, the following comments can be made, which confirm the previous observations. For RL, the stable targets maintain low values of DA and high of COH, but only COH allows any distinguishing between no signal and vegetated areas: The DA of RL cannot improve the knowledge about these kind of scenarios. On the other hand, for DA in VV and RL, different behaviors are evident for the three sets (see Figure 23A,B).

The statistical analysis of these parameters of terrestrial radar interferometry represents a further characterization of the various polarization configurations and it highlights/suggests possible applications. For example, the proposed classes can be adapted to the scenario, and in the case of an alpine glacier, they can distinguish glacier surface and rocks, which is very important for atmospheric phase screen (APS) correction and for understanding purposes. Therefore, as expected, the analysis of the DA in VV configuration allows classification of different targets [32].

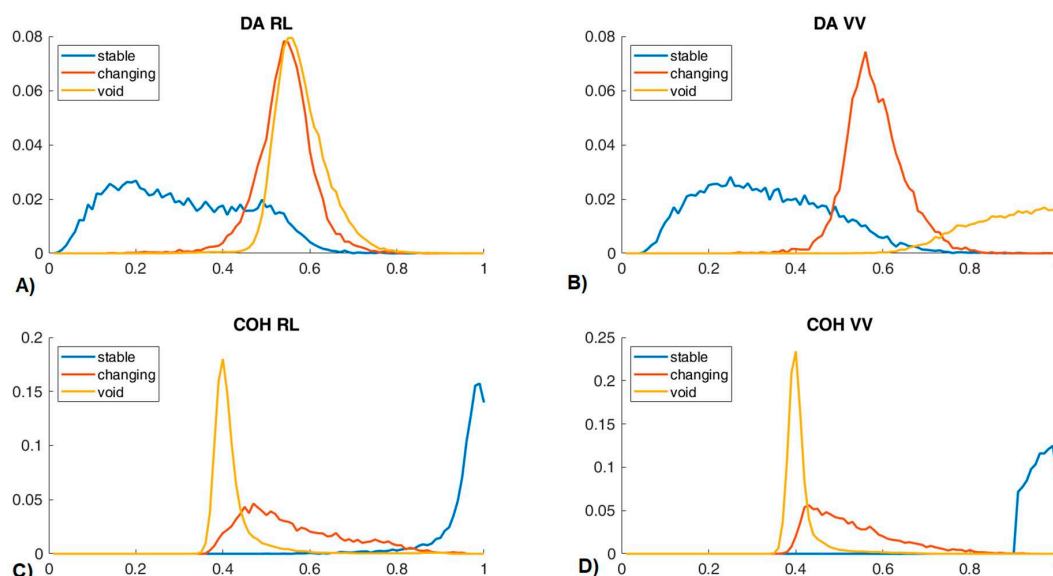


Figure 23. PDF calculated for the three classes: (A) DA RL, (B) DA VV, (C) COH RL, and (D) CO VV.

4. Discussion of the Results

Based on the experimental data analyzed in the previous section, we can assess and discuss the following outcomes. First, the radar system arranged with the novel antennas, despite the lack of a rigorous polarimetric calibration, was demonstrated to be appropriate to provide a polarization capability to distinguish single and multiple bounce responses from reference targets. Although fully polarimetric high performing systems have been used by other researchers to investigate the response of natural surfaces ([15–18]), so far, these systems have not measured circular polarizations. In this preliminary study, we demonstrated that the arranged system was adequate for attainment of the study's goals. This was first demonstrated by the tests carried out in the RAR mode, measuring the response of the wall and of the light pole. Both range profiles shown in Figures 8 and 10, corresponding to the backscattering responses of these two targets clearly distinguish between different responses for co- and cross- polarized antennas. Nevertheless, it must be underlined that the CP antennas' gain is low, and their efficiency is small, due to reasons already commented on in Section 2. The three polarimetric configurations, i.e., the radar acquisitions with VV, co- and cross- circular polarization, were carried out with sufficient accuracy: The value of the 23 dB difference between the co- and cross response from the wall test gives an estimate of this sensitivity. Also, the lightpole data confirm that the co- and cross-pol CP responses significantly diverge, as expected: A difference higher than 20 db of SNR (see Figure 10A) was achieved.

In the GB SAR data analysis, we focused on the radar response considering two parameters: DA and COH, which are the main parameters related to the statistical reliability of interferometric processing. High values of coherence and/or low values of DA are quality indexes related to the accuracy of the retrieved interferometric parameters. In the short time interval data set, all the tested polarization configurations showed a sufficient dynamic range to detect some outstanding targets whose response confirmed the expected difference between the single and double bounce effect. Although the goal to disclose a straightforward classification capability of the circular polarization responses was not sufficiently proven, some remarks can be made.

Among the two analyzed parameters, coherence appears to be better indicator for image interpretations. Indeed, by focusing on single targets (see Figures 17 and 18), specific behaviours where single and double bounces are separated (see Figure 19) were found.

The relative phase between RR and RL was calculated and analyzed, but probably due to a significant atmospheric phase screen affecting the monitored area, no affordable remarks can be made, at least for the short time interval. On the other hand, the RR/RL amplitude ratio seems to provide useful information: The ratio was not homogeneous on all the structures, and the odd bounce modes prevailed. About the importance of this parameter, this confirms the results available from the literature coming from other application fields [23,24]. The presence of an evident double bounce effect in the urban area was confirmed by a detailed analysis of the backscattering geometry: See Figure 19 and Figure 19b.

Regarding the long time series, where the co-pol LP (V) and the cross-pol CP were compared, the main outcome is that the DA of RL is quite uniform and assumes values similar to the areas subjected by relevant decorrelation in void areas, such as wood or grass, while COH RL is high on trees despite the large temporal interval for long series. Analyzing the two PDF distributions, it can be seen that the use of a circular polarization, despite a lower SNR, does not jeopardize the quality of the images; on the contrary, it provides a higher coherence on stable scatters.

On the basis of these preliminary experiments, we can assess that radar monitoring based on cross polarized circular antennas is able to provide detailed information about the scattering mechanism, which is not available with the conventional VV linear polarized observation. An important aspect to be considered is the low gain of the used CP antennas with respect to that of the LP antennas: Although in this study it did not jeopardize the measuring conditions, it affects the SNR of the measurements, and can be improved by upgrading the antenna design, or using different antennas with a higher gain. This technical issue must be taken into account in order to improve the measuring conditions in further experiments.

5. Conclusions

In this paper, some experimental results obtained during a GB-SAR data collection based on the use of a commercial apparatus used in its standard polarization configuration, copolar vertical, and with novel antennas, operating in circular cross- and co-polar configuration, were shown. For the first time, the circular polarization and linear polarization of a natural scenario, typical of landslides' monitoring, were compared and analyzed. The polarimetric capability of the radar system was first tested with reference targets using the radar transceiver without synthetic aperture. The polarimetric capability of the measuring system was assessed on an empirical basis. Using the data acquired with a commercial apparatus during the monitoring of a landslide, the parameters of main interest in GB-SAR interferometry, such as the coherence and dispersion of amplitude, were analyzed at two different temporal scales. Although the main outcomes of the study are based on a simple empirical and statistical approach, the partial capability to differentiate some scatters using co-polar and cross-polar circular polarization was verified, as expected from basic considerations about the propagation and the single/multiple bounce rationale.

Author Contributions: G.L. conceived the study, designed and performed the experiments; N.D. processed the data. G.L. and N.D. analyzed the data and wrote the paper.

Funding: This research was partially funded by the Horizon 2020 Framework Programme Collaborative Project, Call/Topic H2020-s-2016-2017/H2020-SEC-2016-2017-1, grant number 740689.

Acknowledgments: The data collection carried out in Monesi has been partially financed by HEIMDALL (Multi-Hazard Cooperative Management Tool for Data Exchange, Response Planning and Scenario Building), a Collaborative Project, Call/Topic H2020-s-2016-2017/H2020-SEC-2016-2017-1. Project Number 740689. Thanks are also due to the Municipality and *Pro Loco* of Briga Alta (CN) for their kind hospitality.

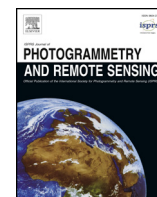
Conflicts of Interest: The authors declare no conflict of interest.

References

1. Caduff, R.; Schlunegger, F.; Kos, A.; Wiesmann, A. A review of terrestrial radar interferometry for measuring surface change in the geosciences. *Earth Surf. Process. Landf.* **2015**, *40*, 208–228. [CrossRef]
2. Monserrat, O.; Crosetto, M.; Luzi, G. A review of ground-based SAR interferometry for deformation measurement. *ISPRS J. Photogramm. Remote Sens.* **2014**, *93*, 40–48. [CrossRef]
3. Ferretti, A.; Prati, C.; Rocca, F. Permanent Scatterers in SAR Interferometry. *IEEE Trans. Geosci. Remote Sens.* **2001**, *39*, 8–20. [CrossRef]
4. Abdikan, S.; Sekertekin, A.; Ustunern, M.; Sanli, F.B.; Nasirzadehdizaji, R. Backscatter analysis using multi-temporal Sentinel-1 SAR data for crop growth of maize in Konia basin, Turkey. In Proceedings of the ISPRS TC III Mid-Term Symposium “Developments, Technologies and Applications in Remote Sensing”, Beijing, China, 7–10 May 2018; Volume XLII-3, pp. 9–13.
5. Iglesias, R.; Aguasca, A.; Fabregas, X.; Mallorqui, J.J.; Monells, D.; López-Martínez, C.; Pipia, L. Ground-Based Polarimetric SAR Interferometry for the Monitoring of Terrain Displacement Phenomena—Part I: Theoretical Description. *IEEE J. Sel. Top. Appl. Earth Observ. Remote Sens.* **2015**, *8*, 980–993. [CrossRef]
6. Rodersperger, S.; Coccia, A.; Vicente, D.; Meta, A. Introduction to the new metasensing ground-based SAR: Technical description and data analysis. In Proceedings of the IEEE International Geoscience and Remote Sensing Symposium, Munich, Germany, 22–27 July 2012; pp. 4790–4792.
7. Baffelli, S.; Frey, O.; Werner, C.; Hajnsek, I. Polarimetric Calibration of the Ku-Band Advanced Polarimetric Radar Interferometer. *IEEE Trans. Geosci. Remote Sens.* **2018**, *56*, 2295–2311. [CrossRef]
8. Bennet, J.C.; Morrison, K. Development of a ground-based polarimetric synthetic aperture radar. In Proceedings of the IEEE Aerospace Applications Conference, Aspen, CO, USA, 10 February 1998.
9. European Communications Committee. Compatibility Studies between Ground Based Synthetic Aperture RADAR and Existing Services in the Range 17.1 GHz to 17.3 GHz. Report 111. 2007. Available online: <https://www.ecodocdb.dk/download/04a2c838-7bf3/ECCREP111.PDF> (accessed on 29 January 2019).
10. Kang, M.K.; Kim, K.E.; Lee, H.; Cho, S.J.; Lee, J.H. Preliminary results of Polarimetric Characteristics for C-band quad-polarization GB-SAR images using H/A/a polarimetric decomposition theorem. *Korean J. Remote Sens.* **2009**, *25*, 531–546.
11. Luzi, G. Ground Based SAR Interferometry: A novel tool for Geoscienc. In *Geoscience and Remote Sensing, New Achievements*; Imperatore, P., Riccio, D., Eds.; InTech: London, UK, 2010; ISBN 978-953-7619-97-8.
12. Cloude, S.R.; Papathanassiou, K.P. Polarimetric SAR interferometry. *IEEE Trans. Geosci. Remote Sens.* **1998**, *36*, 1551–1565. [CrossRef]
13. Zhou, Z.S.; Boerner, W.M.; Sato, M. Development of a Ground-Based Polarimetric Broadband SAR System for Noninvasive Ground-Truth Validation in Vegetation Monitoring. *IEEE Trans. Geosci. Remote Sens.* **2004**, *42*, 1803–1810. [CrossRef]
14. Brown, S.C.M.; Quegan, S.; Morrison, K.; Bennett, J.C.; Cookmartin, G. High-Resolution Measurements of Scattering in Wheat Canopies—Implications for Crop Parameter Retrieval. *IEEE Trans. Geosci. Remote Sens.* **2003**, *41*, 1602–1610. [CrossRef]
15. Pipia, L.; Fabregas, X.; Aguasca, A.; Lopez-Martinez, C.; Duque, S.; Mallorqui, J.; Marturia, J. Polarimetric Differential SAR Interferometry: First Results with Ground-Based Measurements. *IEEE Geosci. Remote Sens. Lett.* **2009**, *6*, 157–171. [CrossRef]

16. Pipia, L.; Fabregas, X.; Lopez-Martinez, C.; Aguasca, A.; Mallorqui, J.J.; Marturià, J. Polarimetric Temporal Stability of Urban GB-SAR Measurements. In Proceedings of the 7th European Conference on Synthetic Aperture Radar, Friedrichshafen, Germany, 2–5 June 2008.
17. Baffelli, S.; Marino, A.; Frey, O.; Hajnsek, I.; Werner, C. KAPRI KU Band AND Polarimetric-Interferometric ground Based Real Aperture Radar: Calibration and first observations. In Proceedings of the POLINSAR, Frascati, Italy, 26–30 January 2015.
18. Ferrer, P.J.; López-Martínez, C.; Aguasca, A.; Pipia, L.; González-Arbesú, J.M.; Fabregas, X.; Romeu, J. Transpolarizing Trihedral Corner Reflector Characterization Using a GB-SAR System. *IEEE Geosci. Remote Sens. Lett.* **2011**, *8*, 774–778. [[CrossRef](#)]
19. Izumi, Y.; Demirci, S.; Baharuddin, M.Z.; Sumantyo, J.T.S.; Yang, H. Analysis of Circular Polarization Backscattering and Target Decomposition Using GB-SAR. *Prog. Electromagn. Res. B* **2017**, *73*, 17–29. [[CrossRef](#)]
20. Izumi, Y.; Demirci, S.; Baharuddin, M.Z.; Waqar, M.M.; Sumantyo, J.T.S. The Development and Comparison of Two Polarimetric Calibration Techniques for Ground-Based Circularly Polarized Radar System. *Prog. Electromagn. Res. B* **2017**, *73*, 79–93. [[CrossRef](#)]
21. Najibi, N.; Jin, S. Physical Reflectivity and Polarization Characteristics for Snow and Ice-Covered Surfaces Interacting with GPS Signals. *Remote Sens.* **2013**, *5*, 4006–4030. [[CrossRef](#)]
22. Spudis, P.D.; Bussey, D.B.J.; Baloga, S.M.; Butler, B.J.; Carl, D.; Carter, L.M.; Chakraborty, M.; Elphic, R.C.; Gillis-Davis, J.J.; Goswami, J.N.; et al. Initial results for the north pole of the Moon from Mini-SAR, Chandrayaan-1 mission. *Geophys. Phys. Res. Lett.* **2010**, *37*, L06204. [[CrossRef](#)]
23. Campbell, A. High circular polarization ratios in radar scattering from geologic targets. *J. Geophys. Res.* **2012**, *117*, E06008. [[CrossRef](#)]
24. Ferré, R.; Mira, F.; Luzi, G.; Mateu, J.; Kalialakis, C. A Ku band circularly polarized 2×2 microstrip antenna array for remote sensing applications. In Proceedings of the International Applied Computational Electromagnetics Society Symposium, Florence Italy, 26–30 March 2017.
25. Coppi, F.; Gentile, C.; Ricci, P. A software tool for processing the displacement time series extracted from raw radar data. In Proceedings of the 9th International Conference on Vibration Measurements by Laser and Non-Contact Techniques, Ancona, Italy, 22–25 June 2010.
26. Pieraccini, M. Monitoring of Civil Infrastructures by Interferometric Radar: A Review. *Sci. World J.* **2013**, *2013*, 786961. [[CrossRef](#)] [[PubMed](#)]
27. Boskovic, N.; Jokanovic, B.; Olivieri, F.; Tarchi, D. High gain printed antenna array for FMCW radar at 17 GHz. In Proceedings of the 12th International Conference on Telecommunication in Modern Satellite, Cable and Broadcasting Services, Nis, Serbia, 14–17 October 2015.
28. Toh, B.Y.; Cahill, R.; Fusco, V.F. Understanding and Measuring Circular Polarization. *IEEE Trans. Educ.* **2003**, *46*, 313–318.
29. Ansys Corporation. *HFSS*; Suite v15; Ansys Corporation: Pittsburg, CA, USA, 2014.
30. Skolnik, M. *Introduction to Radar Systems*, 2nd ed.; McGraw Hill Book Co.: New York, NY, USA, 1980.
31. Heimdall Collaborative Project Call/Topic H2020-SEC-2016-2017/H2020-SEC-2016-2017-1 Title Multi-Hazard Cooperative Management Tool for Data Exchange, Response Planning and Scenario Building. Project Number 740689 Project Acronym HEIMDALL. Available online: <http://heimdall-h2020.eu/> (accessed on 29 January 2019).
32. Dematteis, N.; Luzi, G.; Giordan, D.; Zucca, F.; Allasia, P. Monitoring Alpine glacier surface deformations with GB-SAR. *Remote Sens. Lett.* **2017**, *10*, 947–956. [[CrossRef](#)]





4D surface kinematics monitoring through terrestrial radar interferometry and image cross-correlation coupling

Niccolò Dematteis^{a,b}, Daniele Giordan^{a,*}, Francesco Zucca^b, Guido Luzi^c, Paolo Allasia^a

^a Geohazard Monitoring Group, Institute of Research for Hydro-Geological Protection, National Council of Research, Torino, Italy

^b Department of Earth and Environmental Sciences, Università di Pavia, Pavia, Italy

^c Geomatics Division, Centre Tècnologic de Telecomunicacions de Catalunya, Castelldefels, Spain

ARTICLE INFO

Keywords:

3D motion
Surface kinematics
GBSAR
Image cross-correlation
Sensor network
Data integration
Interferometry
Glacier kinematics
Remote sensing
Monitoring

ABSTRACT

Complex gravitational phenomena can require terrestrial remote sensing solutions for monitoring their possible evolution, especially when in situ installations are not possible. This study merges terrestrial radar interferometry (TRI) and image cross-correlation (ICC) processing, which can detect complementary motion components, to obtain a 3-dimensional system able to measure the actual surface motion field of a pre-defined target. The coupling can be carried out on data acquired from different installations of the devices, and by applying specific transformations of the related coordinate systems. The data georeferencing is a critical issue that affects the correct spatial correspondence of the data and a new approach for georeferencing radar data is proposed. The result is a spatio-temporal (3 + 1-dimensional) high-resolution representation of the surface kinematics. The presented method has been tested for the measurement of the Planpicioux glacier surface kinematics (NW of Italy). The error analysis revealed a millimeter accuracy and precision of the measurement and a georeferencing uncertainty of a few metres.

1. Introduction

The necessity of strategies of preventive alert and risk mitigation related to gravitational slope processes, especially in mountain areas (e.g., landslides, avalanches, glacier outbursts, rock falls), requires systematic observation in order to a full understanding of these phenomena (Kääb et al., 2005). A particular attention is addressed to the surface kinematics monitoring, because in some cases it is possible to detect failure precursors (Faillettaz et al., 2015; Fukuzono, 1985).

Often, these processes are located in remote and harsh environments, consequently the access in these areas is usually difficult and perilous or even impossible. Therefore, various technologies and techniques have been developed and proposed for remotely monitoring gravitational slope phenomena (Arenson et al., 2016; Delacourt et al., 2007; Kääb et al., 2005; Leprince et al., 2008). Actually, the majority of the monitoring systems suffer some limitations. E.g., terrestrial radar and monoscopic photogrammetry can measure only partial components of the actual motion. Total stations and GPSs require the in-situ installation of artificial targets or sensors and they provide only punctual data. Other approaches produced digital elevation models (DEMs) and derived the kinematics through volume difference (e.g., structure-from-motion, SFM, and terrestrial laser scanner, TLS). Finally, space- or air-

based remote sensing systems measure spatially distributed data over wide areas with high precision, though they require high financial costs and the survey repeatability is strongly limited; moreover, the measurement can be affected by unfavorable geometries.

In literature, different studies focused on remote sensing applications that can estimate the 3D surface deformations. Among the category of space-based systems, Wright et al. (2004) proposed a sort of multi-viewed stereoscopy of interferometric synthetic aperture radar (SAR) data that relies on the availability of SAR images acquired with four different look directions.

Concerning the ground-based systems, some studies proposed solutions for estimating the surface motion through the difference of DEMs acquired either by TLS (Bitelli et al., 2004) or by SFM (Piermattei et al., 2016; Roncella et al., 2014). But, cause the DEMs are defined on a 2D surface, $f(x, y) = z$, their difference provides 1D deformation measurements along the vertical axis (Monserrat and Crosetto, 2008). Monserrat and Crosetto (2008) proposed an algorithm of surface matching able to provide 3D deformations that proved to perform well for TLS data acquired from short distances. However, the main drawback of the TLS acquisitions remains the limited revisiting time of the measurement. Manconi et al. (2013) proposed an estimate of the 3D deformation by spatially interpolating over a DEM the punctual data

* Corresponding author.

E-mail address: daniele.giordan@irpi.cnr.it (D. Giordan).

acquired by a total station. Other works projected the data acquired by GBSAR (Dematteis et al., 2017; Luzi et al., 2007), satellite SAR (Huang and Li, 2011) or produced through image cross-correlation (ICC) (Gabrieli et al., 2016; Giordan et al., 2016) along the expected maximum gradient direction or the expected flow direction (Schwalbe and Maas, 2017). Similarly, Ahn and Box (2010), Messerli and Grinsted (2015), and Travelletti et al. (2012) applied the image orthorectification and consequently adjusted the ground sampling distance (GSD) of each pixel according to the incident angle. Both approaches made the strong assumption of the invariance of the surface morphology during the survey (Travelletti et al., 2012), though this might be not valid in presence of quite active phenomena or measurements separated by long time intervals. Schwalbe and Maas (2017) adopted a multi-camera network to produce updated DEM integrated in the processing chain.

In recent years, the research is focusing on the integration of different types of monitoring systems; thereby it is possible to overtake the limitations of the single devices and acquire information that are more representative of the phenomenon. Kenner et al. (2014) merged airborne LiDAR data to assess vertical deformations by means of DEM difference with aerial photogrammetry for detecting horizontal movements through ICC. Also, TLS and terrestrial radar interferometry (TRI) were coupled for monitoring 3D deformations of archaeological monuments (Tapete et al., 2013), buildings (Marambio et al., 2009) and cliff evolution (Lim et al., 2005). Piermattei et al. (2016) used ground-based photogrammetry and Scaioni et al. (2017) combined unmanned aerial vehicles (UAVs) and ground-based photogrammetry for assessing the evolution of 3D glacial processes, in particular related to mass balance change. Malet et al. (2016) monitored a set of landslides adopting a network of permanent GPSs, TLS, and photogrammetric cameras.

In the present paper, we propose a method for measuring the actual 3 + 1D surface kinematics of a gravitational slope phenomena through the coupling of the data collected by two different ground-based remote sensing systems, (i) a ground-based SAR (GBSAR) and (ii) a monoscopic visual-based system (VBS). Their data are processed respectively through radar interferometry and image cross-correlation (ICC) techniques. The 3-dimensional reconstruction of the motion vector is possible because the devices observe different and complementary motion components: the line of sight (LOS) -parallel component is measured by the GBSAR, while the VBS detects the two components orthogonal to the LOS. One of the objectives of our approach is the application of the method to purely remote sensing measurements from medium range (i.e., a few thousand metres).

Furthermore, we present the method application and results related to a 24 days-long campaign surveying the Planpincieux glacier that was carried out on September 2015. The conclusive part of the paper is dedicated to some considerations and comments concerning the proposed method.

2. Dataset and study site

The data presented in this paper were collected during the period 04 – 27 September 2015. The goal of the study was the measurement of the surface displacements of the Planpincieux glacier that is placed on the southern side of the Mont Blanc massif, in the Italian Alps (Fig. 1).

The Planpincieux glacier is a polythermal glacier with elevation ranging between 2500 and 3500 m. This paper deals with the analysis of the data related to the lower part of the glacier, which is classified as a “temperate terrace avalanching glacier” (Faillettaz et al., 2015; Giordan et al., 2016; Pralong, 2005). It reaches an altitude of approximately 2900 m and it is composed of two main icefalls separated by a central ridge of partly-exposed bedrock. The western side is the most active and shows a highly crevassed texture with a mean slope of 32°; it is characterized by a frontal 20 m-high vertical ice wall just above a steep bedrock face from which several failures of ice are triggered periodically during the warm season. In the past, several major

ice avalanches and outbursts of water pocket occurred, and in some cases they threatened the underlying village of Planpincieux and damaged the road.

The entire body of the Planpincieux glacier is continuously monitored for research and civil protection purposes since 2013 by a monoscopic visual-based system (VBS) that is installed on the opposite valley side w.r.t. the glacier, at an elevation of 2305 m and a distance of approximately 3800 m (Giordan et al., 2016). It consists of two consumer-grade cameras with APS-C sensors of 18 Mpx that are equipped with 297 mm (TELE module) and 120 mm (WIDE module) focal lens (camera specifications are provided in Table 1).

The cameras are installed on a concrete plinth that is placed inside a plastic shelter box. An energetic module composed of two solar panels supplies electricity to the VBS, therefore the system can work autonomously and it is completely controlled by remote; both modules of the VBS acquire one image per hour. Since shadows and illumination changes can deeply affect the results of the ICC (Ahn and Box, 2010; Debella-Gilo and Käab, 2011; Giordan et al., 2016; Messerli and Grinsted, 2015; Piermattei et al., 2016; Travelletti et al., 2012), we manually selected for the processing one image per day acquired between 5 and 7 pm. During the period of the study, adverse weather conditions prevented the correct acquisition of some data, 21 of 25 and 20 of 25 images of the TELE and WIDE modules respectively were adopted for the processing.

During the same period, a commercial Ku-band (IBIS-L) ground-based SAR (GBSAR) was installed in the Planpincieux hamlet at the elevation of 1582 m. The mean distance from the glacier was approximately 2500 m. That positioning aimed at maximizing the parallelism between the LOS and the expected motion direction of the western icefall; also, a portion of the eastern tongue was visible from the GBSAR location. The radar acquired one image every 16 min and it collected more than 2200 images during the time span of the experimental setup.

Furthermore, a 1-m resolution digital elevation model (DEM) was available for the study, which was acquired by an airborne LiDAR survey in June 2014; during the LiDAR measurement, it was acquired also a high-resolution orthophoto of the glacier.

For further details concerning the site study and the datasets refer to Dematteis et al. (2017) and Giordan et al. (2016).

3. Methods

The method we propose enables estimating the glacier surface deformations measured by GBSAR and VBS devices. These instruments can detect different and complementary components of the motion vector; therefore, their results can be coupled to reconstruct the actual 3D surface kinematics.

Overall, the data processing is composed by three main procedures: (i) interferometric processing of the radar images; (ii) image cross-correlation (ICC) of the photographic data and (iii) georeferencing and coupling of the results of the two different instruments. The workflow of the method is depicted in Fig. 2.

3.1. Image cross-correlation

Digital image processing methodologies for measuring fluid motion fields were initially developed in the '90s for particle images velocimetry (PIV) (Willert and Gharib, 1991). Applications in earth sciences are more recent and they aim at estimating the deformations of natural active surfaces such as landslides or glaciers with the support of airborne (Debella-Gilo and Käab, 2011; Käab et al., 1998; Scherler et al., 2008) and ground-based images (Ahn and Box, 2010; Fallourd et al., 2010; Giordan et al., 2016; Messerli and Grinsted, 2015; Schwalbe and Maas, 2017; Travelletti et al., 2012; White et al., 2003). Similar approaches were also applied to non-visual images, e.g., radar amplitude maps (Casu et al., 2011; Strozzi et al., 2002) or interferometric maps (Raucoules et al., 2013).

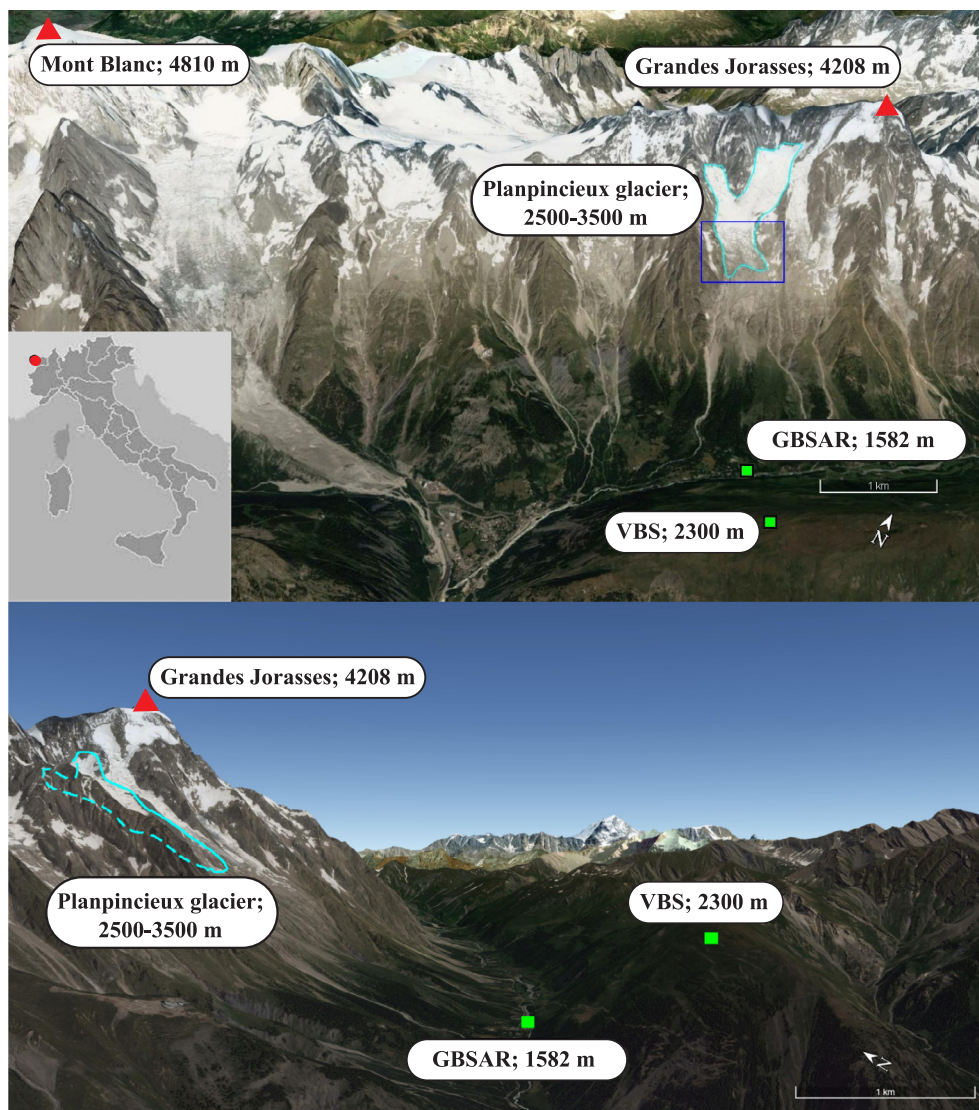


Fig. 1. Overview of the study area. The entire Planpincieux glacier is highlighted in sky blue and the lower part is surrounded by a blue box. The locations of the GBSAR and visual-based station are depicted as green squares.

Table 1
DSLR camera specifications.

	Camera model	Sensor	Resolution (px)	Focal length (mm)	ISO	Aperture lens
TELE	Canon EOS 600D	CMOS APS-C	3456 × 5184	120	200	f/8
WIDE	Canon EOS 100D	CMOS APS-C	5184 × 3456	297	200	f/8

Usually, the surface motion is evaluated by computing the cross-correlation between a template image and a searching image; the displacement is then estimated according to the location of the maximum correlation coefficient.

In this study, we computed the ICC in the frequency domain (often referred as phase correlation) via discrete Fourier transform (DFT) with the algorithm proposed by Guizar-Sicairos et al. (2008), which allows a cost-efficient sub-pixel offset estimation with a two-step matrix-multiply; that operation strongly limits the amount of zero-padding, thus reducing the computational costs. That matching algorithm runs two passes of the DFT, after the first pass it shifts the center of the

interrogation area according to the obtained pixel offset and then runs the DFT only in the neighbourhood of a limited subset of the data to achieve a finer accuracy. This solution reduces the loss of information caused by the displacement of the searching area that usually affects phase correlation algorithms (Thielicke and Stamhuis, 2014). Other methods, such as the minimum quadratic difference (Gui and Merzkirch, 1996), as well as the direct cross-correlation (Keane and Adrian, 1992) were considered but not applied because they have higher computational costs. Pust (2000) and Thielicke and Stamhuis (2014) estimated a difference of the computational time of two orders of magnitude for searching windows of 128 px between phase cross-correlation and direct cross-correlation.

The image processing chain adopted in our work consists in five main procedures: (i) manual images selection, (ii) illuminant correction, (iii) co-registration, (iv) pixel offset matching and (v) automate outlier detection. Fig. 3 we illustrates the steps of the ICC chain.

The first step concerned the manual selection of one image per day to obtain a sequence with homogeneous and uniform illumination and visibility conditions (Ahn and Box, 2010; Debella-Gilo and Käb, 2011; Giordan et al., 2016; Messerli and Grinsted, 2015; Piermattei et al., 2016). Therefore, we selected the images acquired when the sun did not lit the glacier surface directly and the diffuse illumination prevailed; in

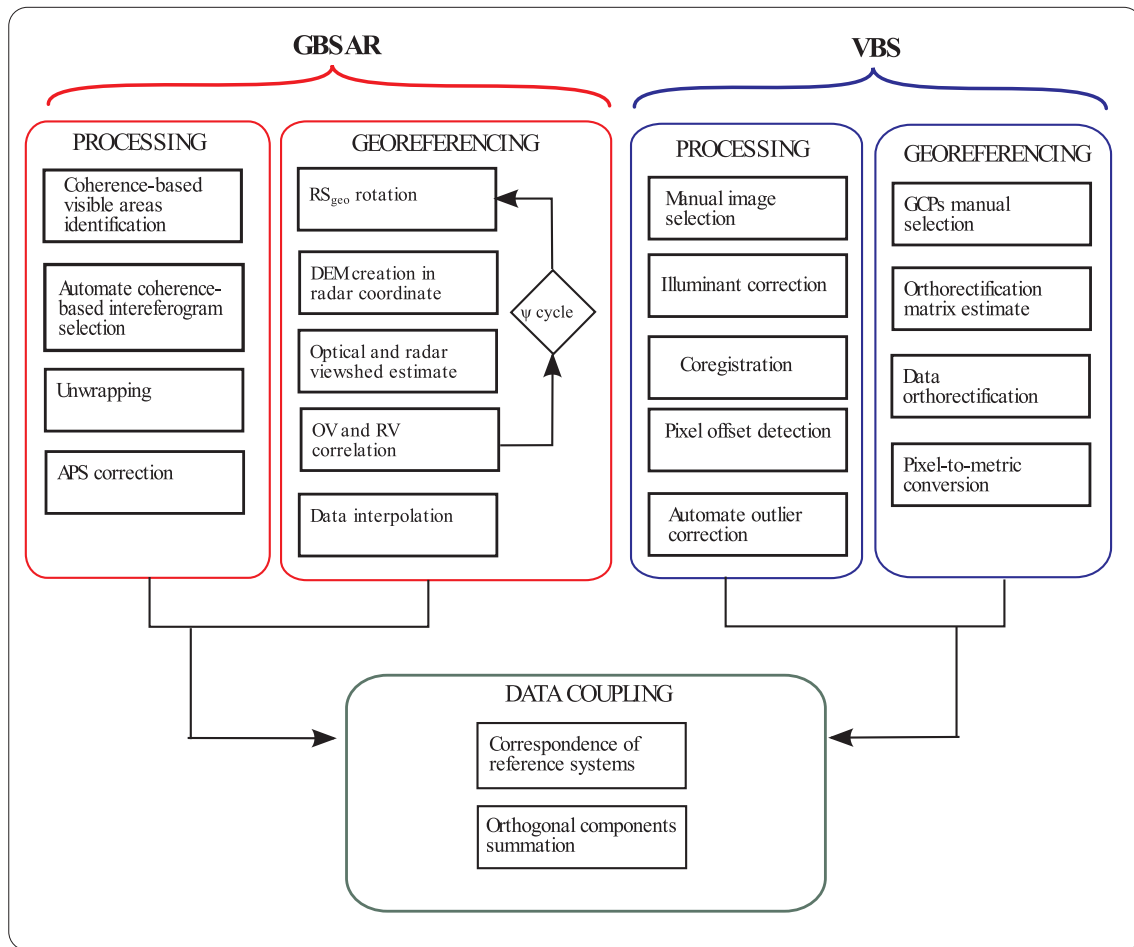


Fig. 2. Workflow of the proposed method for 3D data coupling.

particular, we used pictures taken during the late-afternoon hours (i.e., 5–7 pm). Thus, the shadow changes due to the surface roughness had a minimum impact on the cross-correlation computation.

Next, we estimated the scene illuminant with principal component analysis (Cheng et al., 2014) and then we subtracted it from the scene; thereby, we further make the illumination conditions more uniform among the different images.

In the third step, all the images were coregistered with respect to (w.r.t.) a common image (i.e., the first image of the stack) in order to correct possible movements of the camera or optical path changes. The matching algorithm was applied to an area of stable surface (i.e., bedrock) and the images were translated in the vertical and horizontal directions according to the obtained pixel offsets; most coregistration

absolute values ranged between 0 and 5 px, only in a few images the horizontal offset was approximately 10 px. Further analysis did not reveal image rotations.

The subsequent operation was the displacement assessment by means of the sequential ICC computation on chips identified by a sliding window. For the TELE images, we adopted a 256 px-side sliding window with 75% overlapping (i.e., sliding steps of 64 px), while for the WIDE images the window size and sliding step were of 128 px and 64 px. Thereby obtaining a motion field mapped on a 64 px-side grid for both cases.

Finally, we dealt with the refinement of the results. Multiple sources of error can intervene during the processing (i.e., shades and shadows, non-optimal illumination, image defocusing or morphological surface

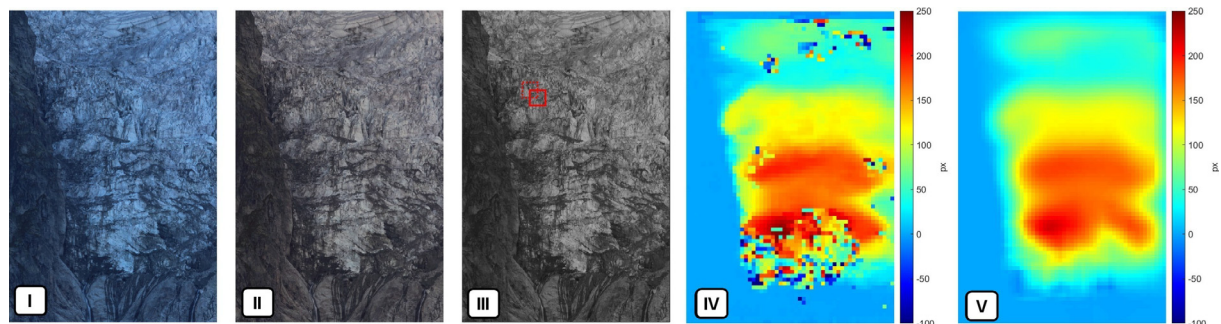


Fig. 3. Step sequence of the image processing method: (i) the raw image is acquired, (ii) the illuminant is removed, (iii) the image is converted in grey scale and coregistered, then (iv) the ICC is computed with the sliding window obtaining the raw results, finally (v) the automate outlier detection and removal is operated. The picture was acquired by the TELE module on 06/09/2015 at h19:00.

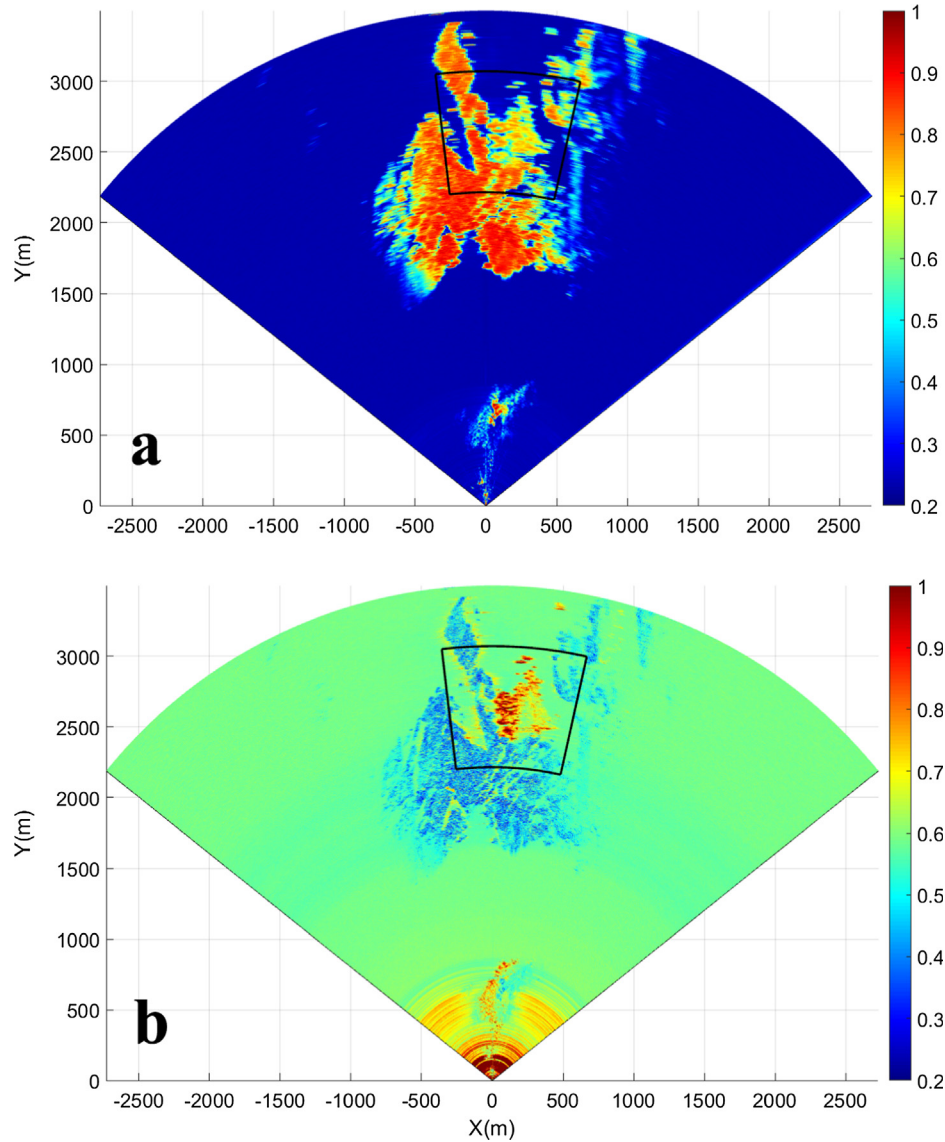


Fig. 4. (a) Map of mean temporal coherence ($\bar{\gamma}$) and (b) map of amplitude dispersion (DA) of the backscattered signal of the GBSAR. The investigated area is included in the black box; the glacier area is characterized by high values of DA, while bedrock displays lower values. Low values of $\bar{\gamma}$ are associated to areas in shade.

changes) often difficult to detect and evaluate separately (Gabrieli et al., 2016). Actually, correcting the correlation anomalies is a crucial step to obtain reliable results. Various methods have been proposed to this aim, some studies adopted optimized methods to remove the outliers directly during the correlation computation (Ahn and Box, 2010; Hart, 1998), while other approaches rely on empirical or statistical analysis in the post-interrogation phase (Debella-Gilo and Käb, 2011; Giordan et al., 2016; Westerweel and Scarano, 2005). We opted for the normalized median test proposed by Westerweel and Scarano (2005); it consists in the analysis of the parameter r_0 defined through the following equation

$$r_0 = \frac{|U_0 - U_m|}{r_m + \epsilon} \quad (1)$$

where U_0 is the investigated datum, U_m is the median of the 5×5 neighbours of U_0 , $\{U_1, U_2, \dots, U_{24}\}$, excluding U_0 from the computation, r_m is the median of the residuals defined as $r_i = |U_i - U_m|$, with $U_i = \{U_1, U_2, \dots, U_{24}\}$, and ϵ is an offset introduced in case r_m was too close to zero. Westerweel and Scarano (2005) found out that a value of $r_0 > 2$ corresponds approximately to the 90th-percentile of the residuals, whatever the data values or distributions are and it is rather insensitive

to the window size. That means that the method can be considered a “universal outliers’ detection”. They also suggest the value of 0.1 for the ϵ term.

After outliers rejection, missing data were estimated by Natural Neighbour interpolation (Sibson, 1981) and a low-pass filter was applied to the resulting maps for taking into account the sliding window overlapping; the averaging filter had 7×7 and 3×3 side for the TELE and WIDE images respectively.

3.2. Interferometry

TRI proved to be a valuable tool in the monitoring of glaciers (Allstadt et al., 2015; Noferini et al., 2009; Riesen et al., 2011). In our study, we performed the interferometric processing to detect the surface motion of the glacier along the LOS direction.

Radar interferometry is the process that analyses the differential phase between two different images, aiming at estimating the displacement occurred during the two acquisitions. For the sake of completeness, the basic theory of interferometry is briefly described in the following. For a more exhaustive explanation of the SAR interferometry we refer to Bamler and Hartl (1998) and Rosen et al. (2000); while in

Caduff et al. (2015); and Monserrat et al. (2014) it is possible to find recent reviews of the TRI literature.

Let consider the electromagnetic wave scattered by a single target; the distance covered by the emitted signal is $R = n\lambda + \frac{\lambda}{2\pi}\phi$, where λ is the wave length and ϕ is the phase. Therefore, a motion occurred between two acquisitions is equal to

$$R_2 - R_1 = \frac{\lambda}{4\pi}(\phi_2 - \phi_1 + 2n\pi) = \frac{\lambda}{4\pi}(\Phi + 2n\pi) \quad (2)$$

where $2n\pi$ belongs to the intrinsic ambiguity of the phase periodicity (i.e., phase wrapping).

Actually, in the cases when the radar is maintained in the same position (zero baseline), the interferometric phase is given by the sum of different terms, that is

$$\Phi = \varphi_d + \varphi_a + \varphi_s \quad (3)$$

where φ_d is the phase directly related to the displacement of the target, φ_a is due to the atmospheric condition change (often named atmospheric phase screen, APS), which alters the optical path of the electromagnetic wave, and φ_s is the term including thermal noise and phase change caused by the variation of the scattering properties (Luzi et al., 2004). Accordingly, some data processing is necessary to determine the contribute of the different terms and correctly estimate φ_d .

In our work, we discriminated the areas illuminated by the radar signal from the shadowed regions. To this aim, points displaying a mean temporal coherence $\bar{\gamma}$ lower than an empirical threshold (i.e., $\bar{\gamma} < 0.55$) were masked out (Fig. 4). In other studies, the selection of the scattering points was driven by an amplitude dispersion- (DA) based criterion (Ferretti et al., 2001). Ice metamorphisms and snow deposition introduced strong changes of the dielectric properties of the target, causing high variability of the scattered signal amplitude and yielding substantial values of DA. In fact, the DA observed on the glacier area displayed values ranging between 0.4 to more than 1 (Fig. 4). Therefore, a DA-based criterion to select shaded areas was not suitable.

The second operation aimed at resolving the phase ambiguity by applying a 2-D unwrapping algorithm (Costantini, 1998). Such algorithm introduced different phase offsets among not connected regions. Therefore, it was necessary to manually identify the main compact areas and then subtract the corresponding phase offsets. That operation further reduced the unwrapping errors and significantly improved the result accuracy and precision.

Subsequently, the interferograms affected by strong decorrelation were discarded by the temporal stack of the interferograms, thereby reducing errors due to noise or residual phase wrapping. The huge amount of data made necessary to establish an automate criterion to reject decorrelated interferograms; therefore, we established an empirical threshold of the mean spatial coherence $\langle \gamma \rangle < 0.65$ to identify the interferograms to be discarded (Dematteis et al., 2017).

Eventually, we dealt with the APS removal. The glacier was located 1200 m higher than the GBSAR positioning and it was characterized by significant elevation changes in the investigated area. As a consequence, the atmospheric variables, which drive the optical path length of the electromagnetic wave, might significantly vary and thus affect the measurement of the interferometric phase. Hence, being that for stable areas we expected $\varphi_d = 0$ and $E\{\varphi_s\} = 0$ (i.e., white noise), the value of φ_a was estimated with a polynomial regression of degree two of the interferometric phase observed on 5190 points, corresponding to the stable areas (i.e., points with $DA < 0.35$); the elevation coordinates were introduced as an explicit variable to take into account the topographic influence on the atmosphere (Dematteis et al., 2017; Iglesias et al., 2014; Noferini et al., 2005).

The results of the interferometric process are represented on the radar maps with a constant range resolution (i.e., 0.43 m). Conversely, the azimuth resolution varies linearly with the range and it is approximately 11 m @2500 m. As a result, the radar data are mapped on a grid with non-uniform resolution.

3.3. Data georeferencing and coupling

TRI and ICC provide different and complementary motion components that can be merged to obtain a 3-dimensional representation of the surface motion. The necessary conditions to couple the different data is that they must be represented in the same coordinate system (CS). Therefore, (i) the reference axes must be parallel and (ii) the map resolutions of the data must be equal.

The former condition is automatically achieved if the two measurement systems observe the target area with the same LOS. Conversely, when the systems acquire from different spots, their CSs must be geometrically transformed in order to make their axes parallel. In addition, in this second case, the motions measured by the different systems are not orthogonal, thus it is necessary to identify only the linearly independent components to obtain the actual 3D motion vector. The second necessary condition can be achieved through the application of spatial interpolation on a regular grid. Therefore, it is required the support of a DEM on which the data are projected; in our case, we used a 1-m resolution DEM. Finally, the georeferencing allows identifying the corresponding data with the same spatial coordinates.

Hereafter we will refer to CS_{geo} as the 3D geographic CS in UTM 32 T (WGS84) coordinates (X, Y, Z); CS_v stands for the 2D CS of the visual images, expressed in pixel coordinates (u, v); and CS_r for the 2D radar CS with local Cartesian coordinates (x, y^*). Here and in the following the apex $*$ is used to highlight that the related coordinates are not horizontal.

3.3.1. Photographic images

A transformation matrix was computed using an image orthorectification procedure to obtain a correct georeferencing of the ICC displacement map. The photographic images were handled through the orthorectification process that allowed projecting the photographs on a 3D surface (i.e., the DEM) adjusting the deformations due to topography and perspective, thereby the scale of the image was constant when it was projected in the new CS. The principle of the image orthorectification is based on the pinhole camera model, according to which, each point in the real 3D world is projected in the 2D image plane by a straight line passing through the ideal centre of the camera.

It is well known (Luhmann, 2009) that the necessary camera external and internal parameters to operate the image orthorectification can be estimated by the knowledge of the coordinates in the real 3D world and in the CS_v of at least six corresponding points within the observed area. The most common approach consists in measuring the coordinates of a set of ground control points (GCPs) clearly recognizable within the photograph by means of GPSs or other topographic instruments; sometimes, this is achieved by placing artificial targets within the study area (Aguilar et al., 2008; Messerli and Grinsted, 2015; Schwalbe and Maas, 2017; Travelletti et al., 2012).

Instead, our work aimed at measuring surface deformations purely from remote, thus avoiding any access in the studied area, including the installation of artificial GCPs. Therefore, we manually selected a set of 38 and 35 recognizable features in the TELE and WIDE images respectively, such as bedrock cracks, pinnacles or sharp edges (Messerli and Grinsted, 2015; Piermattei et al., 2016). We had available TELE photographs taken on July 2014 (i.e., contemporary to the DEM and orthophoto acquisitions), therefore we could also identify features of the glacier morphology, such as crevasses and seracs, thus allowing a more uniform GCP distribution on the scene. For the WIDE images, we recognized features only on the stable bedrock surrounding the entire glacier (Fig. 5). The geographical coordinates were extracted from the orthophoto and the DEM acquired during the 2014 LiDAR survey.

We performed the image orthorectification using the open-source Matlab™ toolbox, ImGRAFT (Messerli and Grinsted, 2015); the algorithm estimates the camera parameters in order to minimize the squared projection error of the GCPs.

Eventually, the transformation matrix was applied to the

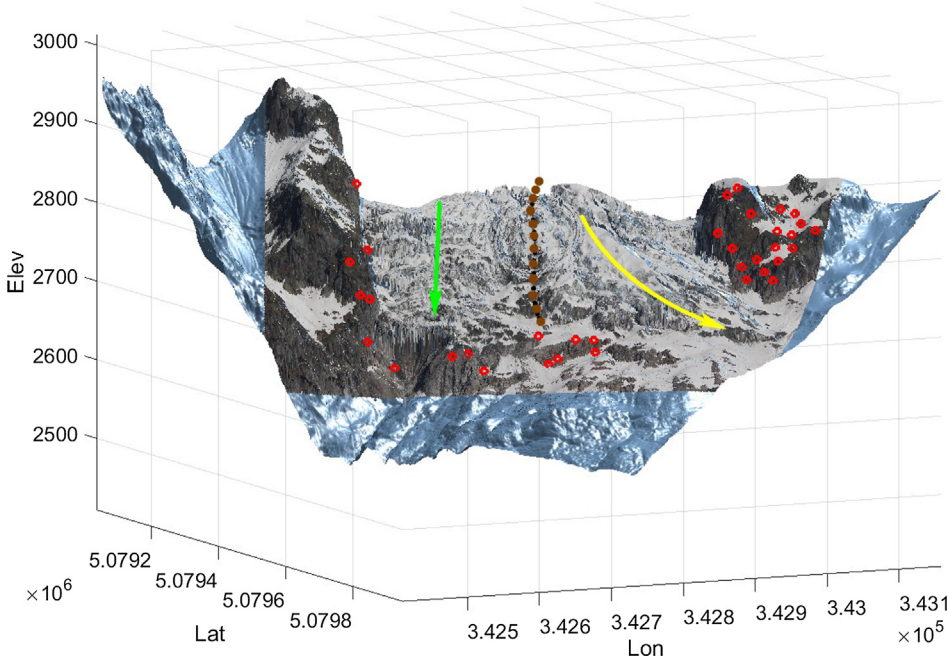


Fig. 5. WIDE image orthorectified and re-projected onto the DEM. GCPs are reported as red circles. The camera position is frontal to the western tongue (green arrow), thus the vertical motion component prevails. Conversely, the eastern tongue (yellow arrow) flows diagonally w.r.t. the LOS. A ridge of bedrock, highlighted by brown dots, separates the two tongues.

displacement maps obtained during the ICC processing and then the motion expressed in pixel was converted to metric units. To attain that, we computed the ground sampling distance (GSD) projected on the plane orthogonal to the LOS.

$$GSD = 2D \cdot \tan\left(\arctan\left(\frac{S/2f}{R}\right)\right) \quad (4)$$

where D , S , R and f are respectively the target distance, the sensor size, the images resolution (in px) and the focal length of the optical system.

According to Eq. (4), the GSD increased linearly with the distance and it varied across the images with values ranging between approximately 5.0–5.9 cm and 12.4–14.5 cm for the ZOOM and WIDE images respectively. Hence, considering that the tiles of the motion map had a side of 64-px, the mean tile sizes were roughly 3.5-m side and 8.7-m side respectively for the TELE and WIDE data. At each tile was associated a single value of surface motion.

We remark that the GSD computation in Eq. (4) corresponds to the pixel footprint on a plane orthogonal to the LOS and that the only variable is the distance D , while the other terms are fixed parameters. Therefore, the pixel-to-metric conversion (often called scaling) is rather insensitive to the possible morphological changes of the surface, because the distance change is likely to be negligible w.r.t. D ; e.g., a hypothetical distance variation of 10 m would yield a relative error of 0.2%. By contrast, the estimate of the adjusted GSD in accordance with the incident angle of the optical ray on the surface is subjected to significant errors when dealing with not updated DEMs or in situations that involve high morphology change (Gabrieli et al., 2016; Messerli and Grinsted, 2015; Travelletti et al., 2012).

3.3.2. Interferometric data

For what concerns the georeferencing of the radar data, a common procedure consists in identifying on the radar maps a set of artificial GCPs with known coordinates, such as passive (Marambio et al., 2009) or active (Lingua et al., 2008) corner reflectors (CRs), in order to estimate the unknown transformation parameters and then interpolate on the DEM with the least squared method. We propose a different solution that can be adopted in cases where neither the installation of artificial CRs nor the identification of high reflective areas with known coordinates are feasible, a situation quite occurring when monitoring inaccessible areas.

Let first describe the characteristics of the radar maps, whose Cartesian coordinates are $(x = r \cos \alpha, y^* = r \sin \alpha)$, where α is the azimuth angle and r is the range. Actually, given the vertical aperture of the radar beam and the elevation angle of the LOS that can be non-null, y^* is the curvilinear surface $y^* = \sqrt{y^2 + z^2}$, where z is the height of the target w.r.t. the radar position and y is the horizontal projection of y^* . Therefore, y and z must be determined for correctly georeferencing the radar data in a 3D space.

The surface in geographic coordinates $f(X, Y^*) = Z$ is known, where Y^* is the equivalent of y^* ; f is well defined as X and Y^* are linearly independent. Hence, it is possible to estimate z with Natural Neighbour Interpolation (Sibson, 1981) by evaluating $f(x, y^*) = z$; the y coordinate is estimated consequently with $y = \sqrt{r^2 - x^2 - z^2}$.

The method above can be applied only if the axes origins of CS_r and CS_{geo} coincide and the respective axes are parallel. Therefore, when this condition is not fulfilled, it is first necessary to rotate the geographical coordinates according to the angle ψ included between the radar LOS and the geographic north.

In optimal contexts, ψ can be estimated by measuring the coordinates of the radar edges by means of GPSs. We propose an alternative method that is suited in situations where accurate GPS measurements are not available and ψ is only approximately assessed or even unknown; moreover, we will explain that the uncertainties are comparable to the GPS-based method, or even lower especially for long range measurements.

Let consider the optical viewshed (OV) (i.e., the visible geographical area) from the radar position that can easily be computed from the DEM (Messerli and Grinsted, 2015), actually it corresponds with the area illuminated by the radar microwave bundle. The areas visible by the radar return a high amplitude backscattered signal (Tapete et al., 2013); therefore, the “radar viewshed” (RV) can be estimated as the areas on the radar maps with the mean amplitude greater than an empirical threshold (Fig. 6). The amplitude is expressed in dB w.r.t. the environmental noise.

Consequently, the OV and RV differ mainly for the map resolution where they are projected. The method we developed for estimating ψ consists in varying the value of ψ within a cycle whose each iterate is composed by three steps: (i) first, the DEM coordinates are rotated according to the current value of ψ (being (x_r, y_r, z_r) the GBSAR positioning in UTM coordinates)

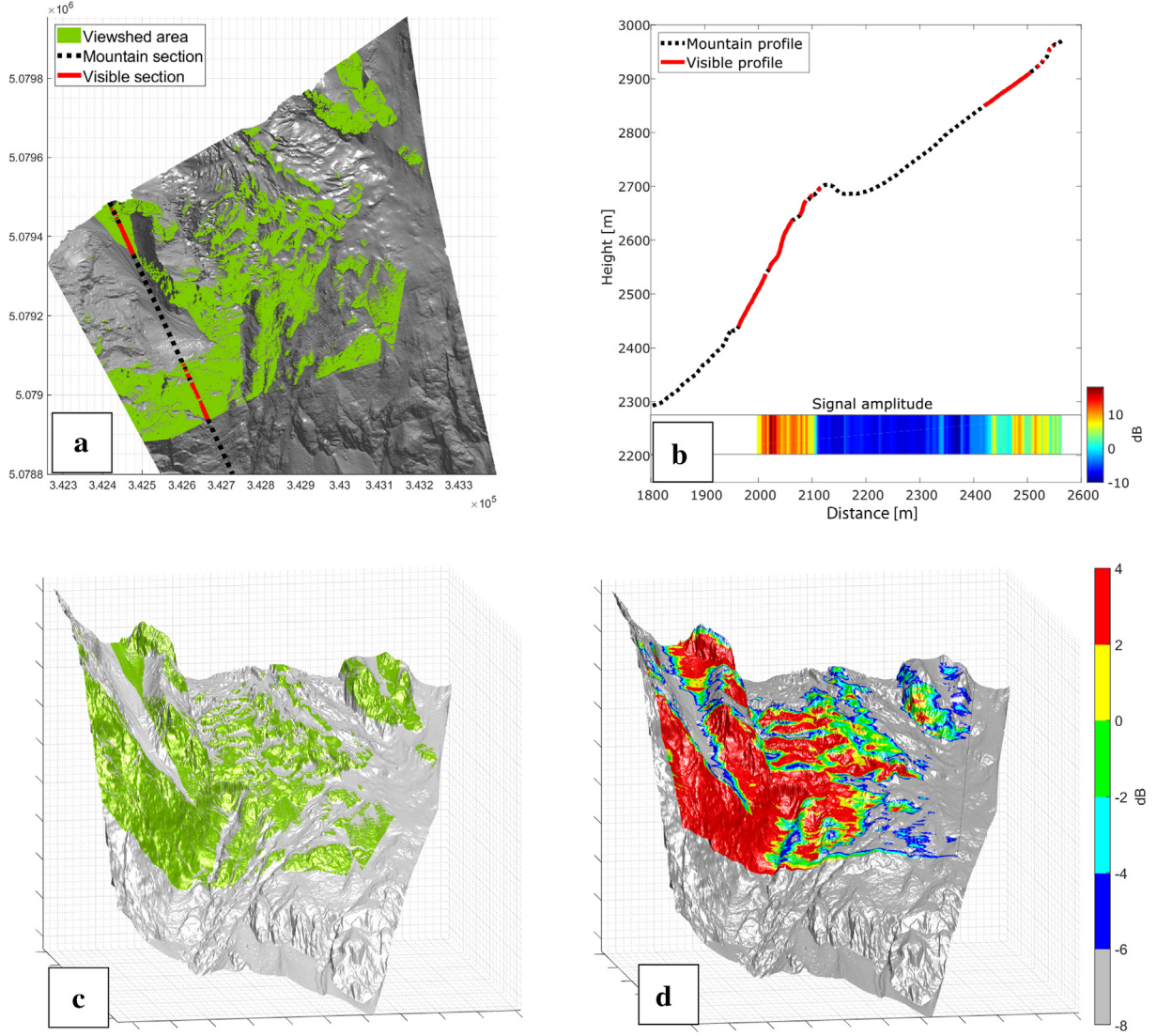


Fig. 6. (a) The optical viewedshed is depicted in green on the DEM. The solid red line is the visible part of the slope section (black dashed line) from the GBSAR location. (b) The mountain profile of the selected section is represented (black dashed line) with the visible part in red (solid line). In the lower part is reported the signal amplitude corresponding to the DEM section. The high amplitude values in correspondence of the visible profile are evident. In the blank part, the amplitude was not processed. (c) Maps of optical viewedshed and (d) mean amplitude map of the radar backscattered signal; the different empirical thresholds adopted to estimate the viewedshed correlation are depicted.

$$\begin{cases} X'(\psi) = X \cos(\psi) + Y \sin(\psi) - x_r \\ Y'(\psi) = X \sin(\psi) - Y \cos(\psi) - y_r \\ Z' = Z - z_r \end{cases} \quad (5)$$

(ii) Second, the RV map is interpolated (Natural Neighbour Interpolation) on the DEM in order to have the RV_{interp} and OV with the same uniform spatial resolution.

$$g(x, y^*) = RV \mapsto g(X'(\psi), Y'(\psi)) = RV_{interp}(\psi) \quad (6)$$

(iii) Third, we compute the spatial correlation between the $RV_{interp}(\psi)$ and OV maps.

$$\rho = corr[OV, RV_{interp}(\psi)] \quad (7)$$

The best estimate of the actual rotation angle is assumed to be the ψ value that maximizes the correlation coefficient ρ . The procedure to determine ψ can cease according to a heuristic stopping rule (e.g., small ρ improvements). Once determined the angle ψ , the correct axes rotation of the geographical coordinates is computed with Eq. (5), in order to fulfill the condition of having the corresponding axis parallel and the axes origin coincident w.r.t. the CS_r ; thereafter, the radar data and

results are interpolated on the DEM with Eq. (6).

In Fig. 6 we report the maps of OV and RV, highlighting different possible choices of the amplitude threshold for the correlation assessment.

3.3.3. Data coupling

The last step of the processing concerns the data coupling. The actual 3D motion vector $\mathbf{v} = [v_x, v_y, v_z]^T$ is represented into a local right-handed coordinate system with the following convention: v_x, v_y are the horizontal components, respectively rightward and incoming increasing, while v_z is the vertical downward-increasing component. With this convention, v_y is mainly provided by the GBSAR measurements, while v_x, v_z are mainly provided by the VBS. Therefore, their respective vectors can be written in their own CSs as

$$\begin{aligned} \mathbf{h}^r &= [0, h_y^r, 0]^T \\ \mathbf{h}^v &= [h_x^v, 0, h_z^v]^T \end{aligned} \quad (8)$$

Eq. (8) explicitly expresses that they measure only partial components of the actual 3D motion vector. As previously mentioned, if the

radar and photographic data lie within a space where the corresponding axis are parallel, the three components are mutual perpendicular, thus they represent directly the three components of \mathbf{v} . On the other hand, when this condition is not satisfied, it is necessary to carry out a geometrical transformation in order to rotate one CS and make the correspondent axes parallel; the choice of the CS to be rotated is arbitrary.

It must be considered that in general, when a vector is rotated, all the three components assume non-null values; but for reconstructing the 3D motion only the linearly independent (i.e., orthogonal) components must be summed.

Therefore, applying the rotation matrix \mathbf{R} to a generic motion vector \mathbf{h} , we have

$$\mathbf{R}\mathbf{h} = \mathbf{h}' = [h'_x, h'_y, h'_z]^T \quad (9)$$

It is worth noting that the components measured by each device correspond to the actual components of \mathbf{v} in their own CS; i.e., in the CS_v : $v_x = h_x$ and $v_z = h_z$, while in the CS_r : $v_y = h_y$. Therefore, if it rotated CS_r , the component $v_y = h'_y$, while the other two components of \mathbf{h}' are not considered to reconstruct \mathbf{v} because their contribution is already present in h'_x and h'_z . Thus, in CS_v the motion vector is $\mathbf{v} = [h'_x, h'_y, h'_z]^T$. Following the same principle, if the CS_v was rotated, in the CS_r we would have $\mathbf{v} = [h'_x, h'_y, h'_z]^T$. Finally, once that the three motion components are obtained in a generic CS, \mathbf{v} can be reported in CS_{geo} adopting Eq. (9). Fig. 7 shows a scheme of the rotation in the specific case where the radar vector is transformed in CS_v .

In principle, a rotation in three dimensions is fulfilled around a reference axis, whose versor does not change during the transformation. In practice, the reference axis is usually unknown and it is necessary to operate a sequence of elemental rotations around the three canonical axes, conventionally corresponding to the geographical axes (Cai et al., 2011).

This solution has the advantage that, being the data georeferenced, the angles (ψ, θ, ϕ) are known for every points within the interested areas, where ψ is the angle included between the LOS and the geographical north, θ is the LOS elevation w.r.t. the horizontal plane and ϕ is the rotation of the x-axis w.r.t. the horizontal plane, which is usually assumed zero. Therefore, Eq. (9) is applied to the motion vectors of each single georeferenced point, according with the corresponding known angles, therefore, \mathbf{R} is a combination of elemental rotations in three dimensions.

It is worth noting that the application of a sequence of rotations

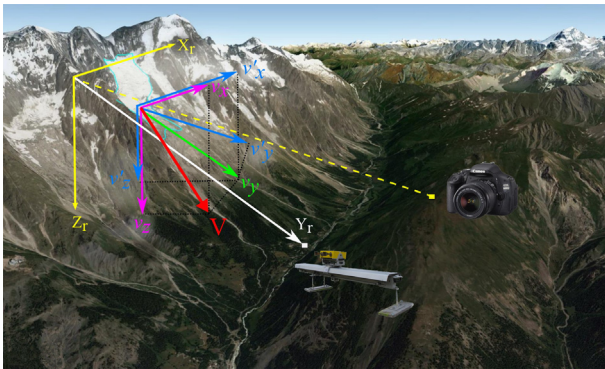


Fig. 7. Scheme of the vector transformation in the specific case in which the velocity vector measured by the radar is rotated in the coordinate system of the VBS. The components v_x, v_z measured by the VBS are represented in magenta and the respective axes X_v, Z_v orthogonal to the LOS (yellow dashed line) of the VBS are in yellow. The green arrow depicts the component v_y measured by the GBSAR; the Y_r axis of the CS_r is colored in white and it coincides with the LOS of the GBSAR. The blue arrows indicate the components v'_x, v'_y, v'_z formed by the decomposition of v_x when it is rotated in CS_v . The actual velocity vector $\mathbf{V} = [v_x, v_y, v_z]$ is drawn in red. The white and yellow squares are the locations of the GBSAR and VBS respectively.

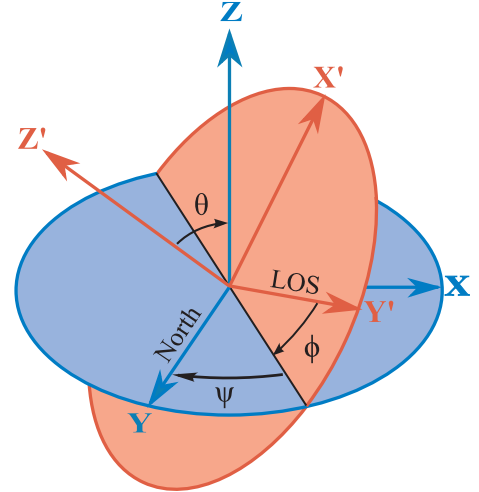


Fig. 8. Euler angles yaw, pitch and roll (ψ, θ, ϕ) between a generic coordinate system $CS'(X', Y', Z')$ and the canonical axes corresponding to the geographic coordinate system $CS_{geo}(X, Y, Z)$. The red and blue planes are the horizontal planes $(X'Y', XY)$ of the CS' and CS_{geo} respectively. The sequence of the rotation angles to make coincide the CS' with CS_{geo} is: (i) $\mathbf{R}_y(\phi)$, (ii) $\mathbf{R}_x(\theta)$, (iii) $\mathbf{R}_z(\psi)$. The inverse rotation order transform the CS_{geo} in CS' .

around different axes is not commutative in three dimensions. To evaluate the unique sequence of rotations, we can consider (ψ, θ, ϕ) as the Euler angles *yaw*, *pitch* and *roll*. With the present axes convention, the angle sequence for rotating the local CS in the CS_{geo} is known, i.e., (i) rotation around the y-axis of the *roll* angle ϕ , (ii) rotation around the x-axis of the *pitch* angle θ , and (iii) rotation around the z-axis of the *yaw* angle ψ (Cai et al., 2011) (Fig. 8).

Therefore, the transformation introduced in Eq. (9) is explicitly expressed as the composite rotation given by the matrix multiply of six elemental rotations expressed by the following formula

$$\mathbf{R}\mathbf{h} = \mathbf{R}_y(\psi)\mathbf{R}_x(\theta)\mathbf{R}_z(\phi)\mathbf{R}_x(\phi_v)\mathbf{R}_x(\theta_v)\mathbf{R}_y(\psi_v)\mathbf{h} = \mathbf{h}' \quad (10)$$

where \mathbf{R}_i indicates the rotation axis, and (ψ, θ, ϕ) are the Euler angles of the two CSs. That is, \mathbf{h} is initially rotated from the first local CS in CS_{geo} and subsequently is transformed from CS_{geo} to the second local CS applying the inverse sequence of Euler rotations. We remind that the sign of the rotation angles for a right-handed coordinate system is positive for clockwise rotations and negative for counter-clockwise rotations.

4. Sources of error

The uncertainties that affected the results of our work mainly originated from two sources: (i) data processing and (ii) georeferencing.

To the former group belong the errors of the motion measurement carried out by the two single devices (i.e., VBS or GBSAR). We evaluated the measurement uncertainties by investigating the cumulative motion observed in selected areas corresponding to stable surfaces, i.e., bedrock (Dematteis et al., 2017). Since we expected a null cumulative motion, we associated the average cumulative motion to the measurement accuracy, while its variability, estimated as the mean absolute deviation (MAD), was associated to the precision. The results of the error analysis are presented in Table 2. Because the results of the ICC methods are expressed in pixel units, we converted the values in metric displacement, adopting an approximate GSD of 5.5 cm and 13.6 cm for the TELE and WIDE modules respectively (i.e., the GSD corresponding to the glacier average distance).

From the error analysis emerged that the performances of the ICC were comparable with those obtained in previous studies (Ahn and Box, 2010; Schwalbe and Maas, 2017; Travelletti et al., 2012). The slightly

Table 2

Estimates of measurement accuracy and precision. The accuracy is computed as the mean cumulative motion on stable areas, while the precision is the mean absolute deviation. The values are computed on the 24 days-cumulative motion. H, V stand for horizontal and vertical directions respectively, for the TELE and WIDE images.

	Accuracy (cm)	Precision (cm)
TELE H	−0.23	0.78
TELE V	0.45	0.89
WIDE H	−0.72	1.62
WIDE V	−0.02	0.58
GBSAR	−1.37	4.56

worse precision of the GBSAR measurements can be ascribed to unresolved unwrapping errors. However, the relative precision is of the order of less than 1% of the maximum cumulative motion.

The second major error source belongs to the georeferencing uncertainty. For what concerns the image orthorectification, we carried out a 1000-iterations Monte Carlo simulation, randomly dividing the selected GCPs in two sets composed by one-half of the GCPs. With the former one, we calibrated the image orthorectification, while with the other group we estimated the mean absolute error (MAE) between the original location of the GCPs and the projected position that minimizes the squared error during the camera parameter bundle adjustment (Travelletti et al., 2012). We obtained mean MAEs of 21 px and 12.5 px for the TELE and WIDE images respectively. Using the whole set of GCPs we had MAEs of 18 px and 12.4 px. Converting these values in metric units, we obtained a georeferencing error of approximately 0.99 m and 1.69 m (TELE and WIDE images respectively); similar uncertainties were obtained by (Liu et al., 2007). Finer results can be achieved by measuring the GCP coordinates with GPSs systems (Messerli and Grinstead, 2015) or performing multi-views photographic acquisition (e.g., stereoscopy, SFM) (Piermattei et al., 2016).

The radar data georeferencing was attained with the procedure described in Section 3.3.2. The method is based on the considerations that the RV and OV coincide and that the RV corresponds to the areas with high amplitude scattered signal. Both assumptions are strongly plausible, but the correspondence between RV and signal amplitude might suffer the arbitrary choice of the empirical amplitude threshold defined to detect the visible areas. In Fig. 9, we show the correlation coefficients computed between the OV and RV w.r.t. different rotation angles and thresholds (Fig. 6d depicts the areas on the DEM corresponding of different amplitude thresholds); it emerged that the proposed method is quite insensitive to the choice of the amplitude threshold. In fact, all the ψ estimates that maximized the correlation coefficient ρ obtained with different amplitude thresholds, lay within a range of $\pm 0.1^\circ$. Therefore, we judged the best estimate, $\hat{\psi}$, the angle that provided the absolute maximum value of ρ (i.e., $\hat{\psi} = 24.35^\circ \pm 0.1^\circ$). A rotation angle change of $\pm 0.1^\circ$ is equivalent to an azimuth uncertainty of ± 4.36 m at a distance of 2500 m, while the range uncertainty is negligible.

We compared the precision and accuracy of the proposed method with the rotation angle assessment through the measurement of the radar edges coordinates. With the aid of GPSs, we carried out the measurements of the positions of two couples of points on the GBSAR rail, and consequently we derived the orientation of the instrument. The obtained estimates of ψ are reported in Table 3 together with the corresponding uncertainty being the error ranging between 0.5 and 1 cm of each horizontal coordinate of the GPSs measurements.

From that comparison, it emerged that the value of the rotation angle evaluated with the correlation method is approximately the same resulting from the GPSs method, but in the latter case the uncertainty was approximately seven times greater. The geometric schemes of the two methods are different, and the measurement of the edge positioning with GPSs can amplify the error of the measurement. However,

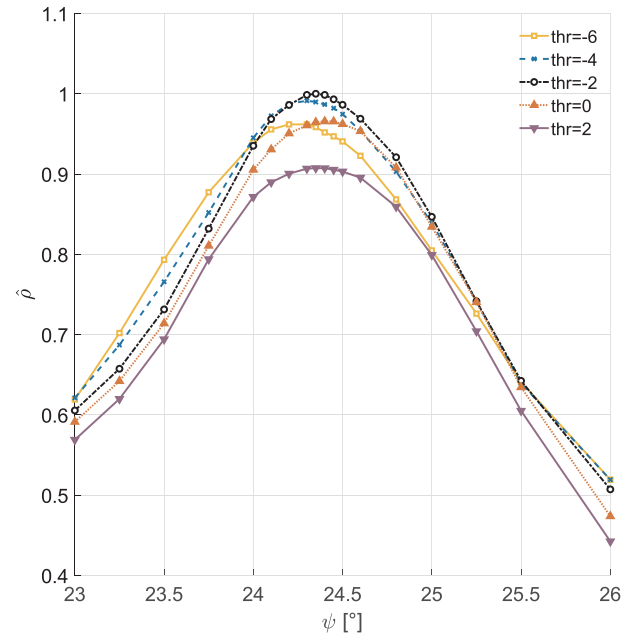


Fig. 9. Curves of normalized correlation coefficient between the visual and radar viewsheds vs. the rotation angle of the visual viewshed. The radar viewsheds were estimated adopting different thresholds of the mean amplitude signal in dB.

Table 3

Rotation angles and corresponding uncertainties. GPS1 and GPS2 stand for the two measurements performed with the GPSs to estimate the rotation angle, GPSmean is the average of the two values. AngCorr indicates the angle assessment obtained with the correlation between radar and visual viewsheds.

	θ	Metric uncertainty
GPS1	$24.70^\circ \pm 0.3^\circ$	13.35m (azimuth) @2500 m
GPS2	$24.22^\circ \pm 0.7^\circ$	29.93m (azimuth) @2500 m
GPSmean	$24.46^\circ \pm 0.75^\circ$	32.77m (azimuth) @2500 m
AngCorr	$24.35^\circ \pm 0.1^\circ$	4.36m (azimuth) @2500 m

Table 4

Map resolutions and uncertainties at the average distances sensor-to-glacier; i.e. 2500 m the GBSAR and 3800 m the VBS. The photographic images have the same resolution and uncertainty values in azimuth and range. The GBSAR range error is negligible.

	Azimuth resolution (m)	Azimuth uncertainty (m)	Range resolution (m)	Range uncertainty (m)
VBS tele	3.51	0.99	3.51	0.99
VBS wide	8.65	1.68	8.65	1.68
GBSAR	11	4.36	0.43	–

presently, to our knowledge, this is the common method used to estimate the orientation angle from remote. We proposed an alternative approach that can reduce the uncertainties of the georeferencing.

In Table 4 we summarize the values of the map resolutions of the different systems and the corresponding georeferencing errors. All the values were of comparable size of the order of a few metres; therefore, we considered the georeferencing uncertainties adequate for the data coupling.

5. Results

In this section, we report the results obtained by the single remote sensing devices, i.e., the VBS and the GBSAR; these data represent partial components of the surface motion. The actual 3-dimensional

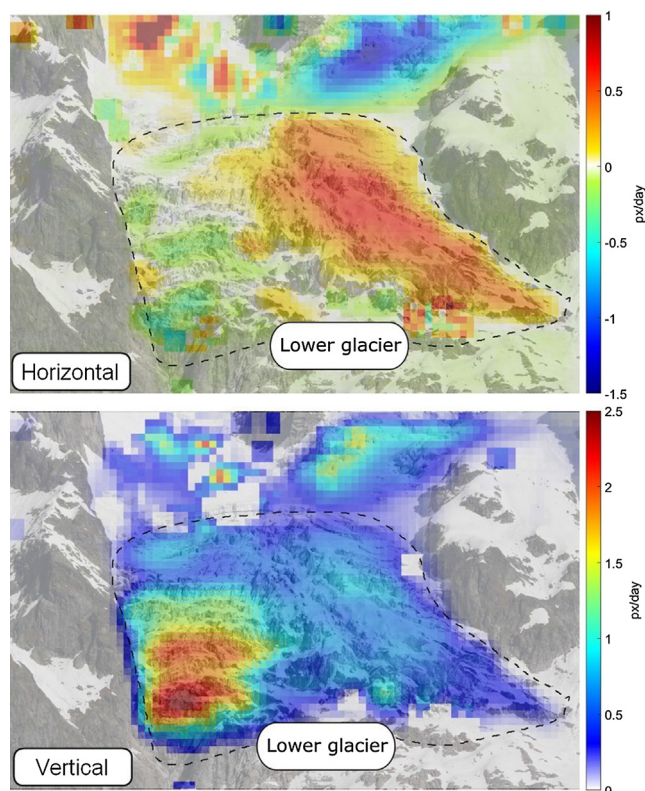


Fig. 10. Upper image: map of the horizontal component of the velocity obtained by ICC of the WIDE images; positive values represent rightward motion, while negative represent leftward movement. Lower image: map of the vertical component of the velocity obtained by ICC of the WIDE images. A dashed line surrounds the lower portion of the glacier (i.e., the investigated part).

kinematics is achieved by the coupling of the two single results, and it is shown below.

In Fig. 10, we present the horizontal and vertical components of the velocity of the WIDE images, as they are obtained by the ICC processing; the raw results of the ICC are expressed in px/day because the metric conversion is possible only after the image orthorectification.

Fig. 11 depicts the mean daily motion measured by the GBSAR (in rad/day). It is evident the difference of the data representations between the two processing methods.

The actual 3-dimensional surface kinematics was produced by the coupling of the visual and interferometric data. Fig. 12 shows the daily velocity map projected on the orthophoto. The colours of motion field represent the module of the velocity, while the arrows indicate the direction and versus; the arrow length is proportional to the module.

The 3D results can be achieved only in the areas visible by both the devices. Therefore, the blank areas correspond to the points in shade from the perspective of the devices; in particular, due to its location the GBSAR had a limited view of the eastern tongue. Note that the 3D motion is mostly influenced by the v_z and v_y components that show a similar pattern; v_x is almost irrelevant for it has quite low values.

The velocity field was estimated with a daily frequency allowing the precise observation of the evolution of the actual surface kinematics. That offered the opportunity to identify the occurrence of short-term phenomena; i.e., we registered a deceleration in the last period of the survey.

The knowledge of the three velocity components allowed analyzing in detail the behaviour (e.g., the motion direction) of particular areas of interest. Interestingly, we observed that the motion vector was not uniformly parallel to the local glacier surface; on the contrary, in the steepest areas the v_y component was dominant, while v_z was more relevant in the gentler parts. Usually, if a recent DEM is available, the 3D motion is estimated by adjusting the 1D or 2D measurements according to the local slope (Gabrieli et al., 2016; Giordan et al., 2016; Huang and Li, 2011; Luzi et al., 2007). Though, as we proved, this assumption might be misleading in particular cases.

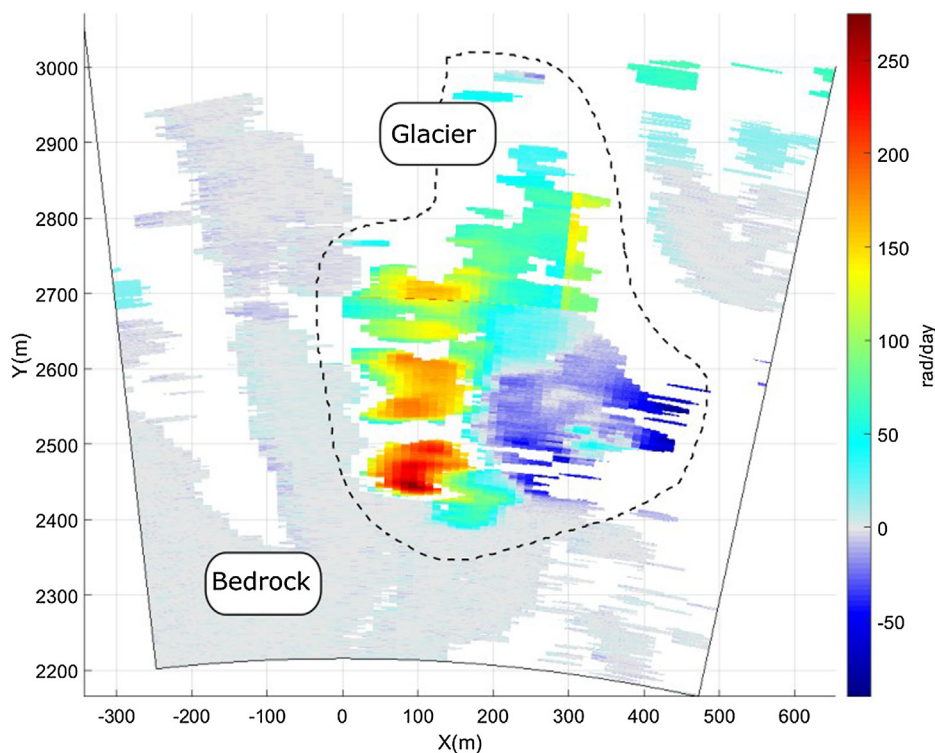


Fig. 11. Map of the velocity component parallel to the LOS, obtained by radar interferometry. Positive values represent incoming motion, while negative values represent motion going away. A dashed line surrounds the glacier; the grey areas indicate the bedrock.

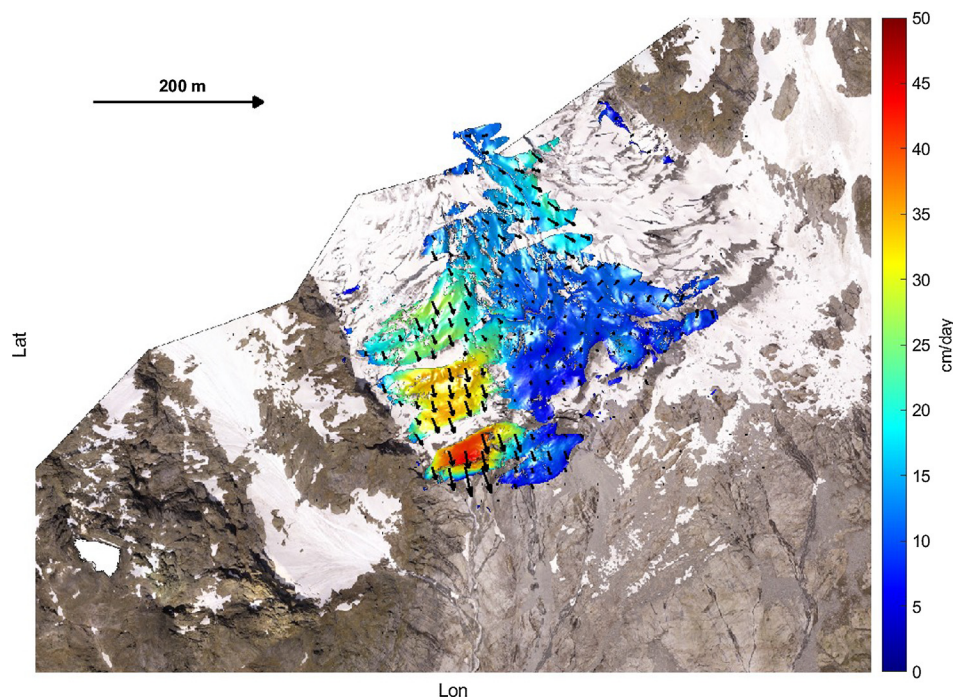


Fig. 12. Velocity field of the surface kinematics. Colours and arrows represent the velocity module and direction respectively.

In the present situation, the surface displacements were not parallel to the local slope probably because the vertical areas corresponded to single ice bodies (e.g., seracs and ice block faces) that slid according with the entire glacier body along the global valley slope. Whereas, in the flatter regions, the surface deformations (i.e., ice creeping) are a relevant component of the motion, thus the vertical component is dominant. The same phenomena might be valid also in situations where the investigated surface is characterized by the presence of prominent volumes moving as single bodies (e.g., icefalls, deep gravitational deformations or toppling-affected areas).

6. Conclusions

In this paper, we presented an innovative methodology that couples the partial measurements of the surface kinematics obtained through terrestrial radar interferometry (TRI) and image cross-correlation (ICC) as they can detect complementary motion components.

The technique we developed allows at estimating the spatio-temporal evolution (daily frequency) of the actual 3-dimensional surface kinematics, providing module, direction and versus of the motion field. It is possible to employ it purely from remote from medium range (i.e., a few thousand metres). Therefore, that approach is particularly suited in situations where the access to the investigated area is difficult or hazardous. Moreover, the method can be applied either when the two remote sensing instruments are placed in coincident or different locations. That feature lends our approach a flexible logistic.

The major issue concerns the data georeferencing, which is accomplished with the support of a DEM. The visual images are orthorectified through bundle adjustment using a set of ground control points (GCPs) manually selected on the scene. The orthorectification process also provides the metric scaling of the data. A relevant characteristic of the general method is that the data merging is quite insensitive to possible morphological changes of the surface, mainly because the pixel-to-metric conversion depends only on the sensor-to-target distance, whose variation is negligible.

We propose a new approach to georeference the radar data purely from remote. The idea consists in estimating the unknown transformation parameter (i.e., the rotation angle) that maximize the spatial

correlation between the optical and the radar viewsheds; the radar viewshed is evaluated from the analysis of the amplitude of the back-scattered signal. Once the data are georeferenced, the orthogonal components of the motion are summed.

We applied the technique to the dataset collected during a survey campaign of the Planpincieux glacier, in the Italian side of the Mont Blanc massif, carried out on 4–27 September 2015.

We acquired the data with a ground-based synthetic aperture radar (GBSAR) and a monoscopic visual-based system (VBS). The measurements of the cumulative motion with both the instruments revealed millimeter accuracy and precision. The georeferencing uncertainty was estimated in a few metres; that is comparable with the resolution of the maps of the results. Therefore, we judged the georeferencing method satisfying for the data coupling.

Besides the georeferencing error, the main limitations of the method are those related to the single remote sensing system; e.g., the ICC method requires the manual selection of the images to be processed, it works only during suited visibility conditions, and it suffers the shadow-light effects. The terrestrial radar interferometry drawback is primarily connected to the high financial costs and the relatively limited portability of the instrumentation.

References

- Aguilar, M.A., Agüera, F., Aguilar, F.J., Carvajal, F., 2008. Geometric accuracy assessment of the orthorectification process from very high resolution satellite imagery for Common Agricultural Policy purposes. *Int. J. Remote Sens.* 29, 7181–7197.
- Ahn, Y., Box, J.E., 2010. Glacier velocities from time-lapse photos: technique development and first results from the Extreme Ice Survey (EIS) in Greenland. *J. Glaciol.* 56, 723–734. <http://dx.doi.org/10.3189/002214310793146313>.
- Allstadt, K.E., Shean, D.E., Campbell, A., Fahnestock, M., Malone, S.D., 2015. Observations of seasonal and diurnal glacier velocities at Mount Rainier, Washington, using terrestrial radar interferometry. *The Cryosphere* 9, 2219–2235.
- Arenson, L.U., Kääb, A., O'Sullivan, A., 2016. Detection and analysis of ground deformation in permafrost environments. *Permafr. Periglac. Process.* 27, 339–351.
- Bamler, R., Hartl, P., 1998. Synthetic aperture radar interferometry. *Inverse Probl.* 14, R1.
- Bitelli, G., Dubbini, M., Zanutta, A., 2004. Terrestrial laser scanning and digital photogrammetry techniques to monitor landslide bodies. *Int. Arch. Photogramm. Remote Sens. Spat. Inf. Sci.* 35, 246–251.
- Caduff, R., Schlunegger, F., Kos, A., Wiesmann, A., 2015. A review of terrestrial radar interferometry for measuring surface change in the geosciences. *Earth Surf. Process. Landf.* 40, 208–228.

- Cai, G., Chen, B.M., Lee, T.H., 2011. *Unmanned Rotorcraft Systems*. Springer Science & Business Media.
- Casu, F., Manconi, A., Pepe, A., Lanari, R., 2011. Deformation time-series generation in areas characterized by large displacement dynamics: the SAR amplitude pixel-offset SBAS technique. *IEEE Trans. Geosci. Remote Sens.* 49, 2752–2763.
- Cheng, D., Prasad, D.K., Brown, M.S., 2014. Illuminant estimation for color constancy: why spatial-domain methods work and the role of the color distribution. *JOSA A* 31, 1049–1058.
- Costantini, M., 1998. A novel phase unwrapping method based on network programming. *IEEE Trans. Geosci. Remote Sens.* 36, 813–821.
- Debella-Gilo, M., Kääb, A., 2011. Sub-pixel precision image matching for measuring surface displacements on mass movements using normalized cross-correlation. *Remote Sens. Environ.* 115, 130–142.
- Delacourt, C., Allemand, P., Berthier, E., Raucoules, D., Casson, B., Grandjean, P., Pambrun, C., Varel, E., 2007. Remote-sensing techniques for analysing landslide kinematics: a review. *Bull. Société Géologique Fr.* 178, 89–100. <http://dx.doi.org/10.2113/gssgfbull.178.2.89>.
- Dematteis, N., Luzi, G., Giordan, D., Zucca, F., Allasia, P., 2017. Monitoring Alpine glacier surface deformations with GB-SAR. *Remote Sens. Lett.* 8, 947–956.
- Faillietaz, J., Funk, M., Vincent, C., 2015. Avalanching glacier instabilities: review on processes and early warning perspectives. *Rev. Geophys.* 53, 203–224.
- Fallourd, R., Vernier, F., Friedt, J.-M., Martin, G., Trouvé, E., Moreau, L., Nicolas, J.-M., 2010. Monitoring temperate glacier with high resolution automated digital camera-s-application to the Argentiére Glacier. In: *PCV 2010, ISPRS Commission III Symposium*.
- Ferretti, A., Prati, C., Rocca, F., 2001. Permanent scatterers in SAR interferometry. *IEEE Trans. Geosci. Remote Sens.* 39, 8–20.
- Fukuzono, T., 1985. A method to predict the time of slope failure caused by rainfall using the inverse number of velocity of surface displacement. *Landslides* 22, 8–13.1.
- Gabrieli, F., Corain, L., Vettore, L., 2016. A low-cost landslide displacement activity assessment from time-lapse photogrammetry and rainfall data: application to the Tessina landslide site. *Geomorphology* 269, 56–74.
- Giordan, D., Allasia, P., Dematteis, N., Dell'Anese, F., Vagliasindi, M., Motta, E., 2016. A low-cost optical remote sensing application for glacier deformation monitoring in an alpine environment. *Sensors* 16, 1750.
- Gui, L.C., Merzkirch, W., 1996. A method of tracking ensembles of particle images. *Exp. Fluids* 21, 465–468.
- Guizar-Sicairos, M., Thurman, S.T., Fienup, J.R., 2008. Efficient subpixel image registration algorithms. *Opt. Lett.* 33, 156–158.
- Hart, D.P., 1998. The elimination of correlation errors in PIV processing. In: *9th International Symposium on Applications of Laser Techniques to Fluid Mechanics*, pp. 13–16.
- Huang, L., Li, Z., 2011. Comparison of SAR and optical data in deriving glacier velocity with feature tracking. *Int. J. Remote Sens.* 32, 2681–2698.
- Iglesias, R., Fabregas, X., Aguasca, A., Mallorqui, J.J., López-Martínez, C., Gili, J.A., Corominas, J., 2014. Atmospheric phase screen compensation in ground-based SAR with a multiple-regression model over mountainous regions. *IEEE Trans. Geosci. Remote Sens.* 52, 2436–2449.
- Kääb, A., Gudmundsson, G.H., Hoelzle, M., 1998. Surface deformation of creeping mountain permafrost. *Photogrammetric investigations on rock glacier Murtèl, Swiss Alps*. In: *Proceedings of the 7th International Conference on Permafrost*, pp. 531–537.
- Kääb, A., Huggel, C., Fischer, L., Guex, S., Paul, F., Roer, I., Salzmann, N., Schläefli, S., Schmutz, K., Schneider, D., et al., 2005. Remote sensing of glacier-and permafrost-related hazards in high mountains: an overview. *Nat. Hazards Earth Syst. Sci.* 5, 527–554.
- Keane, R.D., Adrian, R.J., 1992. Theory of cross-correlation analysis of PIV images. *Appl. Sci. Res.* 49, 191–215.
- Kenner, R., Bühler, Y., Delaloye, R., Ginzler, C., Phillips, M., 2014. Monitoring of high alpine mass movements combining laser scanning with digital airborne photogrammetry. *Geomorphology* 206, 492–504.
- Leprince, S., Berthier, E., Ayoub, F., Delacourt, C., Avouac, J.-P., 2008. Monitoring earth surface dynamics with optical imagery. *Eos Trans. Am. Geophys. Union* 89, 1–2. <http://dx.doi.org/10.1029/2008EO010001>.
- Lim, M., Petley, D.N., Rosser, N.J., Allison, R.J., Long, A.J., Pybus, D., 2005. Combined digital photogrammetry and time-of-flight laser scanning for monitoring cliff evolution. *Photogramm. Rec.* 20, 109–129.
- Lingua, A., Piatti, D., Rinaudo, F., 2008. Remote monitoring of a landslide using an integration of GB-INSAR and LIDAR techniques. *Int. Arch. Photogramm. Remote Sens. Spat. Inf. Sci.* 37, 133–139.
- Liu, X., Zhang, Z., Peterson, J., Chandra, S., 2007. LiDAR-derived high quality ground control information and DEM for image orthorectification. *GeoInformatica* 11, 37–53.
- Luhmann, T., 2009. Precision potential of photogrammetric 6DOF pose estimation with a single camera. *ISPRS J. Photogramm. Remote Sens.* 64, 275–284.
- Luzi, G., Pieraccini, M., Mecatti, D., Noferini, L., Guidi, G., Moia, F., Atzeni, C., 2004. Ground-based radar interferometry for landslides monitoring: atmospheric and instrumental decorrelation sources on experimental data. *IEEE Trans. Geosci. Remote Sens.* 42, 2454–2466.
- Luzi, G., Pieraccini, M., Mecatti, D., Noferini, L., Macaluso, G., Tamburini, A., Atzeni, C., 2007. Monitoring of an alpine glacier by means of ground-based SAR interferometry. *IEEE Geosci. Remote Sens. Lett.* 4, 495–499.
- Malet, J.P., Ferhat, G., Ulrich, P., Boetzel, P., Travelletti, J., 2016. The French National Landslide Observatory OMIV—Monitoring surface displacement using permanent GNSS, photogrammetric cameras and terrestrial LiDAR for understanding the landslide mechanisms.
- Manconi, A., Allasia, P., Giordan, D., Baldo, M., Lollino, G., Corazza, A., Albanese, V., 2013. Landslide 3D surface deformation model obtained via RTS measurements. In: *Landslide Science and Practice*. Springer, pp. 431–436.
- Marambio, A., Pucci, B., Jungner, A., Núñez, M., Buill, F., 2009. Terrestrial laser scanner, terrestrial synthetic aperture radar and topographic data: an integration proposal. In: *Proc 8th Int. Geomat. Week Barc.*
- Messerli, A., Grinsted, A., 2015. Image georectification and feature tracking toolbox: ImGRAFT. *Geosci. Instrum. Methods Data Syst.* 4, 23.
- Monserrat, O., Crosetto, M., 2008. Deformation measurement using terrestrial laser scanning data and least squares 3D surface matching. *ISPRS J. Photogramm. Remote Sens.* 63, 142–154.
- Monserrat, O., Crosetto, M., Luzi, G., 2014. A review of ground-based SAR interferometry for deformation measurement. *ISPRS J. Photogramm. Remote Sens.* 93, 40–48.
- Noferini, L., Mecatti, D., Macaluso, G., Pieraccini, M., Atzeni, C., 2009. Monitoring of Belvedere Glacier using a wide angle GB-SAR interferometer. *J. Appl. Geophys.* 68, 289–293.
- Noferini, L., Pieraccini, M., Mecatti, D., Luzi, G., Atzeni, C., Tamburini, A., Broccolato, M., 2005. Permanent scatterers analysis for atmospheric correction in ground-based SAR interferometry. *IEEE Trans. Geosci. Remote Sens.* 43, 1459–1471.
- Piermattei, L., Carturan, L., de Blasi, F., Tarolli, P., Fontana, G.D., Vettore, A., Pfeifer, N., 2016. Suitability of ground-based SfM-MVS for monitoring glacial and periglacial processes. *Earth Surf. Dyn.* 4.
- Pralong, A.J.W., 2005. On the instability of hanging glaciers: Study on the fracture processes and the predictability of failures (PhD Thesis). ETH, Zürich.
- Pust, O., 2000. Piv: Direct cross-correlation compared with fft-based cross-correlation. In: *Proceedings of the 10th International Symposium on Applications of Laser Techniques to Fluid Mechanics*, Lisbon, Portugal. p. 114.
- Raucoules, D., De Michele, M., Malet, J.-P., Ulrich, P., 2013. Time-variable 3D ground displacements from high-resolution synthetic aperture radar (SAR). Application to La Valette landslide (South French Alps). *Remote Sens. Environ.* 139, 198–204.
- Riesen, P., Strozzi, T., Bauder, A., Wiesmann, A., Funk, M., 2011. Short-term surface ice motion variations measured with a ground-based portable real aperture radar interferometer. *J. Glaciol.* 57, 53–60.
- Roncella, R., Forlani, G., Fornari, M., Diotri, F., 2014. Landslide monitoring by fixed-base terrestrial stereo-photogrammetry. *ISPRS Ann. Photogramm. Remote Sens. Spat. Inf. Sci.* 2, 297.
- Rosen, P.A., Hensley, S., Joughin, I.R., Li, F.K., Madsen, S.N., Rodriguez, E., Goldstein, R.M., 2000. Synthetic aperture radar interferometry. *Proc. IEEE* 88, 333–382.
- Scaioni, M., Corti, M., Diolaiuti, G., Fugazza, D., Cernuschi, M., 2017. Local and general monitoring of Forni glacier (Italian Alps) using multi-platform structure-from-motion photogrammetry. *Int. Arch. Photogramm. Remote Sens. Spat. Inf. Sci.* 42.
- Scherler, D., Leprince, S., Strecker, M.R., 2008. Glacier-surface velocities in alpine terrain from optical satellite imagery—accuracy improvement and quality assessment. *Remote Sens. Environ.* 112, 3806–3819.
- Schwalbe, E., Maas, H.-G., 2017. The determination of high-resolution spatio-temporal glacier motion fields from time-lapse sequences. *Earth Surf. Dyn.* 5, 861.
- Sibson, R., 1981. A brief description of natural neighbor interpolation. *Interpret. Multivar. Data* 21–36.
- Strozzi, T., Luckman, A., Murray, T., Wegmuller, U., Werner, C.L., 2002. Glacier motion estimation using SAR offset-tracking procedures. *IEEE Trans. Geosci. Remote Sens.* 40, 2384–2391.
- Tapete, D., Casagli, N., Luzi, G., Fanti, R., Gigli, G., Leva, D., 2013. Integrating radar and laser-based remote sensing techniques for monitoring structural deformation of archaeological monuments. *J. Archaeol. Sci.* 40, 176–189.
- Thielicke, W., Stamhuis, E., 2014. PIVlab—towards user-friendly, affordable and accurate digital particle image velocimetry in MATLAB. *J. Open Res. Softw.* 2.
- Travelletti, J., Delacourt, C., Allemand, P., Malet, J.-P., Schmittbuhl, J., Toussaint, R., Bastard, M., 2012. Correlation of multi-temporal ground-based optical images for landslide monitoring: application, potential and limitations. *ISPRS J. Photogramm. Remote Sens.* 70, 39–55.
- Westerweel, J., Scarano, F., 2005. Universal outlier detection for PIV data. *Exp. Fluids* 39, 1096–1100.
- White, D.J., Take, W.A., Bolton, M.D., 2003. Soil deformation measurement using particle image velocimetry (PIV) and photogrammetry. *Geotechnique* 53, 619–631.
- Willert, C.E., Gharib, M., 1991. Digital particle image velocimetry. *Exp. Fluids* 10, 181–193.
- Wright, T.J., Parsons, B.E., Lu, Z., 2004. Toward mapping surface deformation in three dimensions using InSAR. *Geophys. Res. Lett.* 31.

CLASSIFICATION AND KINEMATICS OF THE PLANPINCIEUX GLACIER BREAK-OFFS USING PHOTOGRAPHIC TIME-LAPSE ANALYSIS

Daniele GIORDAN¹, Niccolò DEMATTEIS¹, Paolo ALLASIA¹, Elena MOTTA²

¹ Geohazard monitoring group, Research Institute for Hydrogeological Protection, National Council of Research of Italy, Torino, Italy

² Safe Mountain Foundation, Courmayeur, Italy

Correspondence to: N. Dematteis (niccolo.dematteis@irpi.cnr.it)

Abstract. Herein, we present results obtained from time-lapse imagery acquired by a digital single-lens reflex camera during 2014-2018 used to monitor the Planpincieux Glacier on the Italian side of the Grandes Jorasses (Mont Blanc massif). We processed the images using image cross-correlation to measure the surface kinematics of the most active lobe of the glacier that presents a high velocity and frequent ice detachments. During the monitoring, we observed two or three periods of sharp acceleration per year that culminated with large break-offs followed by analogous decelerations. Overall, we registered more than 350 failures with a volume greater than 100 m³, of which, 14 events had volumes larger than 10000 m³. The study identified a monotonic positive relationship between the velocity and failure volume that may be used to estimate the volume of the collapses before an event. We identified the thresholds of velocity and acceleration that characterise the activation of the speed-up periods. The study allowed the characterisation of three different instability processes that lead to the break-off of ice chunks from the glacier terminus: i) *disaggregation*, ii) *slab fracture* and iii) *water tunnelling failure* which can be differentiated based on the rheology, the volume involved and the trigger process.

1. INTRODUCTION

Climate change is having a profound impact on the cryosphere, in particular on alpine glaciers (Vaughan and others, 2013). In this environment, ice loss and warmer temperatures can amplify slopes and glacier instabilities according to site-specific environmental features, e.g., morphology, hydrology, thermal conditions, prior slope histories (Deline and others, 2012, 2014). The identification and characterisation of instabilities that can affect glacier termini are often important for the quantitative risk assessment of alpine valleys. The acquisition of monitoring data is important for understanding glacier evolution and the characterisation of the processes considered as precursors of the detachment of large portions of the glacier.

Many studies have been dedicated to ice avalanching and dry calving of hanging glaciers (Flotron, 1977; Röthlisberger, 1981; Alean, 1985; Haeberli and others, 2004; Huggel and others, 2005; Evans and others, 2009; Faillettaz and others, 2011b). Most studies have focused on the identification of the critical evolution that can cause the activation of an ice avalanche. Several studies analysed the possible evolution of a steep glacier and identified the sequence of events that can occur before failure (Pralong and others, 2005; Faillettaz and others, 2015, 2016; Gilbert and others, 2015). The correct identification of the geometry of a fracture and its propagation are important parameters for the assessment of the possible evolution of a glacier and the evaluation of the dimension of the volume that could break off from it (Pralong and Funk, 2006).

The effectiveness of the monitoring systems for identifying the critical conditions and the characterisation of the break-off evolution of a glacier has been demonstrated, in particular, for cold hanging glaciers. Faillettaz and others (2016) described the Grandes Jorasses Glacier failure that occurred in 2014 and identified a power-law behaviour for the velocity evolution before the rupture (Pralong and others, 2005). Therefore, the failure tendency can be studied using the evolution of the displacement behaviour, as is currently applied for landslides (Wegmann and others, 2003; Manconi and Giordan, 2015, 2016).

It is more difficult to predict break-offs that can occur in the temperate portion of the glaciers. Faillettaz and others (2015) presented a detailed review of break-off events and concluded that the possibility of an accurate prediction for the rupture timing of steep temperate glacier is far from achievable, but some critical conditions promoting the final failure can be identified. The identification of critical conditions can be conducted using monitoring solutions able to detect i) the surface velocity, ii) the water pressure and discharge (Vincent and Moreau, 2016) and iii) the icequakes (Dalban Canassy and others, 2012).

In this paper, we present the results of the Planpincieux Glacier monitoring system on the Italian side of the Grandes Jorasses (Mont Blanc massif). Planpincieux is a polythermal glacier that has been characterised by heavy break-off activity in the past, such as in 1952 and 1982, when two ice avalanches were recorded. For this reason, in late 2013, the Research Institute for Geo-Hydrological Protection (IRPI) of the Italian National Research Council (CNR) and the Safe Mountain Foundation (FMS) initiated a joint research project aimed at

developing a low-cost monitoring system able to detect and measure the surface activity of the glacier. The monitoring system has been installed on the opposite side of the Ferret valley just in front of the glacier and it acquires high-resolution red-green-blue (RGB) images. The surface velocity is assessed using image cross-correlation (ICC) that has proven to be a valuable technique for the kinematics study of glaciers (Scambos and others, 1992; Ahn and Box, 2010; Debella-Gilo and Kääb, 2011; Messerli and Grinsted, 2015; Schwalbe and Maas, 2017; Petlicki, 2018). A foremost feature of that approach is the possibility to perform measurements without the need to access hazardous areas and to provide data with high temporal and spatial resolution.

Since 2014, the monitoring station registered images of the glacier every hour (Giordan and others, 2016). The monitoring apparatus belongs to the wider monitoring activity of the Planpincieux-Grandes Jorasses glacial area that is now used as an open field monitoring laboratory. In previous years, several different approaches, i.e., terrestrial laser scanner (TLS) and helicopter-borne LiDAR, ground-penetrating radar (GPR), terrestrial radar interferometry (TRI), ICC and robotised total station (RTS) (Faillietaz and others, 2016; Giordan and others, 2016; Dematteis and others, 2017, 2018), have been tested in this complex and challenging environment.

During five years of monitoring the Planpincieux Glacier, the available dataset consists of more than 15000 images, which can be used for a detailed description of the glaciers most active lobe evolution and the classification of the instability processes. The work we propose describes the possibility to monitor break-off onset and development of a glacier with one single monoscopic camera. Using this method, we were able i) to measure the glacier kinematics and determine empirical thresholds of acceleration and velocity that characterise the activation of sharp velocity fluctuations, ii) to observe and classify the instability processes that involved the glacier terminus and to provide an estimation of the break-off volumes in relationship to the glacier velocity peaks.

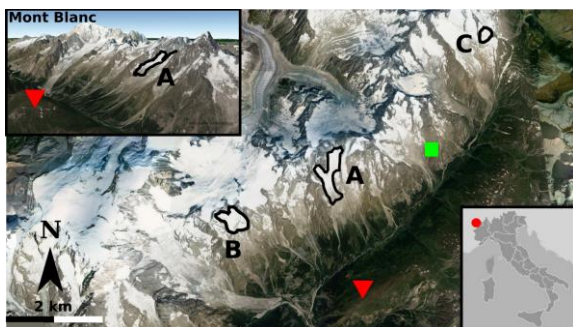


Fig. 1. A general overview of the Ferret Valley in the Mont Blanc massif area. The black outlines are the Planpincieux (A), Toulua (B) and Petit Grapillon (C) Glaciers. The red triangle indicates the location of the monitoring station in front of the Planpincieux Glacier. The green square is the position of the Ferrachet automatic weather station. In the upper left box, a 3D view of the Ferret Valley is shown (Spot image of 14/07/2015 from Google Earth).

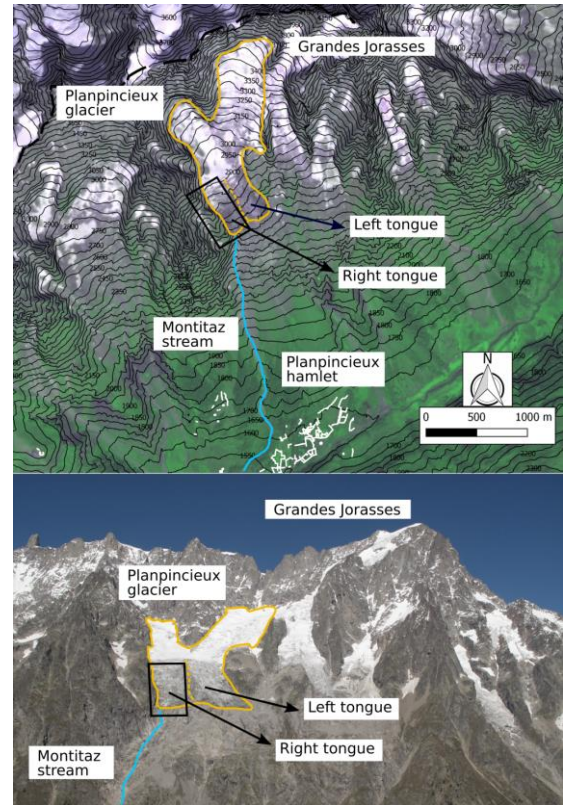


Fig. 2. Study area. The upper figure shows the right side of the Ferret valley. The limits of the Planpincieux Glacier are depicted in yellow. The dashed yellow line indicates the margin between the lower right and left lobes of the glacier. The Montitaz stream (blue line) flows from the right lobe. The buildings of the Planpincieux hamlet are marked in white outlines. The black rectangle delimits the area observed by the TELE module. The lower figure shows a panoramic picture of the Grandes Jorasses massif acquired from the monitoring station.

2. STUDY AREA

The Planpincieux Glacier is a polythermal glacier on the Italian side of the Grandes Jorasses (Mont Blanc massif) (Fig. 1 and Fig. 2) with elevations ranging from 2500 – 3500 m a.s.l. The accumulation area of the glacier is formed of two cirques of which the most important is at the base of the Grand Jorasses. Even though in situ measurements of ice temperature have never been conducted in this area, the mean annual air temperature (MAAT) ranges between -2.3°C to -5.2°C from 3000 m a.s.l. to 3500 m a.s.l. Such values are compatible with the presence of cold firn in the accumulation area (Suter and others, 2001). The ice from these cirques converges in a bowl-shaped area characterised by a gentle slope that alimments two lower lobes separated by a central moraine and whose termini are at an altitude of approximately 2600 m a.s.l. This study investigated the lower temperate lobe in the orographic right of the glacier that is classified as an unbalanced terrace avalanching glacier. A terrace glacier is defined as “an avalanching glacier with a bedrock

characterised by a significant increase in slope at the glacier margin, which induces calving” and the “unbalanced glacier under constant climatic conditions, [...] must release, by calving, a substantial quantity of ice to maintain a finite size geometry” (Pralong and Funk, 2006). Such a lobe is the most active region and exhibits a highly crevassed texture with a mean slope of 32°. It is characterised by frontal 20-30 m-high vertical ice cliff just above steep bedrock face where many ice failures occur during the warm season.

The left lobe is less active and not limited frontally by a bedrock step. The ice flux seems to be mainly channelled in the right lobe, which is also characterised by the presence of the Montitaz stream that flows from the glacier snout. Discharge measurements from the Montitaz stream are not available.

In the past, several major ice avalanches and outbursts of englacial water have occurred (Table 1) and, in some cases, have threatened the village of Planpincieux and damaged the road. Increased attention has been placed on this glacier since 2011, when a large crevasse opened in the lower part of the right lobe (Motta, 2016, personal communication). Since then, the glacier has been intensively monitored using different remote sensing techniques.

3. DATASET

3.1. Meteorology and glacial indexes

We collected meteorological data acquired by the Ferrachet automatic weather station (AWS) placed approximately 5 km far from the Planpincieux Glacier at an elevation of 2300 m a.s.l. The Ferrachet AWS represents the closest and most representative meteorological station provided by the regional meteorological service. Furthermore, we analysed the vertical profiles of the temperature and geopotential heights provided by the ERA5 reanalysis (Copernicus Climate Change Service Climate Data Store (CDS), 2017). The ERA5 is the most recent reanalysis database

produced by the European Centre for Medium-Range Weather Forecasts (ECMWF) and the data are available on a regular grid at a 0.25° x 0.25° resolution and hourly frequency. Also, we considered the surface mass balance (SMB) of the glacier that is closely related to the climatic conditions. There are no available records for the mass balance of the Planpincieux Glacier.

Nevertheless, FMS periodically measures the mass balance of two glaciers in the Ferret Valley, the Toulà Glacier and the Petit Grapillon Glacier (Attività glaciologiche - Fondazione Montagna sicura http://app.fondazionemontagnasicura.org/multimedia/cr_gv/default.asp?sezione=16&principale=32&indice=32). Both glaciers range in elevation between 2700 and 3300 m a.s.l. and have a south-easterly aspect, similar to the Planpincieux Glacier. Therefore, it is reasonable to assume that their behaviour should be comparable to Planpincieux. During the considered period, the SMB of these glaciers was positive in 2012-2013 and 2013-2014 and negative in the subsequent years.

3.2. Monitoring station

The lowest part of the Planpincieux Glacier has been continuously monitored for research purposes since September 2013 by a monoscopic visual-based system (VBS) that is installed on the side of the valley opposite to that of the glacier (Fig. 1) at an elevation of 2305 m a.s.l. and a distance of approximately 3800 m (Giordan and others, 2016). The VBS was developed by CNR IRPI and continuously updated since its installation. Presently, the apparatus is composed of two DSLR cameras (Canon EOS 100D and 700D) and a Raspberry Pi™ computer that manages the scheduling of the image acquisition. The cameras are equipped with different focal lengths to observe the glacier at different levels of detail. The WIDE module (focal length of 120 mm) observes the Planpincieux Glacier and its boundaries, while the ZOOM module (focal length of 297 mm) focuses on the lower right lobe of the glacier.

The cameras were installed on a concrete plinth that was placed inside a plastic shelter box. An energetic module

Table 1. Historical records of the break-off events occurring in the Planpincieux Glacier (Report of the forest rangers of the Pré Saint Didier station of 20/02/1982, 1982; Gianbastiani, 1983; Ceriani and others, 2010).

Date	Event
1920	Glacier outburst flood.
17/06/1929	Glacier outburst flood. The flood wave was observed until Morgex, about 14 km downstream on the Aosta Valley main river. It damaged the road of Val Ferret and its bridges.
21/12/1952	Ice avalanche? An enormous snow avalanche reached Planpincieux, but it is unclear if this avalanche was triggered by an ice break-off or if the hypothetical ice fall originated from the Planpincieux Glacier or the Whymper Glacier.
22/08/1974	Glacier outburst flood.
19/02/1982	Snow avalanche triggered by an ice break-off.
1984, 1985, 1986, 1987, 1996, 1998	Glacier outburst flood damaged the road of the Val Ferret and its bridges. The floods struck the hamlet and the Planpincieux campground.
November 2005	Ice avalanche of about 25000 m ³ . The avalanche stopped in the Montitaz stream.
2008	Glacier outburst. The Montitaz stream bridge was destroyed.

Table 2. Total number of images acquired by the monitoring station in each year and number of images processed using image cross-correlation (ICC). The fourth column reports the number of days without images suitable processing using ICC.

Period	total	processed	voids
15 May-04 Oct 2014	5029	99	44
18 May-14 Oct 2015	3192	109	41
30 May-12 Oct 2016	2350	109	27
16 May-31 Oct 2017	2886	135	0
18 May-25 Oct 2018	1904	141	20

composed of two solar panels supplies electricity to the VBS; therefore, the apparatus can work autonomously and is entirely remote-controlled. During the cold season, the system hibernates and reactivates autonomously when the snow on the solar panels clears. For more details on the developed system, please refer to Giordan and others (2016).

From late October to April-June, the glacier is usually covered by fresh snow; therefore, the glacier surface is mostly invisible and the ICC processing is avoided. The images acquired when the glacier was snow-covered were not processed because the ice surface is not directly visible. However, in limited periods during the cold season when the glacier was uncovered by snow, we observed that the motion of the glacier was almost zero. At the operating regime, the photographs were acquired on an hourly basis, from 7:00 to 19:00.

In this study, we focused our attention on the images of the ZOOM module taken during 2014-2018 from May to October and processed using ICC. In 2014, we acquired a higher frequency for the initial setup of the system. Table 2 reports the total number of collected images and the number of photographs used for the ICC. In total, we collected more than 15000 images and almost 600 images were processed using ICC. The processed dataset corresponds to a time interval of 754 days over five years. To the authors' knowledge, this is the longest series of photographs acquired for a ground-based evaluation of the surface motion of an Alpine glacier.

The acquired images were transferred using a UTMS connection to the CNR server where they are stored. The images with unsuitable illumination or unsatisfactory visibility conditions were manually discarded. The

selected images were processed and the displacement maps were obtained using ICC. Moreover, possible failures were classified according to the instability process and their volume was estimated.

3.3. Ancillary data

Besides time-lapses photography, we acquired ancillary data. We collected several orthophotos provided by the WebGIS service of the Regione Autonoma Valle d'Aosta (GeoPortale – Portale dei dati territoriale della Valle d'Aosta <http://geoportale.regione.vda.it/>) relative to years 1999, 2005 and 2012, with ground sampling distances (GSD) of 1 m, 0.2 m and 0.2 m respectively. Moreover, we conducted periodic helicopter-borne surveys to directly observe the geomorphological conditions of the glacier and acquired corroborative photographic data.

On 2 April 2013, a helicopter-borne GPR (central frequency 65 MHz) survey measured the glacier thickness and allowed a description of the bedrock morphology. Furthermore, on 9 June 2014, we conducted a helicopter-borne LiDAR (sensor RIEGL LMS-Q680i) survey where we acquired a digital surface map (DSM) of the lower part of the glacier and an orthophoto with a ground sample distance (GSD) of 0.08 m. The DSM was sampled at a resolution of 0.5 m. We also conducted a terrestrial laser scanner (TLS, sensor RIEGL LMS-Z420i) survey on 2 October 2015, when we obtained a 3D point cloud.

Moreover, we conducted four monitoring campaigns using the terrestrial radar interferometry (TRI) technique that provided the LOS-aligned measurements of the glacier motion. The results of the TRI confirmed the velocity values and the surface kinematic pattern obtained using ICC.

Table 3. Survey campaigns and datasets collected during the monitoring period

Survey	Dates	Reference
Time-lapse ICC	September 2013-in course	Giordan and others (2016)
Terrestrial radar interferometry	August 2013, August 2014, September 2015, June 2016	Gamma remote sensing (2013, 2014); Dematteis and others (2016); Dematteis and others (2017)
Terrestrial laser scanner	2 October 2015	Ise-Net (2015)
LiDAR	9 June 2014	Baldo (2014)
Orthophotos	1999, 2005, 2012, 2014, 2017	(GeoPortale – Portale dei dati territoriale della Valle d'Aosta http://geoportale.regione.vda.it/)
Aerial observation	2011-2018	---
GPR	2 April 2013	Augeos (2013)

4. METHODS

4.1. Meteorological analysis

The meteorological series were characterised by strong fluctuations during the five years of study regarding temperature and precipitation. Using the ERA5 reanalysis data, we calculated the positive degree-day (PDD) at the top height of the glacier, shown in Fig. 3a, where the PDD is the cumulative sum of the daily mean positive temperatures (Hock, 2003). We derived the temperature by assuming a constant lapse rate between two known geopotential levels. We observed that 2014 was much colder than the other years (Nimbus Web <http://www.nimbus.it/clima/2014/140903Estate2014.htm>) that registered similar temperatures, especially in summer. Moreover, the temperatures in September and October 2018 were much higher than usual.

The 2018 winter season was characterised by exceptional snowfalls (Fig. 3c). Therefore, the surface remained covered by snow longer than in the previous years, even though the summer was rather warm. Similarly, in 2014 and 2016, the surface cleared by mid-July, while in 2015 and 2017, the snow melted completely by the second half of June. The periods of glacier surface clearance were evaluated through visual inspection. Concerning the liquid precipitation (Fig. 3b), 2014 was the wettest year and 2016 and 2018 were characterised by very dry warm seasons.

4.2. Glacier surface velocity measurement

ICC is a well-known methodology used for applications in the field of glaciological surveying (Scambos and others, 1992; Leprince and others, 2007; Fallourd and others, 2010; Ahn and Box, 2010; Debella-Gilo and Käab, 2011; Vernier and others, 2011; Benoit and others, 2015; Messerli and Grinsted, 2015; Giordan and others, 2016; Schwalbe and Maas, 2017). It provides two-dimensional maps of the motion components perpendicular to the line of sight (LOS) with a sub-pixel sensitivity.

In this study, we followed the procedures described in Dematteis and others (2018) to measure the glacier surface velocity. The cross-correlation is calculated on sliding windows extracted on image pairs for estimating the displacement between the master and the slave tiles. We computed the phase correlation using the algorithm of Guizar-Sicairos and others (2008), which allows for fast calculations and minimal decorrelations. The motion of the slave tile S with respect to the master tile M is extracted from the cross-correlation matrix C , obtained with

$$C = \mathcal{F}^{-1}\{\mathcal{F}\{M\} \times \mathcal{F}\{S\}^*\} \quad (1)$$

where \mathcal{F} and \mathcal{F}^{-1} represent the two-dimensional Fourier transform and inverse transform respectively and the symbol $*$ represents the complex conjugate. The position of the maximum peak of C corresponds to the relative pixel shift between the two tiles.

We adopted sliding windows of 128 pixels per side with an overlap of 50% to increase data redundancy and

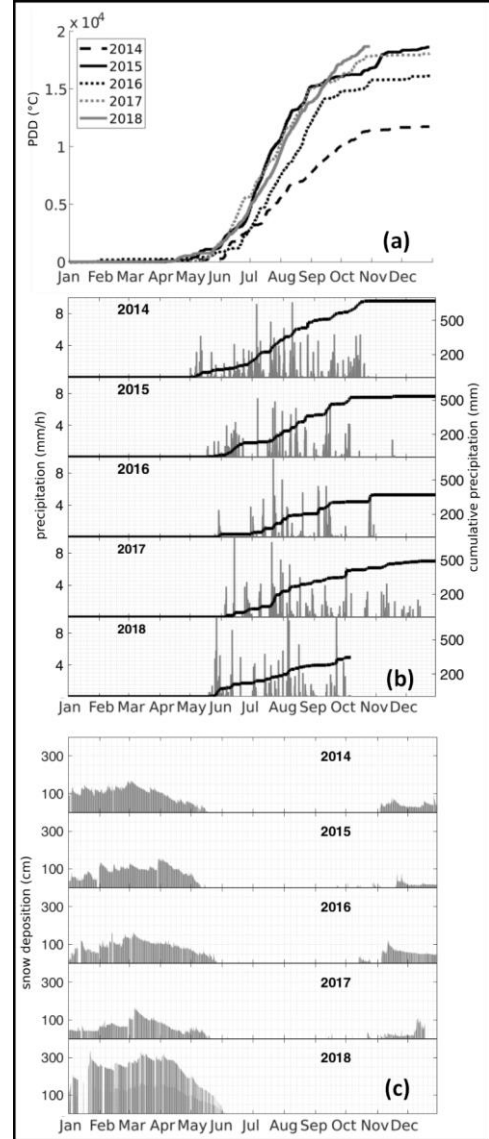


Fig. 3. (a) Positive degree day at the elevation of the glacier. (b) Hourly and cumulative rainfall. (c) Snow deposition. Precipitation and snow were recorded by the Ferrachet atmospheric weather station.

facilitate outlier identification. Thereby, we obtained a motion field mapped on regular grids with a 3.5 m resolution. We obtained analogue results also by adopting different sliding windows sizes and overlapping ratios. We discarded the images with unsuitable illumination or visibility and we manually selected the photographs to conduct the ICC. We used one image per day, when available, acquired in conditions of diffuse illumination to minimise the noise introduced by the shadows produced by direct light (Ahn and Box, 2010; Giordan and others, 2016). The shadow-related noise impeded the use of sub-daily time-lapses because it lowered the signal-to-noise ratio and increased the error (Dematteis and others, 2019). We estimated the ICC uncertainty by analysing the displacement measured on the stable surfaces (i.e., exposed bedrock). We calculated the mean μ and standard deviation δ of the motion of 116 displacement maps, obtaining a $\mu = 0.1$ cm and $\delta =$

2.4 cm. We considered μ and δ as the estimates of the measurement accuracy and precision.

4.3. Break-off detection and volume estimation

A visual inspection of the available dataset allowed for the detection of break-offs, crevasse widening and the aperture of channels at the bedrock-glacier interface that can indicate the outburst of englacial water.

For each detected failure, we analysed the sequence of images pre- and post-event and classified the break-off according to the trigger process. The principal features that we considered in classifying the detachment processes were: i) the collapsed volume, ii) evidence of the water involvement in the process, iii) the morphology of the glacier pre- and post-event and iv) the observed shape of the detachment.

During the monitoring, we manually counted the number of collapses. In this study, we considered only those events with a volume greater than 100 m^3 , even though minor and less relevant break-offs occurred almost daily. To estimate the volume of the ice detachments, we followed the subsequent procedure: we delimited the area corresponding to the collapse and we subdivided it into irregular polyhedra. Then, we manually counted the number of pixels included in the polyhedra (Fig. 4b). Similarly to Le Meur and Vincent (2006), we made some geometrical assumptions: we assumed that the frontal and rear faces were vertical and that the bedrock underneath was regular and with a uniform slope. The bedrock inclination is assumed equal to the mean slope of the glacier surface, calculated with the DTM. Therefore, we transformed the vertex x, z picture coordinates in pixel in the spatial metric 3D coordinates x', y', z' , where the x' -axis is positive rightward, the z' -axis is positive upward and the y' -axis is positive moving away (y is the depth dimension).

With reference to Fig. 4c, we considered the lowest vertex, B_0 , as the origin of the xyz -axes. Then, the vertex coordinates of the lower face B (the base of the polyhedron) became $x'_{B_i} = x_{B_i} - x_{B_0}$, $z'_{B_i} = z_{B_i} - z_{B_0}$ and $y'_{B_i} = \frac{z'_{B_i}}{\tan \alpha}$, where α is the slope angle assumed uniform and the subscript i indicates a generic point of the face B . The assumption of verticality of the frontal and rear faces implies that there is not a depth shift between the i^{th} -point in the upper face F and the corresponding i^{th} -point in the face B , i.e., $y'_{F_i} = y'_{B_i}$. Finally, it holds $x'_{F_i} = x_{F_i} - x_{B_0}$, $z'_{F_i} = z_{F_i} - z_{B_0}$.

The uncertainty E_V of the volume estimation is given by the sum of three principal contributors:

$$E_V = \epsilon_g + \epsilon_v + \epsilon_p \quad (2)$$

where ϵ_g is the actual validity of the geometric assumptions, ϵ_v is the precision of the polyhedra vertexes identification and ϵ_p is the degree of approximation in the volume subdivision in the irregular polyhedra.

ϵ_g could be the most questionable term because it involves specific assumptions on the geometry of the break-off volumes, namely, the vertical frontal and rear faces and the regular bedrock. The DSMs from 2014 and

2015 clearly show that the glacier terminus presented a vertical ice cliff. The visual analysis of the photographic dataset revealed that the morphology of the front remained the same during the study period. A comparable morphology of the rear faces was evident after the break-off events (Fig. 4a-c). Analogously, the observation of the bedrock surface did not reveal significant irregularities in the proximity of the snout.

The ϵ_v and ϵ_p terms are closely related and they have to do with the manual delimitation of the detached ice blocks. The delimitation is conducted by comparing the photographs before and after the failure. The expert-based teamwork and training during the 5-year study allowed us to obtain reliable results for the volume delimitation. On this basis, we conservatively estimated the uncertainty of the vertex selections as $\delta_v = \pm 10 \text{ px}$. Therefore, considering a cube of side ℓ , we obtained an absolute error $\epsilon_v = V \cdot 3 \left(\frac{\delta_v}{\ell} \right) = 3\delta_v V^{\frac{2}{3}}$.

Furthermore, for ϵ_p , we evaluated the error given by the ice block division in the polyhedra with respect to the following geometric problem. We considered the ice chunk as a single convex curvilinear volume that we approximated with a polyhedron. Considering that we assume that the rear face is flat and vertical and that the base is flat and with uniform slope, the problem reduces to the case of a hemicylinder circumscribed in a parallelepiped. In such a situation, the error is $\epsilon_p = \pm 0.21V$.

We were able to validate our volume estimation method on one occasion. Just a few hours after the LiDAR survey from 9 June 2014, a break-off occurred (Fig. 4). The collapsed block was recognisable on the orthophoto and it was easy to compute the volume from the DSM where we obtained a volume of $V = 3120 + 163 \text{ m}^3$. Adopting

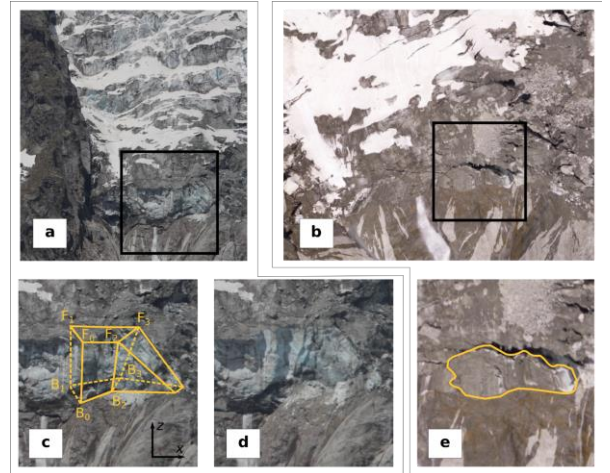


Fig. 4. Volume estimate of the break-off occurring on 9 June 2014. (a) Image of the glacier before the break-off. (b) Orthorectified nadir photo before the failure. (c) Detail of figure (a), where the manual decomposition of the volume in irregular polyhedra is shown. The solid lines indicate the frontal edges, while the dashed lines indicate the rear (inner) edges. (d) Image of the glacier after the break-off. (e) Detail of figure (b), where the margins of the collapsed ice are depicted in yellow.

the image-based volume estimation, we obtained $V = 3190 \pm 836 \text{ m}^3$. Therefore, the results of the proposed method are comparable and in good agreement with the reference values obtained using the DSM and georeferenced orthophoto.

4.4. Velocity-break-off relationship

We analysed the velocity time series and investigated the possible relationship between the kinematics and the break-off.

We observed several periods of rapid acceleration of the frontal glacier portion that culminated with a voluminous break-off. Therefore, we examined the behaviour during these periods using the power-law originally proposed by Flotron (1977) that was adopted to predict the instant of the failures

$$v(t) = v_0 + \alpha(t_c - t)^m \quad (3)$$

where $v(t)$ is the velocity at time t , v_0 is a constant velocity, t_c is the time of the failure and α, m are the parameters that characterise the acceleration. We fitted Equation (3) with the velocity from the 10 days prior to the failure; namely, $t = \{t_c - 9, t_c - 8, \dots, t_c\}$. We also investigated the fit of Equation (3) at different time intervals (i.e., from 7 to 20 days), but we did not obtain significantly different results.

Faillietaz and others (2008) observed the presence of log-periodic oscillations superimposed to the power-law behaviour of the velocity and they showed that by considering such oscillations it could be possible to improve the forecasting of the instant of failure. We did not observe any evidence on the presence of such log-periodic oscillations.

We further analysed the volume of the break-offs in relation with the glacier kinematics. We searched for a relationship between the volume of the detached ice and

the velocity peaks during the active phases and between the volume and the average acceleration of the previous five days before the rupture. The previous five days corresponded to the period of sharp acceleration of the power-law curve that can be approximated to a linear trend. This could be compared to the findings of Faillietaz and others (2011a) that observed an energy and frequency increase in the icequake activity related to the glacier motion in the five days prior to the break-off.

Considering the limited number of sampled data, we conducted two stochastic analyses to assess the statistical significance of the results. The first one was a Monte Carlo simulation (Wilks, 2011) in which, during each iteration, we calculated the Spearman correlation coefficient r_s , or rank correlation and the p-value between the velocity v and the adjusted volume $V_i^* = V_i + wE_V^i$, where V_i was the volume of the i^{th} observation, w was a random weight in the range ± 1 and E_V^i was the estimated error of the volume V_i . The Spearman correlation is more robust and resistant to a few outlying point pairs than the ordinary Pearson (or linear) correlation coefficient (Wilks, 2011). Therefore, it should be more significant for a dataset with a limited number of samples. The second analysis was a bootstrap analysis (Wilks, 2011) in which the coupled velocity-volumes used to compute the relationship were randomly selected using resubmission, i.e., at each iteration, a specific couple might be excluded from the dataset, or it might be selected more times. In both simulations, we analysed the p-value using the student T-test against the null hypothesis of the zero velocity-volume relationship. We used the T-test because it has proven effective even with extremely small datasets (De Winter, 2013).

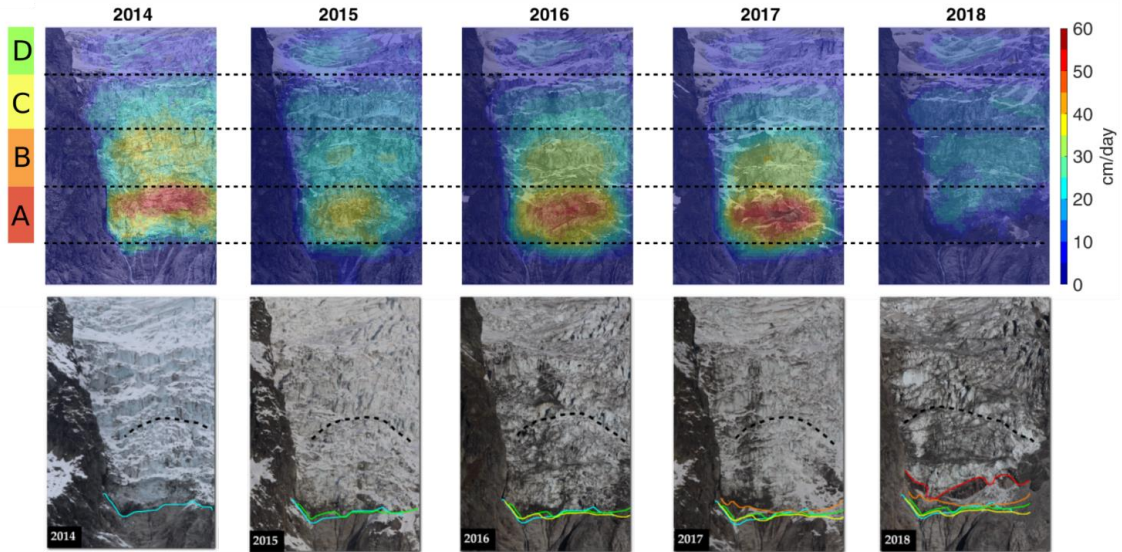


Fig. 5. The lower panels show the evolution of the position of the glacial front at the end of the warm seasons during 2014–2018. The coloured lines indicate the position in each year: 2014 (cyan), 2015 (green), 2016 (yellow), 2017 (orange) and 2018 (red). The front width is approximately 100 m. The black dashed line indicates the large recurrent crevasse that opens each year during the warm season. The upper panels show the velocity in cm day^{-1} from July to September. On the left, the limits of the kinematic domains are approximately illustrated and projected on the maps with dashed black lines.

5. RESULTS

5.1. Glacier evolution and instability processes

During the last decades, the Planpincieux Glacier has experienced relevant shrinkage and morphological changes. Within 2014-2017, the position of the right lobe front was approximately constant (Fig. 5). Subsequently, in August 2017 a very large collapse occurred (i.e., volume $> 5 \cdot 10^4 \text{ m}^3$) and this caused the front to move several tens of metres backwards. Furthermore, during the warm season of 2018, the front experienced a very large retreat due to ice calving. During the past years, the motion of the glacier rapidly balanced the mass loss from the margin, allowing the front to be maintained at approximately the same position. In contrast, in 2018, the reduced velocity of the glacier could not balance the ice detachments and the snout position remained at this new retreated position.

The 2018 retreat revealed a 20 m-high rock cliff orthogonal to the flow direction. Therefore, the bedrock morphology at the snout was similar to that during the past years, i.e., the front ended above a steep slope gradient. Presently, this morphology makes the glacier prone to ice calving in correspondence of the second upper rock cliff. Thus, it is quite possible that the present position of the front will remain unaltered for the near future.

Besides the evolution of the terminus morphology, the kinematics of the glacier also changed during the study period. Fig. 5 presents the maps of the mean daily motion of the period from 1 July to 30 September of each year.

The analysis revealed that during 2014-2017, the velocity values and patterns of the glacier were similar. In 2018, the glacier showed very different behaviour in two major aspects; i) on average, the surface velocity was quite low and ii) the patterns of the surface kinematic maps were considerably dissimilar (Fig. 5).

From the combined analysis of the evolution of the glacier morphology and kinematics, we identified different surface kinematic domains that are likely linked to the subglacial bedrock (Fig. 6d). The limit definitions were supported by the identification of different velocity regimes and by the presence of morphological features. In particular, we identified a discontinuity corresponding to a large crevasse approximately halfway on the glacier lobe, whose position and morphological shape was constant among the years (Fig. 5 and Fig. 6a-c). The crevasse usually opened in late August and progressively widened up to the beginning of October. In 2014, the crevasse was less evident than in the subsequent years, probably because the stresses were partially compensated by the greater glacier thickness. The volume of the ice mass under that crevasse was estimated to be on the order of $5 \cdot 10^5 \text{ m}^3$.

In Fig. 5 and Fig. 6a-c, we show the limits of the kinematics domains. Sector A is the frontal area that is characterised by the fastest surface velocity and the highest break-off activity. Sector B corresponds to the portion between sector A and the crevasse placed approximately halfway on the lobe. Sector C is the steep area above the aforementioned crevasse and sector D is the gentle upper area.

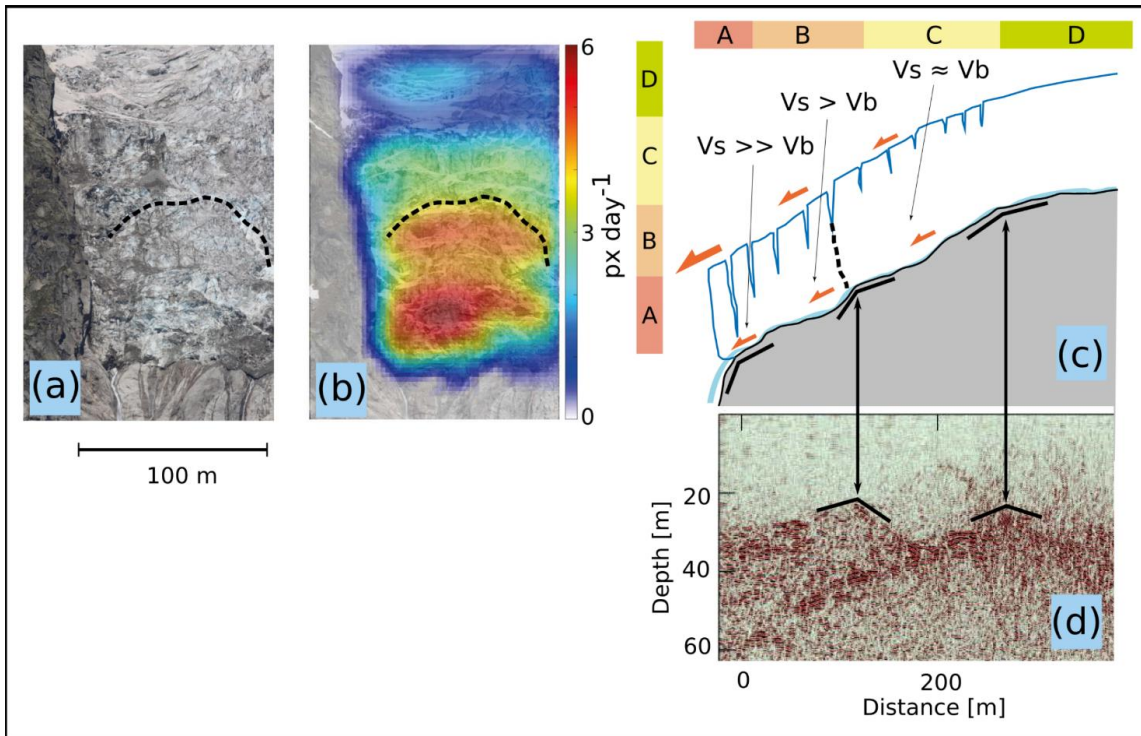


Fig. 6. Morphodynamical scheme of the glacier. (a) Image of the glacier lobe. (b) Example map of the surface velocity. (c) Longitudinal section of the glacier (not to scale). (d) GPR profile. The limits of the kinematic domains are represented by coloured bars. The black dashed lines indicate the position of the crevasse that opens each year at the same position. The bedrock discontinuities are highlighted with black solid lines and are easily recognisable in the GPR profile. V_b , V_s are the basal and surface velocities, respectively.

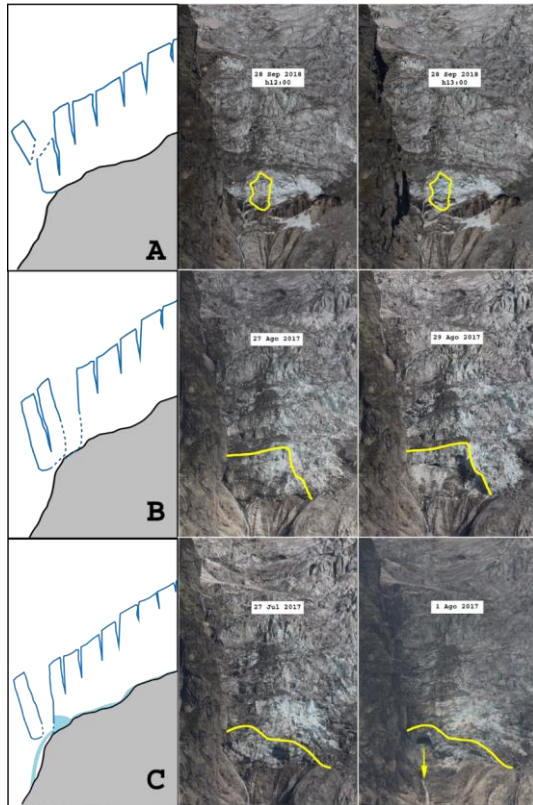


Fig. 7. Instability processes. Panel A) On the left, the of the *disaggregation* detachment scheme is shown. On the right, images of the pre- and post-event are shown. Panel B) On the left, the *slab* break-off scheme is shown. On the right, images of the pre- and post-event are shown. Panel C) On the left, the *water tunnelling* scheme of the break-off is shown. The light-blue line indicates englacial water. On the right, the pre- and post-event images are shown. The yellow lines delimit the collapsed volume before (left photo) and after (right photo) the break-off events. The front width is approximately 100 m.

The daily acquisition of a high-resolution image dataset was fundamental for the detailed description of the phenomena that affected the study area. During the warm season, the glacier snout was subjected to intensive ice calving that manifested three processes that led to break-offs: i) disaggregation, ii) slab fracture and iii) water tunnelling.

Disaggregation (Pralong and Funk, 2006) of the frontal ice cliff (Fig. 7a) occurred most frequently and was usually characterised by a series of limited volume collapses usually on the order of $10^2 - 10^3 \text{ m}^3$ that occurred in limited portions of the terminus. This process was activated by the progressive toppling caused by the movement of the glacier beyond the frontal step. The continuous disaggregation limits the presence of large unstable masses near the glacier margin.

Slab fractures are the second type of detachment and are triggered by the propagation of a fracture that reaches the bedrock (Pralong and Funk, 2006), which fosters increased ice sliding, causing the detachment of an ice lamella. The failures usually involve large portions of the glacier lobe, with volumes on the order of 10^4 m^3 and their activation is quite rapid. In many cases, we noticed a velocity increment before the detachment, related to the progressive spreading of the fracture. After such events,

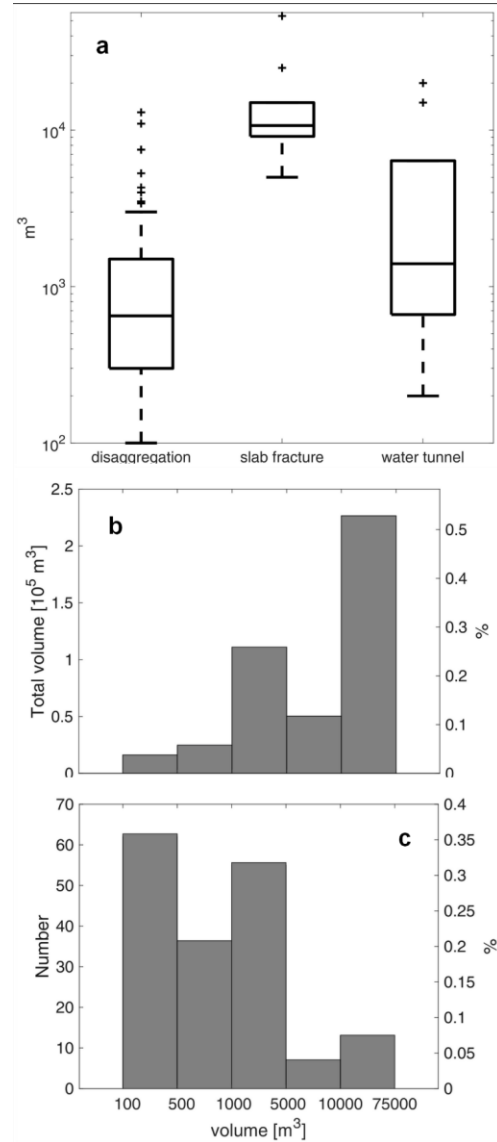


Fig. 8. (a) Boxplot of the break-off volume caused by different processes. The number of disaggregation, slab fractures and water tunnelling events is 151, 13 and 9 respectively. (b) Total amount of collapsed volume. (c) Number of break-off events.

the subglacial bedrock remains almost uncovered (Fig. 7b).

Water tunnelling is the third instability process that has been observed during a few events when the ice collapsed with the presence of substantial volumes of water. The collapses revealed cavities beneath the glacier body (Fig. 7c). Such cavities can indicate the presence of a channelled hydraulic network where the water flows in river-like tunnels, i.e., Röthlisberger-channels (Röthlisberger, 1972). In this situation, the pressure exerted by the water directly on the frontal ice face can provoke detachments of considerable volume; furthermore, the cavities produced by the erosion and melting of the englacial water can collapse. We observed channels with a diameter of more than 10 m, possibly indicating a very large amount of water inside and beneath the glacier body. During the event on 1 August

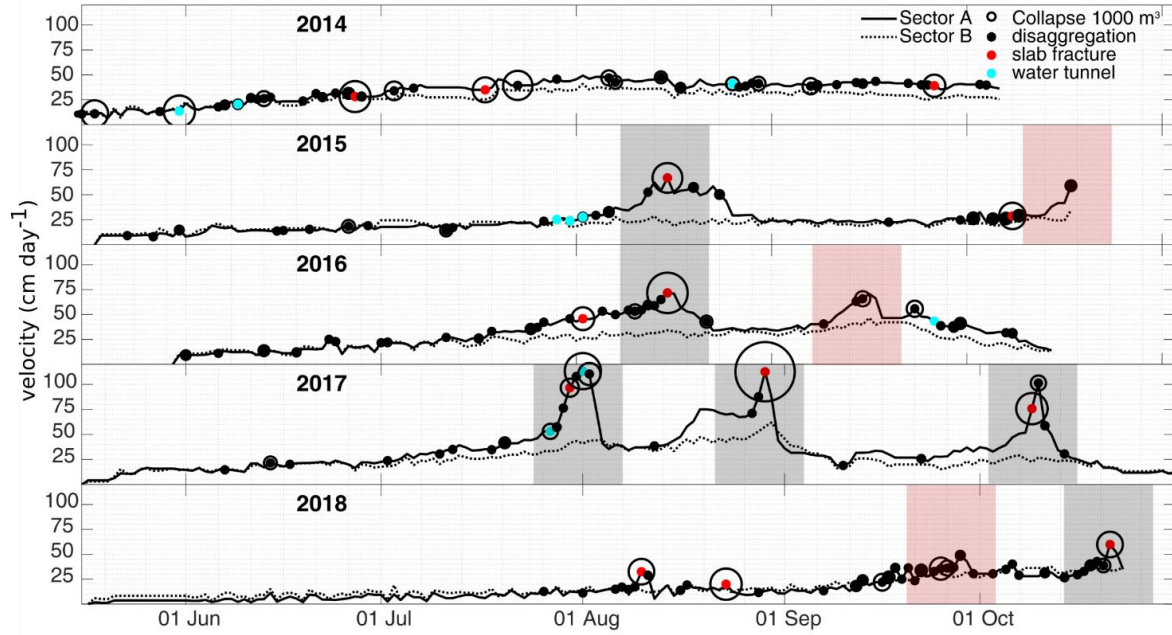


Fig. 9. Time series of the daily velocity of sectors A and B during 2014-2018. The collapse events are displayed as coloured dots according to the instability process: *disaggregation* events are black, *slab fractures* are red and *water tunnelling failures* are cyan. The dimension of the black circles is proportional to the volume of the break-off. The grey rectangles indicate the active phases that culminate with *slab-induced* failures. The red rectangles indicate potential active phases whose evolution was probably interrupted by temperature decreases and snowfalls; these accelerations culminated with *disaggregation* events.

2017, in concomitance with a rainstorm, an impressive water spurt that came out from the snout base was directly observed (Motta, 2016, personal communication). In the past, similar phenomena occurred when great glacier outbursts were accompanied by floods that endangered the Planpincieux village (Table 1).

Moreover, depicted in Fig. 8, we analysed the average magnitude of the events triggered by the different instability processes. As expected, the *slab fracture* type involves the greatest volume of ice, on the order of 10^4 m^3 . The *water tunnelling failures* were less frequent and the volume was rather variable. The *disaggregation* process usually involved less ice, although a few events had volumes over $5 \cdot 10^3 \text{ m}^3$.

Considering the ensemble of all the break-off events, it appears that, even though the collapses smaller than 1000 m^3 are more than half of the total number, they account for only 10% of the total volume approximately. On the contrary, the few collapses larger than 10000 m^3 contribute for more than 50% of the total volume collapsed (Fig. 8).

5.2. Glacier kinematics

According to the identification of the different sectors, we analysed the evolution of the mean velocity of sectors A and B. In Fig. 9, we present the time series of the two sectors during the considered periods and the occurrence of the break-off phenomena, distinguishing their different geneses. We highlighted the periods that are characterised by a strong acceleration of sector A.

The comparison of the time series among the years showed that, on average, the maximum registered

velocity of sector A progressively increased from 2014 to 2017 and lowered in 2018. Table 4 presents the maximum velocities of sector A for each year.

Concerning glacier break-off, 2014 and 2018 registered more events, while the global volume amount of the ice failures was at a maximum in 2014 and 2017. Table 4 shows the total number of observed collapses with estimated volume greater than 100 m^3 in each year and the cumulative volume.

Furthermore, Fig. 9 shows the presence of a particular behaviour in the glacier lobe evolution. It is possible to identify a series of velocity fluctuations that always occurred during the second half of the warm season. These periods of abrupt acceleration were particularly evident in 2015, 2016 and 2017. In late 2018, two such fluctuations were noticed, although the acceleration was less pronounced, while in 2014, the seasonal behaviour of the velocity increased from mid-June to mid-August,

Table 4. Maximum velocity, cumulative volume of collapsed ice and number of disaggregation/slab fracture/water tunnelling events of the different processes in each year

Year	Maximum velocity [cm day ⁻¹]	Cumulative volume [10 ³ m ³]	Break-off events
2014	49.2 ± 2.4	115 ± 26	38/3/3
2015	66.8 ± 2.4	51 ± 12	23/2/3
2016	71.8 ± 2.4	67 ± 15	33/2/1
2017	113.2 ± 2.4	121 ± 27	20/3/2
2018	59.8 ± 2.4	75 ± 17	37/1/0

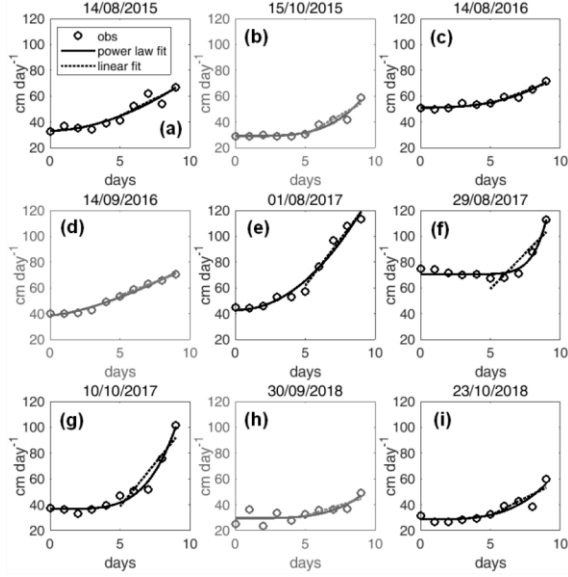


Fig. 10. Active phases of the ten days before *slab fracture* collapses (a, c, e, f, g, i). Active phases of the 10 days before *disaggregation* collapses (b, d, h). The circles represent the observed velocity, the solid lines are the power-law fit and the dotted lines are the linear fit of the previous 5 days of the active phases.

where it reached the maximum value and then slowly decreased without the occurrence of the active phases. Interestingly, each speed-up period culminated in a voluminous break-off, usually a *slab* type. The process of *slab fracture* adapts well to such velocity behaviour as it involves a progressive crevasse opening, causing an increase in the sliding motion. In a few cases (highlighted in red in Fig. 9), the acceleration process was interrupted by significant temperature decreases and the active phase ended with a *disaggregation* failure.

For each active phase, we fitted Equation (3) with the velocity data from the 10 days prior to the ruptures (highlighted in Fig. 9) with the volume of the corresponding break-off. We present the results of the fit in Fig. 10 and the regression statistics in Table 5. We

Table 5. The table reports the dates of the break-offs during the active phases. The dates with asterisks refer to *disaggregation* type failures. The coefficient of determination (R^2) and root mean squared error ($rmse$) were computed for the power-law fit of Equation (3) using the 10 days before the break-off. The p -value was computed against the null-hypothesis of the linear fit.

break-off	R^2	$rmse$ [cm day $^{-1}$]	p -value
14/08/2015	0.89	4.6	0.20
15/10/2015*	0.94	2.7	0.01
14/08/2016	0.96	1.5	<0.01
14/09/2016*	0.98	1.8	0.05
01/08/2017	0.97	5.7	0.02
29/08/2017	0.95	3.5	<0.01
10/10/2017	0.98	3.7	<0.01
30/09/2018*	0.67	4.7	0.25
23/10/2018	0.83	4.1	0.07

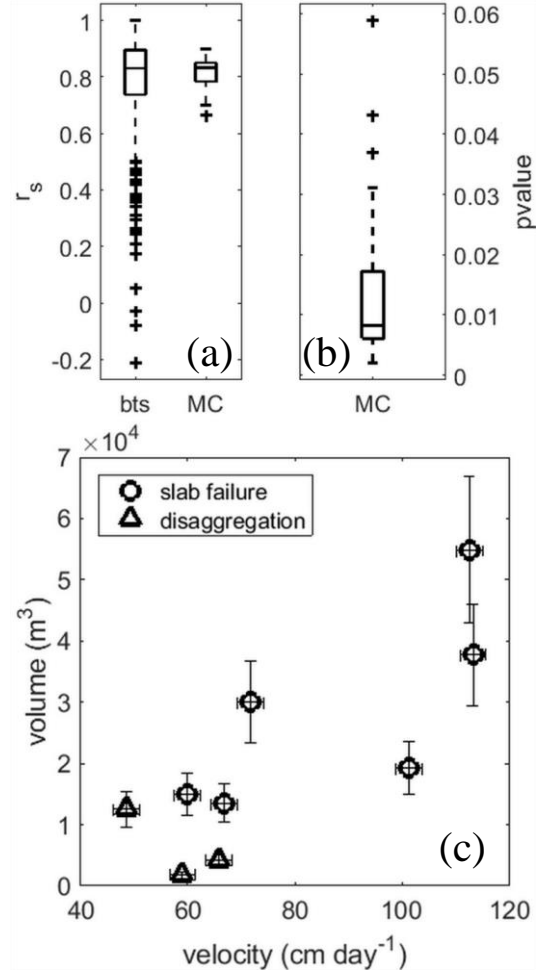


Fig. 11. (a) Spearman correlation coefficient between the velocity and volume obtained with bootstrap (bst) and Monte Carlo (MC) analyses. (b) p -value of the spearman correlation for the Monte Carlo analysis. (c) Relationship between the velocity and break-off volume.

observed that the behaviour of the active phases was in good agreement with the power-law regression (Flotron, 1977).

Besides the analysis of the power-law behaviour of the active phases, we also investigated the relationship between their maximum velocity and the volume of the break-off events (Fig. 11c). As expected, the fastest active phases were associated with *slab fracture*-induced failures that are the most voluminous detachments.

The statistical significance of the monotonic relationship is supported by the analysis of the 1000-iteration bootstrap and Monte Carlo analyses. In fact, in both cases, the Spearman correlation coefficient assumed values above 0.7 on average (Fig. 11a). Moreover, the p -value computed within the Monte Carlo simulation revealed that the relationship was verified at a 0.02 significance. This result is not trivial because it can permit a quantitative estimation of the possible volume of break-off events. Conversely, we did not discover any significant relationship between the acceleration and the volume.

Table 6. Dates of potential active phases and volume of the relative break-off. α is the angular coefficient (i.e., the acceleration) of the linear fit of 5 consecutive days and v_0 is the velocity at the first day of each potential active phase. The rows in italic refer to a *disaggregation* detachment. The date with asterisks indicates events that did not culminate in a break-off.

potential active phase	volume [m ³]	α [cm day ⁻²]	v_0 [cm day ⁻¹]
14/08/2015	13500 \pm 2500	5.3	41.0
<i>15/10/2015</i>	<i>1800 \pm 370</i>	<i>6.1</i>	<i>30.0</i>
14/08/2016	30000 \pm 5500	4.0	54.0
<i>14/09/2016</i>	<i>4150 \pm 820</i>	<i>4.1</i>	<i>54.2</i>
01/08/2017	37700 \pm 6900	14.3	57.3
19/08/2017*	n.a.	6.0	40.3
29/08/2017	54900 \pm 10000	11.1	67.3
10/10/2017	19300 \pm 3600	13.4	47.5
<i>30/09/2018</i>	<i>12500 \pm 2350</i>	<i>3.3</i>	<i>32.8</i>
23/10/2018	15000 \pm 2800	5.4	32.8

Furthermore, we noticed that each active phase that ended with failure was characterised by an average acceleration over five days $\alpha \geq 3 \text{ cm day}^{-2}$ and by an initial velocity $v_0 \geq 30 \text{ cm day}^{-1}$ (Table 6). Considering these acceleration and velocity values, only in one case (18 August 2017) we observed higher velocity and acceleration without the occurrence of a collapse. In that circumstance, we identified the detachment of an ice chunk from the glacial body that remained leaned onto the bedrock, separated from the main glacial mass. Since we did not register a paroxysmal collapse, we did not categorise it as a break-off. Nevertheless, even in this case, the velocity fluctuation was caused by an ice detachment from the main body.

6. DISCUSSION

The observations during the five-year monitoring study allowed for the acquisition of specific knowledge regarding the Planpincieux Glacier and its dynamics. In this section, we report the principal features of the glacier that were identified during the analysis of the surface kinematics, the instability dynamics and the morphology evolution.

6.1. Instability processes

In the Planpincieux Glacier, we identified three main instability processes: *disaggregation*, *slab fracture* and *water tunnelling*. The former two are related to the glacier geometry; *disaggregation* is typical of ice cliffs (Diolaiuti and others, 2004; Pralong and Funk, 2006; Deline and others, 2012). In the Mont Blanc massif, *disaggregation* is frequent in warm glaciers and it involves small volumes (usually <1000 m³) (Alean, 1985b; Deline and others, 2012). *Disaggregation* acts as a stability process because it does not allow the formation of a homogeneous ice chunk that could collapse at once. Larger events are triggered by *slab fracture* process. *Slab fractures* occur in glacier termini that end in correspondence of a bedrock cliff (Alean, 1985a; Pralong and Funk, 2006) and they can induce a larger volume that

can reach a few hundred thousands cubic metres (Alean, 1985a; Huggel and others, 2004). On the contrary, *water tunnelling* is related to the presence of englacial liquid water, which can form R-channels (Röthlisberger, 1972). Such tunnels might develop pockets that can provoke water outburst and subsequently they can collapse. *Water tunnelling* rarely yields surface velocity raise, therefore it is more difficult to recognise break-off precursors with the analysis of the glacier kinematics. According to Faillettaz and others (2015), a possible solution for the acquisition of representative data to identify this process is the analysis of the seismicity and water discharge.

We conducted a meteorology analysis to evaluate the effects of temperature and precipitation on the activation of velocity fluctuations and break-offs. The atmospheric conditions should have a strong influence on glacier stability because they force ice melting and hence water percolation. Nevertheless, we did not find a clear relationship with the active phase occurrence. Probably, this could be ascribed to the non-diffuse configuration of the hydraulic system, which is one of the primary forcings for glacier sliding (Björnsson, 1998).

In Fig. 6, we presented a conceptual longitudinal section of the glacier. According to the identification of different kinematic and morphological domains, we divided the right glacier lobe into four sectors with different velocities. These velocity differences and the limits of the zones are likely influenced by the topography of the bedrock, as the limits of such domains are positioned along corresponding bedrock discontinuities detected by the GPR. In fact, it is known that the geometry of the bedrock is one conditioning factor for the creation of crevasses (Pralong and Funk, 2006). The presence of different kinematic domains with dissimilar velocities indicates the action of strong tensile stresses that cause the aperture of crevasses. The induced strain rates can be identified in the velocity gradient between different sectors. In Fig. 9, we can observe that the strain rate increases during the active phases, while it remains close to zero during the normal regime. According to our findings, we identified a critical scenario that could provoke a very large rupture in the hypothetical case where the sectors A and B accelerate together and move

at the same rate. Such a condition implies that the stresses are concentrated in correspondence of the crevasse above sector B. The occurrence of *slab fractures* in this part of the glacier would involve an estimated volume of more than $5 \cdot 10^5 \cdot \text{m}^3$.

6.2. Interannual variability of glacier kinematics

Thanks to a dataset characterised by a high temporal and spatial resolution, we detected a relevant variability in the glacier kinematics. Specifically, we identified two different regimes in the velocity evolution. The first was in 2014, where an evident seasonal trend with a progressive velocity increment from May to August was identified. It reached a maximum value in August and then slowly decreased together with the diminished temperature. The break-offs were homogeneously distributed during the warm season and the volume of the detachments was not linked to the velocity. A different behaviour was observed in 2015-2017, when the kinematics presented a series of velocity fluctuations and an empirical relationship between the velocity and the volume of the break-off. Moreover, we also registered a remarkable positive trend in the glacier activity year-by-year. In 2018, the glacier showed a quite limited activity for most of the warm season. The motion and instabilities increased in September and the glacier remained rather active up to the end of October, showing non-regular behaviour compared to the previous years. The reason for the reduced motion in 2018 is probably due to the considerable snow cover that cleared in late July and resulted in a delayed beginning of the summer sliding process. The study of the evolution of the glacier started in 2014, which was characterised by different kinematics. Since we did not have data before 2014, we are not able to know the glacier behaviour prior the 2014 and if the 2014 behaviour was anomalous. Probably, the dissimilar behaviour between 2014 and the subsequent years can be ascribed to a colder melting season and a positive mass balance. Low temperatures and a large amount of snow that partially covered crevasses even during the summer season limited the water percolation. Conversely, since 2015 the glacier surface was very crevassed and the melted water could flow easily through the fractures and reach the bedrock, increasing the glacier sliding.

6.3. Seasonal behaviour: velocity fluctuations and break-offs

In 2015, 2016, 2017 and 2018, the surface velocity showed a peculiar behaviour that was characterised by a sequence of fluctuations lasting for 2-3 weeks on average. These fluctuations always occurred during the second half of the warm seasons when the motion of the glacier reached its maximum activity. In correspondence of the oscillation peaks, we always registered a break-off event of relevant volume. Recalling the study of Röthlisberger (1981), Faillettaz and others (2015) described similar active phases in the Allalingsletcher Glacier. They noticed that on several occasions the active phases did not culminate with an ice break-off, but that

the collapses only occurred during the accelerations. Therefore, they stated that such active phases are a necessary but not sufficient condition for the occurrence of ice ruptures. Conversely, we observed that large break-offs always occur, but not exclusively, during such speed-up periods. Therefore, the active phases can be considered a sufficient but not necessary condition for the occurrence of ice ruptures. Faillettaz and others (2015) and Vincent and Moreau (2016) observed active phases occurring at the end of the warm season due to the action of the subglacial water flow when the partial closure of the hydraulic system can cause an increase in interstitial pressure. Hence, diminished water discharge from the terminus might be a precursor of a possible break-off event. In the case of the Planpincieux, although we cannot provide a quantitative analysis of the water discharge, we did not detect any evident change in the water discharge from the snout through visual analysis of the images.

In the presented case study, the registered surface velocity raise that precedes a break-off is due to the positive combination of rotational movement of the ice chunk with the translative sliding of the glacier. Such behaviour was already described by Iken (1977), which measured with a kryokinometer and numerically modelled the displacements of a 20 m-thick ice lamella. She showed that the fracture opened in the zone of maximum tensile stress and then propagated through the entire ice thickness. Then, the ice chunk collapsed when the centre of gravity moved past the supporting edge of bedrock. Notably, its model showed that the velocity reached by the ice chunk is proportional to the volume, as confirmed by our observations (Fig. 11). The deceleration that follows the break-off derives from the lower stresses due to mass loss, which yielded strain rate decrease. The ice acceleration before an ice break-off has been already described in other studies (Iken, 1977; Le Meur and Vincent, 2006; Vincent and others, 2015; Faillettaz and others, 2016). In the majority of the studies, the observations concerned cold-based hanging glaciers, for which the dynamics of the failure follows a power-law behaviour and the time of the failure can be forecasted (Faillettaz and others, 2016). The lower portion of the Planpincieux Glacier is wet-based and the mechanisms that drive the sliding are more complex and difficult to investigate. Therefore, at the state of the art, the break-off prediction is not achievable in this case. Nevertheless, we have found kinematic thresholds that characterise the activation of a velocity fluctuation that always leads to a break-off. Velocity thresholds for early warning purposes have also been defined by Margreth and others (2017) based on heuristic criteria. In the Tacconaz Glacier, Vincent and others (2015) also identified thresholds of critical volume that could lead to major collapses. The kinematic thresholds we determined for Planpincieux Glacier can help in the identification of break-off precursors and the monotonic velocity/volume relationship can be adopted to provide a quantitative estimation of possible collapses. The results of this study may have a profound relevance toward the assessment of alert strategies and civil protection as we present a

criterion (i.e., thresholds of velocity and acceleration) that defines the occurrence of potential active phases that culminated with a break-off in 90% of the cases. Even if we assume that these results should be considered site-dependent, the scientific approach we followed can be reproduced and the methodology can be applied in different glaciers or contexts.

In October 2018 and in September 2019, we observed that sectors A and B were moving together and this was considered a critical condition that could evolve in a large ice break-off. The analysis of the kinematics in 2018 revealed low strain rates and velocity; therefore, the risk of a large break-off was limited. Conversely, in 2019, the strain rates were very high and they provoked the aperture of a large crevasse that underlined an ice lamella of more than $2.5 \cdot 10^5 \text{ m}^3$ (<https://www.nytimes.com/2019/09/25/world/europe/glacier-italy-climate-change.html>).

7. CONCLUSIONS

This paper presents the application and potential of an image-based remote sensing approach for glacier monitoring. In particular, we were able to observe and classify the main instability processes at the Planpincieux Glacier terminus. Moreover, we estimated surface kinematics and ice break-off volumes and we found a monotonic relationship between the velocity peaks and the volume of the collapses. The glacier annual maximum velocities ranged between $50 - 113 \text{ cm day}^{-1}$. We observed a few break-off events per year with volumes larger than 10000 m^3 and in one circumstance the estimated volume was approximately 55000 m^3 .

We presented the results of the image-based monitoring of the Planpincieux Glacier during the melt seasons of 2014-2018. The proposed low-cost monitoring system was used to study the evolution of the Planpincieux Glacier and it is part of the wider open field laboratory that monitors the evolution of the glaciers on the Italian side of the Grandes Jorasses massif using various monitoring techniques (Faillettaz and others, 2016; Dematteis and others, 2018). The original aim of the monitoring plan was the study of the glacier evolution and the possibility to identify precursors of large ice avalanches. The availability of a long sequence of daily images allowed us to detect the most relevant processes that occurred at the glacier terminus. In particular, the study focused on the break-off processes of the right glacier lobe. We conducted a visual analysis and classified three different categories of instability processes related to the geometry (*disaggregation* and *slab fracture*) and to the hydraulic system (*water tunnelling*). Moreover, we measured the surface velocity using an image cross-correlation (ICC) procedure. Visual inspection and ICC coupling allowed at identifying the kinematic sectors in the ice tongue and their relative velocities. This is essential for a more detailed analysis of the glacier evolution and the study of break-off events. In particular, we determined kinematic thresholds, i.e.,

velocity $> 30 \text{ cm day}^{-1}$ and acceleration $> 3 \text{ cm day}^{-2}$, for the activation of speed-up periods that provoke collapse with high probability (i.e., 90% of the cases). Moreover, we found a direct monotonic relationship between the velocity of the frontal part of the glacier lobe and the volume of ice failures that allows the quantification of the collapsed ice amount. This link is evident especially for *slab fractures*, which have the largest detachment volume of the three break-off process categories. The identification of this relationship can help in the quantitative assessment of the unstable areas and for warning purposes.

LICENSES

The manuscript contains modified Copernicus Atmosphere Monitoring Service information from 2018. Neither the European Commission nor the ECMWF is responsible for any use that may be made of the Copernicus information or the data it contains.

AUTHOR CONTRIBUTION

D. Giordan conceived the study. N. Dematteis processed the data. D. Giordan and N. Dematteis dealt with the analysis and wrote the paper. D. Giordan and P. Allasia developed the monitoring apparatus and collected the data. E. Motta contributed with valuable advices toward the paper preparation.

COMPETING INTERESTS

The authors declare that they have no conflict of interest.

ACKNOWLEDGMENTS

The authors are grateful for the relevant and constructive suggestions of two anonymous reviewers and the Scientific Editor Dr. Rachel Carr for its support during the manuscript preparation that helped to improve our work and increased the overall paper quality.

REFERENCES

- Ahn Y and Box JE (2010) Instruments and Methods Glacier velocities from time-lapse photos: Technique development and first results from the Extreme Ice Survey (EIS) in Greenland. *J. Glaciol.* **56**(198), 723–734 (doi:10.3189/002214310793146313)
- Alean J (1985a) Ice Avalanches: Some Empirical Information about their Formation and Reach. *J. Glaciol.* **31**(109), 324–333 (doi:10.3189/s0022143000006663)
- Alean J (1985b) Ice Avalanche Activity and Mass Balance of a High-Altitude Hanging Glacier in the

- Swiss Alps. *Ann. Glaciol.* **6**, 248–249 (doi:10.3189/1985aog6-1-248-249)
- Augeos GmbH (2013) Helicopter-borne ground-penetrating radar (GPR) investigations on the Planpincieux Glacier. Internal report.
- Baldo M (2014). Helicopter-borne LiDAR survey of the Planpincieux glacier for GMG. Internal report.
- Benoit L and 9 others (2015) Multi-method monitoring of Glacier d'Argentière dynamics. *Ann. Glaciol.* **56**(70), 118–128 (doi:10.3189/2015AoG70A985)
- Bjornsson H (1998) Hydrological characteristics of the drainage system beneath a surging glacier. *Nature* **395**(6704), 771–774
- Ceriani E, Fiou M and Castello P (2010) Report redacted for the Valle d'Aosta region authority.
- Copernicus Climate Change Service Climate Data Store (CDS) (2017) Copernicus Climate Change Service (C3S): ERA5: Fifth generation of ECMWF atmospheric reanalyses of the global climate. *Copernicus Climate Change Service (C3S): ERA5: Fifth generation of ECMWF atmospheric reanalyses of the global climate* <https://cds.climate.copernicus.eu/cdsapp#!/home>
- Dalban Canassy P, Faillettaz J, Walter F and Huss M (2012) Seismic activity and surface motion of a steep temperate glacier: A study on Triftgletscher, Switzerland. *J. Glaciol.* **58**(209), 513–528 (doi:10.3189/2012JoG11J104)
- Debella-Gilo M and Kääb A (2011) Sub-pixel precision image matching for measuring surface displacements on mass movements using normalized cross-correlation. *Remote Sens. Environ.* **115**(1), 130–142 (doi:10.1016/j.rse.2010.08.012)
- Deline P, Gardent M, Magnin F and Ravanel L (2012) The morphodynamics of the mont blanc massif in a changing cryosphere: A comprehensive review. *Geogr. Ann. Ser. A Phys. Geogr.* **94**(2), 265–283 (doi:10.1111/j.1468-0459.2012.00467.x)
- Deline P and 12 others (2014) Ice Loss and Slope Stability in High-Mountain Regions. *Snow and Ice-Related Hazards, Risks, and Disasters*. Academic Press, 521–561 (doi:10.1016/B978-0-12-394849-6.00015-9)
- Dematteis N (2017) Experimental survey of glacier monitoring with Metasensing FastGBSAR. Internal report R.I. 2017/04
- Dematteis N, Luzi G, Giordan D, Zucca F and Allasia P (2017) Monitoring Alpine glacier surface deformations with GB-SAR. *Remote Sens. Lett.* **8**(10), 947–956 (doi:10.1080/2150704X.2017.1335905)
- Dematteis N, Giordan D, Zucca F, Luzi G and Allasia P (2018) 4D surface kinematics monitoring through terrestrial radar interferometry and image cross-correlation coupling. *ISPRS J. Photogramm. Remote Sens.* **142**, 38–50 (doi:10.1016/j.isprsjprs.2018.05.017)
- Dematteis N, Giordan D and Allasia P (2019) Image Classification for Automated Image Cross-Correlation Applications in the Geosciences. *Appl. Sci.* **9**(11), 2357 (doi:10.3390/app9112357)
- Diolaiuti G, Smiraglia C, Vassena G and Motta M (2004) Dry calving processes at the ice cliff of Strandline Glacier, northern Victoria Land, Antarctica. *Ann. Glaciol.* **39**, 201–208 (doi:10.3189/172756404781813880)
- Evans SG and 6 others (2009) Catastrophic detachment and high-velocity long-runout flow of Kolka Glacier, Caucasus Mountains, Russia in 2002. *Geomorphology* **105**(3–4), 314–321 (doi:10.1016/j.geomorph.2008.10.008)
- Faillettaz J, Pralong A, Funk M and Deichmann N (2008) Evidence of log-periodic oscillations and increasing icequake activity during the breaking-off of large ice masses. *J. Glaciol.* **54**(187), 725–737
- Faillettaz J, Funk M and Sornette D (2011) Icequakes coupled with surface displacements for predicting glacier break-off. *J. Glaciol.* **57**(203), 453–460 (doi:10.3189/002214311796905668)
- Faillettaz J, Sornette D and Funk M (2011) Numerical modeling of a gravity-driven instability of a cold hanging glacier: Reanalysis of the 1895 break-off of Altelsgletscher, Switzerland. *J. Glaciol.* **57**(205), 817–831 (doi:10.3189/002214311798043852)
- Faillettaz J, Funk M and Vincent C (2015) Avalanching glacier instabilities: Review on processes and early warning perspectives. *Rev. Geophys.* **53**(2), 203–224 (doi:10.1002/2014RG000466)
- Faillettaz J, Funk M and Vagliasindi M (2016) Time forecast of a break-off event from a hanging glacier. *Cryosphere* **10**(3), 1191–1200 (doi:10.5194/tc-10-1191-2016)
- Fallourd R and 6 others (2010) Monitoring temperate glacier with high resolution automated digital cameras - Application to the argentière glacier. *International Archives of the Photogrammetry, Remote Sensing and Spatial Information Sciences - ISPRS Archives*.
- Flotron A (1977) Movement Studies on a Hanging Glacier in Relation with an Ice Avalanche. *J. Glaciol.* **19**(81), 671–672 (doi:10.3189/s0022143000029592)
- Gamma Remote Sensing (2013) Monitoraggio del Ghiacciaio di Planpincieux in Valle d'Aosta (Italia). Internal report.
- Gamma Remote Sensing (2014) Monitoraggio del Ghiacciaio di Planpincieux in Valle d'Aosta (Italia). Internal report.
- Gianbastiani M (1983) Valutazione geomorfologica del rischio di frana, di valanga e di piena di rotta glaciale in un'area alpina (Courmayeur, Valle d'Aosta). *Geol. Tec.* **2**, 5–16
- Gilbert A, Vincent C, Gagliardini O, Krug J and Berthier E (2015) Assessment of thermal change in cold avalanching glaciers in relation to climate warming. *Geophys. Res. Lett.* **42**(15), 6382–6390 (doi:10.1002/2015GL064838)
- Giordan D and 5 others (2016) A low-cost optical remote sensing application for glacier deformation



- monitoring in an alpine environment. *Sensors* **16**(10) (doi:10.3390/s16101750)
- Guizar-Sicairos M, Thurman ST and Fienup JR (2008) Efficient subpixel image registration algorithms. *Opt. Lett.* **33**(2), 156 (doi:10.1364/ol.33.000156)
- Haerberli W and 7 others (2004) The Kolka-Karmadon rock/ice slide of 20 September 2002: An extraordinary event of historical dimensions in North Ossetia, Russian Caucasus. *J. Glaciol.* **50**(171), 533–546 (doi:10.3189/172756504781829710)
- Hock R (2003) Temperature index melt modelling in mountain areas. *J. Hydrol.* **282**(1–4), 104–115 (doi:10.1016/S0022-1694(03)00257-9)
- Huggel C, Haerberli W, Kääb A, Bieri D and Richardson S (2004) An assessment procedure for glacial hazards in the Swiss Alps. *Canadian Geotechnical Journal* **41**(6), 1068–1083 (doi:10.1139/T04-053)
- Huggel C and 6 others (2005) The 2002 rock/ice avalanche at Kolka/Karmadon, Russian Caucasus: assessment of extraordinary avalanche formation and mobility, and application of QuickBird satellite imagery. *Nat. Hazards Earth Syst. Sci.* **5**(2), 173–187 (doi:10.5194/nhess-5-173-2005)
- Iken A (1977) Movement of a Large Ice Mass Before Breaking off. *J. Glaciol.* **19**(81), 595–605 (doi:10.3189/s0022143000215505)
- Ise-Net (2015) Terrestrial Laser Scanner Survey of the Planpincieux Glacier for GMG. Internal report.
- Leprieux S, Barbot S, Ayoub F and Avouac JP (2007) Automatic and precise orthorectification, coregistration, and subpixel correlation of satellite images, application to ground deformation measurements. *IEEE Trans. Geosci. Remote Sens.* **45**(6), 1529–1558 (doi:10.1109/TGRS.2006.888937)
- Manconi A and Giordan D (2015) Landslide early warning based on failure forecast models: The example of the Mt. de la Saxe rockslide, northern Italy. *Nat. Hazards Earth Syst. Sci.* **15**(7), 1639–1644 (doi:10.5194/nhess-15-1639-2015)
- Manconi A and Giordan D (2016) Landslide failure forecast in near-real-time. *Geomatics, Nat. Hazards Risk* **7**(2), 639–648 (doi:10.1080/19475705.2014.942388)
- Margreth S and 5 others (2017) Analysis of the hazard caused by ice avalanches from the hanging glacier on the Eiger west face. *Cold Reg. Sci. Technol.* **144**, 63–72 (doi:10.1016/j.coldregions.2017.05.012)
- Messerli A and Grinsted A (2015) Image georectification and feature tracking toolbox: ImGRAFT. *Geosci. Instrumentation, Methods Data Syst.* **4**(1), 23–34 (doi:10.5194/gi-4-23-2015)
- Le Meur E and Vincent C (2006) Monitoring of the Tacconnaz ice fall (French Alps) using measurements of mass balance, surface velocities and ice cliff position. *Cold Reg. Sci. Technol.* **46**(1), 1–11 (doi:10.1016/j.coldregions.2006.05.001)
- Petlicki M (2018) Subglacial topography of an icefall inferred from repeated terrestrial laser scanning. *IEEE Geosci. Remote Sens. Lett.* **15**(9), 1461–1465 (doi:10.1109/LGRS.2018.2845342)
- Pralong A, Birrer C, Stabel WA and Funk M (2005) On the predictability of ice avalanches. *Nonlinear Process. Geophys.* **12**(6), 849–861 (doi:10.5194/npg-12-849-2005)
- Pralong A and Funk M (2006) On the instability of avalanching glaciers. *J. Glaciol.* **52**(176), 31–48 (doi:10.3189/172756506781828980)
- Report of the forest rangers of the Pré Saint Didier station of 20/02/1982 (1982)
- Röthlisberger H (1972) Water Pressure in Intra- and Subglacial Channels. *J. Glaciol.* **11**(62), 177–203 (doi:10.3189/s0022143000022188)
- Röthlisberger H (1981) Eislawinen und Ausbrüche von Gletscherseen. *Gletscher und Klima - Glaciers et climat. Jahrbuch der Schweizerischen Naturforschenden Gesellschaft. Wissenschaftlicher Teil.* P. Kasser, Birkhäuser Verlag Basel, Boston, Stuttgart., 170–212 <https://books.google.ch/books?id=VkRGMwEACAAJ>
- Scambos TA, Dutkiewicz MJ, Wilson JC and Bindshadler RA (1992) Application of image cross-correlation to the measurement of glacier velocity using satellite image data. *Remote Sens. Environ.* **42**(3), 177–186 (doi:10.1016/0034-4257(92)90101-O)
- Schalwe E and Maas HG (2017) The determination of high-resolution spatio-temporal glacier motion fields from time-lapse sequences. *Earth Surf. Dyn.* **5**(4), 861–879 (doi:10.5194/esurf-5-861-2017)
- Suter S, Latenser M, Haerberli W, Frauenfelder R and Hoelzle M (2001) Cold firn and ice of high-altitude glaciers in the Alps: measurements and distributions modelling. *J. Glaciol.* **47**(106), 85–96 (doi:10.3189/172756501781832566)
- Vaughan D and 9 others (2013) Observations: Cryosphere. *Climate Change 2013 the Physical Science Basis: Working Group I Contribution to the Fifth Assessment Report of the Intergovernmental Panel on Climate Change.* 317–382 (doi:10.1017/CBO9781107415324.012)
- Vernier F and 6 others (2011) Fast correlation technique for glacier flow monitoring by digital camera and space-borne SAR images. *EURASIP J. Image Video Process.* **2011**(1), 11 (doi:10.1186/1687-5281-2011-11)
- Vincent C, Thibert E, Harter M, Soruco A and Gilbert A (2015) Volume and frequency of ice avalanches from Tacconnaz hanging glacier, French Alps. *Ann. Glaciol.* **56**(70), 17–25 (doi:10.3189/2015AoG70A017)
- Vincent C and Moreau L (2016) Sliding velocity fluctuations and subglacial hydrology over the last two decades on Argentière glacier, Mont Blanc area. *J. Glaciol.* **62**(235), 805–815 (doi:10.1017/jog.2016.35)
- Wegmann M, Funk M, Flotron A and Keusen H (2003) Movement Studies to Forecast the Time of Breaking off of Ice and Rock Masses. *Early*

Warning Systems for Natural Disaster Reduction.
Springer, 565–568 (doi:10.1007/978-3-642-
55903-7_76)

Wilks DS (2011) *Statistical Methods in the Atmospheric Sciences*. Academic press (doi:10.2307/2669579)

De Winter J (2013) Using the student's t-test with extremely small sample sizes. *Pract. Assessment, Res. Eval.* **18**(10), 1–12

Ground-based remote-sensing techniques for diagnosis of the current state and recent evolution of the Monte Perdido Glacier, Spanish Pyrenees

J. I. LÓPEZ-MORENO,¹ E. ALONSO-GONZÁLEZ,¹ O. MONSERRAT,² L. M. DEL RÍO,³ J. OTERO,⁴  J. LAPAZARAN,⁴  G. LUZI,² N. DEMATTEIS,^{5,6} A. SERRETA,⁷ I. RICO,^{1,8} E. SERRANO-CAÑADAS,⁹ M. BARTOLOMÉ,¹ A. MORENO,¹ S. BUISAN,¹⁰ J. REVUELTO¹¹

¹Instituto Pirenaico de Ecología, CSIC. Avda Montañana 1005. Zaragoza, 50059, Spain

²Centre Tecnològic de Telecomunicacions de Catalunya (CTTC/CERCA), Av. C.F. Gauss, 7, E-08860 Castelldefels (Barcelona), Spain

³Departamento de Física Aplicada. Escuela Politécnica, Universidad de Extremadura, Cáceres 10071, Spain

⁴Departamento de Matemática Aplicada a las Tecnologías de la Información y las Comunicaciones, E.T.S.I. de Telecomunicación, Universidad Politécnica de Madrid, Av. Complutense, 30, ES-28040 Madrid, Spain

⁵Geohazard Monitoring Group, Research Institute for Hydro-Geological Protection, National Council of Research of Italy, Torino, Italy

⁶Department of Earth Science and Environment, University of Pavia, Pavia, Italy

⁷Escuela Politécnica Superior de Huesca. Universidad de Zaragoza, Crta Cuarte s/n 22071 Huesca, Spain

⁸University of the Basque Country, Department Geography, Prehistory and Archaeology. 01006. Vitoria, Spain

⁹Departamento de Geografía, Universidad de Valladolid, Valladolid, Spain

¹⁰Delegación Territorial de AEMET (Spanish State Meteorological Agency) en Aragón, Paseo del Canal 17, 50007 Zaragoza, Spain

¹¹Météo-France – CNRS, CNRM, UMR 3589, CEN, Grenoble, France

Correspondence: J. I. López Moreno <nlopez@ipe.csic.es>

ABSTRACT. This work combines very detailed measurements from terrestrial laser scanner (TLS), ground-based interferometry radar (GB-SAR) and ground-penetrating radar (GPR) to diagnose current conditions and to analyse the recent evolution of the Monte Perdido Glacier in the Spanish Pyrenees from 2011 to 2017. Thus, this is currently one of the best monitored small glacier (<0.5 km²) worldwide. The evolution of the glacier surface was surveyed with a TLS evidencing an important decline of 6.1 ± 0.3 m on average, with ice losses mainly concentrated over 3 years (2012, 2015 and 2017). Ice loss is unevenly distributed throughout the study period, with 10–15 m thinning in some areas while unchanged areas in others. GB-SAR revealed that areas with higher ice losses are those that are currently with no or very low ice motion. In contrast, sectors located beneath the areas with less ice loss are those that still exhibit noticeable ice movement (average 2–4.5 cm d⁻¹ in summer, and annual movement of 9.98 m a⁻¹ from ablation stakes data). GPR informed that ice thickness was generally <30 m, though locally 30–50 m. Glacier thinning is still accelerating and will lead to extinction of the glacier over the next 50 years.

KEYWORDS: glacier monitoring, ground-penetrating radar, remote sensing

1. INTRODUCTION

Most glaciers in the world have retreated significantly during the 20th century, and there is evidence that shrinkage and wastage of ice bodies have accelerated in the last two decades (Marshall, 2014). Glaciers in the Pyrenees are among the most meridional glaciers in Europe (Grunewald and Scheithauer, 2010) and all of them are currently in a critical situation, with clear evidence of very advanced stages of degradation (Rico and others, 2017). According to the results reported by Rico and others (2017), 33 out of 52 existing glaciers in 1850 (the end of the Little Ice Age, LIA) have already disappeared, 20 of them melted out since 1984. It has implied an 88.25% loss of the glaciated area (–18.18 km²). From 1850 to 1984, glacier area changed from 20.6 to 8.1 km² (61% surface reduction). In 2016, glacier area was reduced to only 2.42 km²,

distributed in 19 glaciers of small size but still exhibiting clear ice motion indicators.

Despite their reduced size, small glaciers such as those existing in the Pyrenees are interesting to study (Dyurgerov and Meier, 2000). This is because 80% of the glaciers in the world with a surface area <0.5 km² represent more than 80% of the total number of glaciers in mid- to low-latitude mountain ranges (Fischer and others, 2016); and they are a relevant component of the cryosphere contributing to landscape formation, local hydrology and sea-level rise (Huss and Fischer, 2016). In addition, they are highly sensitive geo-indicators of the most recent climatic variations (Grunewald and Scheithauer, 2010). However, the response of glacier mass balance to climate fluctuations during their very last stage before disappearing is not fully understood, since there is a positive and negative feedback that has not

yet been properly quantified (Carturan and others, 2013; Huss and Fischer, 2016). In this way, the last glacier remnants are often confined at the most elevated areas, sheltered from radiation and in the most favourable zones for snow accumulation (receiving avalanches or in the leeside of dominant winds) which may slow their response to regional climatic anomalies (DeBeer and Sharp, 2009; Carrivick and others, 2015). Another process that influences the glacier evolution is the thickness of debris cover. This cover usually expands when glaciers' motion decreases and, depending on its thickness, it causes an acceleration or deceleration of the glacier ice wastage (Brock and others, 2010). Finally, the slope of the ice surface tends to increase with glacier shrinkage, and this can negatively impact snow accumulation (López-Moreno and others, 2016). Rocky outcrops may appear within the glacier which enhances incoming longwave radiation to the surrounding ice, and frequent ice collapses may occur, associated with many hollows that generally exist between the ice body and the substrate (Fountain and Walder, 1998), all of these leading to accelerated ice shrinkage and wastage.

An appropriate diagnosis of the condition of a given glacier needs an accurate estimate of remaining ice volume and quantification of ice motion. Additionally, providing evidences of past and recent changes in ice volume allows understanding the evolution of the glacier in previous and present periods of climate change. This information will assist in understanding the response of mass balance to current climatic variability and change. Moreover, geomorphological studies of moraines, as long as they can be accurately dated, will provide useful information on past glacier evolution (Solomina and others, 2016). An array of different techniques allows measurement of the above-mentioned glacier's characteristics. These include traditional ablation stakes for mass balance and surface ice motion, GPS, ground-penetrating radar (GPR), topographic restitution from aerial imageries, optical and radar remote-sensing images, terrestrial and aerial LIDAR (Light Detection and Ranging) and photogrammetry. Their suitability will depend on the contrasted features of the glaciers to be studied. In the case of small glaciers, their reduced size represents an advantage in monitoring the entire ice body but also limits the application of some of these techniques due to the necessity of higher spatial resolution information. The steepness of the slope, the existence of numerous hollows and frequent rockfalls that usually occur in small glaciers also restrict or prevent in situ measurements (Fischer and others, 2016).

The Monte Perdido Glacier is the third largest glacier in the Pyrenees. Recent significant losses have been reported, both in its glacier surface area (from aerial photographs) and in the elevation of its ice surface. It has been measured by comparing digital elevation model (DEMs) derived from topographic maps from 1981 and 1999 (Julián and Chueca, 2007), a new DEM obtained in 2010 from airborne LIDAR, and four successive terrestrial laser scanning (TLS) acquisitions obtained near the end of the ablation period (from 2011 to 2014, López-Moreno and others, 2016). In the most recent years (from 2014 to present time), laser scans (TLS acquisitions) have also been conducted in late April or early May to better understand the full mass balance of the glacier. There has been one-field campaign conducted on ground-based interferometry radar (ground-based synthetic aperture radar, GB-SAR) to retrieve glacier motion and two GPR surveys to estimate ice thicknesses. This work presents

the application of TLS, GB-SAR and GPR techniques to diagnose the current state of the Monte Perdido Glacier and its recent evolution, allowing an in-depth discussion of the applicability of these geomatic techniques for small and highly degraded glaciers.

2. STUDY AREA

The Monte Perdido Glacier (42°40'50"N; 0°02'15"E) is located in the Central Spanish Pyrenees (Fig. 1). The ice masses are north facing and lie on structural flats beneath the main summit of the Monte Perdido Peak (3355 m) in the Ordesa and Monte Perdido National Park.

Its evolution along the Holocene was determined using ³⁶Cl ages derived from moraines and polished surfaces (García-Ruiz and others, 2014).

Numerous old photographs and the location of the LIA moraines indicate a unique glacier at the foot of the large north-facing wall of Monte Perdido during the LIA (Fig. 1). The ice body was divided into three stepped ice masses connected by serac falls by the mid-20th century, and the lower ice body disappeared during the 1970s (García-Ruiz and others, 2014). The two remaining glacier bodies, which are currently unconnected, are referred to in this paper as the upper and lower Monte Perdido Glaciers. The upper and lower ice bodies have mean elevations of 3110 and 2885 m a.s.l. (Julián and Chueca, 2007). Despite the high elevation of the upper glacier, snow accumulation is limited due to minimal avalanche activity above the glacier and its marked steepness (≈40°).

According to recent measurements of air temperature (July 2014 to October 2017) at the foot of the glacier (2700 m a.s.l.) and near the summit of the Monte Perdido peak (at 3295 m a.s.l.), the 0°C isotherm is found to lie at 2945 m a.s.l. In an average summer (June to September), the temperature at the foot of the glacier is 7.3°C. No direct observations of precipitation are available at the glacier location, but maximum mean accumulation of snow in late April during the three available years was 3.23 m (see Section 4.1), and average snow density was 454 kg m⁻³ measured in the field, indicating that total water equivalent during the main accumulation period (October to April) could be close to 1500 mm.

3. METHODS

Table 1 shows the field campaigns carried out and considered in this study and the periods when different geomatic and geodetic techniques were developed for the study of Monte Perdido Glacier. In addition to geomatic data, ten ablation stakes were installed in the glacier in 2014; however, three of them were not measured in the following years because the terrain was too steep or crevassed to reach them safely. Location was monitored using RTK GPS for the other seven stakes (Fig. 2), and the information used to obtain annual values of ice speed (see Section 4.2). Ablation stakes were not used to validate TLS ice elevation changes, as the potential uncertainty of TLS data is expected to be lower than the variability of elevation surface changes within the area that some stakes are displaced each year (up to 10 m a⁻¹).

We have also used long-term (1983–2017) meteorological data managed by the Spanish Meteorological Service (AEMET) in a nearby (2.5 km from the glacier) mountain hut (Goriz) at 2250 m a.s.l. that generates temperature

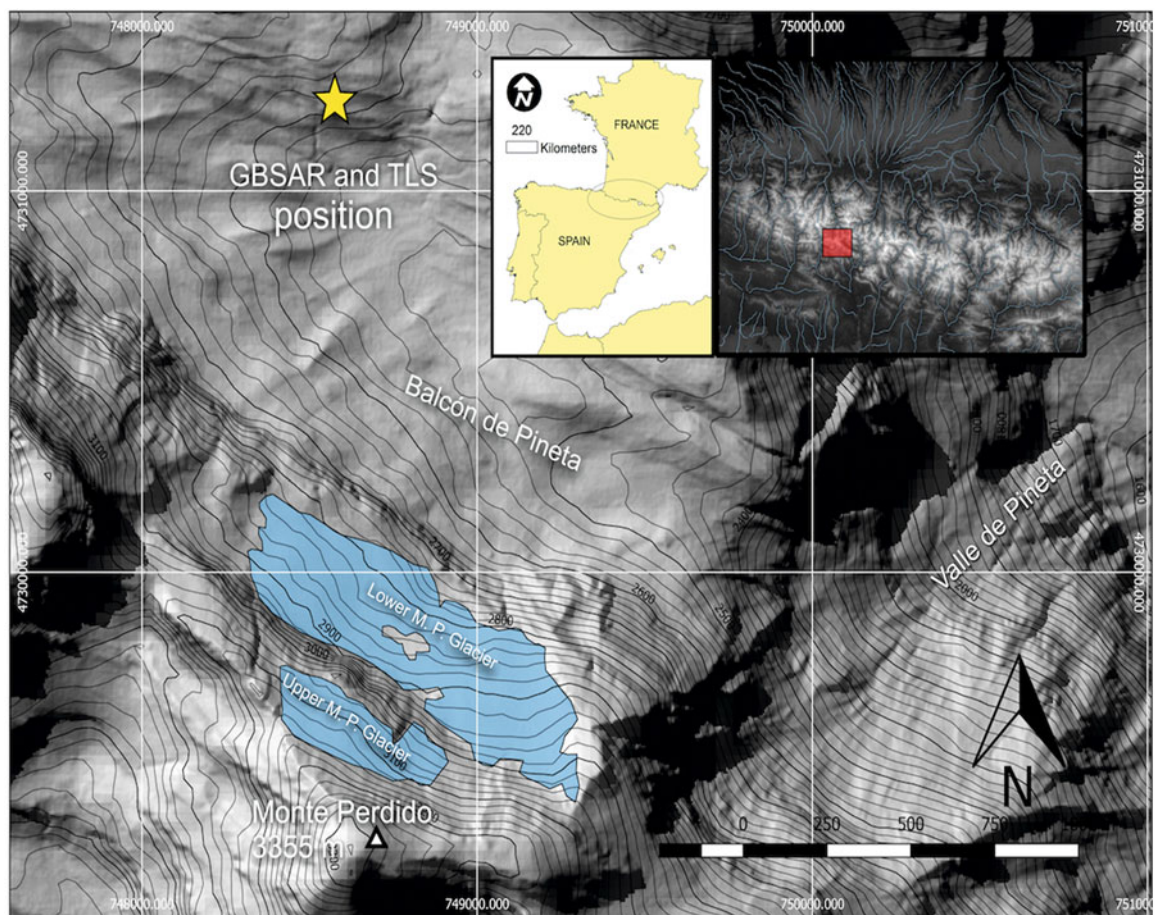


Fig. 1. Location of the Monte Perdido Glacier, including the scan position for TLS and GB-SAR (coordinates in extended UTM zone 30 T).

(from daily maximum and minimum readings) and precipitation (from daily measurements) anomalies in the study period and places the analysed years in this study in a broader temporal context (López-Moreno and others, 2016).

3.1. Terrestrial laser scanner

The use of LIDAR technology, including TLS, has rapidly increased in recent years, and its application has become very frequent for monitoring different aspects of the cryosphere (see the reviews by Deems and others, 2013; Bhardwaj and others, 2016). TLS has the advantage of being a mobile device that acquires data at the time and the frequency required by users (compared with airborne acquisitions, which are limited by flight conditions). For this reason, TLS is becoming a popular device to estimate changes in the volume of glaciers, substituting for or complementing the use of traditional estimation of mass balance by ablation stakes (Fischer and others, 2016).

The device employed in the present study is a long-range TLS (RIEGL LPM-321) that uses time-of-flight technology to measure the time between the emission and detection of a light pulse (at 905 nm, near infrared) from which the distance between the device and the scanned surface is derived. This information allows production of a three-dimensional (3-D) point cloud from real topography. The minimum angular step is 0.0188°, with a laser beam divergence of 0.0468° and a maximum working distance of 6000 m, although there is a considerable loss of accuracy when a range of 3000 m is exceeded (López-Moreno and others, 2017).

We used an almost frontal view of the glacier with minimal shadow zones (<5% of the full area) in the glacier and a scanning distance of 1500–2500 m. As well, we used indirect registration, also called target-based registration (Revuelto and others, 2014), so that scans from different dates (September of 2011–2017) could be compared. Indirect registration uses fixed reference points (targets) that are located in the study area (see Fig. 2). Eleven reflective targets of known shape and dimensions were placed at

Table 1. Field campaigns conducted in the glacier during the period 2011–2017

Instrument	Year	Measured variable
TLS	2011–2017 September 2014–2017 late April	Measurement of elevation of ice surface for ice thinning estimation Measurement of snow accumulation and snow density over the glacier
GB-SAR	2016, from mid July to mid August	Deformation and motion speed of the ice surface (only the lower glacier)
Ablation stakes	Installed in September 2014 and measured every year	Annual ice movement
GPR	2016, late April and late September	Ice thickness of the lower glacier

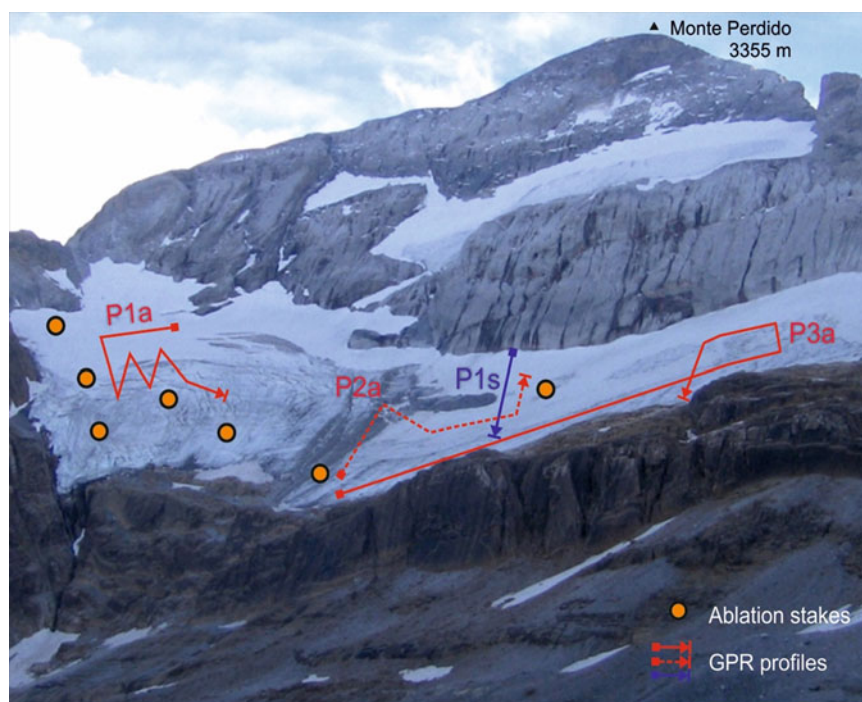


Fig. 2. Location of the seven ablation stakes, the profile obtained with GPR in spring 2016 (P1s, in blue) and the three sets of profiles obtained in autumn 2016 (P1a, P2a and P3a, in red) indicating the starting (S) and end (E) points. The photography was taken in 2011. The width of the photo view is ~ 1 km.

reference points on rocks situated 200–500 m from the scan station. Using standard topographic methods, we obtained accurate (± 0.02 m in planimetry and ± 0.05 m in altimetry) global coordinates for the targets by using a differential GPS (DGPS) with post-processing. A total of 65 reference points around the ice bodies (identifiable sections of rocks and cliffs) were used to assess measurement accuracy. Ninety per cent of the reference points had an error in altimetry of < 0.32 m during the surveys carried out in the fall and 0.43 m during the springtime. The increase of error during spring is associated with small instabilities of the tripod located on snow or frozen ground. The TLS survey carried out on 1 May 2016 was problematic due to very strong winds and low temperatures (ranging between -8 and -14°C during the scanning period) and it was only possible to scan 62% of the lower glacier. This is why the results are shown for the whole glacier when possible, and only for the common area scanned in 2016 in benefit of the inter-annual comparability.

3.2. Interferometry radar

The GB-SAR is a radar-based terrestrial remote-sensing system with interferometric capabilities (Tarchi and others, 1999) by exploiting the interferometric capability of centimetre-wavelength microwaves (Monserrat and others, 2014). It is a long-range measurement device, which can work up to 5 km. It can provide, in an automatically way, massive deformation measurements. The used GB-SAR can acquire an image every few minutes. This means that for those points of the imaged area which maintain sufficient coherence, we can estimate the component of the radar line of sight (LOS) of the displacement with respect to the radar location with a sampling down to a few minutes. Averaging the data acquired during an entire day, we can estimate with millimetre accuracy the deformation of the

pixels and hence of the corresponding areas. Exhaustive reviews of the GB-SAR technique, different systems available and main applications are available in Caduff and others (2015) and Monserrat and others (2014).

The potential of this technique for measuring changes on a glacier has been reported in previous works (Luzi and others, 2007; Noferini and others, 2009; Strozzi and others, 2012; Voytenko and others, 2012). As a main feature, it provides a reliable tool for measuring relative displacements within the glacier body at long range and high resolution (Riesen and others, 2011; Dematteis and others, 2017). The relatively small displacements of glacier surfaces lead to long acquisition times with the GB-SAR to retrieve significant deformations. In this way, GB-SAR campaigns last several days. This information can provide a better understanding of glacier dynamics at a superficial level. The penetration depth of microwaves strongly depends on the condition of the ice or snow. While at Ku band, it can be almost 1 m for dry snow, on the contrary for wet snow depends on the liquid content; for example, at Ku band, with a 2% of wetness, it is only a few centimetres. In addition, in case of wet snow also volumetric scattering is of main concern. This is one of the reason why for wet snow the radar signal decorrelates fast, and the interferometric approach became more challenging at this frequencies (Riesen and others, 2011).

The GB-SAR was installed close to the TLS scan position (Fig. 1) which has a frontal view of the Monte Perdido Glacier. Figure 3 shows the point of view of the GB-SAR. The measurement campaign lasted 28 d, starting the 23 July 2015 and ending the 18 August 2015. The system used was the IBIS-L, produced by IDS spa. The power supply consisted of two solar panels of 140 Wps. The main system parameters are summarized in Table 2.

Unfortunately, it was not possible to obtain continuous measurements during the whole campaign due to bad weather conditions affecting the efficiency of the solar

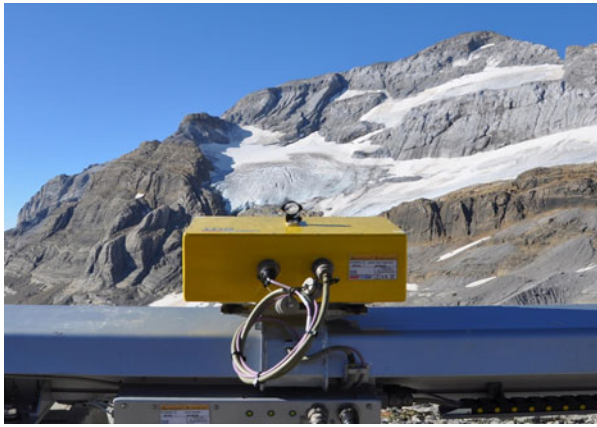


Fig. 3. GB-SAR point of view.

panels, with periods of heavy rains and strong winds. The final dataset consisted of 163 images which were acquired in three different periods: 144 were acquired without interruption between 23 and 30 July. The system was then stopped because the wind destroyed one of the solar panels. The system was reactivated on 11 August and acquired 18 images over 2 d, and finally two images were acquired before removing the system on 18 August. To complete the analysis, the GB-SAR information was contextualized with meteorological data and with a Digital Surface Model (DSM) derived from the closest Terrestrial Laser Scanner campaign (September 2016). For this work, we only analysed the continuous data (from 23 to 30 July).

Figure 4 shows an interpretation of the GB-SAR image using a TLS DSM and identifying the different areas of the glacier in the radar image. The dispersion of amplitude shown in Figure 4d and coherence are parameters usually estimated in radar interferometry to identify the areas where the phase information used to retrieve the displacement of the monitored surface is statistically reliable according to Caduff and others (2015); in this case, values lower than 0.6 can be considered trustworthy measurements.

Deriving deformation estimates from the GB-SAR interferometric phases is not a straightforward process. It requires complex processing in order to properly separate the different components that contribute to the phase differences: atmospheric effects, phase unwrapping and temporal decorrelation (see Monserrat and others, 2014). In most of the approaches described in the literature, the processing can be summarized in five steps: pixel selection, 2-D phase unwrapping, phase integration, estimation of the atmospheric component and displacement computation. A detailed description of the processing used for this work is provided by Dematteis and others (2017).

There were two different processing types: (1) processing only nocturnal data (i.e. 0000–0600) and (2) processing the entire dataset. The first was performed with the aim of

minimizing the effects of the atmosphere, given that its behaviour is more stable during the night. The second was performed in order to fully exploit the whole dataset and to compare the velocity changes between day and night cycles. Before processing these datasets, an analysis of the images was performed in order to discard the noisier images (Dematteis and others, 2017) resulting in 73 images discarded of 144. The final dataset consisted of 71 images.

3.3. Ground-penetrating radar

During the last decades, the techniques based on GPR have been widely used in cryospheric studies. Their use allows determination of thickness and characteristics of the underlying substrate. They also reveal the physical and structural properties of the different underground media: snowpack, ice or permafrost (Schwamborn and others, 2008; Arcone and Kreutz, 2009; Del Río and others, 2014; Liu and others, 2014).

Ground-based GPR prospecting in Monte Perdido Glacier had serious difficulties due to the surface steepness (average slope 20° with wide areas exceeding 40°), frequent rockfalls and abundant water circulating on the surface and within the ice body (López-Moreno and others, 2016).

We conducted two GPR campaigns in 2016, in spring (30 April and 1 May), and in autumn (19–20 September). Figure 2 shows the prospecting itineraries followed during the field surveys, performed with a Måla Geoscience GPR system, using 50, 200 and 500 MHz antennas. The first campaign had little liquid water circulating above and in the glacier, and a smooth snow-covered surface, but the survey was carried out under adverse meteorological conditions (winds $>60 \text{ km h}^{-1}$ and temperatures less than -8°C). The existence of a thick snowpack required the discrimination between ice and snow to accurately quantify glacier thickness. In contrast, the autumn campaign was performed under optimal meteorological conditions but with abundant liquid water circulating over and within the ice body. The presence of water negatively affects GPR prospecting, partly because the water inclusions produce a lot of scattering (resulting in noisy radargrams) and partly because the attenuation of radar waves are highly sensitive to the presence of liquid water on ice (resulting in less intense radargrams) (Daniels, 1996; Murray and others, 2007; Bradford and others, 2009).

In the first GPR campaign, we endeavoured to carry out a detailed multifrequency study of the glacier structure at the lower Monte Perdido Glacier. Due to the bad weather conditions and avalanche risk, we conducted only one profile, although using three different antennas of 50, 200 and 500 MHz, in order to determine the radio wave velocity (RWV) in the ice, the ice thickness and the glacier structure in the study area. During the autumn campaign, it was possible to perform much longer transects using 200 MHz antennas, covering wider areas of the glacier.

In the spring campaign, the 50 and 200 MHz antennas were respectively configured to reach a depth of 30–60 m, with resolutions of 0.9 and 0.25 m respectively ($\lambda/4$), estimated approximately a quarter of the wavelength of the GPR radio wave inside the ice. To properly characterize the snowpack, we also used a 500 MHz antenna, with a resolution of 0.09 m and a maximum depth capability of ~ 11 m. The autumn profiling covered as much glacier area as possible, prospecting ~ 2 km of profiles, walking on the glacier

Table 2. Main GB-SAR acquisition parameters

Parameter	Value
Operating frequency/wavelength	17 GHz (Ku band) /17.6 mm
Maximum distance	3500 m
Spatial resolution: range/cross-range@ 1 km	0.5 m/4.5 m
Acquisition rate	30 min

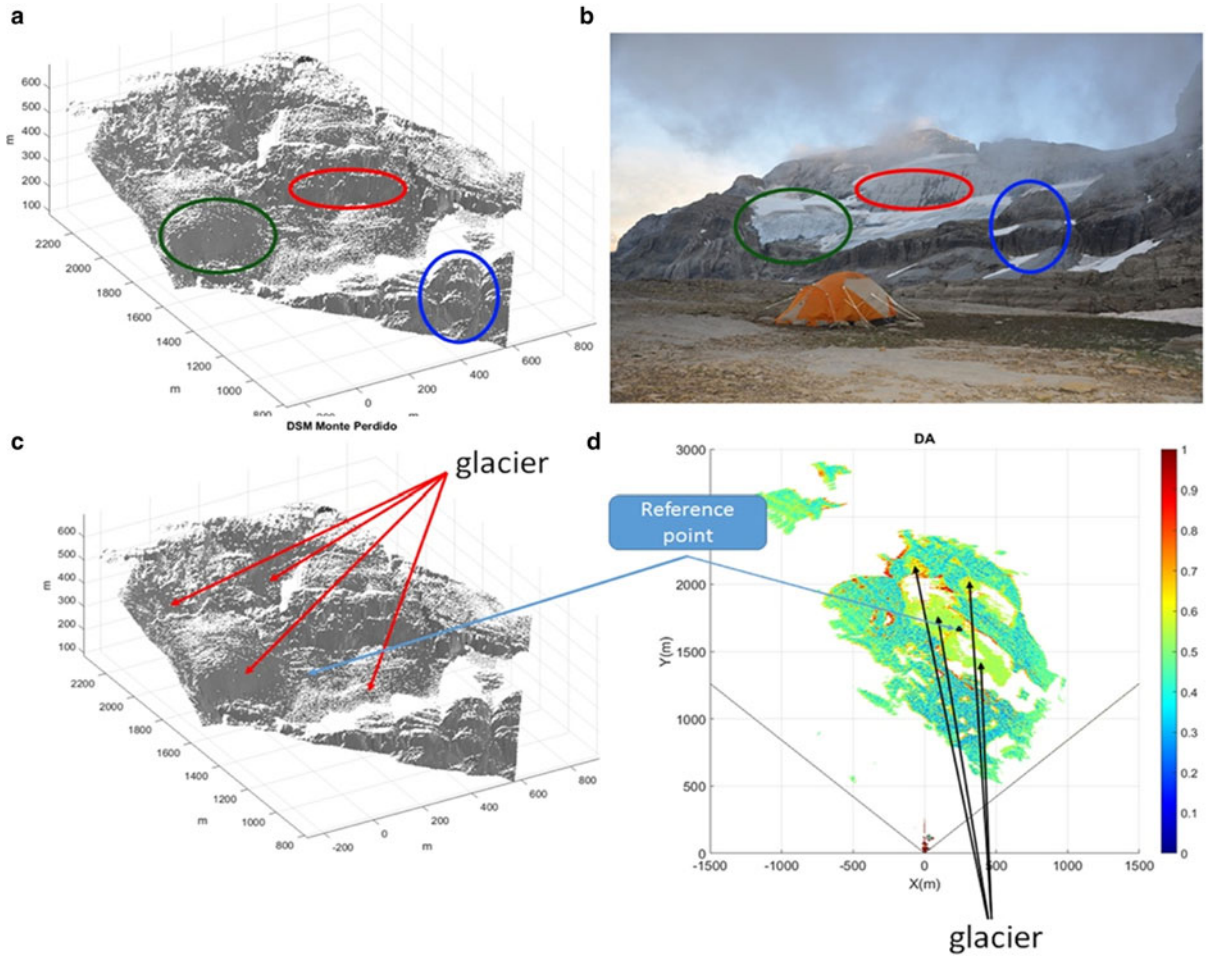


Fig. 4. (a and c) Digital elevation model generated from TLS data acquired from the same position of the GB-SAR. (b) Photo of the glacier from the GB-SAR point of view (summer 2016). The coloured ellipses in a and b identify the same areas in both images. (d) GB-SAR dispersion of amplitude (DA) image obtained from the whole dataset and represented in GB-SAR geometry.

surface. The 200 MHz GPR was configured to reach maximum depths of up to 100 m, registering two traces per second, and using a DGPS Leica 1200 (postprocessed subsequently) for the trace positioning. However, the presence of water caused a very low signal to noise ratio, generating high uncertainty in the majority of the reflections, which led to ± 5 m of uncertainty in estimations of ice thickness.

In order to determine ice thickness, we estimated the RWV in the underlying media assuming a simple model of two homogeneous and isotropic (in terms of velocity) layers (snow + ice), and using the diffraction hyperbolae method (e.g. Clarke and Bentley, 1994; Moore and others, 1999).

The model assumes that the underlying medium can be split into two different media with constant RWVs: (1) snow and (2) ice. The addition of two-way travel times (TWTT) through both media (T_1 and T_2 , respectively) provides the total TWTT (T). This also can be applied for thicknesses measurement, relating thickness to TWTTs via RWVs (V_1 , V_2 and V), thus obtaining the RWV in the second (deeper) layer and expressing it as:

$$V_2 = (VT - V_1 T_1) / (T - T_1). \quad (1)$$

This method can generate large errors in the V_2 estimate (e.g. Benjumea and others, 2003). The main sources of error are the use of hyperbolae from off-nadir diffractors (those that are out from the vertical profiling plane), and the unknown

diffractor size. Both overestimate the RWV of the shallower layer, while underestimating the size of the reflector, although both effects diminish with depth.

4. RESULTS

4.1. Climatic context of the studied period

Figure 5 shows the interannual evolution of precipitation (accumulation period, December to April) and temperature (ablation period, May to September) at the Goriz station. Precipitation during the accumulation period shows strong interannual oscillations, ranging from 350 to 1360 mm, but it does not show any statistically significant temporal trend for the period 1982–2017. Mean temperature during ablation season also exhibits strong interannual variability and presents a statistically significant trend (Spearman's ρ : 0.42; $\alpha < 0.01$) at a rate of $0.33^\circ\text{C decade}^{-1}$. It is interesting to note that all values above the 75th percentile appear after 2003 and onwards.

In line with the interannual variability of temperature and precipitation shown in Figure 5, the study period (2011–2017) exhibited very contrasting climatic conditions. The period of 2011–12 was drier and warmer than the average; 2012–13 was drier than the long-term average with a very cool ablation period; 2013–14 was wet and cool; whereas the last 3 years exhibited average or above average

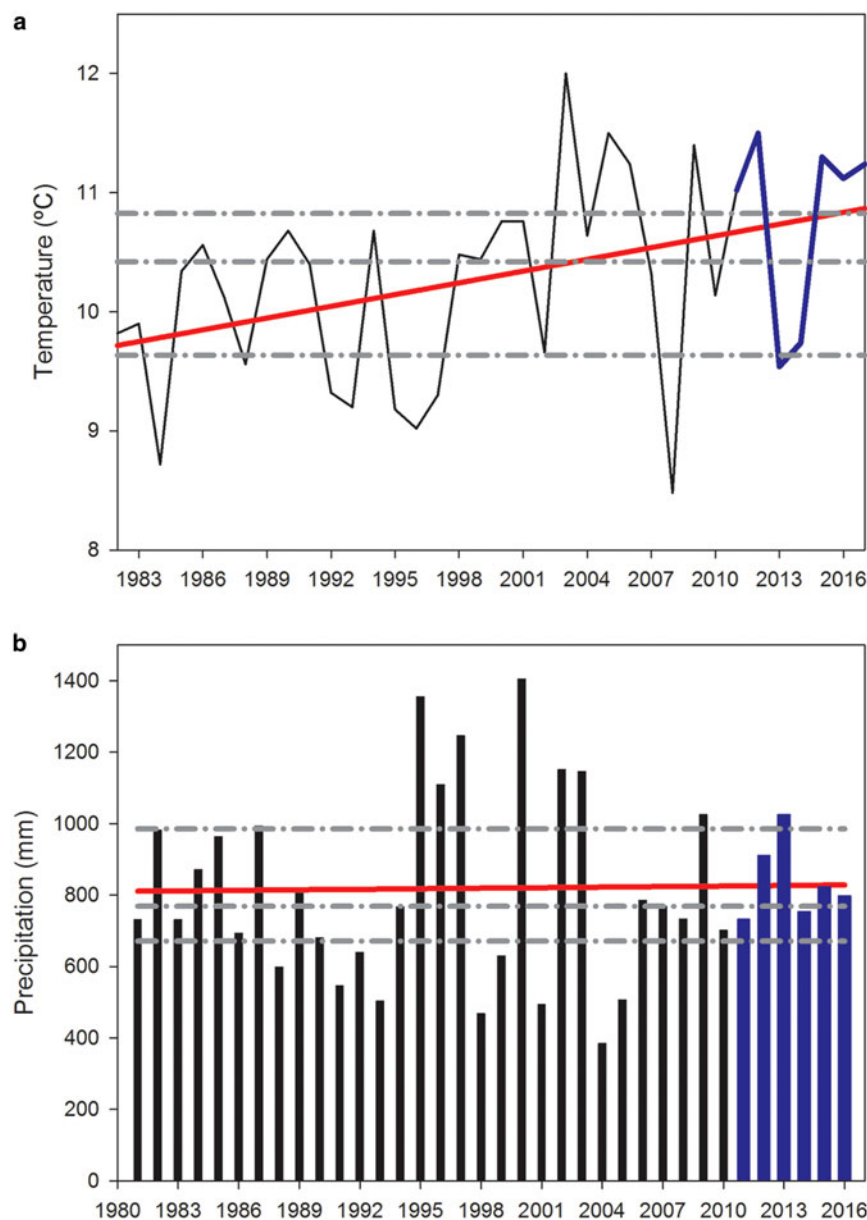


Fig. 5. Temporal series of (a) temperature (ablation season, May to September) and (b) mean precipitation (accumulation period, December to April) in Goriz station. The 2011–2016 period is highlighted with blue colour. Dashed lines indicate the mean and the 25th and 75th percentiles.

precipitation and warm or very warm conditions during the ablation period.

4.2. Changes in elevation of ice surface and snow accumulation from terrestrial laser scanner

Figure 6 shows the difference in the elevation of the ice surface from September 2011 to September 2017 obtained through TLS. Table 3 shows the mean measured annual differences and the coefficient of correlation to illustrate the spatial consistence of changes in ice surface between the different analysed years. During the last 6 years, ice thickness of the glacier has reduced 6.1 m on average, but such losses have exhibited strong spatial and temporal differences. Thus, there are some sectors of the glacier where ice thickness decreased more than 15 m (mainly in the western sectors of the lower glacier and less elevated zones of the upper glacier) while other areas have exhibited almost no changes in ice elevation. The annual change in ice surface

has exhibited very large interannual variability. Thus, during 2013–14 and 2015–16, the changes in the elevation of the ice surface were very small, being measured as very small average ice losses (−0.05 and −0.35 m, respectively), or being slightly dominated by accumulation (+0.35 m in 2012–13). The reductions in ice thickness were concentrated in 2011–12, 2014–15 and 2015–16, with average reductions of 1.8, 1.7 and 2.5 m, respectively. The coefficients of correlation show that the spatial pattern of ice thinning exhibits a statistical significant correlation ($p < 0.01$) during the 3 years of highest ice losses (2011–12, 2014–15 and 2016–17), but correlations were low with the spatial patterns observed in years with low changes in the elevation of the ice surface.

Figure 7 shows the average snow accumulation over the glacier in late spring of 2014, 2015 and 2017 (when no scanning limitations occurred and the whole glacier was scanned). Table 4 shows the mean accumulation over the glacier for the same years, and also for the area that was

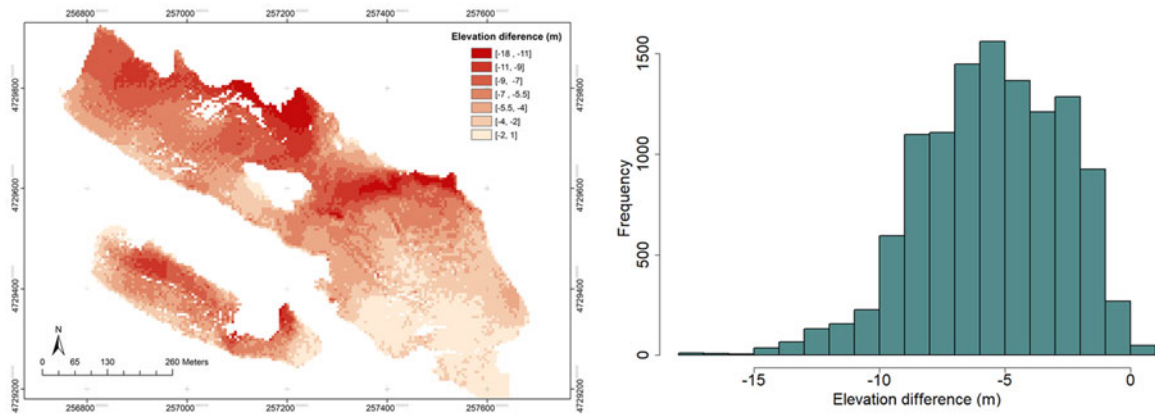


Fig. 6. (a) Difference in the elevation of the ice surface from September 2011 to September 2017. (b) Frequency distribution of differences in elevation of ice surface from 2011 and 2017.

possible to be scanned in 2016. An average accumulation of 3.25 m (3.04 for the common area in the period 2014–2017) of snow (with an average snow density of 454 kg m^{-3}) was registered for the 3 years. For the 2016 spring survey, the area from which it was possible to retrieve information with the TLS showed an average accumulation of 4.5 m, suggesting that it was the snowiest of the four analysed years. The data show that some areas, mainly located in the western part of the glaciers, registered average accumulations over 5 m, exceeding often 6–8 m; while some areas had very low average accumulation mainly due to wind and gravity redistribution. The interannual variability of average snow accumulation appears much lower than that observed for changes in the elevation of the ice surface. Only 2016 clearly registered a higher accumulation, with 33% more snow thickness compared with the average of the other 3 years. Measured snow density in the 4 years was rather constant, oscillating between 437 and 471 kg m^{-3} . According to the correlation matrix, the spatial patterns of snow distribution were rather similar between 2014 and 2015 ($r > 0.75$, $p < 0.01$), but the distribution of 2016–17 exhibited more differences compared with 2014 and 2015 ($r = 0.43$ and 0.36 ; $p > 0.01$, respectively).

Figure 8 shows the slope angle of the glacier surface in 2011 and 2017. Despite being a relatively short period, the glacier surface exhibited significant changes, with a slight increase in average slope from 0.28° in 2011 to 0.31° in 2017. Some areas, mainly located at the bottom western part of the lower glacier, exhibited a decrease in slope angle as a consequence of the recent thinning of this frontal sector. Other wide areas have exhibited a clear

increase in average slope, with a marked increase of the surface for slopes over 30° , which is a threshold often associated with noticeable reduction in snow accumulation (López-Moreno and others, 2017). Indeed, when Figures 7 and 8 are compared, it is possible to observe that areas with high slope angle are coincident with those with the lowest snow accumulation ($r = -0.42$; $p < 0.01$).

4.3. Ice deformation and velocities from GB-SAR

Figure 9 shows the deformation velocity map obtained from the 71 images. The deformation values are in LOS, i.e. the measured displacements are a projection of the real displacement in the line between each point and the GB-SAR. Negative values represent points moving towards the GB-SAR. The values are between -4 cm d^{-1} (red) and 1 cm d^{-1} (blue). The estimated precision, based on the Std dev. of the accumulated displacement map, is 4.5 mm. It can be observed that most of the ice surface presents movement towards the GB-SAR, ranging from 1.5 to 4 cm d^{-1} . However, it must be taken into account that sensitivity to the displacement changes has a high dependence on the main direction of movement. In this context, better sensitivity is obtained in the frontal part with respect to the GB-SAR (the green ellipse in Fig. 4b). The main reason for this is that the expected movements are almost parallel to the LOS. If we focus in this area, movements ranging from 2.5 to 3.5 cm d^{-1} are observed. However, other areas showed almost no movement during the analysed periods. These areas mainly correspond to the upper part of the easternmost ice body, and the majority of the western part of the glacier. A similar

Table 3. Changes in ice elevation measured with the TLS over the glacier from 2011 to 2017. The table also shows a correlation matrix of the different years from 100 points randomly selected over the glacier

Year	Change (m)	2011–12	2012–13	2013–14	2014–15	2015–16	2016–17
2011–12	−1.8	1					
2012–13	0.35	−0.18	1				
2013–14	−0.05	0.19	0.23	1			
2014–15	−1.7	0.55*	−0.24	−0.14	1		
2015–16	−0.35	0.12	0.58*	0.31	0.03	1	
2016–17	−2.5	0.61*	−0.16	0.08	0.43*	0.04	1
2011–17	−6.1	0.69*	0.34	0.38	0.34	0.64*	0.49*

*Indicates statistically significant correlations ($p < 0.01$).

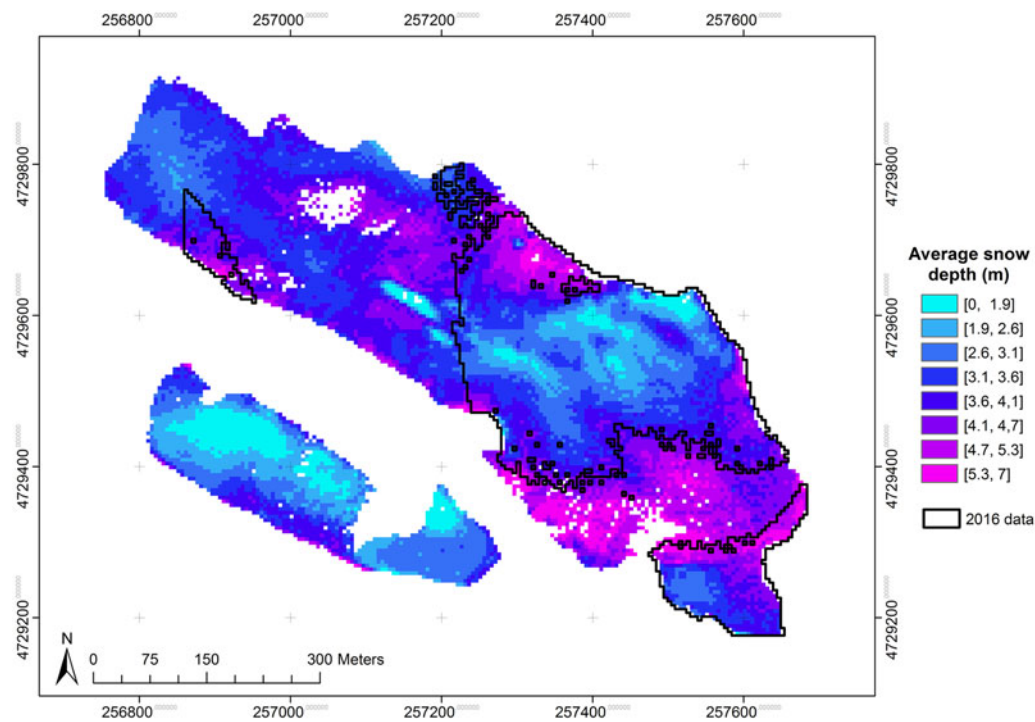


Fig. 7. Average snow accumulation (m) for the years 2014, 2015 and 2017, and the area from which it was possible to retrieve snow depth data in 2016.

spatial pattern has been observed from the measured movement in seven ablation stakes, monitored by differential GPS each September for the period 2014–2017. Even the magnitudes measured in the ablation stakes (ranging from 32 cm a^{-1} to 9.98 m a^{-1}) are slightly lower (note that ablation stakes are average daily values calculated from annual displacements) but comparable to those measured with GB-SAR.

Figure 10 shows some examples of time series obtained for points 1–6 (depicted by circles) in Figure 9, and for the points (a–e, depicted as rhomboids) located in rock areas where no displacements are expected and observed: this check can be considered an estimate of the precision of the GB-SAR measurements (in order of mm); there are minor fluctuations and trend, which can be due to accumulation of atmospheric residue and noise introduced by ice melt runoff on the rock faces. Focusing on the moving points (1–7 in Fig. 9), the time series shows that the observed movements are almost linear. However, it is observed that during some nights the movement becomes slower, e.g. July 27 and 28. This has been confirmed by nocturnal images. These results show velocities $\sim 50\%$ slower during night time.

4.4. Ice thickness estimates and internal structure

Both the processing of the radar profiles and the RWV estimates have been implemented using the software ReflexW v7.6 (Sandmeier Geophysical Research, <http://www.sandmeier-geo.de/reflexw.html>). To estimate the RWV in the underlying media, we used the diffraction hyperbolae method in the spring profiles, assuming a simple model of two homogeneous and isotropic layers of snow (shallower layer 1) and ice (deeper layer 2). Since the autumn profiles did not contain diffraction hyperbolae of sufficient quality to apply this method, we used the spring results to estimate the RWV values for the whole study.

Figure 11 shows the three radargrams collected in the spring 2016 campaign, with a first post-processing consisting in energy decay correction, background removal and dewow. From the different hyperbolae in the radargrams collected with the 200 and 500 MHz antennas (T200 and T500 in Fig. 10), we estimate that V , the RWV for the averaged media, and V_1 , the RWV for the snow, are 169 ± 4 and $200 \pm 5 \text{ m } \mu\text{s}^{-1}$, respectively. For these estimates, we assumed that the diffractor sizes were $\sim 1 \text{ m}$ (wavelength of the 200 MHz wave), large enough to generate strong

Table 4. Snow accumulation measured with the TLS over the glacier during the 4 years. Values in parentheses correspond to the area where it was only possible to acquire data in 2016. The table also shows snow density measured in one snow pit over the glacier, and a correlation matrix for the years based on 100 points randomly selected over the glacier

Year	Average (m)	Density (kg m^{-3})	2013–14	2014–15	2015–16	2016–17
2013–14	3.55 (3.2)	462	1			
2014–15	3 (2.8)	448	0.75*	1		
2015–16	– (4.55)	437	–	–	1	
2016–17	3.2 (3.15)	471	0.43*	0.36*	–	1
Average	3.25	454	0.85	0.82	–	0.76

*Indicates statistically significant correlations ($p < 0.01$).

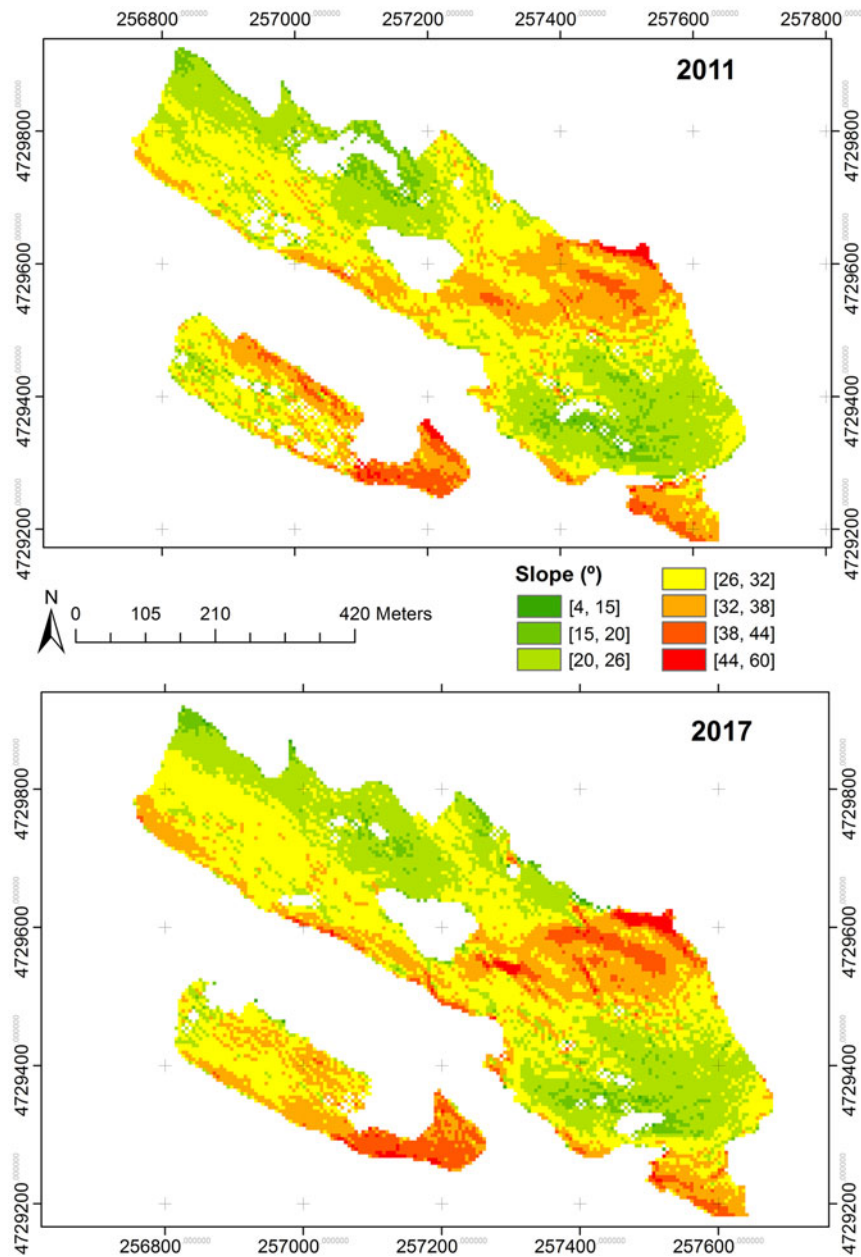


Fig. 8. Slope angle of the glacier ice surface in 2011 and 2017.

hyperbolae at 200 MHz but small enough to explain the weaker hyperbolae at 50 MHz. Thus, knowing the RWVs and thicknesses of the mixed medium and of the snow layer, we use Eqn (1) to obtain the RWV in the ice layer, $V_2 = 163 \pm 7 \text{ m } \mu\text{s}^{-1}$. Then, we can estimate relative permittivities of 3.39 ± 0.30 and 2.25 ± 0.11 for ice and snow, respectively (Bogorodsky and others, 1985).

Although this method is usually affected by large uncertainty, we consider that the resulting RWVs in this case are adequate, and we use them because the profiles contain a large amount of hyperbolae confirming such velocities, which diminishes the error. Using the estimated velocities, the maximum thickness we determined in the spring was $31.7 \pm 1.3 \text{ m}$, located at a horizontal distance of 93 m from the start of the radargram. At that point, the thickness of the snow layer was $5.9 \pm 0.3 \text{ m}$ and the ice thickness was also at a maximum, reaching a value of $25.8 \pm 1.6 \text{ m}$.

Figure 12 shows three examples of the 200 MHz radargrams conducted in the autumn. For their processing, we chose the RWV for the ice estimated from the spring

profiles (i.e. $163 \text{ m } \mu\text{s}^{-1}$). Their processing included horizontal and vertical filters, time-dependent signal amplification, dynamic correction, deconvolution, migration and time-to-depth conversion. Panels A, B and D also include topographic correction. Profile A, one of the set P1a in Figure 2, suggests the existence of more than 10 m of firn. The central part of the profile exhibits a very attenuated reflection of the basal bedrock, although a thickness of $\sim 46 \pm 5 \text{ m}$ can be inferred. The first half of profile B (from the set P2a in Fig. 1) does not exhibit bedrock reflection, probably due to a thicker ice layer and the presence of circulating liquid water. However, a clear reflection starts at $27 \pm 5 \text{ m}$ depth. Profile C (from the set P3a in Fig. 2) is also shown in panel D after its topographic correction. It exhibits noticeable ice thickness in its central part ($\sim 40 \pm 5 \text{ m}$), though with very diffuse reflection, probably due to the presence of abundant interstitial water and impurities near the bedrock. This radargram shows the existence of a marked concave shape in the bedrock (panel D), which could facilitate the accumulation of liquid water in this part of the glacier.

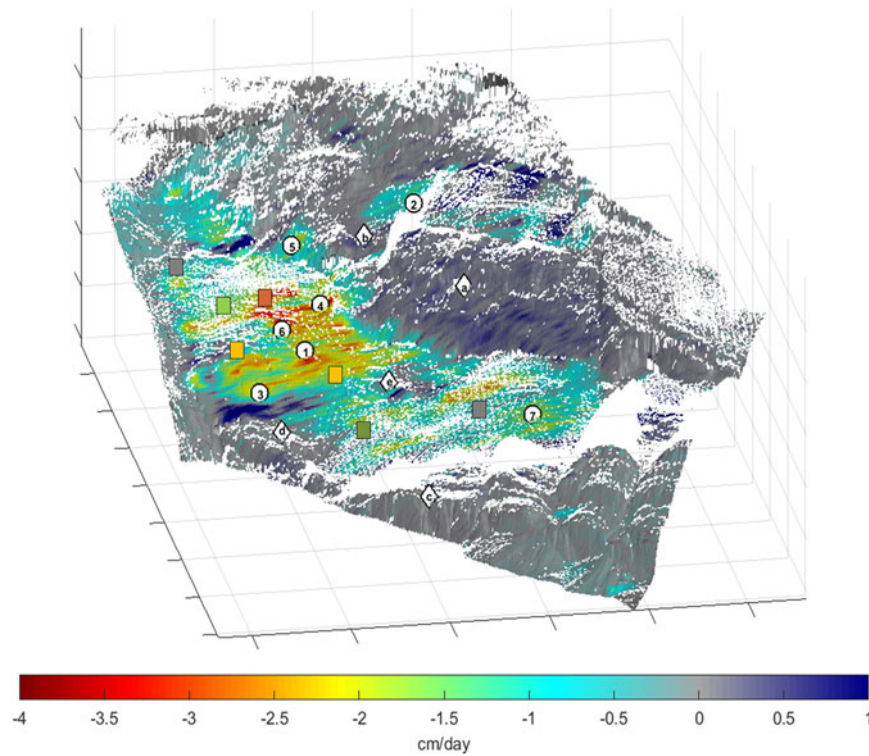


Fig. 9. Deformation velocity map in cm d^{-1} obtained from the whole GB-SAR dataset (71 images). Numbers indicate the time series depicted in Figure 10. Rectangles inform of the average daily displacement (cm a^{-1}) measured in seven ablation stakes during 4 years (2014–2017) of observations (measured in September each year).

A more detailed picture of the glacier structure can be seen in Figure 13, which shows the T200 radargram of profile P1S, once processed (with additional gain filter, migration and topographic correction). It is possible to identify three vertical layers from top to bottom: (i) the snowpack composed of different layers; (ii) the next layer of firn; and the (iii) glacial ice. It suggests that boulders and tills compose the basal zone. In Figure 12 we have also shown the estimated

evolution, since 1981, of the surface elevation at profile P1S, indicating the lowering of the glacier surface observed in the last decades.

5. DISCUSSION

Acquiring in situ observations of this glacier, although possible, was very challenging and very likely it will become more

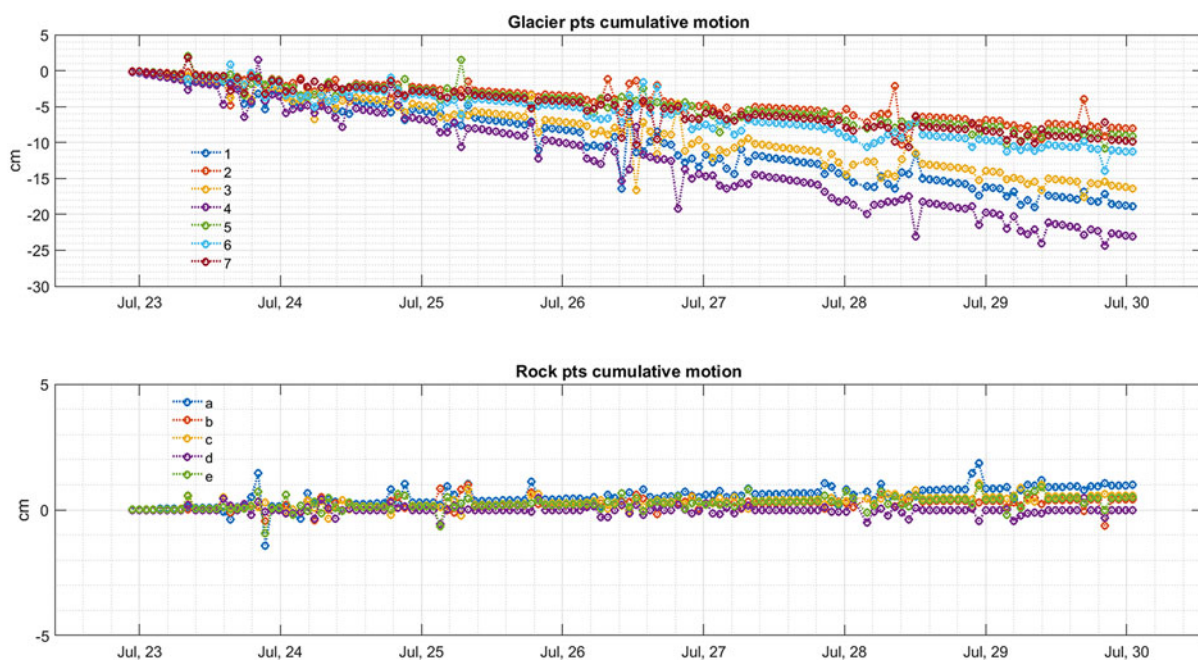


Fig. 10. (a) Deformation time series of the points marked by number (circles) in Fig. 9 (above); and (b) the points marked by letters (marked with rhomboids in Fig. 9) (below).

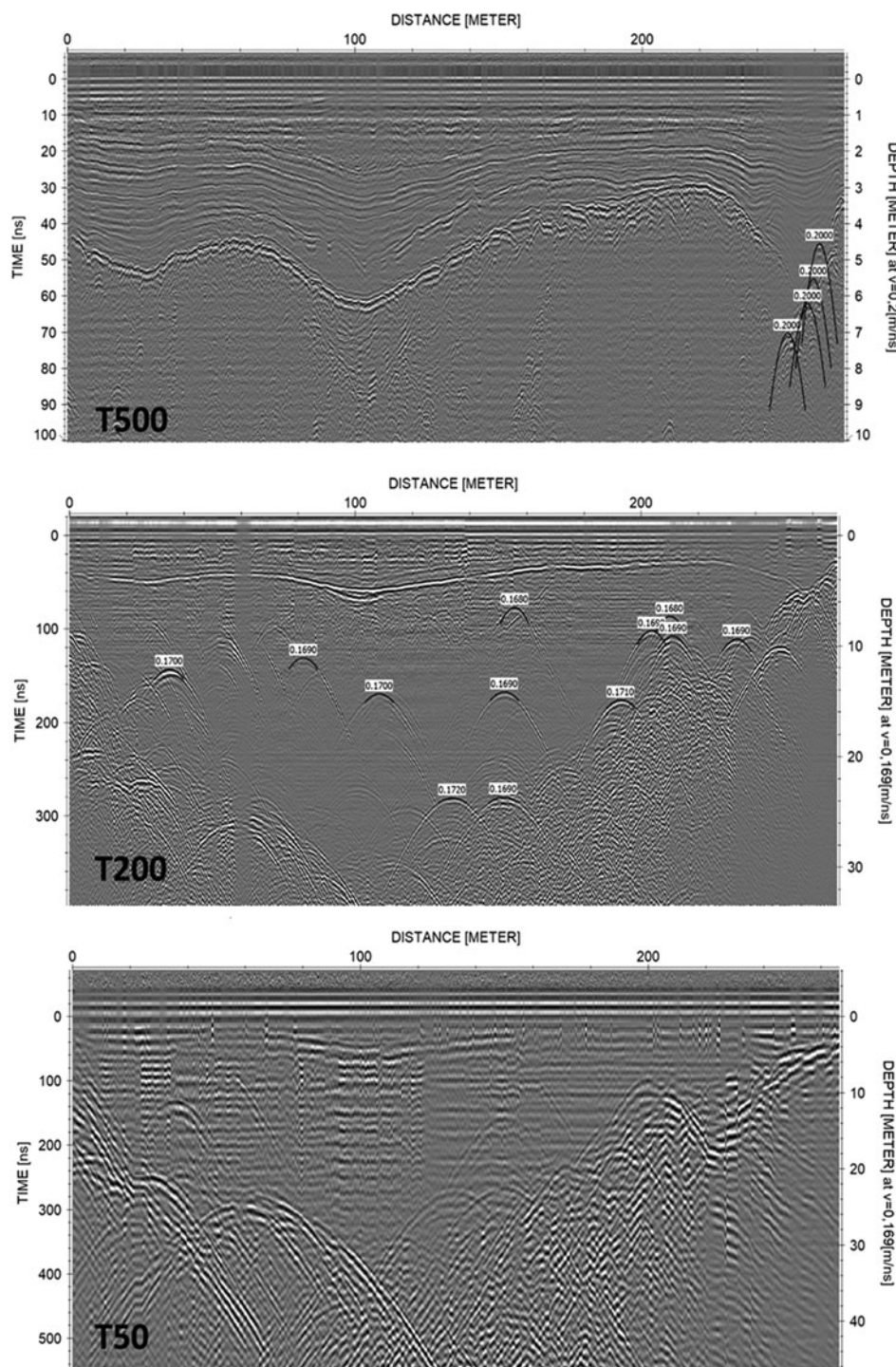


Fig. 11. Radargrams obtained in spring (30 April/1 May) with 500 (T500), 200 (T200) and 50 (T50) MHz antennas.

difficult due to increased steepness, ice collapses and rockfalls in the next years. The current characteristics of the glacier in terms of topography, existence of hollows and water circulating above and beneath the ice surface also made it difficult to properly apply GB-SAR and GPR methods. Also, the severe meteorological conditions are a limiting factor in the use of TLS in such a high mountain environment.

5.1. Interannual changes in thickness and slope of the Monte Perdido Glacier

Errors using TLS for calculating changes in the elevation of the ice surface were estimated at ± 0.30 m at the

working distance for this glacier (1000–2000 m from the scanning position; López-Moreno and others, 2016); and the error increased to ± 0.40 m for the estimation of snow thickness, as a consequence. Slight instabilities of the tripod on frozen soils (Revuelto and others, 2014) required point cloud alignment (ICP algorithm; Pomerleau and others, 2015) in the post-processing. In addition, unexpected windy conditions recorded in late April 2016 impeded proper scanning of the whole glacier, and it was only possible to cover an area of $\sim 62\%$ of the lower glacier. This shows the strong dependence on atmospheric conditions during TLS acquisition (Revuelto and others, 2014).

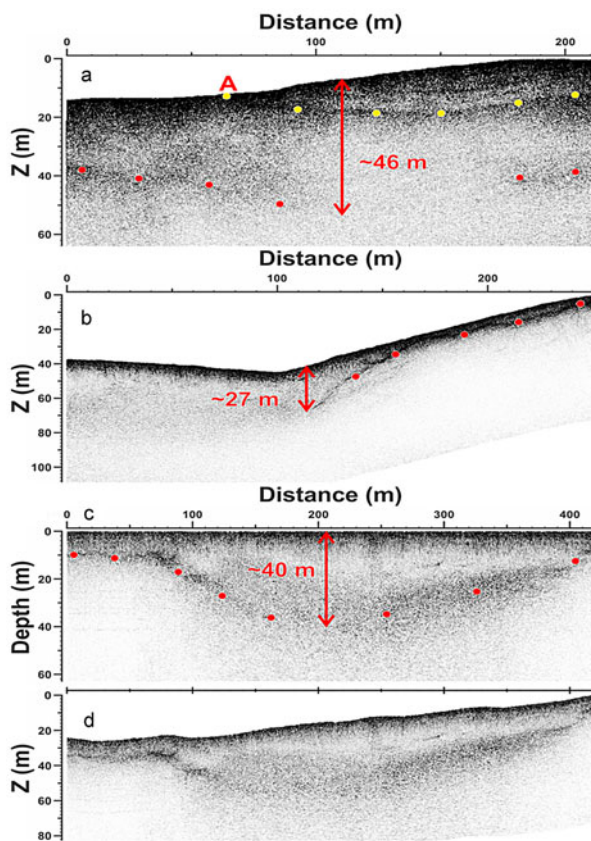


Fig. 12. Examples of 200 MHz radargrams obtained in the autumn campaign. Red dots delineate the estimated basal zone, and yellow points indicate the estimated transition between ice and firm. Panels a, b and c show processed profiles, converted into depth and affected by a topographic correction, thus Z representing relative altitude from a datum placed at the highest point of the profile. Panels c and d represent the same profile, without and with such a topographic correction.

Despite the uncertainties mentioned above, TLS has provided clear information on the irregular thinning of the ice body in time, occurring mostly in specific years and certain zones when average ice losses over the entire glacier exceed 1.5 m, whereas other years the glacier remained rather stable. To our knowledge, TLS has not been used yet for monitoring interannual snow accumulation on a glacier, although it has been used for isolated years with very similar uncertainty to that obtained in our studies (Xu and others, 2017). Our observations have resulted in useful information on the dynamics of snow over the glacier at the end of the accumulation season. Snow has recorded less interannual variability than ice surface lowering, with variability lower than 30% with respect to the interannual average. The patterns of snow distribution tend to change from one year to another, with rather low correlation coefficients between years, probably due to wind redistribution effects under contrasting annual dominant directions (Dadic and others, 2010). However, for some years, high correlations have been observed, and thus longer observation periods may allow acquisition of stronger conclusions. In general, there is not a clear relationship between snow accumulation and the magnitude of ice losses during summer, since during years with high snow accumulation, the glacier has exhibited strong ice losses during the ablation period (i.e. 2016 and 2017). This could suggest that the annual mass balance of

the glacier is dominated by melting during ablation rather than by accumulation during winter and spring. Additionally, some areas of the glacier have noticeably increased slope angle in the last 6 years, which may markedly affect snow accumulation in these areas. Indeed, these areas have presented bare ice at the end of the accumulation period, which could accelerate degradation of the glacier at these specific spots.

5.2. Estimation of ice deformation and glacier movement

The GB-SAR measurements have shown the potential of this technique to monitor glacier movements. The results have confirmed surficial movements during the monitored summer period ranging from 2.5 to 4 cm d⁻¹ in LOS. Moreover, the results obtained using only nocturnal data have shown that the movement is, on average, up to 50% slower at night than during the day. We have also observed some variability in ice motion speed over different days. Values of ice motion speed from ablation stakes exhibited a very similar spatial pattern to that obtained from GB-SAR but, in general, lower speeds with maximum annual average displacements of 2.7 cm d⁻¹, which could suggest a decrease in ice motion during the cold season, as it has been observed in other glaciers (Burgess and others, 2013; Satyabala, 2016). The results also showed one of the weakest points of the technique is dependence on the acquisition geometry. The main results have been obtained in the frontal part of the glacier with respect to GB-SAR point of view. In this area, sensitivity to displacement was high. However, in the more lateral area, sensitivity to displacement can be very small, preventing a direct interpretation of the results.

5.3. Ice thickness and internal structure

The application of GPR techniques was problematic in the autumn, probably due to the large amount of water circulating over and beneath the glacier surface. Nonetheless, it allowed us to estimate ice thickness (within an uncertainty of 5 m) for large areas of the glacier, revealing that it is still possible to find ice thicknesses between 30 and ~50 m in some sectors of the glacier. The GPR survey conducted in spring covered a much smaller area but provided noticeably better radargrams, with resolutions better than 1.5 m. The ice thickness measurements from both campaigns are compatible, thus confirming their results. However, the use of three different antennas in the spring profiling, and the clarity of their radargrams, allowed better identification of the internal structure of the snow cover and the ice, revealing that remnant ice has a high content of tills that may translate into a noticeable increase of debris cover as thawing continues.

The estimated values for the RWV, 200 and 163 m μs⁻¹, and relative permittivities of 3.39 and 2.25 are consistent with those in snow and ice (Daniels, 1996; Eisen and others, 2002; Benjumea and others, 2003).

5.4. Current behaviour of Monte Perdido Glacier and future expectations

Overall, results confirm the advanced stage of degradation of the Monte Perdido Glacier. At the beginning of this period, during 1981–2010, the thinning rate was measured by López-Moreno and others (2016) at 0.6 ± 0.3 m a⁻¹. However,

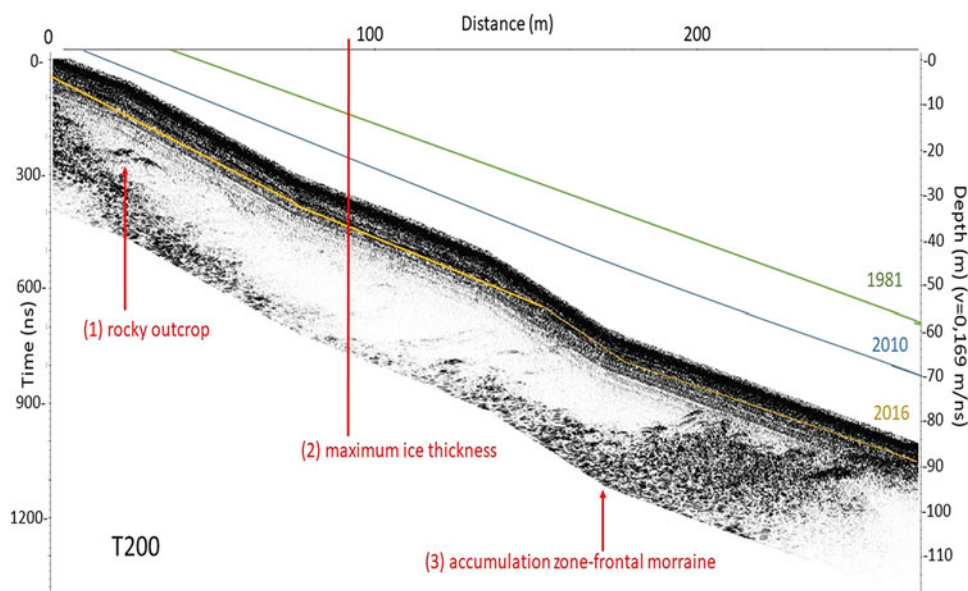


Fig. 13. Structure of the glacier obtained from the radargram 200 (T200) MHz after post-processing from GPR survey conducted in spring (P1S in Fig. 1). The estimated surface of the glacier from TLS data and previous geomatic analysis (López-Moreno and others, 2016) are also indicated.

the thinning of the glacier is accelerating, given that it has lost, on average, 6.1 m of ice thickness in the last 6 years (1 m a^{-1}), with 10–15 m of ice loss in wide areas. Mean annual average ice depth loss reported in our study matches closely to the study of Marti and others (2015) for the Ossoue glacier, who reported a mean ice thinning between 20 and 50 m for the period 1983–2013. These values illustrate the critical situation of the glacier, considering that the ice thickness in most parts of the glacier is $<30 \text{ m}$, and that the thicker ice measured is $46 \pm 5 \text{ m}$. Assuming a similar trend in the future (e.g. not $<1 \text{ m a}^{-1}$), extinction of the entire glacier could be expected within the next 50 years. This dramatic situation is leading to further study the glacier ice in Monte Perdido from a paleoenvironmental point of view analysing an ice core retrieved in 2017 as a final opportunity to extract information of past climate conditions (e.g. determining the glacier stage during past warm periods such as the Medieval Climate Anomaly).

The hypothesis that glacier mass balance clearly responds to summer ablation more than winter and spring accumulation leads to a pessimistic scenario for the short-term future, since precipitation in the cold season has not shown clear trends in the past (Fig. 4) and projected scenarios do not inform of clear changes. However, spring and summer temperatures have significantly increased and are foreseen to continue increasing (López-Moreno and others, 2011), which means a longer and more intense ablation season. This situation is also evidenced by the very reduced, or inappreciable (with GB-SAR technique) movement in wide areas of the glacier, especially in the westernmost part of the glacier, where ice is near stagnant and ice losses are particularly high. The easternmost sector presents lower ice losses and areas with noticeable movement (annual average of 1.5–2.5 and 3–4.5 cm d^{-1} during summer 2015) and, in turn, it is also the area where a thicker ice has been measured. The glacier has not exhibited a slowdown yet in melt rates as could be hypothesized (DeBeer and Sharp, 2009) for a very degraded ice body, and it could happen once most of the western part of the glacier disappears

(which could occur two decades or less if current conditions persist). Only the eastern part of the glacier will last, and it is expected that it will melt at lower rates. The high content of till in the remnant ice, shown by GPR data, informs that debris cover, already rapidly increased in the last years, will expand and get thicker in coming years. Mass-balance measurements carried out in the Maladeta and Ossoue glaciers (together with Monte Perdido Glacier, the biggest glaciers in the Pyrenees) (Marti and others, 2015) for the last years, and recent estimations of decline of glaciated surface for the entire Pyrenees (Rico and others, 2017), highlight that degradation of the Monte Perdido Glacier is highly representative of the current situation of the other 18 existing glaciers, which identifies the Pyrenean glaciers as some of the most endangered glaciers in the world.

6. CONCLUSIONS

Results shown in this study highlight the potential of combining information from TLS, GPR and GB-SAR to obtain valuable information on current conditions of the Monte Perdido Glacier and recent evolution. TLS data have allowed to determine an average ice thinning of 6.1 m for the period 2011–2017 (1 m a^{-1}), with wide sectors exhibiting losses of 10–15 m of ice depth. There is not a clear relationship between snow accumulation and the magnitude of ice losses, suggesting that the annual mass balance would be dominated by melting during ablation season. GBSAR have allowed to quantify average ice motion of the glacier during summertime in 2.5–4.0 cm d^{-1} . A fluctuation in ice speed is suggested by collected data during day and night period, and also a noticeable variability between different measurement days. GPR campaigns indicated that ice thickness in the glacier ranges among 30 and $\sim 50 \pm 5 \text{ m}$ in the best preserved areas of the glacier. The maximum measured ice thickness for the glacier, the annual rates of ice thinning and the evidence of stagnation in much of the ice-covered area confirm the critical situation of the Monte Perdido

glacier that could evolve to a glaciaret of very reduced size in the next three to five decades.

ACKNOWLEDGEMENTS

E. Alonso-González is supported by a FPI fellowship of the Spanish Ministry of Economy and Competitiveness (BES-2015-071466). J. Revuelto is supported by a Post-doctoral Fellowship of the AXA research foundation. This research was made possible partially by funding granted by the Junta de Extremadura and the Fondo Europeo de Desarrollo Regional-FEDER, through the reference GR15107 to the research group COMPHAS and the EXPLORA PaleolCE project (ref. CGL2015-72167-EXP), and CLIMPY (FEDER-POCTEFA). The research of J. Lapazaran and J. Otero was funded by the Spanish State Plan for Research and Development project CTM2014-56473-R. We thank the two anonymous reviewers and the scientific editor (Bernd Kulessa) for their constructive comments and help to improve our work.

REFERENCES

- Arcone SA and Kreutz K (2009) GPR reflection profiles of Clark and Commonwealth Glaciers, Dry Valleys, Antarctica. *Ann. Glaciol.*, **50**(51), 121–129
- Benjumea B, Macheret Y, Navarro FJ and Teixidó T (2003) Estimation of water content in a temperate glacier from radar and seismic sounding data. *Ann. Glaciol.*, **37**, 317–324
- Bhardwaj A, Samb L, Bhardwaj A and Martín-Torres J (2016) LiDAR remote sensing of the cryosphere: present applications and future prospects. *Remote Sens. Environ.*, **177**, 125–143
- Bogorodsky VV, Bentley CR and Gudmandsen PE (1985). *Radioglaciology*. D. Reidel Publishing Company, Dordrecht, Holland. 254 p
- Bradford JH, Nichols J, Mikesell TD and Harper JT (2009) Continuous profiles of electromagnetic wave velocity and water content in glaciers: an example from Bench Glacier, Alaska, USA. *Ann. Glaciol.*, **50**(51), 1–9
- Brock BW and 5 others (2010) Meteorology and surface energy fluxes in the 2005–2007 ablation seasons at the Miage debris-covered glacier, Mont Blanc Massif, Italian Alps. *J. Geophys. Res. Atmos.*, **115**, D09106. doi: 10.1029/2009JD013224
- Burgess EW, Larsen CF and Forster R (2013) Summer melt regulates winter glacier flow speeds throughout Alaska. *Geophys. Res. Lett.*, **40**, 6160–6164. doi: 10.1002/2013GL058228
- Caduff R, Schlunegger F, Kos A and Wiesmann A (2015) A review of terrestrial radar interferometry for measuring surface change in the geo-sciences. *Earth Surf. Process. Landf.*, **40**, 208–228
- Carrivick JL and 5 others (2015) Decadal-scale changes of the ödenwinkelkees, Central Austria, suggest increasing control of topography and evolution towards steady state. *Geografiska Ann. Ser. A Phys. Geogr.*, **97**, 543–562. doi: 10.1111/geoa.12100
- Carturan L and 5 others (2013) Current behaviour and dynamics of the lowermost Italian glacier (Montasio Occidentale, Julian Alps). *Geografiska Ann. Ser. A Phys. Geogr.*, **95**, 79–96. doi: 10.1111/geoa.12002
- Clarke TS and Bentley CR (1994) High-resolution radar on Ice Stream B2, Antarctica: measurements of electromagnetic wave speed in firn and strain history from buried crevasses. *Ann. Glaciol.*, **20**, 153–159
- Dadic R, Mott R, Lehning M and Burlando P (2010) Wind influence on snow depth distribution and accumulation over glaciers. *J. Geophys. Res.*, **115**, F01012. doi: 10.1029/2009JF001261
- Daniels S (1996) Surface Penetrating Radar. The Institution of Electrical Engineers. IEE Radar, Sonar, Navigation and Avionics. Series 6
- Debeer CM and Sharp MJ (2009) Topographic influences on recent changes of very small glaciers in the Monashee Mountains, British Columbia, Canada. *J. Glaciol.*, **55**, 691–700. doi: 10.3189/002214309789470851
- Deems J, Painter TH and Finnegan DC (2013) Lidar measurement of snow depth: a review. *J. Glaciol.*, **59**(215), 467–479
- Del Río M, Rico I, Serrano E and Tejado JJ (2014) Applying GPR and laser scanner techniques to monitor the Ossoue Glacier (Pyrenees). *J. Environ. Eng. Geophys.*, **19**(4), 239–248
- Dematteis N, Luzi G, Giordan D, Zucca F and Allasia P (2017) Monitoring Alpine glacier surface deformations with GB-SAR. *Remote Sens. Lett.*, **8**(10), 947–956
- Dyurgerov MB and Meier MF (2000) Twentieth century climate change: evidence from small glaciers. *Proc. Natl. Acad. Sci. USA* **97**(4), 1406–1411
- Eisen O, Nixdorf U, Wilhelms F and Miller H (2002) Electromagnetic wave speed in polar ice: validation of the CMP technique with high resolution dielectric profiling and gamma-density measurements. *Ann. Glaciol.*, **34**, 150–156
- Fischer M, Huss M, Kummert M and Hoelzle M (2016) Application and validation of long-range terrestrial laser scanning to monitor the mass balance of very small glaciers in the Swiss Alps. *Cryosphere*, **10**, 1279–1295, <https://doi.org/10.5194/tc-10-1279-2016>
- Fountain AG and Walder JS (1998) Water flow through temperate glaciers. *Rev. Geophys.*, **36**(3), 299–328. doi: 10.1029/97RG03579
- García-Ruiz JM and 5 others (2014) Holocene and ‘Little Ice Age’ glacial activity in the Marboré Cirque, Monte Perdido Massif, Central Spanish Pyrenees. *Holocene*, **24**, 1439–1452. <https://doi.org/10.1177/0959683614544053>
- Grunewald K and Scheithauer J (2010) Europe’s 2010 southernmost glaciers: response and adaptation to climate change. *J. Glaciol.*, **56**(195), 129–142
- Huss M and Fischer M (2016) Sensitivity of very small glaciers in the Swiss Alps to future climate change. *Front. Earth Sci.*, **4**, 34. <https://doi.org/10.3389/feart.2016.00034>
- Julián A and Chueca J (2007) Pérdidas de extensión y volumen en los glaciares del macizo de Monte Perdido (Pirineo central español): 1981–1999. *Boletín Glaciológico Aragonés*, **8**, 31–60
- Liu H, Takahasi K and Sato M (2014) Measurement of dielectric permittivity and thickness of snow and ice on a brackish lagoon using GPR. *IEEE J-STARS*, **7**(3), 820–827
- López-Moreno JI and 5 others (2011) Impact of climate evolution and land use changes on water yield in the ebro basin. *Hydrol. Earth Syst. Sci.*, **15**, 311–322, <https://doi.org/10.5194/hess-15-311-2011>
- López-Moreno JI and 10 others (2016) Thinning of the Monte Perdido Glacier in the Spanish Pyrenees since 1981. *Cryosphere*, **10**, 681–694, <https://doi.org/10.5194/tc-10-681-2016>
- López-Moreno JI and 9 others (2017). Different sensitivities of snow-pack to warming in Mediterranean climate mountain areas. *Environ. Res. Lett.*, **12**, 074006
- Luzi G and 6 others (2007) Monitoring of an Alpine glacier by means of ground-based SAR interferometry. *IEEE Geosci. Remote Sens. Lett.*, **4**(3), 495–499
- Marshall S (2014). Glacier retreat crosses a line. *Science*, **345**(6199), 872. <https://doi.org/10.1126/science.1258584>
- Marti R and 11 others (2015) Evolution of Ossoue Glacier (French Pyrenees) since the end of the Little Ice Age. *Cryosphere*, **9**(5), 1773–1795. <https://doi.org/10.5194/tc-9-1773-2015>
- Monserrat O, Crosetto M and Luzi G (2014) A review of ground-based SAR interferometry for deformation measurement. *ISPRS J. Photogramm.*, **93**, 40–48
- Moore JC and 8 others (1999) High-resolution hydrothermal structure of Hansbreen, Spitsbergen, mapped by ground-penetrating radar. *J. Glaciol.*, **45**(151), 524–532
- Murray T, Booth A and Rippin DM (2007) Water-content of glacier-ice: limitations on estimates from velocity analysis of surface ground-penetrating radar surveys. *J. Environ. Eng. Geophys.*, **12**(1), 87–99

- Noferini L, Mecatti D, Macaluso G, Pieraccini M and Atzeni C (2009) Monitoring of Belvedere Glacier using a wide angle GB-SAR interferometer. *J. Appl. Geophys.*, **68**(2), 289–293
- Pomerleau F, Colas F and Siegwart R (2015) A review of point cloud registration algorithms for mobile robotics. *Found. Trends Robotics*, **4**(1), 1–104. doi: 10.1561/23000000035
- Revuelto J and 5 others (2014) Mapping the annual evolution of snow depth in a small catchment in the Pyrenees using the long-range terrestrial laser scanning. *J. Maps*, **10**(3), 359–373
- Rico I, Izaguirre E, Serrano E and López-Moreno JI (2017) Current glacier area in the Pyrenees: an updated assessment 2016. *Pirineos*, **172**, e029. <http://doi.org/10.3989/Pirineos.2017.172004>
- Riesen P, Strozzi T, Bauder A, Wiesmann A and Funk M (2011) Short-term surface ice motion variations measured with a ground-based portable real aperture radar interferometer. *J. Glaciol.*, **57**(201), 53–60
- Satyabala SP (2016) Spatiotemporal variations in surface velocity of the Gangotri glacier, Garhwal Himalaya, India: study using synthetic aperture radar data. *Remote Sens. Environ.*, **181**, 151–161. doi.org/10.1016/j.rse.2016.03.042
- Schwamborn G, Heinzel J and Schirrmeister L (2008) Internal characteristics of ice-marginal sediments deduced from georadar profiling and sediment properties (Brøgger Peninsula, Svalbard). *Geomorphology*, **95**, 74–83
- Solomina ON and 16 others (2016) Glacier fluctuations during the past 2000 years. *Quat. Sci. Rev.*, **149**, 61–90. <https://doi.org/10.1016/j.quascirev.2016.04.008>
- Strozzi T, Werner C, Wiesmann A and Wegmuller U (2012) Topography mapping with a portable real-aperture radar interferometer IEEE. *Geosci. Remote Sens. Lett.*, **9**(2), 277–281
- Tarchi D and 5 others (1999) SAR interferometry for structural changes detection: a demonstration test on a dam. In: Proc. IGARSS Hamburg, Germany, 1522–1524
- Voytenko D and 6 others (2012) Monitoring a glacier in southeastern Iceland with the portable Terrestrial Radar Interferometer. *Proc. IGARSS*, 3230–3232
- Xu C and 5 others (2017) Using an ultra-long-range terrestrial laser scanner to monitor the net mass balance of Urumqi Glacier No. 1, eastern Tien Shan, China, at the monthly scale. *J. Glaciol.*, **63**(241), 792–802. doi: 10.1017/jog.2017.45

MS received 16 June 2018 and accepted in revised form 13 November 2018

CONCLUSIONS

The study presented in the thesis treats the application, the techniques and the results of ground-based (GB) remote sensing (RS) sensors to monitor glaciological processes. The thesis proposes answers to the following three questions:

Why ground-based remote sensing? Gravitational slope phenomena, and specifically glaciers, can have a strong impact on human activities. Therefore, their monitoring is essential to understand their current state and possible evolution. Remote sensing sensors have the great value of being able to measure physical properties without the need to access into the investigated, and possibly perilous, area. Therefore, they allow at reducing human costs. On the other hand, ground-based systems are complementary to the aerospace-borne sensors, because they provide finer spatio-temporal resolution and they are able to observe phenomena that occur in complex geometries.

How to use/process GBRS sensors? First, a methodological analysis must be conducted to evaluate the sensor features and to develop techniques to couple the data acquired by the different sensors. Then, the methodologies can be applied to monitor natural phenomena.

What are the results? The sensor characterisation provides a clear assessment of their limits and potentialities and it allows to develop innovative processing methods to couple the data in an integrated model to obtain more informative results. The coupled model allows at exploiting the full potentialities of the single sensors and their limitations can be reduced. The application of the techniques to monitor natural processes provides insight into their dynamics and behaviour. This is a crucial aspect of developing strategies for risk mitigation and adaptation against possible hazardous phenomena.

The work expounded in the thesis can be divided into two main parts: a first methodological study on the development of processing techniques and a second study that describes the operative applications of the methodologies to define interpretative models of glacier behaviour and state.

To the methodological part belong three main arguments: i) image analysis, ii) GB-SAR and iii) coupling data from different sensors for 3D displacement estimate.

The image analysis study focused on the development of ICC processing, with which it is possible to measure the two components of the surface deformation orthogonal to the LOS. In particular, the ICC was applied to photographs acquired by DSLR cameras that monitor the Planpincieux glacier.

During the development of the processing methodologies, it emerged an issue related to the presence of shadows that can affect the cross-correlation calculation. The shadows are caused by the direct illumination of the solar radiation on a rough surface. In literature, the most common approach to minimising the problem is the manual selection of images acquired with similar illumination. The best conditions correspond to diffuse illumination, where the shadow presence is minimal. Nevertheless, the manual selection of the images requires important human efforts, especially for long-lasting and continuous monitoring activities. Therefore, to solve this issue, an innovative approach to automatically select the images included in an autonomous ICC processing chain has been developed. The method is based on machine learning techniques for automatic classification. Such solution was experimented in 2018 in the continuous monitoring activity of the Planpincieux glacier and it became operative in 2019, allowing relevant saving of human resources.

The papers “A low-cost optical remote sensing application for glacier deformation monitoring in an alpine environment” and “Image Classification for Automated Image Cross-Correlation Applications in the Geosciences” are dedicated respectively to these two topics of image analysis.

The TRI method was applied for measuring the surface displacement of Planpincieux and Monte Perdido Glaciers. The survey campaigns proved that the GB-SAR is able to operate in mountain environments, where the sensor-to-target difference in altitude is high and the atmospheric conditions are adverse. In particular, a new simple model to solve the disturbing effects produced by the atmosphere has been developed and successfully applied.

One of the difficulties of the TRI is the interpretation of the radar maps, that is crucial to identify stable reference areas, but the recognitions between different surfaces is not trivial.

The radar polarimetry can help in this task. Therefore, circularly polarised antennas have been applied in an experimental site. The combination of different polarisations proved to facilitate the identification of various surfaces. In addition, the circular polarisation is less affected by multipath and atmospheric effects, hence it might be used to improve TRI measurements.

The papers “Monitoring Alpine glacier surface deformations with GB-SAR” and “Terrestrial radar interferometry to monitor glaciers with complex atmospheric screen” describe the TRI application for monitoring glacier, while “Ku band terrestrial radar observations by means of circular polarized antennas” concerns the analysis of circular polarisation.

The core of the methodological part appertains the development of an innovative technique to combine the results of ICC and TRI. The two techniques measure complementary displacement components. In fact, ICC detects the two components orthogonal to the LOS, while TRI detects the component parallel to the LOS. The coupling allows at obtaining the spatial 3D representation of the displacement vectors. The developed technique can be applied also when the two sensors are installed in different locations, therefore guaranteeing great operative flexibility. The most critical part concerns data georeferencing. The georeferencing of radar data is a poor studied argument in literature. Therefore, it has been developed an innovative method that proved to outperform traditional approaches.

The data coupling is described in detail in the paper “4D surface kinematics monitoring through terrestrial radar interferometry and image cross-correlation coupling”.

The second part of the thesis appertains the application of the developed methodologies to specific case studies. Two different glaciers have been studied using image analysis and TRI.

The Planpincieux glacier has been monitored since autumn 2013 with DSLR cameras that acquired a photograph every hour. The ICC provided i) the surface deformation maps, which allowed to recognise the different kinematic domains and ii) the time series of daily velocity of the different domains. The analysis of the time series revealed the activation of velocity fluctuations that occurred a few times every year. Such fluctuations have well-defined velocity and acceleration thresholds. Moreover, the visual inspection of the images allows identifying the break-off occurrence and their volume. This study showed that large break-offs occurred in correspondence of the peaks of the velocity fluctuations. Moreover, with the visual analysis allowed to classify the different instability processes of the glacier terminus and to identify the break-off occurrence.

This study is described in the manuscript “Classification and kinematics of glacier break-offs using photographic time-lapse analysis”.

The second case study is the Monte Perdido glacier, in the Spanish Pyrenees. Since 2011, the glacier was analysed with different remote-sensing and in-situ sensors to evaluate its current state and recent evolution. The contribute of the PhD candidate concerns the processing of GB-SAR data acquired during a 30 days-long campaign, which was characterised by extreme weather.

The results of the analysis conducted using an integrated framework composed by GB-SAR, GPR, TLS and ablation stakes demonstrated that the glacier retreated at least since the 1970s and that the ice mass reduction increased in the recent years in accordance with warmer summer seasons. The advanced stage of degradation is probably due to global warming and the glacier is foreseen to disappear within the few decades.

This research is described in “Ground-based remote-sensing techniques for diagnosis of the current state and recent evolution of the Monte Perdido Glacier, Spanish Pyrenees”.

